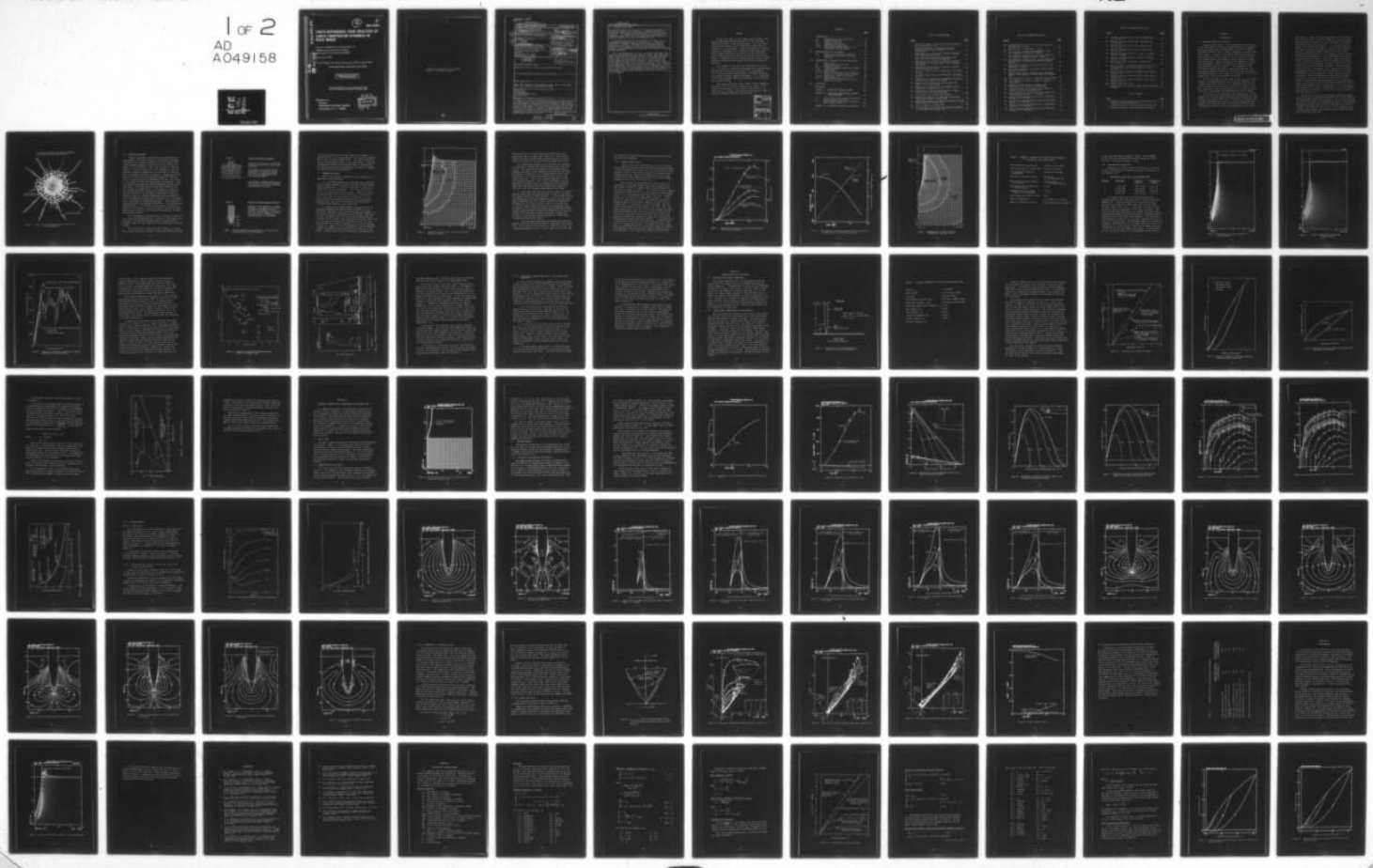
AD-A049 158 CALIFORNIA RESEARCH AND TECHNOLOGY INC WOODLAND HILLS F/G 8/7
FINITE-DIFFERENCE CODE ANALYSES OF EARTH PENETRATOR DYNAMICS IN--ETC(U)
NOV 76 M H WAGNER, C C FULTON DNA001-75-C-0147
UNCLASSIFIED CRT-2080-2 DNA-4069T NL

1 OF 2
AD
A049158



AD-E300 027

AD A049158

AU No.
DDC FILE COPY

(12)

DNA 4069T

FINITE-DIFFERENCE CODE ANALYSES OF EARTH PENETRATOR DYNAMICS IN ROCK MEDIA

California Research & Technology, Inc.
6269 Variel Avenue, Suite 200
Woodland Hills, California 91367

November 1976

Topical Report for Period February 1975—August 1976

CONTRACT No. DNA 001-75-C-0147

APPROVED FOR PUBLIC RELEASE;
DISTRIBUTION UNLIMITED.

THIS WORK SPONSORED BY THE DEFENSE NUCLEAR AGENCY
UNDER RDT&E RMSS CODE B344075464 Y99QAXSB04801 H2590D.

Prepared for
Director
DEFENSE NUCLEAR AGENCY
Washington, D. C. 20305

DDC
RECEIVED
JAN 31 1978
B

Destroy this report when it is no longer needed. Do not return to sender.

DNA PRINTING PLANT

(18) DNA, SBIE

UNCLASSIFIED

SECURITY CLASSIFICATION OF THIS PAGE (When Data Entered)

(19) **REPORT DOCUMENTATION PAGE**

READ INSTRUCTIONS BEFORE COMPLETING FORM

1. REPORT NUMBER: DNA 4069T, AD-E300 027
2. GOVT ACCESSION NO.
3. RECIPIENT'S CATALOG NUMBER (9) rept.

4. TITLE (and Subtitle) (6): FINITE-DIFFERENCE CODE ANALYSES OF EARTH PENETRATOR DYNAMICS IN ROCK MEDIA.

5. TYPE OF REPORT & PERIOD COVERED: Topical Rpt for Period Feb 75—Aug 76

6. PERFORMING ORG. REPORT NUMBER (14): CRT-2080-2

7. AUTHOR(s) (10):
M. H. Wagner
C. C. Fulton
K. N. Kreyenhagen

8. CONTRACT OR GRANT NUMBER(s) (15): DNA 001-75-C-0147

9. PERFORMING ORGANIZATION NAME AND ADDRESS:
California Research & Technology, Inc.
6269 Variel Avenue, Suite 200
Woodland Hills, California 91367

10. PROGRAM ELEMENT, PROJECT, TASK AREA & WORK UNIT NUMBERS (16): NWED Subtask Y99QAXSB048-01 (17) 62704H B048

11. CONTROLLING OFFICE NAME AND ADDRESS (11):
Director
Defense Nuclear Agency
Washington, D.C. 20305

12. REPORT DATE: November 1976

13. NUMBER OF PAGES: 178

14. MONITORING AGENCY NAME & ADDRESS (if different from Controlling Office) (12) 170p.

15. SECURITY CLASS (of this report): UNCLASSIFIED

15a. DECLASSIFICATION/DOWNGRADING SCHEDULE

16. DISTRIBUTION STATEMENT (of this Report)

Approved for public release; distribution unlimited.

17. DISTRIBUTION STATEMENT (of the abstract entered in Block 20, if different from Report)

18. SUPPLEMENTARY NOTES

This work sponsored by the Defense Nuclear Agency under RDT&E RMSS Code B344075464 Y99QAXSB04801 H2590D.

19. KEY WORDS (Continue on reverse side if necessary and identify by block number)

Penetration
Terradynamics
Finite-Difference Codes
Rock Mechanics

20. ABSTRACT (Continue on reverse side if necessary and identify by block number)

Numerical analyses of penetration dynamics have been performed in support of a program to develop technology for earth penetrating weapons. The emphasis in this program has been to apply calculational techniques to the analysis of projectile penetrations in rock media. Observations from penetrator firings into rock show that there is a region of highly comminuted rock surrounding the penetrator and the penetrator cavity. Since the

DD FORM 1 JAN 73 1473 EDITION OF 1 NOV 65 IS OBSOLETE

UNCLASSIFIED

SECURITY CLASSIFICATION OF THIS PAGE (When Data Entered)

391 223 LB

20. ABSTRACT (Continued)

penetration dynamics are sensitive to the physical properties of the material next to the penetrator, it becomes important to account for the breakup and fracture of the rock in the analysis techniques. Accordingly, material models were developed that included fracture and a post-fracture process which degrades the physical properties to that of a comminuted rock.

The penetration analyses were performed with WAVE-L, a two-dimensional Lagrangian finite-difference code. A decoupled calculational method is employed, wherein the penetrator is treated as a rigid body to compute the penetration dynamics. Using the force loadings on the penetrator obtained from this solution, subsequent analyses may be made of the interior response of the penetrator.

To test and demonstrate the code, pre-event calculations of a specific rock penetration field test were made. The field experiment consisted of the vertical firing of a 400 pound steel penetrator into a massive welded tuff site at a velocity of 1500 ft/sec. The code solution was carried out to just beyond the point of peak loading on the penetrator. Detail descri tions of the solution results are provided, covering the force loadings on the penetrator and resulting penetrator dynamics, the predicted fractured regions in the rock, and the stress and motions in the rock. Comparisons with experimental results from four field tests are drawn. Generally good agreement was found for projectile deceleration, peak stresses developed in the rock, and the extent of the fracture.

PREFACE

The work described in this report was performed as one of the tasks under Contract DNA 001-75-C-0147, entitled "Numerical Analyses of Earth Penetrators". This task dealt with numerical analyses of the impact and penetration of projectiles into rock media. Other tasks under this contract include (1) development of a decoupled finite-difference/finite-element method for the analysis of the interior response within projectiles during penetration into the earth and (2) a parametric study to examine effects of basic target properties and projectile design variables on penetration processes.

M. H. Wagner was the principal investigator for this task. Assistance in technical development and general program guidance and liaison was provided by K. N. Kreyenhagen. C. C. Fulton assisted in development of the material models and was the principal computer programmer. W. S. Goerke and C. K. Wilson provided additional assistance in code development and programming.

The Project Officer was Major Todd D. Stong, Strategic Structures Division, Defense Nuclear Agency (DNA). Assistance in coordination of the effort was provided by P. F. Hadala and D. K. Butler, Soil Dynamics Division, U.S. Army Engineer Waterways Experiment Station (WES).

ACCESSION for		
NTIS	White Section	☑
DDC	Buff Section	☐
UNANNOUNCED		☐
JUSTIFICATION		
BY		
DISTRIBUTION/AVAILABILITY CODES		
Dist.	AVAIL. and/or SPECIAL	
A		

CONTENTS

			Page
I.	INTRODUCTION		7
	1.1	Background and Task Objectives	7
	1.2	Technical Approach	10
	1.3	Summary of Results	12
	1.3.1	Computational Results	15
	1.3.2	Experimental Comparisons	20
	1.3.3	Differences Between Conditions in Calculation and Experiment	28
II.	PROBLEM CONDITIONS AND MODELS		30
	2.1	Penetration and Impact Conditions	30
	2.2	Target Media Characteristics and Modeling	30
III.	COMPUTATIONS OF PENETRATION INTO WELDED TUFF		40
	3.1	WAVE-L Code	40
	3.2	Computational Grid Design	40
	3.3	Solution Results	42
	3.3.1	Penetration Deceleration and Loading	42
	3.3.2	Ground Response	52
	3.3.2.1	Peak Stress	52
	3.3.2.2	Stress Profiles and Stress, Velocity, and Density Contours in the Ground	52
	3.3.2.3	Compression - Extension States	69
	3.3.2.4	Energy Partition	70
	3.4	Sensitivity of Penetration to Post-Fracture Properties	76
IV.	CONCLUSIONS		78
	REFERENCES		81
	APPENDIX A - WELDED TUFF MATERIAL MODEL		83
	APPENDIX B - ADDITIONAL COMPUTATIONAL RESULTS-GROUND RESPONSE		103
	B.1	Stress and Velocity Time Histories and Stress Paths in the Field	103
	B.2	Field Plots of Deformation, Velocity, and Principal Stress	104
	APPENDIX C - EXPLORATORY PENETRATION SOLUTION		161

LIST OF ILLUSTRATIONS

Figure		Page
1.	Surface Plan View of Comminution and Fracture of Rock during Penetration	9
2.	Decoupled Approach for Making Analyses of Penetation and Response Dynamics of Earth Penetrators	11
3.	Lagrangian Grid and Fracture Pattern in Welded Tuff, Exploratory Solution.	13
4.	Axial Forces on Penetrator and Deceleration Histories from Principal Calculation.	16
5.	Time Histories of Penetrator Velocity, Depth of Penetration, and Engaged Length from Principal Calculation	17
6.	Lagrangian Grid and Fracture Pattern in Welded Tuff, Principal Solution.	18
7.	Particle Velocity Field in Welded Tuff, Principal Solution.	21
8.	Principal Stress Field in Welded Tuff, Prinicpal Solution.	22
9.	Comparison of Computed and Experimental Projectile Deceleration vs Penetration Depth	23
10.	Comparison of Computed and Experimental Peak Stress vs Horizontal Range.	25
11.	Comparison of Experimental and Computed Stress Histories at a Depth of 12 in.	26
12.	Conditions for Pre-event Calculations of Penetration Test into TTR Welded Tuff	31
13.	Yield Surfaces for Welded Tuff Models	34
14.	Comparison of Model with Laboratory Hydrostatic Load-Unload Paths for Welded Tuff	35
15.	Comparison of Model with Laboratory Uniaxial Strain Stress Paths for Welded Tuff.	36
16.	Friction Rules for Welded Tuff.	38
17.	Initial Computational Grid for Principal Solution of Penetration into Welded Tuff	41

LIST OF ILLUSTRATIONS (Cont'd)

Figure		Page
18.	Contribution of Friction to Axial Deceleration of Penetrator vs Time	44
19.	Radial Forces on Penetrator vs Time	45
20.	Distributions of Normal and Tangential Stress (σ_n,τ) Applied to Penetrator Surface	46
21.	Distributions of Axial Force Per Unit Length of the Penetrator along Penetrator Surface	47
22.	Distributions of Radial Force per Unit Angle per Unit Length of the Penetrator along Penetrator Surface	48
23.	Normal Stress Loadings at Several Points on the Penetrator Surface	49
24.	Shear Stress Loadings at Several Points on the Penetrator Surface	50
25.	Radial Stress Profiles Outward from Penetrator Surface from Solution of Penetration into Welded Tuff	51
26.	Peak Compressive Stress vs Depth for Several Radii.	53
27.	Peak Compressive Stress vs Radius at Depths of 6 and 12 in.	54
28.	Contours of Peak Compressive Stress (kb) Experienced by 1.32 msec in Welded Tuff	55
29.	Contours of Peak Tensile Stress (bars) Experienced by 1.32 msec in Welded Tuff	56
30.	Stress Profiles in Welded Tuff along Central Axis of Penetrator Surface, t = .278 msec.	57
31.	Stress Profiles along Central Axis or Penetrator Surface, t = .549 msec.	58
32.	Stress Profiles along Central Axis or Penetrator Surface, t = .786 msec.	59
33.	Stress Profiles along Central Axis or Penetrator Surface, t = 1.135 msec	60
34.	Stress Profiles along Central Axis or Penetrator Surface, t = 1.322 msec	61

LIST OF ILLUSTRATIONS (Cont'd)

Figure		Page
35.	Contours of Radial Stress (kb) in Welded Tuff at 1.32 msec.	62
36.	Contours of Axial Stress (kb) in Welded Tuff at 1.32 msec.	63
37.	Contours of Hoop Stress (kb) in Welded Tuff at 1.32 msec.	64
38.	Contours of Shear Stress (kb) in Welded Tuff at 1.32 msec.	65
39.	Contours of Radial Velocity (ft/sec) in Welded Tuff at 1.32 msec	66
40.	Contours of Axial Velocity (ft/sec) in Welded Tuff at 1.32 msec	67
41.	Contours of Density (gm/cm^3) in Welded Tuff at 1.32 msec.	68
42.	$\sigma_1 \geq \sigma_2 \geq \sigma_3$ Sector of Rotated Principal Stress (x,y) Plane Showing Yield Surface Forms at a Given Pressure.	71
43.	Stress States in Rotated Principal Stress Space, Columns 1 to 5.	72
44.	Stress States in Rotated Principal Stress Space, Columns 6 to 10	73
45.	Stress States in Rotated Principal Stress Space, Columns 11 to 15	74
46.	Energy Partition vs Time.	75
47.	Particle Velocity Field in Welded Tuff, Preliminary Solution.	79

LIST OF TABLES

Table		Page
1.	Summary of Results from Principal Code Solution of Penetration into Welded Tuff.	19
2.	Nominal Properties of Thirsty Canyon Welded Tuff.	32
3.	Comparative Results from Penetration Solutions.	77

SECTION I

INTRODUCTION

1.1 BACKGROUND AND TASK OBJECTIVES

A major current effort in the improvement of earth penetrator technology is directed towards providing the capability for penetrating relatively hard target media (e.g. concrete and medium-strength rock) at impact velocities in the 1000-5000 ft/sec range. A part of this effort involves the development and use of a "first principle" finite-difference Lagrangian computer code, called WAVE-L, for the analysis of penetration dynamics. Previous programs have examined the utility and limitations of WAVE-L for analysis of projectile impact and penetration into soil media.[1-3] The objective of the task reported herein has been to modify the predictive and analytical capability afforded by the WAVE-L code and associated material models and to apply it to analysis of projectile penetrations into medium-strength rock media.

To test and demonstrate the WAVE-L code, *pre-event* calculations of a rock penetration field test were required. The specific experiment chosen for this validation test was the planned firing at 1500 ft/sec of a 400-lb, 5-ft long, 6.5-in. dia, ogive nose shape, steel penetrator into a massive welded tuff site at the Tonopah Test Range near Mt. Helen, Nevada.

A key requisite for extending code capabilities to allow calculations of earth penetration into rock media was the formulation of a material model that incorporates the breakup and fracture characteristics occurring in rock during impact and penetration by the projectile. Examination of material surrounding holes left in rock by prior penetration tests shows

PRECEDING PAGE BLANK-NOT FILMED

that there is a region of highly comminuted rock surrounding the penetrator hole. Beyond the comminuted region are zones of brecciated and sheared rock, with the degree of fracture diminishing with increasing radius.[4-5] A typical fracture pattern is illustrated in Figure 1. These failure patterns are important because the physical properties of fractured rock are in general different than those of intact rock. The penetration dynamics will be influenced, perhaps strongly, by these altered properties, since target material near the advancing projectile nose is fractured, rather than intact. It is of particular importance that the comminuted rock has a lower failure surface (shear strength), since this is one of the most sensitive material properties influencing penetration dynamics.[6] Accordingly, it was therefore a necessary preliminary objective of the task reported herein to develop constitutive relations which allow assessment of the extent of failure, which has occurred at a given time and location in the code solution of penetration, and which uses this information to degrade the rock properties in an appropriate manner. The bases for the overall material model for both the intact and fractured rock were data from in situ seismic surveys and data from a series of laboratory tests which measured the constitutive properties of welded tuff samples obtained from the Tonopah site.[7-9]

In this task, the specific information which was sought from the welded tuff penetration analysis was the deceleration history and the loads on the projectile, and the media response during the early stage of the penetration event. (For nominally homogeneous targets, peak loads on a penetrator are usually reached by the time the nose section is fully embedded in the ground.) These results could then be compared with measured data during the field test.

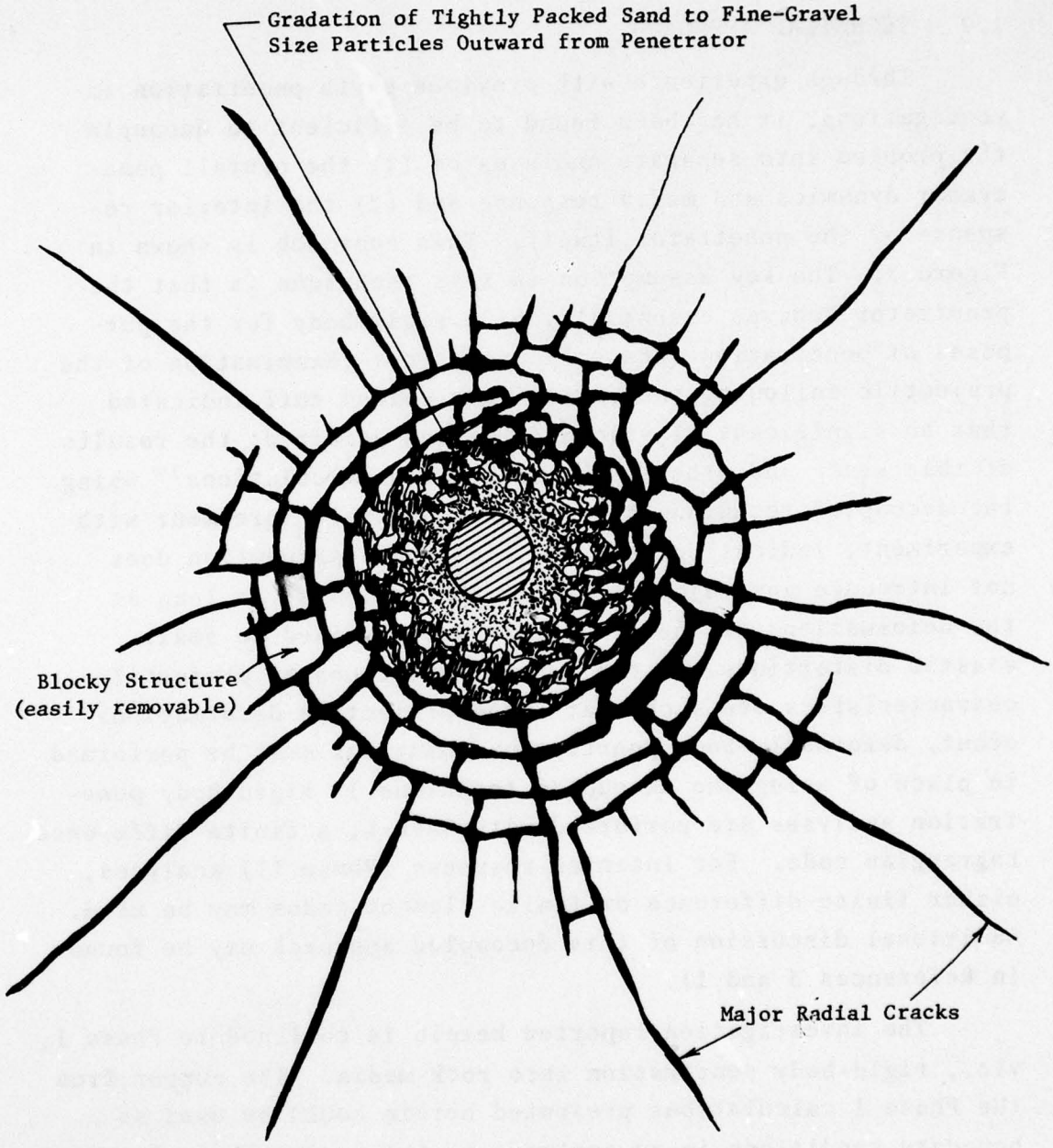


Figure 1. Surface Plan View of Comminution and Fracture of Rock during Penetration

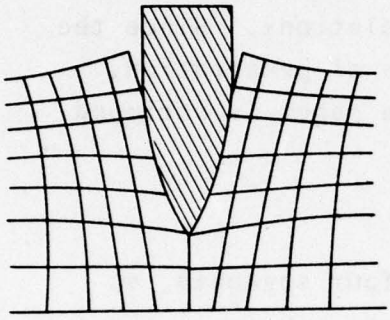
1.2 TECHNICAL APPROACH

Through experience with previous earth penetration investigations, it has been found to be efficient to decouple the problem into separate analyses of (1) the overall penetrator dynamics and media response and (2) the interior response of the penetrator itself. This approach is shown in Figure 2. The key assumption in this technique is that the penetrator behaves essentially as a rigid body for the purposes of penetration (Phase I) analyses. (Examination of the projectile following the firing into welded tuff indicated that no significant plastic deformation occurred; the results of this study and other rock penetration calculations[10] using the decoupled technique have shown reasonable agreement with experiment, indicating that the rigid-body assumption does not introduce any major errors in the analysis, so long as the deformations of the projectile are confined to small, elastic distortions. If the impact conditions or projectile characteristics are such that large projectile deformations occur, deformable-body penetration solutions must be performed in place of using the decoupled technique.) Rigid-body penetration analyses are performed with WAVE-L, a finite-difference, Lagrangian code. For interior response (Phase II) analyses, either finite-difference or finite-element codes may be used. Additional discussion of this decoupled approach may be found in References 3 and 11.

The investigation reported herein is confined to Phase I, viz., rigid-body penetration into rock media. The output from the Phase I calculations presented herein could be used as boundary conditions in an analysis of the projectile's interior response.

In the penetration field test, which employs a vertical gun, the projected mass includes a sabot which remains attached

PHASE I:



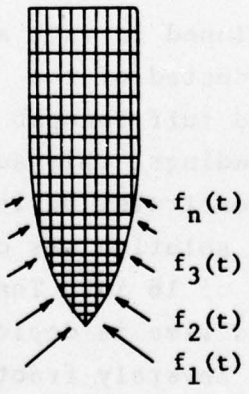
Analysis of penetration dynamics

Penetrator is assumed to be a rigid body having same mass and shape as the actual projectile.

This assumption is justified when the distortions of the projectile during penetration are elastic and so small that they do not significantly affect the penetration dynamics.

From the Phase I analysis, the forces on the projectile surface during penetration are determined (as functions of time and position along the surface).

PHASE II:



Analysis of dynamic structural response

Penetrator is now assumed to be a deformable body, in accordance with the actual configuration and properties of its materials. The response of the projectile and of its internal components, as they are subjected to the surface force loading from Phase I, is determined.

Figure 2. Decoupled Approach for Making Analyses of Penetration and Response Dynamics of Earth Penetrators

to the projectile until the sabot impacts the ground, i.e., during the first 5 ft of penetration. The projectile weighed 400 lb and the sabot weighed 117 lb. The total (517 lb) was used as the penetrator weight in the calculations. Since the calculations covered just the early stages of penetration, the reduction in weight occurring when the sabot is stripped off did not need to be accounted for.

1.3 SUMMARY OF RESULTS

Work on this task was conducted in four segments, as summarized in the following:

a. A new material model for rock media was formulated which includes a fracture criterion and post-fracture degradation of properties. A specific constitutive relation for welded tuff was then determined. This relation was based on in situ seismic and laboratory data. However, initially the only available data on the properties of crushed tuff were failure data at low pressures ($P < 3000$ psi).[8] The failure envelope at higher stresses had to be estimated by extrapolation. This led to an initial relationship with relatively weak properties for crushed tuff.

b. Using the new material model developed in (a), an exploratory penetration calculation was conducted of the full-scale penetrator firing into the welded tuff Tonopah site. To provide a shorter run-up time to peak loadings, this solution was started with the nose tip of the penetrator buried 5 inches into the ground. This exploratory solution was carried out to a time of .64 msec and a penetration of 16 in. The distortional field from the solution at this time is depicted in Figure 3. Regions of totally shattered, severely fractured, lightly fractured, and intact material are indicated in the figure. These regions are seen to generally correspond with

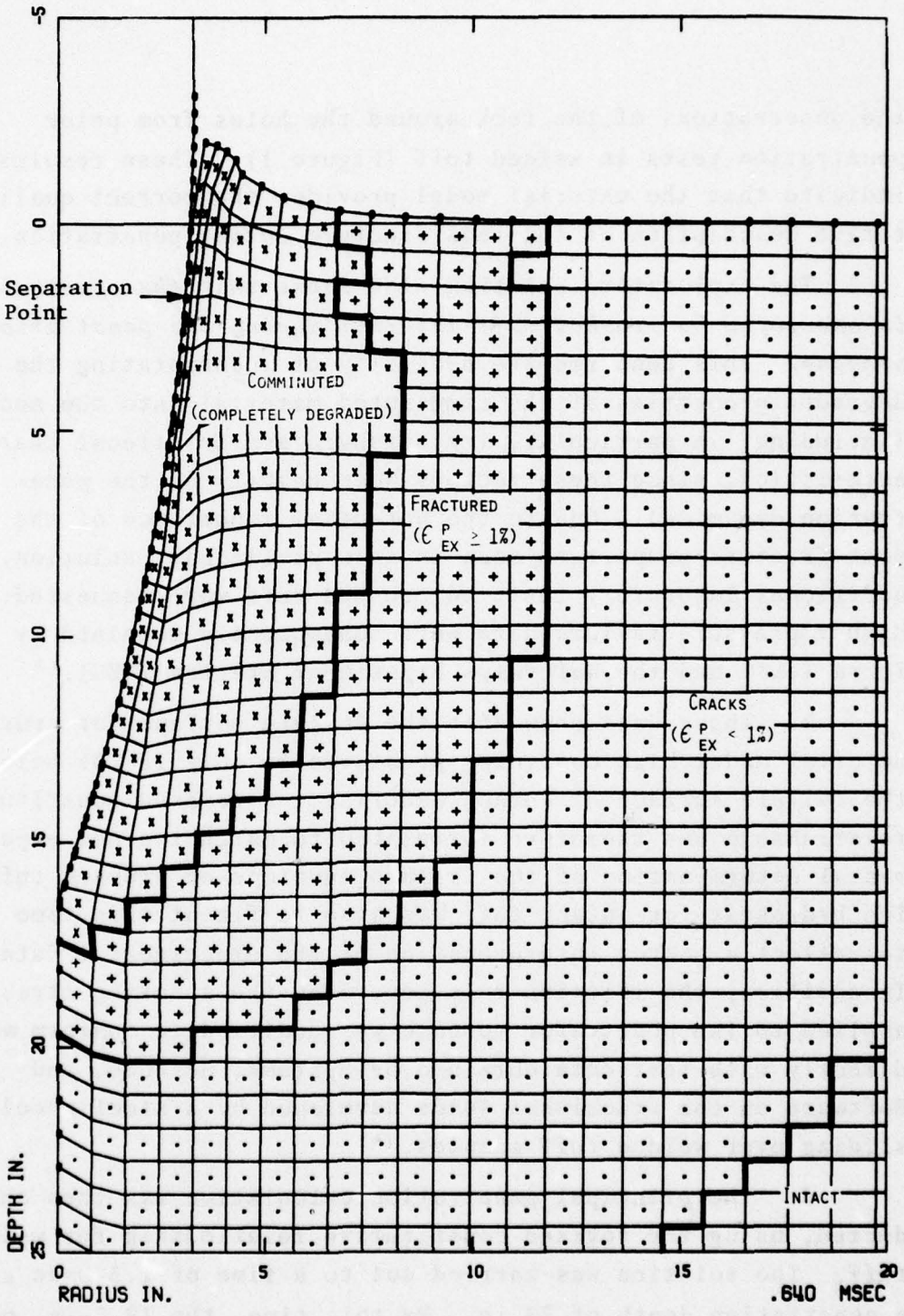


Figure 3. Lagrangian Grid and Fracture Pattern in Welded Tuff, Exploratory Solution

the observations of the rock around the holes from prior penetration tests in welded tuff (Figure 1). These results indicate that the material model provides the correct qualitative description of the rock fracture during penetration.

The exploratory solution also shows that *the penetrator is enveloped by crushed tuff material during the penetration process*. This confirms the necessity of incorporating the degraded properties of the comminuted material into the model (including, in particular, its strength and frictional characteristics, since these factors bear heavily on the penetration dynamics). Due to the potential importance of the post-fracture properties seen in this preliminary solution, additional laboratory tests on crushed tuff were requested. Higher pressure failure data were subsequently obtained by Terra Tek[12] and the Waterways Experiment Station (WES).[13]

c. These data show that the failure surface for crushed material under high confining pressures is only 15-20% below the failure surface of intact material. A revised constitutive relationship was therefore formulated to match the new experimental determination of the failure envelope of crushed tuff. The hydrostat for intact tuff was also re-fit at this time to reflect a better interpretation of the experimental data. In addition, the friction rule governing the shearing stresses applied to the penetrator surface was modified to conform more directly with test data obtained by Systems, Science, and Software on the frictional loads developed by a steel wheel sliding over welded tuff samples.[14]

d. The principal penetration calculation was then conducted, using the revised constitutive relationship for welded tuff. The solution was carried out to a time of 1.3 msec and a penetration depth of 23 in. By this time, the 19.5-in. nose

was completely buried, and the projectile deceleration had peaked and was dropping.

1.3.1 Computational Results

Figure 4 shows the time histories of the axial forces on the penetrator and the rigid-body deceleration experienced. Friction accounted for 35-45% of the total deceleration. (The periodic "blips" in the curves coincide with rezones of the computational grid. These are performed to correct severe distortions of cells near the penetrator as they are dragged downward by the strong frictional forces.)

Time histories of the penetrator velocity, depth of penetration, and engaged length (the vertical dimension of the "wetted" surface of contact between the penetrator and the rock) are shown in Figure 5. As is usually observed during high-velocity penetration, the steady value of engaged length (17.9 in.) is less than the nose length (19.5 in.). Overall results of the solution are summarized in Table 1. At the end of the solution at 1.3 msec, the penetrator velocity is dropping rapidly and the stress levels in the tuff are declining; there is, therefore, no reason to expect that the forces on the penetrator will increase at a later time. (For high-g penetrations, after the nose is fully engaged and the initial deceleration peak has been passed, the decrease in force due to the rapidly declining projectile velocity will generally outweigh any increases in force due to increased confinement at greater penetration depths. A sudden increase in *deceleration* will occur, of course, when the mass of the sabot is stripped away at about 5 ft depth.) Figure 6, which shows the Lagrangian grid at 1.3 msec, delineates the regions of comminuted, severely fractured, lightly fractured, and intact material. The velocity and principal stress fields

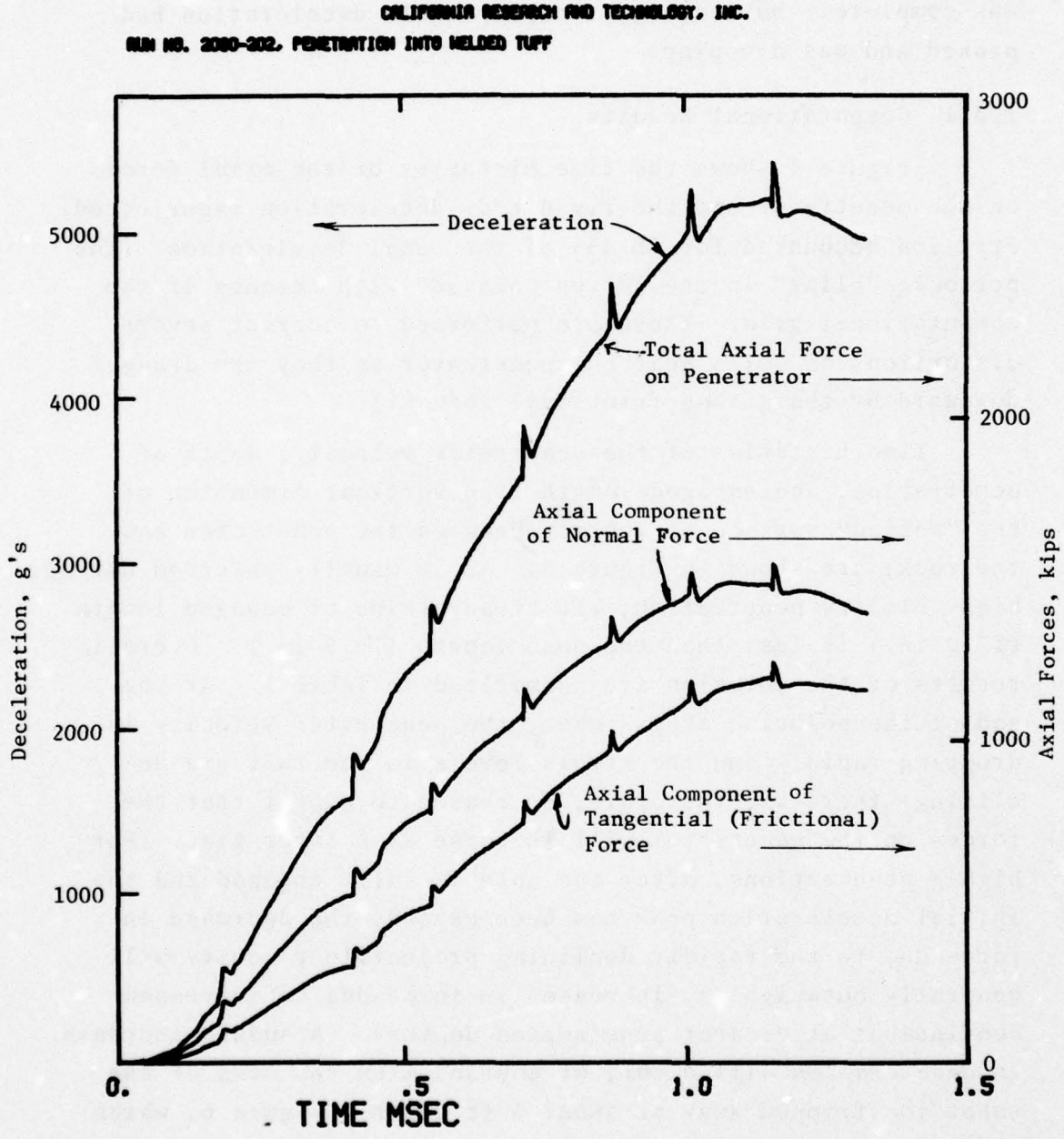


Figure 4. Axial Forces on Penetrator and Deceleration Histories from Principal Calculation

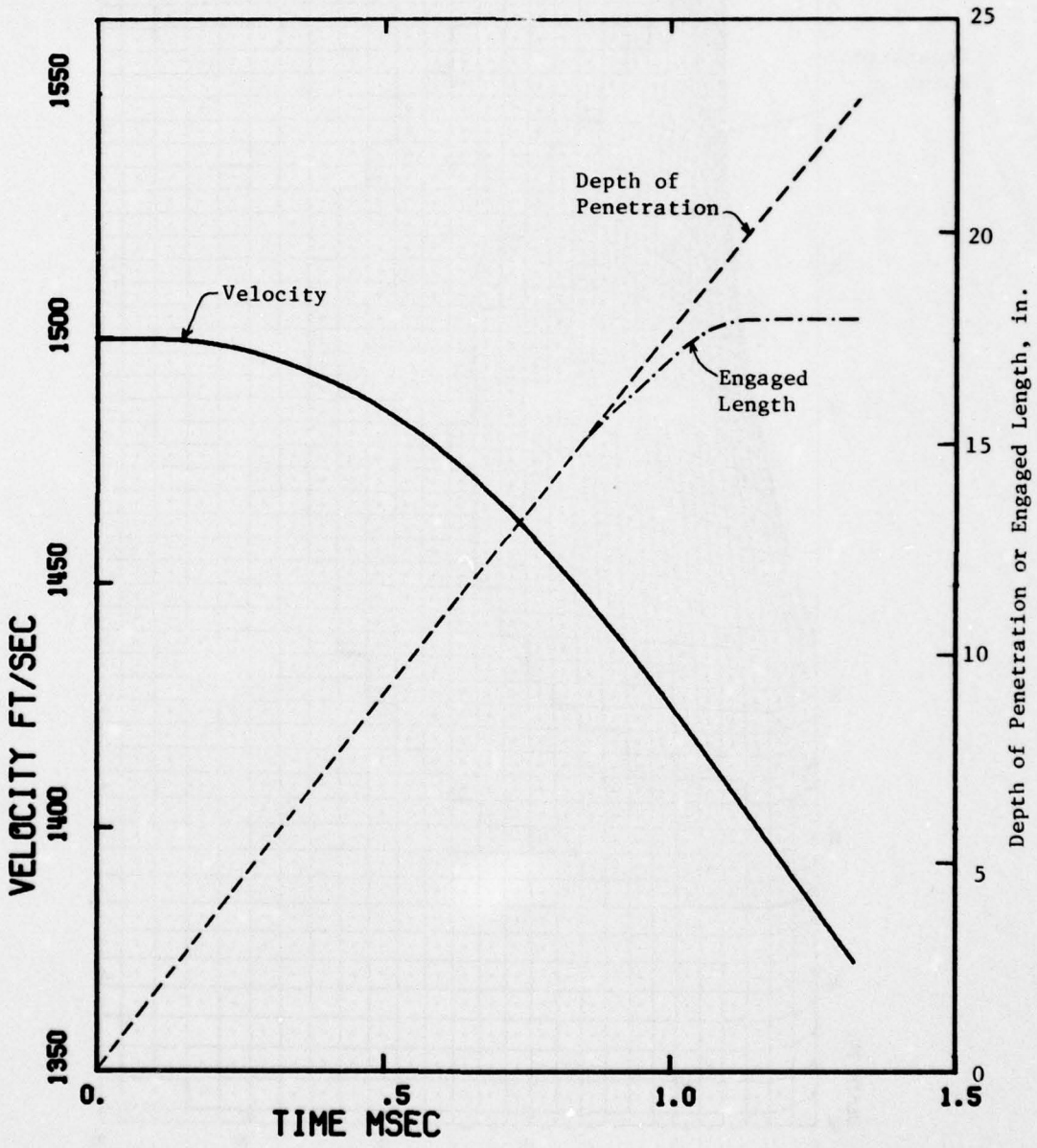


Figure 5. Time Histories of Penetrator Velocity, Depth of Penetration, and Engaged Length from Principal Calculation

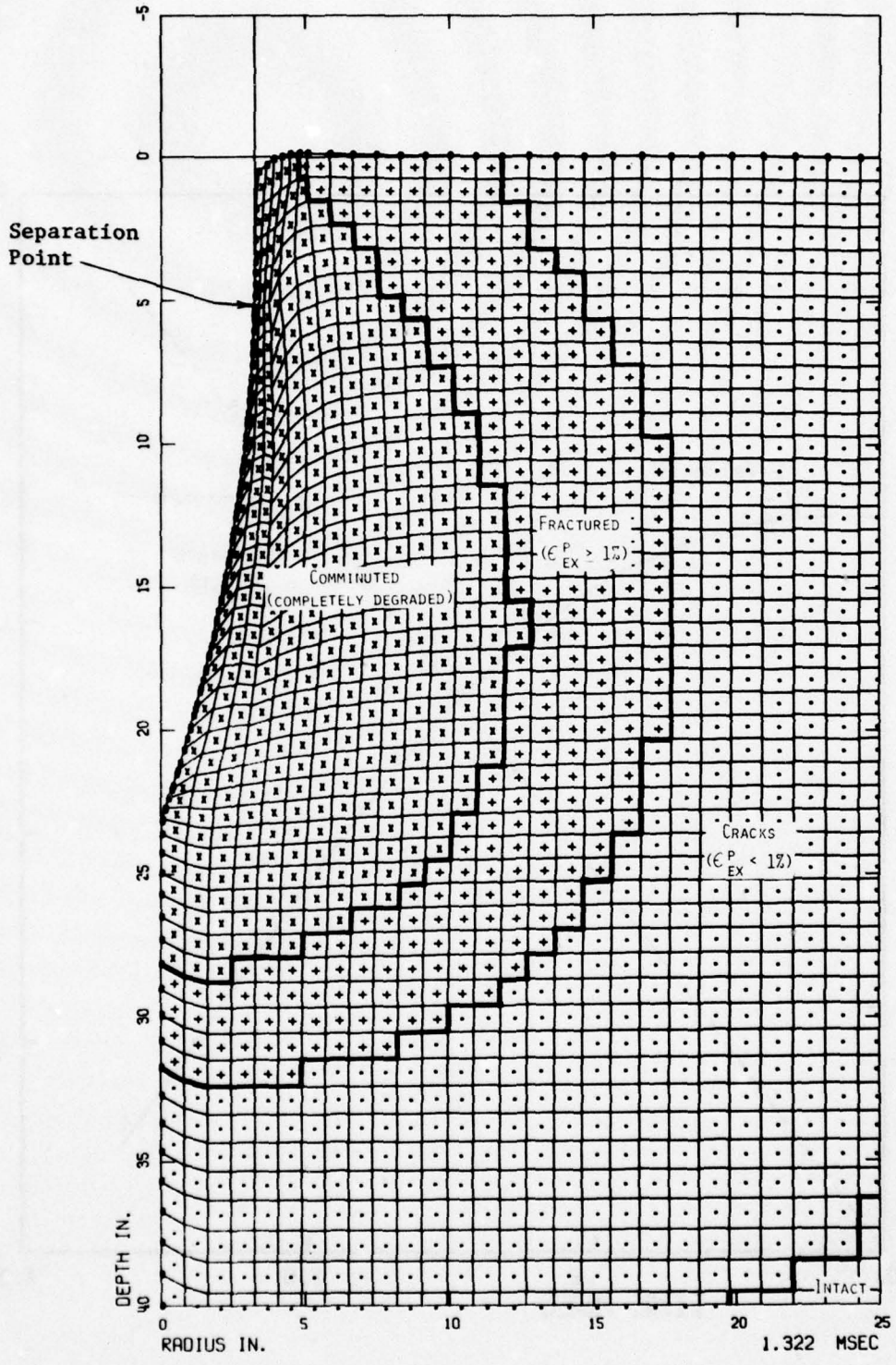


Figure 6. Lagrangian Grid and Fracture Pattern in Welded Tuff, Principal Solution

TABLE 1. SUMMARY OF RESULTS FROM PRINCIPAL CODE SOLUTION OF PENETRATION INTO WELDED TUFF

Peak penetrator deceleration	5200 g's at 1.15 msec
Peak normal stress on penetrator	6.8 kb at 1.08 msec
Peak tangential stress on penetrator	1.04 kb at 1.08 msec
Peak axial force/unit length	260 kips/in., 5 in. back from tip
Peak radial force/unit angle/ unit length	110 kips/rad/in., 7.5 in. back from tip
Frictional force contribution to deceleration	35-45%
Engagement (wetted) length (nose tip to separation)	17.9 in.
Peak compressive stress in tuff	10 kb
Range of comminution	1 ft radius (at 1.3 msec)
Range of cracking on surface	3.3 ft radius (at 1.3 msec)

at this time are shown in Figures 7 and 8. The "dragdown" of the tuff near the penetrator surface, caused by strong friction, is evident in Figures 6 and 7.

1.3.2 Experimental Comparisons

Subsequent to the above code calculations, the four test firings listed below were conducted by Sandia Corporation at the Tonopah site:[15]

Penetration Field Tests in TTR Welded Tuff

Shot No.	Test Date	Projectile Velocity	Penetration Depth
1	1 Jul 1975	1644 ft/sec	11.0 ft
2	19 Aug 1975	1640 ft/sec	11.0 ft
3	25 Feb 1976	1567 ft/sec	11.57 ft
4	28 Apr 1976	1350 ft/sec	8.6 ft

No telemetry data on projectile deceleration were received from the first three tests due to various electronic malfunctions. Projectile deceleration records from both a piezo-resistive gage and a quartz gage were obtained from the last, 1350 ft/sec, test.[16] These data, in terms of deceleration vs depth of penetration, are shown in Figure 9. The piezo-resistive gage apparently was ringing; the quartz gage produced a comparatively smooth record and is considered by Sandia experimenters to be the more representative. The first peak decelerations are 3680 g's for the quartz gage and 4370 g's for the piezo-resistive gage. The subsequent peak at 5 ft depth is presumably associated with the stripping off of the sabot. For comparison, the code solution results, for an impact velocity of 1500 ft/sec, are also shown on the figure. A rough scale-down of the code results to the experimental impact velocity

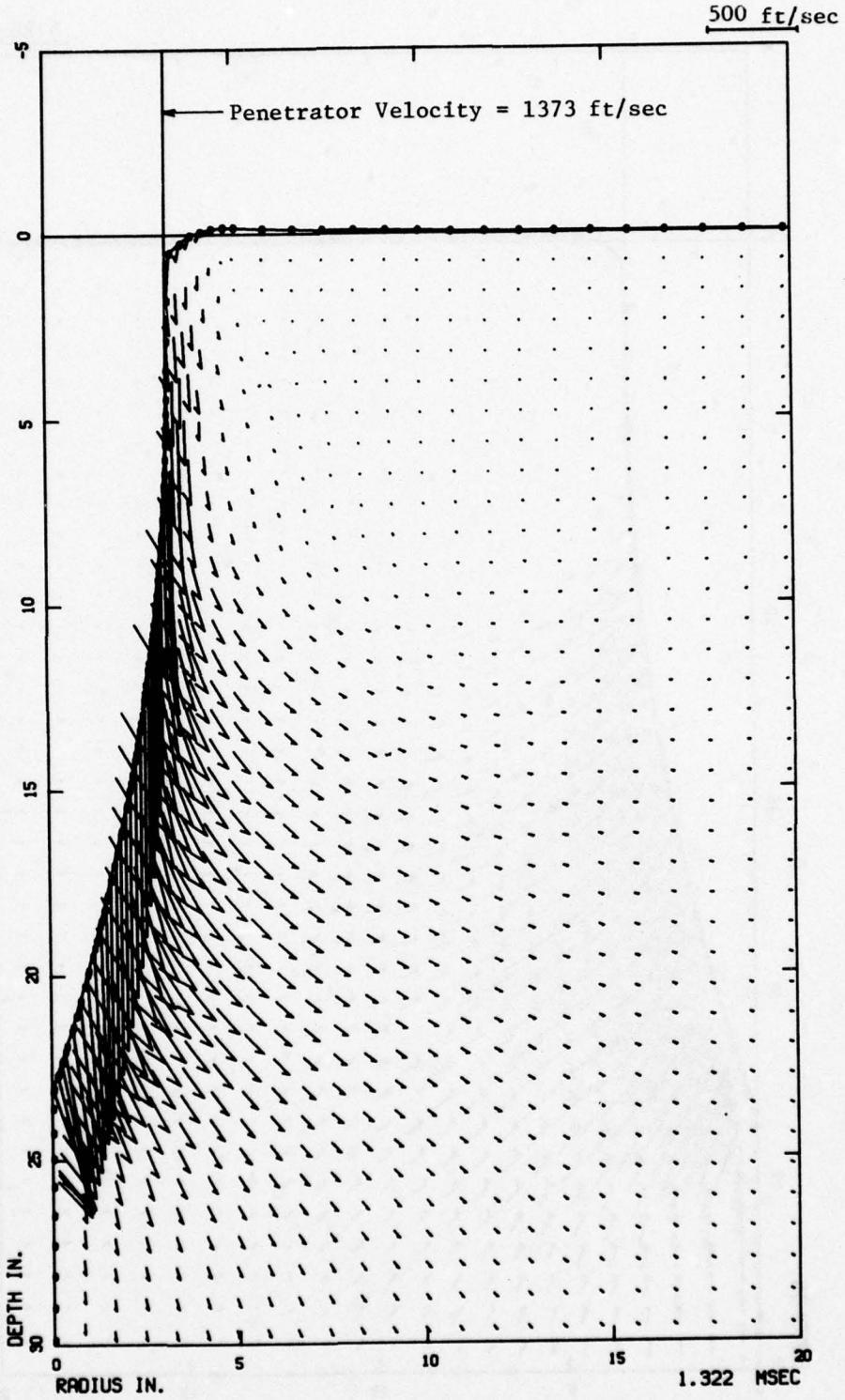


Figure 7. Particle Velocity Field in Welded Tuff, Principal Solution

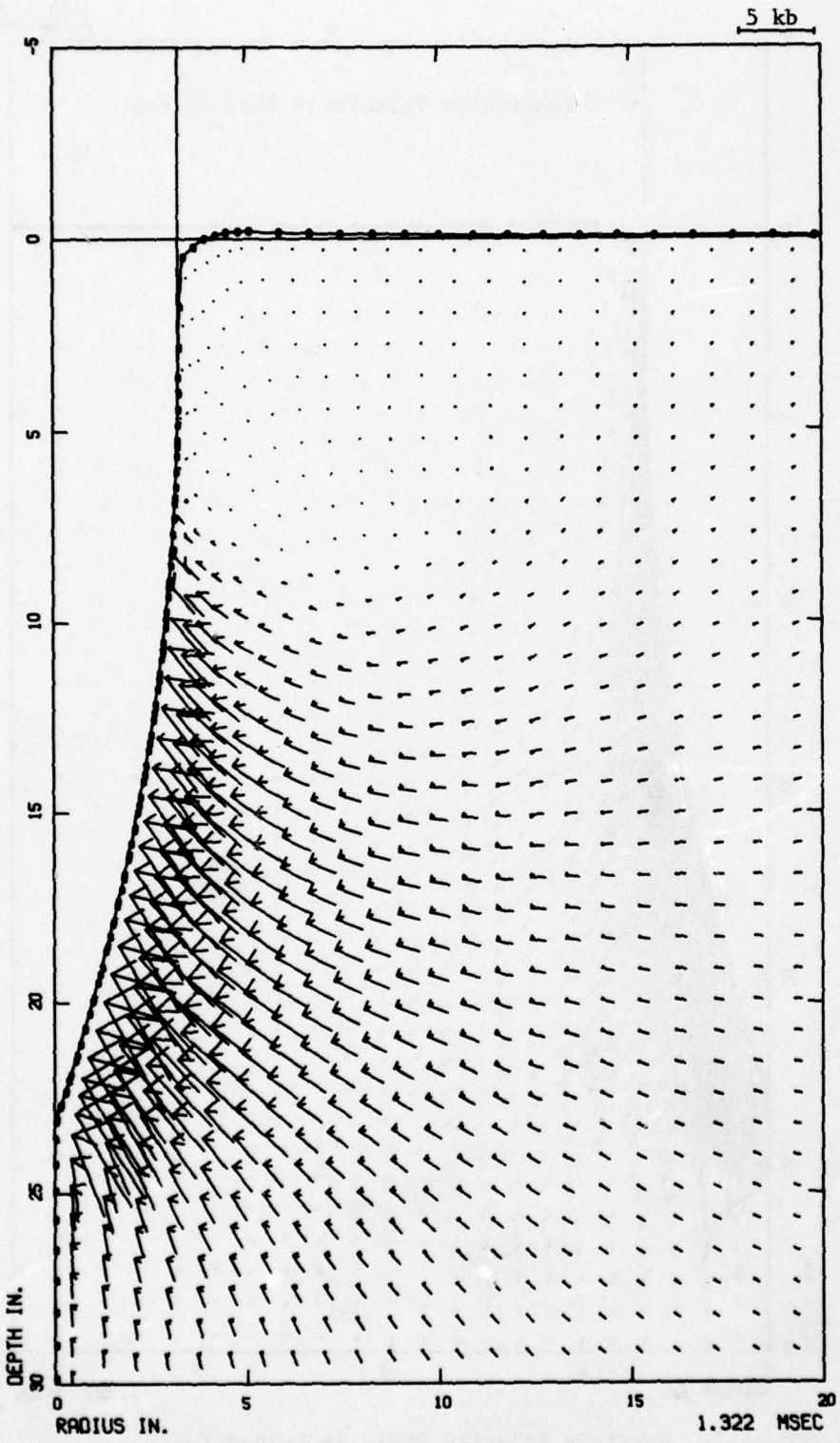


Figure 8. Principal Stress Field in Welded Tuff, Principal Solution

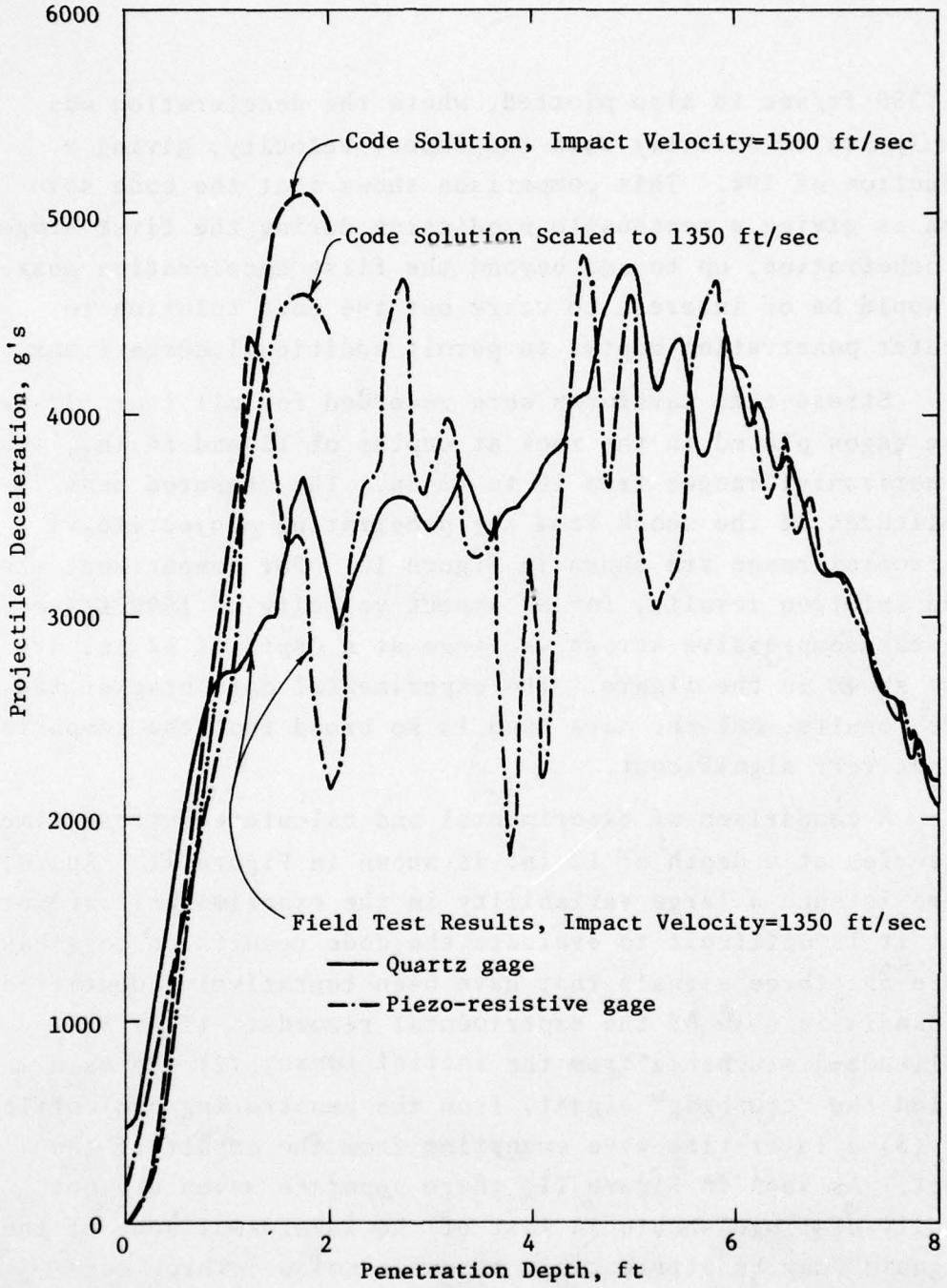


Figure 9. Comparison of Computed and Experimental Projectile Deceleration vs Penetration Depth

of 1350 ft/sec is also plotted, where the deceleration was simply scaled directly with the impact velocity, giving a reduction of 10%. This comparison shows that the code solution is giving a reasonable prediction during the first stage of penetration, up to and beyond the first deceleration peak. It would be of interest to carry out the code solution to greater penetration depths to permit additional comparisons.

Stress-time waveforms were recorded for all four firings from gages placed in the rock at depths of 12 and 36 in., and at horizontal ranges from 10 to 65 in. The measured peak amplitudes of the shock from the penetrating projectile vs horizontal range are shown in Figure 10. For comparison, the code solution results, for an impact velocity of 1500 ft/sec, of peak compressive stress vs range at a depth of 12 in. are also shown in the figure. The experimental data bracket the code results, but the data band is so broad that the comparison is not very significant.

A comparison of experimental and calculated stress-time histories at a depth of 12 in. is shown in Figure 11. Again, there is such a large variability in the experimental waveforms that it is difficult to evaluate the code results on this basis. There are three signals that have been tentatively identified by Sandia in some of the experimental records: (1) a low amplitude disturbance from the initial impact, (2) the main wave, called the "crushing" signal, from the penetrating projectile, and (3) a later-time wave emanating from the impact of the sabot. As seen in Figure 11, these separate waves are not readily distinguishable in most of the waveforms; some of the "signals" may be attributable to cable noise. Three mean-stress time histories are shown from the code solution, at horizontal ranges of 12, 18, and 24 in. These show both the

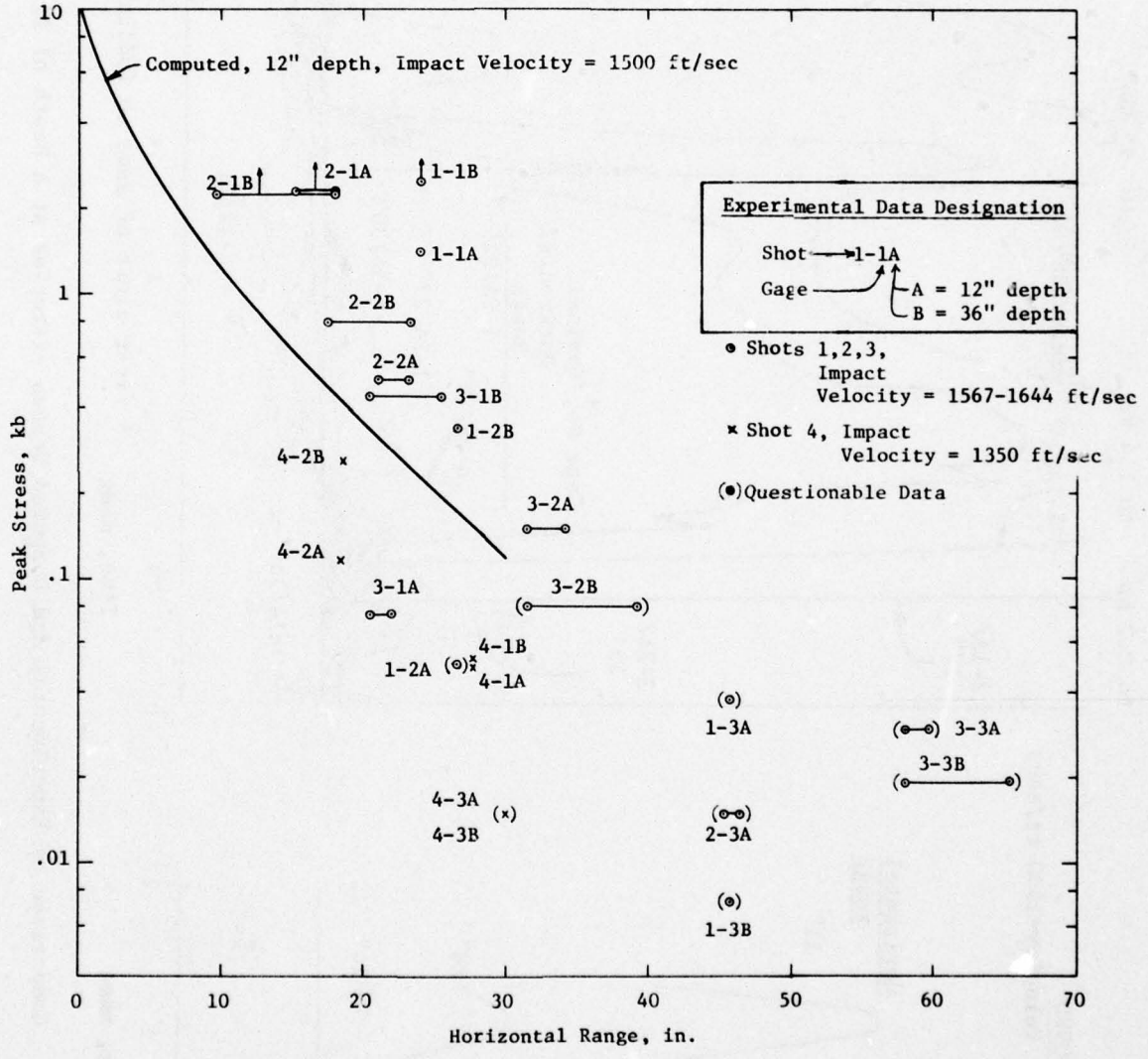


Figure 10. Comparison of Computed and Experimental Peak Stress vs. Horizontal Range

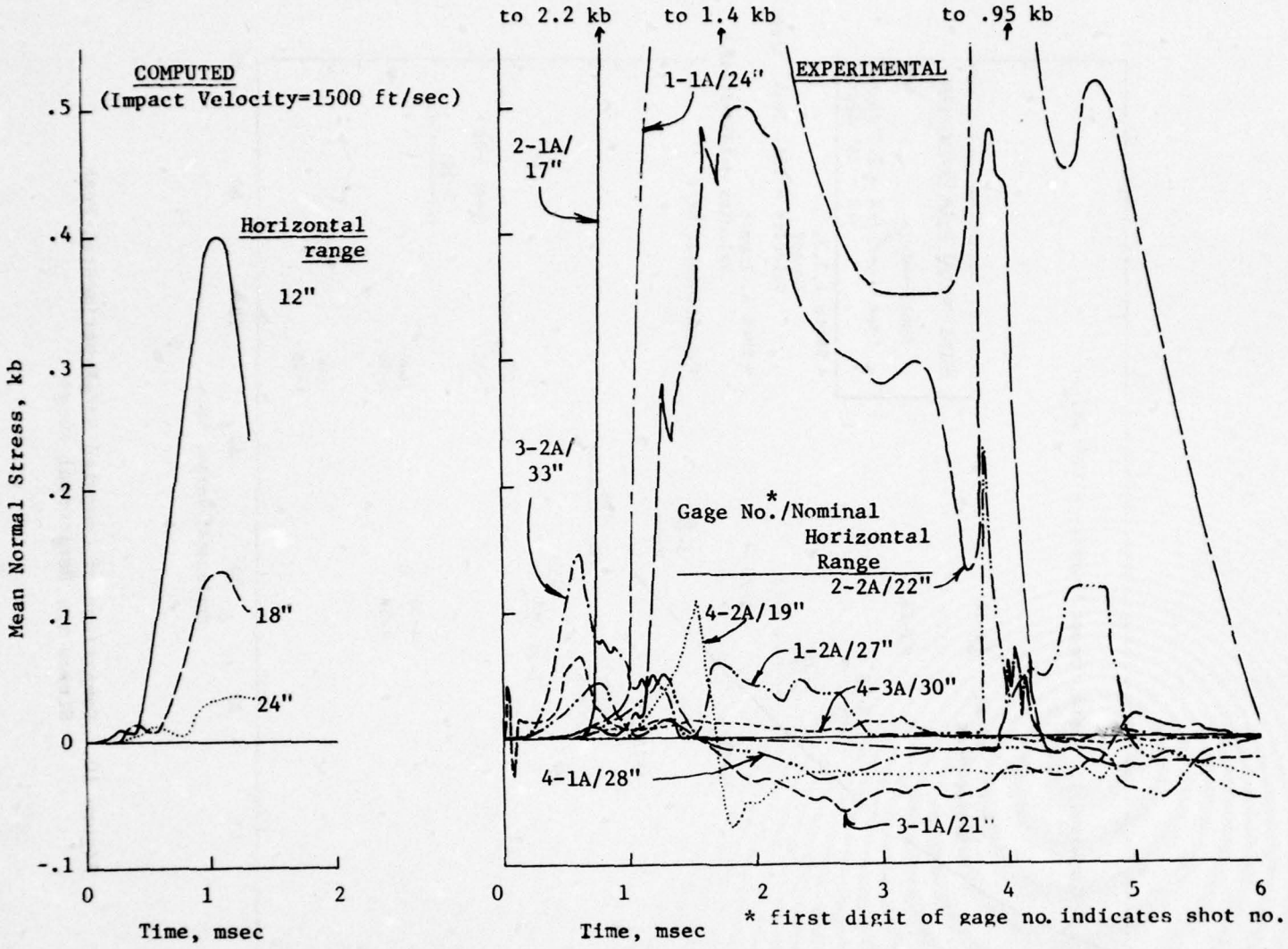


Figure 11. Comparison of Experimental and Computed Stress Histories at a Depth of 12 in.

precursor and main waves. The main wave occurs at an earlier time than that shown in most of the experimental data.

A post-test survey of the crater region from the first penetration test has been reported by WES.[17] The diameter of the crater at the surface is 5.8 ft, with surface cracks extending a few inches beyond. This is in good agreement with the 6.6-ft diameter of the region of cracked material on the surface obtained from the calculation. In the experiment, the tuff next to the penetrator is highly comminuted, ranging from "powder to fractional-inch fragments, and is very tightly packed."[17] Samples of comminuted material were taken at ranges up to 14 in. from the penetrator. Samples taken 7 in. or closer to the penetrator indicated that 60-95% of the material consists of sand-size (<5 mm) particles. A sample 1 ft from the penetrator contained about 30% sand-size particles. The calculation (Figure 6) predicted that highly comminuted material would extend to about 1 ft radius (9 in. behond the penetrator), with highly fractured material extending an additional 6 in.

The projectile was recovered intact, with no apparent structural damage. The paint had been completely stripped off and the nose was slightly abraded. The projectile surface was partially covered with comminuted tuff material. Along the hole wall next to the penetrator there were patches of metal film and comminuted rock fused together. This indicates that sliding friction at the steel/rock interface is significant to the penetration dynamics.

An examination of the amount of wear on the projectile nose has been conducted by Sandia; the wear profile was found to be in close agreement with the shape of the applied stress distribution calculated in the code solution.[18]

1.3.3 Differences Between Conditions in Calculation and Experiment

In view of the scattered and somewhat inconsistent nature of the test data, direct comparisons between the calculation and the experiment are difficult to evaluate. There were also some unintentional differences between conditions in the experiments and in the code simulation which affect direct comparisons. (It was a program requirement that the code solution be performed *prior* to the test.) These differences could be alleviated by repeating the solution using impact conditions identical to these experienced in the test, but such a repetition does not seem justified due to questions about the data.

a. The code solution was run using the anticipated impact velocity of 1500 ft/sec. However, in the test for which deceleration records were obtained (Shot No. 4), the measured impact velocity was 10% less, or 1350 ft/sec. An adjustment to the calculational results to obtain an estimate of projectile deceleration for the lower velocity has been made in Figure 9.

b. The projectile in the code simulation has a pointed nose tip, i.e. the ogival shape of the nose extended to the tip. The test projectile had a beveled nose tip, i.e. a short, relatively blunt, conical shape at the tip of the ogival nose. However, an ogival pointed cap was glued on over the bevel prior to the firing. This cap piece was not recovered and probably broke off early in the event. It would be preferable to use an integral nose tip in future comparisons.

c. The experimental impact angle was slightly oblique (2°) and the projectile trajectory in the ground veered away from the vertical on some shots. The final inclination angle

of the recovered projectiles was as much as 10°. The veering of the projectile path may have been due to the initial yaw or to inhomogenieties in the ground. The initial small impact angle probably did not cause serious discrepancies in the measured axial acceleration or in the magnitudes of the stresses measured in the ground. However, the veering does introduce an uncertainty in the horizontal range of the gages in the ground from the projectile trajectory. This uncertainty is indicated by the horizontal bars on some of the data in Figure 10.

d. The material model includes a provision for degradation of the properties of fractured rock, based on laboratory tests of mechanically crushed samples. The properties of material undergoing *dynamic* high-pressure comminution during the penetration process may differ. For example, the density of the mechanically crushed samples was 1.36 gm/cm^3, whereas the calculations indicate that the material next to the penetrator remains close to normal density (1.95 gm/cm^3) during the comminution process and while it is acting on the penetrator. Property tests on samples of the dynamically comminuted material would be desirable.

SECTION II

PROBLEM CONDITIONS AND MODELS

2.1 PENETRATOR AND IMPACT CONDITIONS

The problem conditions for the calculation of the penetration test into welded tuff at the Tonopah Test Range are shown in Figure 12. The penetrator was steel with a cylindrical aft body and an ogival nose section. The total vehicle weight was 517 lb, consisting of the 400 lb penetrator and a 117 lb sabot. The sabot remains attached to the penetrator until it impacts the ground, corresponding to a depth of penetration of 5 ft. The total 517 lb weight was employed throughout the numerical solutions since they were terminated at a penetration depth of ~2 ft. For the analyses, the penetrator impacted the ground at normal obliquity with a velocity of 1500 ft/sec and was assumed to be a rigid body.

2.2 TARGET MEDIA CHARACTERISTICS AND MODELING

The target media was a massive site of high quality welded tuff, known as Thirsty Canyon welded tuff, located near Mount Helen on the Tonopah Test Range in Nevada. The properties of the site material were characterized through a joint program conducted by WES[7,8] and Terra Tek.[9] Our analysis of these experimental findings led to the set of nominal properties listed in Table 2. These are used to set the initial (undisturbed) properties in the code solution of the problem. The values of these initial mechanical properties are somewhat tenuous, since there is a wide range between the field seismic data, ultrasonic laboratory data, and static and dynamic laboratory test results. For the model, intermediate values were chosen. The results of a related study,[6] however, have shown that the penetration dynamics are faily insensitive to the value of the bulk modulus, so it is believed that the effect of the uncertainty in initial mechanical properties is not serious. Other geological features of the site material are discussed in the WES and Terra Tek test reports.[7-9]

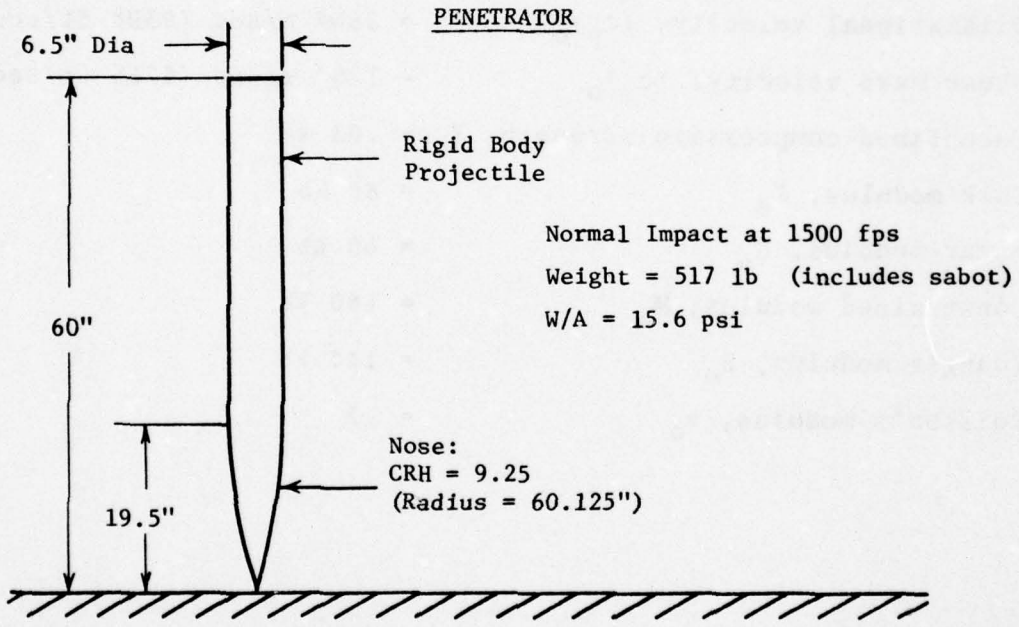


Figure 12. Conditions for Pre-event Calculations of Penetration Test into TTR Welded Tuff

TABLE 2. NOMINAL PROPERTIES OF THIRSTY CANYON WELDED TUFF

Density, ρ_o	= 1.95 gm/cm^3
Water content	= 1.5% (by dry weight)
Air voids	= 22% (by volume)
Dilatational velocity, $(c_p)_o$	= 2864 m/sec (9398 ft/sec)
Shear wave velocity, $(c_s)_o$	= 1754 m/sec (5755 ft/sec)
Unconfined compressive strength, Y_o	= .63 kb
Bulk modulus, K_o	= 80 kb
Shear modulus, G_o	= 60 kb
Constrained modulus, M_o	= 160 kb
Young's modulus, E_o	= 144 kb
Poisson's modulus, ν_o	= .2

A material model for use in code calculations was developed for the welded tuff based on the laboratory constitutive properties data. A hysteretic, elastic-plastic, strain-hardening model with a non-associated flow rule was used. The mechanical properties in loading and unloading depend on the current volumetric strain and maximum volumetric strain which the material has experienced.

The failure/fracture model used to simulate the observed non-linear response is depicted in Figure 13. A basic yield surface, curve ①, was set along the line in stress space where the onset of non-linear response in intact welded tuff was observed in triaxial compression tests. The increase in strength with increasing loading was modeled by means of a strain-hardening model, which raises the yield surface (as a function of generalized plastic strain) until a fracture surface, curve ②, or maximum yield surface, corresponding to the line in stress space where sample failure occurs, is reached. Material reaching this surface is assumed to fracture. A post-fracture model is then used that gradually degrades the yield surface as a function of *excess* generalized plastic strain; i.e., that amount of generalized plastic strain occurring after the onset of fracture. The post-fracture yield surface decreases until it reaches the minimum yield surface, curve ③, used to represent crushed welded tuff in the principal calculation. (The relatively weak minimum yield surface, curve ④, used in the exploratory penetration calculation, is also indicated in the figure.)

The load-unload response of welded tuff under isotropic compression is shown in Figure 14. Load-unload stress paths for uniaxial strain conditions are shown in Figure 15. Both the experimental data and the response predicted by the model are shown in the figures.

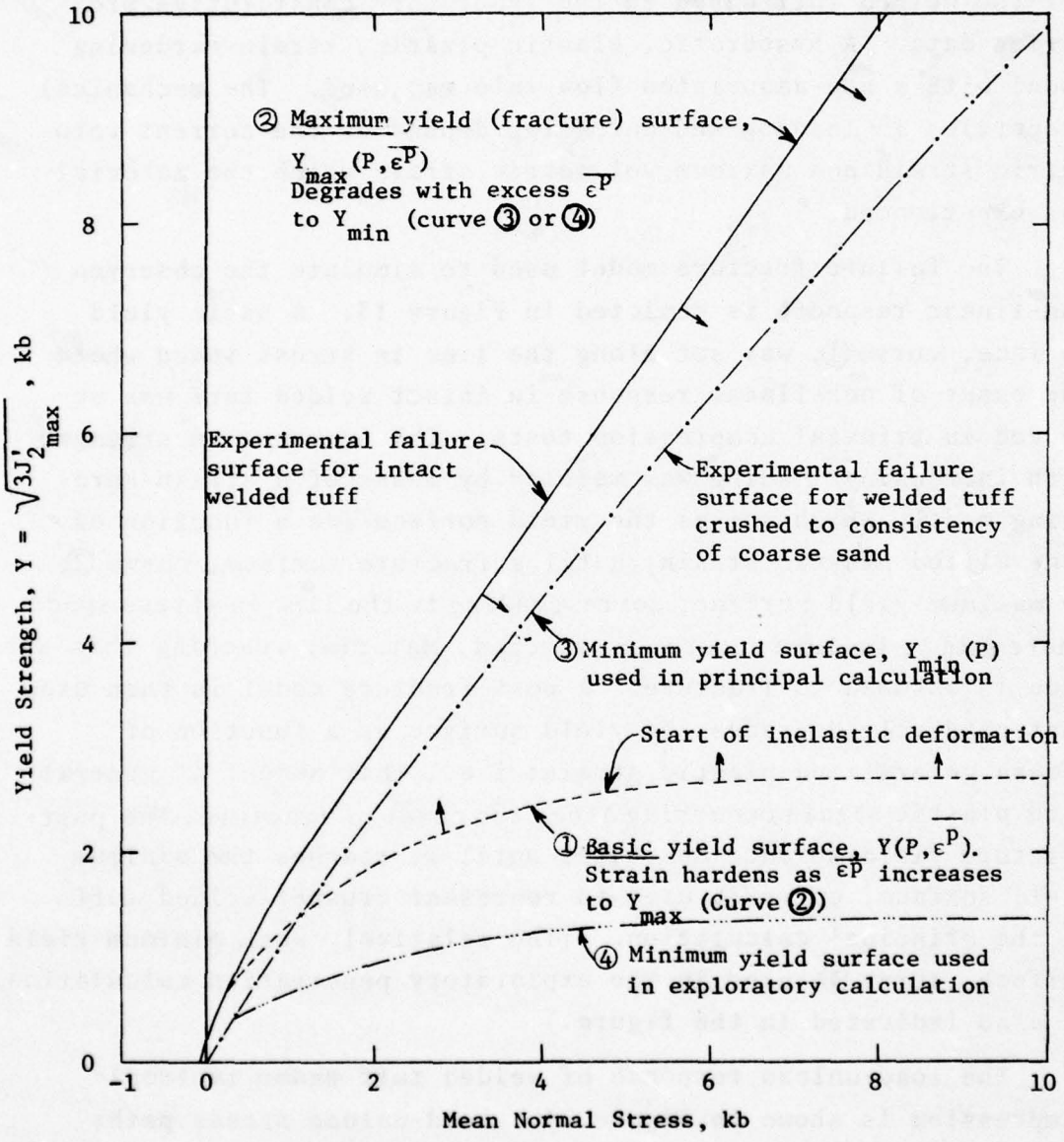


Figure 13. Yield Surfaces for Welded Tuff Models

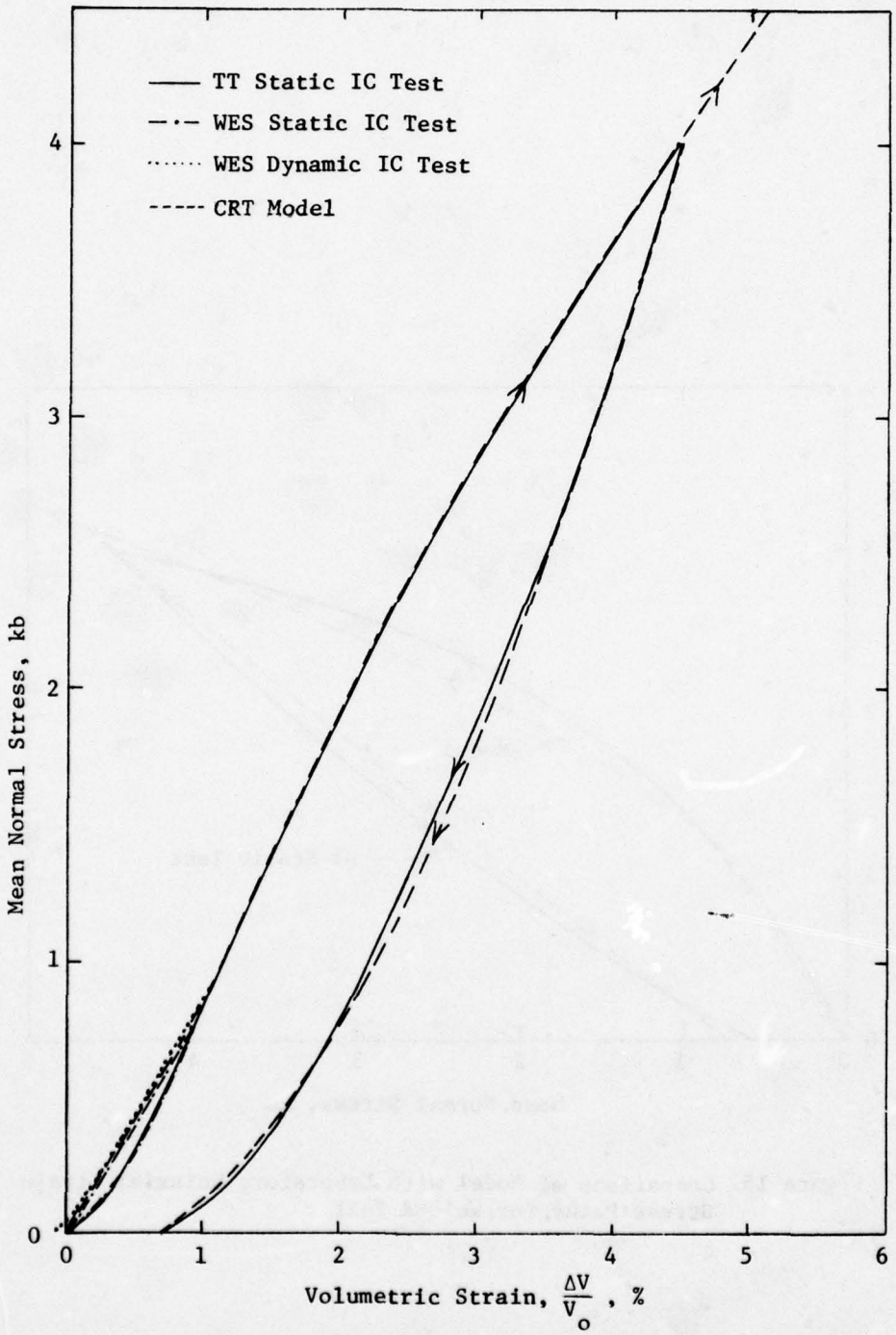


Figure 14. Comparison of Model with Laboratory Hydrostatic Load-Unload Paths for Welded Tuff

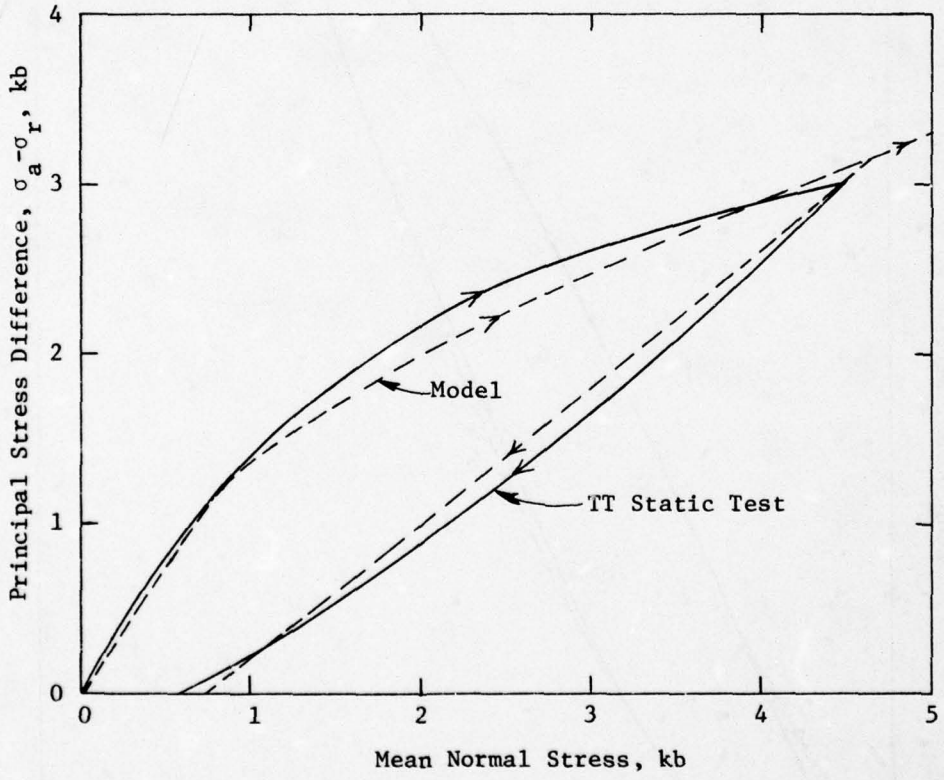


Figure 15. Comparison of Model with Laboratory Uniaxial Strain Stress Paths for Welded Tuff

A detailed description of the material model is given in Appendix A.

A friction rule was adopted that was partially based on an extrapolation of experimental data obtained at Systems, Science, and Software (S^3) for the sliding friction between steel and welded tuff samples.[14] The S^3 tests covered only a limited range of low normal stresses, from .14 to .55 kb, and were at sliding velocities less than 100 ft/sec. Since friction cannot exceed the shear strength of the rock, the applied frictional stress at any point was also limited by the octahedral shear stress associated with the concurrent value of the yield surface, $\tau_{oct} = \sqrt{\frac{2}{3} J_2'}_{max}$, at that point. The frictional stress rules used were:

$$\tau = \text{Min } (\tau_o + \mu_f \sigma_n, \tau_{oct})$$

where $\tau_o = 30$ bars

$\mu_f = .15$

These rules are plotted in Figure 16. Since nearly all the rock next to the penetrator is in the crushed state, the shear stress associated with the minimum yield surface is shown in the plot. As may be seen, the first friction rule predominates except at low applied stresses. For comparison, the predominant friction rule used in the exploratory penetration solutions is also indicated.

Based on the evidence available now, the above friction rule is believed to have overspecified the frictional stress acting at the interface in the calculation.

The calculational results of the ground motions near the surface (Figure 7) appear unrealistic in that they show no debris material moving upward. Instead, there is strong

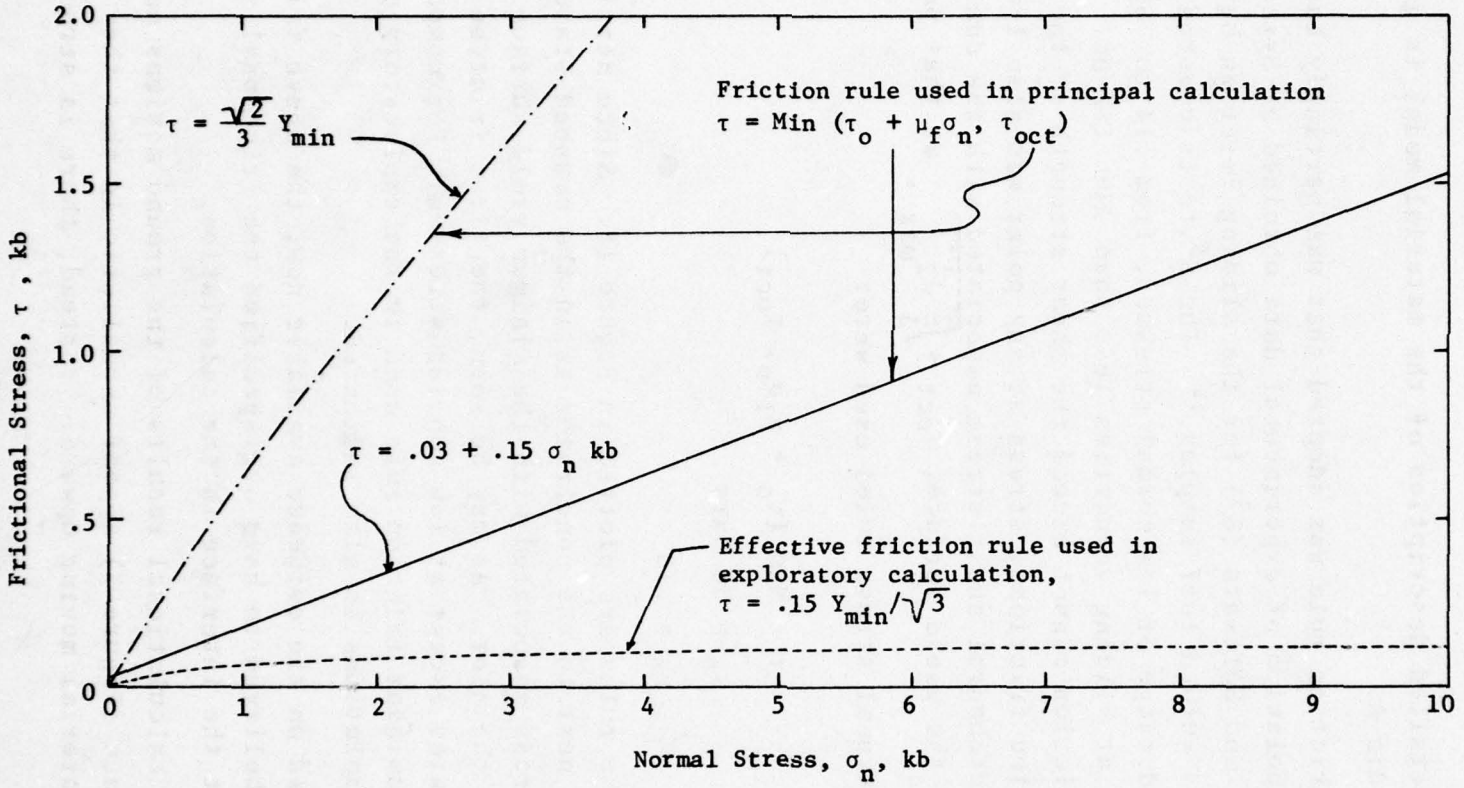


Figure 16. Friction Rules for Welded Tuff

dragdown or sticking of material in contact with the penetrator. The results of the exploratory solutions, where the frictional stress was considerably smaller, gave a velocity pattern which appears to be physically more realistic (as shown in Figure 47, page 78).

Metallurgical examination of the recovered penetrator has shown that melting of a few mils of metal occurred. In addition, patches of metal film and comminuted rock fused together were found along the hole wall. The presence of a melted surface layer should reduce the sliding friction.

Use of a lower friction rule would also decrease the calculated penetrator deceleration, bringing it into closer agreement with the experimental results.

SECTION III

PRINCIPAL COMPUTATION OF PENETRATION INTO WELDED TUFF

Two numerical solutions of the penetrator firings at the Tonopah site were conducted. An exploratory calculation was first performed to evaluate the material model (in particular, the workings of the comminution and post-fracture treatments), and to provide tentative pre-test information on expected penetrator stress loadings and stress levels in the ground. This solution is summarized in Section 1.3; additional results are given in Appendix C. Following revisions to the material model, based on new experimental data regarding the failure properties of crushed tuff, the principal penetration calculation was conducted. Results of this principal solution are described here.

3.1 WAVE-L CODE

The WAVE-L computer program was employed for the penetration calculations. WAVE-L is a two-dimensional code which solves the equations of motion for elastic-plastic bodies, using a finite difference Lagrangian technique. The basic mathematical formulation has been described by Wilkins.[19] A sliding interface, in conjunction with the friction model, was used between the rigid-body projectile and the rock media. This code has been previously used for a number of rigid-body penetration problems.[1-3]

3.2 COMPUTATIONAL GRID DESIGN

The initial grid for the penetration solution is shown in Figure 17. The contour of the penetrator periphery was resolved with a total of 50 lattice points, with a spacing in the vertical (axial) direction along the ogival nose of ~.4 in. (one-eighth of the projectile radius). The initial grid in the rock media

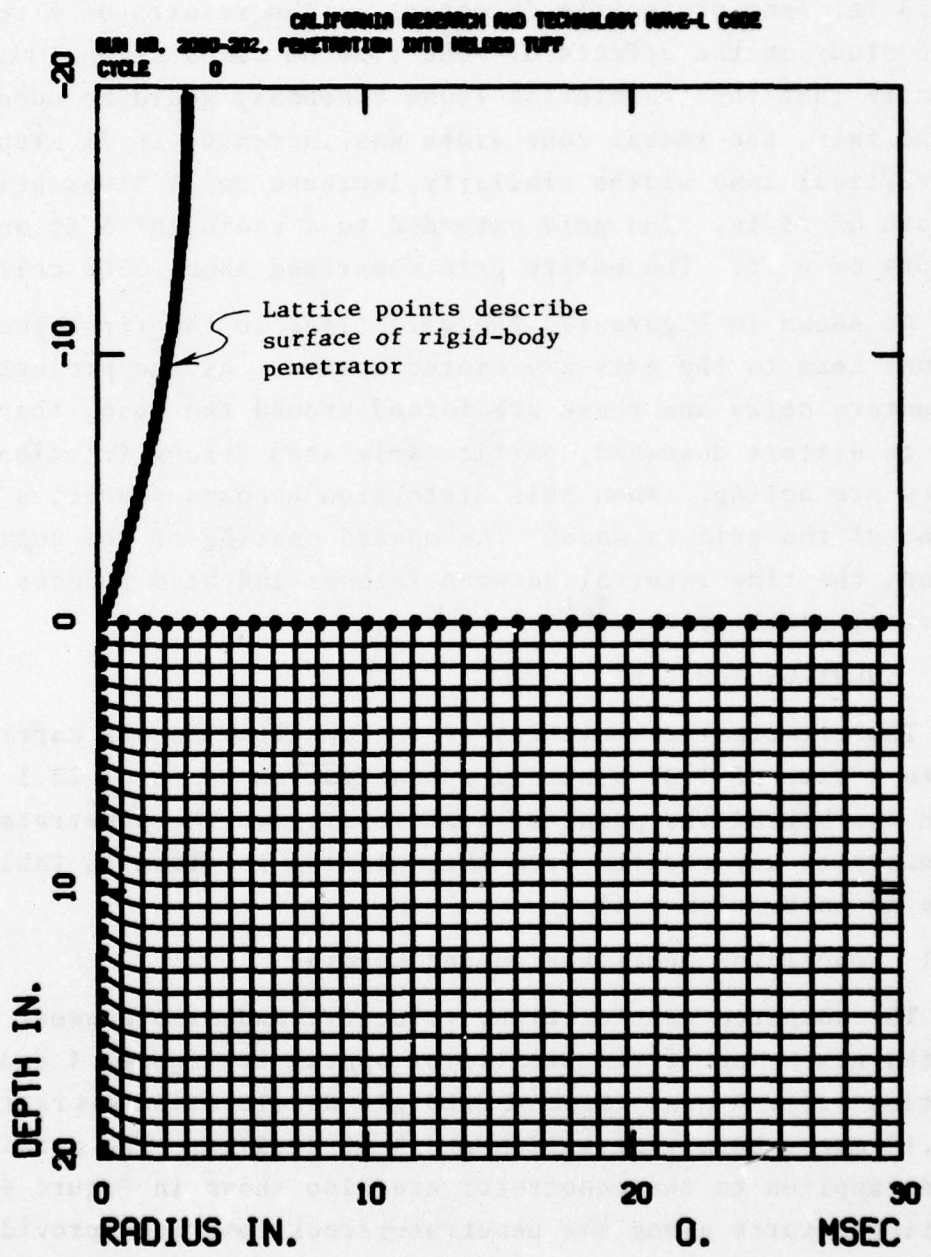


Figure 17. Initial Computational Grid for Principal Solution of Penetration into Welded Tuff

consisted of ~.8 x .8 in. cells (one-fourth of the projectile radius) in the region from the axis of symmetry out to a radius of 6.5 in. (one projectile diameter). (The results of a related study on the effects of zone size on computational results indicate that this resolution (zone fineness) sould be adequate.[6]) Beyond this, the radial zone width was increased in 2% steps. The vertical zone widths similarly increase in 2% steps below a depth of 25 in. The grid extended to a radius of 5 ft and a depth of 6 ft. The entire grid comprised about 3500 cells.

As shown in Figure 17, the grid lines in the first two columns next to the axis are canted upward. As the projectile encounters cells and these are forced around the nose, they tend to distort downward, particularly when strong frictional forces are acting. When this distortion becomes severe, a local rezone of the grid is made. The upward canting of the cells extends the time interval between rezones and also reduces numerical oscillations.[1,2]

3.3 SOLUTION RESULTS

The principal calculation of the penetration was carried out to a time of 1.32 msec and a penetration depth of 23.1 in., which was beyond the point of peak loading on the penetrator. A summary of key results from the solution is given in Table 1 (page 18 in Section 1.3).

3.3.1 Penetrator Deceleration and Loading

The computed deceleration, velocity, and displacement (depth) histories of the penetrator appear in Figures 4 and 5 (Section 1.3). A peak value of 5200 g's deceleration was reached at 1.15 msec, at a penetration depth of 20.3 in. The axial forces applied to the penetrator are also shown in Figure 4. Frictional force along the penetrator/rock interface provided an increasing proportion of the total decelerating force, from

33% to 45%, as shown in Figure 18. The frictional contribution can be expected to increase during the initial entry, as the engaged length increases. A plot of the engaged length vs time is included in Figure 5. The engaged length reaches a steady level (~17.9 in.) as the hole wall separates from the penetrator nose. The *percent* of the frictional contribution in the total decelerating force continues to increase after separation occurs, since the normal forces near the penetrator tip are declining as the projectile velocity drops.

Time histories of the radial forces applied to the penetrator are shown in Figure 19. The peak radial force was 1150 kips/radian, occurring at 1.15 msec.

Distributions of the normal and tangential (frictional) stresses applied to the penetrator at several times during the solution are shown in Figure 20. These stresses are always highest near the nose tip. The peak normal stress was 6.8 kb. Associated force distributions are shown in Figures 21 and 22. After the penetrator is fully engaged, the peak axial force per unit length of the penetrator is sustained at about 5 in. behind the penetrator tip. The peak axial force was 260 kips/in., and the peak radial force was 110 kips/radian/in.

Representative time histories of the normal and shear stresses applied at nine individual points on the penetrator are shown in Figures 23 and 24. The high frequency oscillations in the stresses applied to points near the nose are numerical. They are due to the build-up of stresses in each new computational cell encountered as the nose tip penetrates the grid.

Profiles of the radial stress in the rock vs radial distance (range) from the penetrator at a time of 1.32 msec are shown in Figure 25. The dots on the curves correspond to the radial distance to the cell centers.

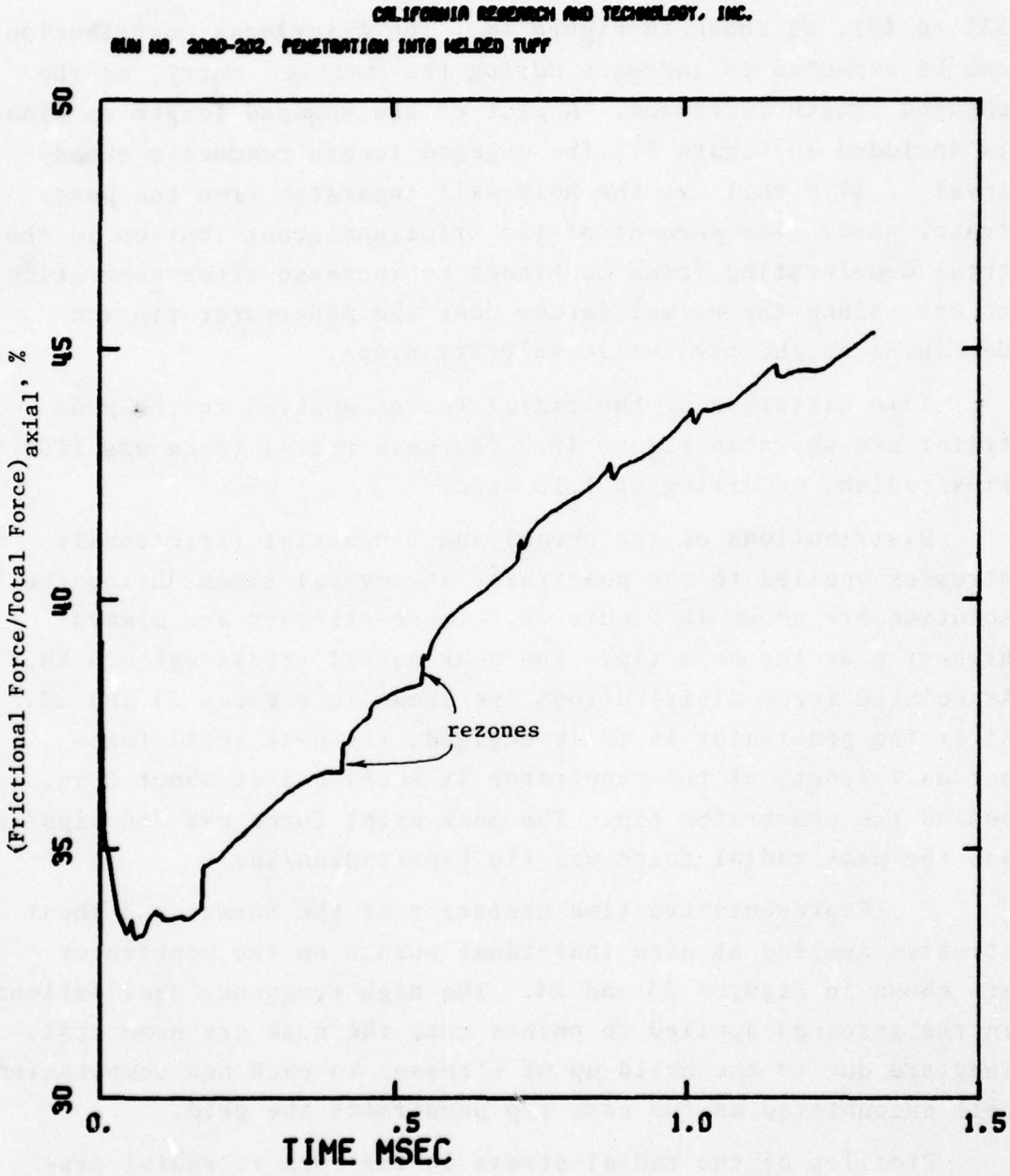


Figure 18. Contribution of Friction to Axial Deceleration of Penetrator vs Time

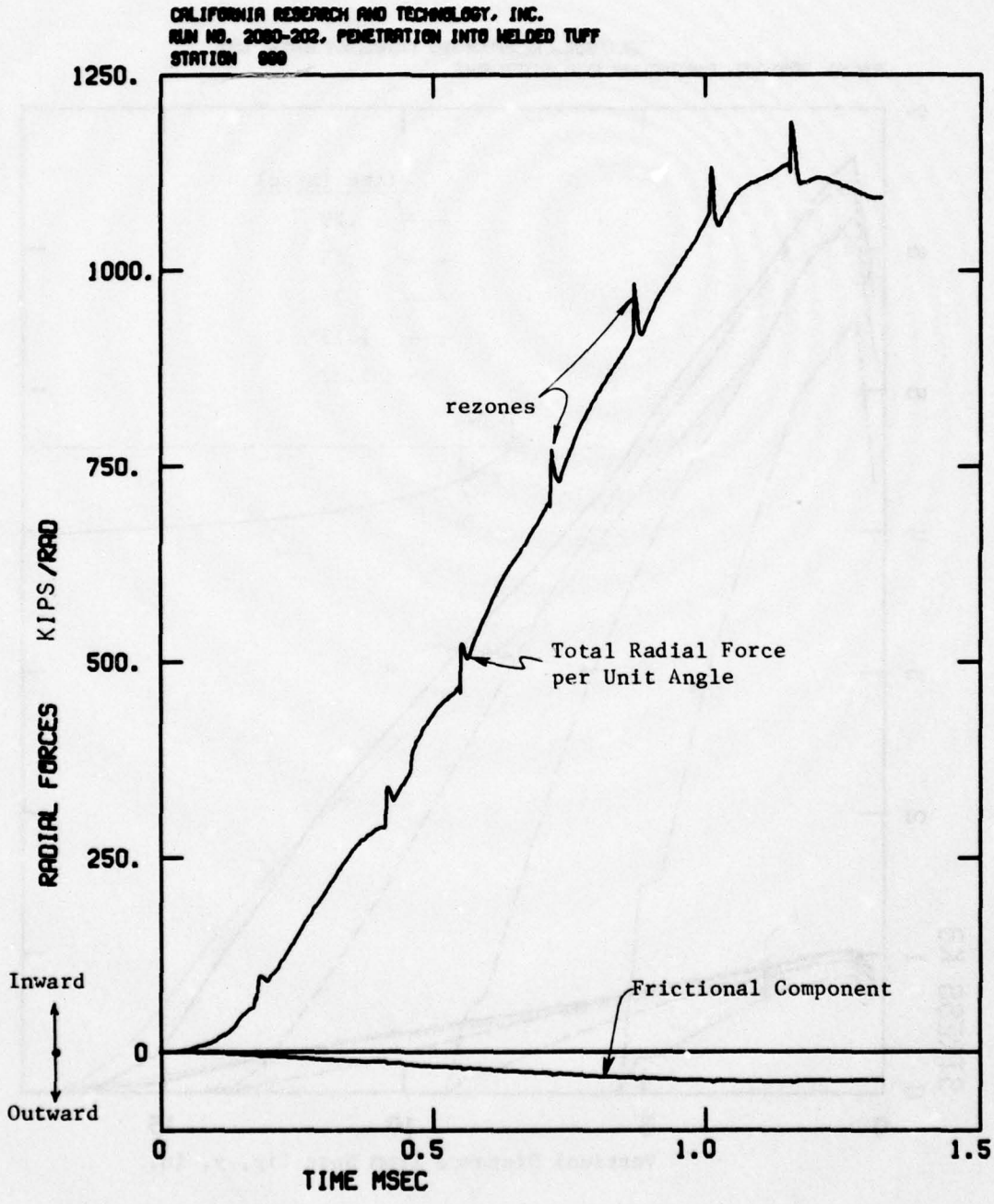


Figure 19. Radial Forces on Penetrator vs Time

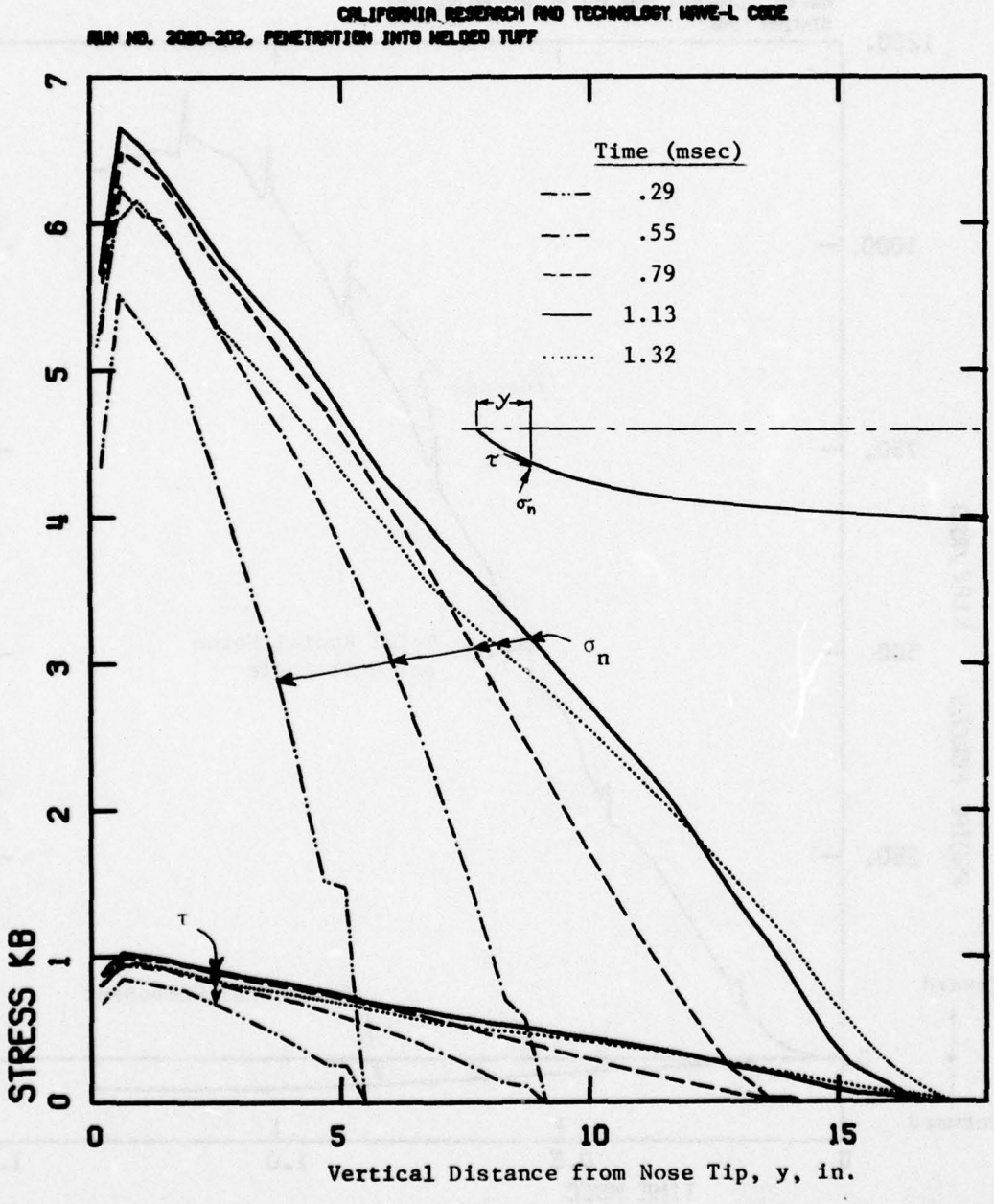


Figure 20. Distributions of Normal and Tangential Stress (σ_n,τ) Applied to Penetrator Surface

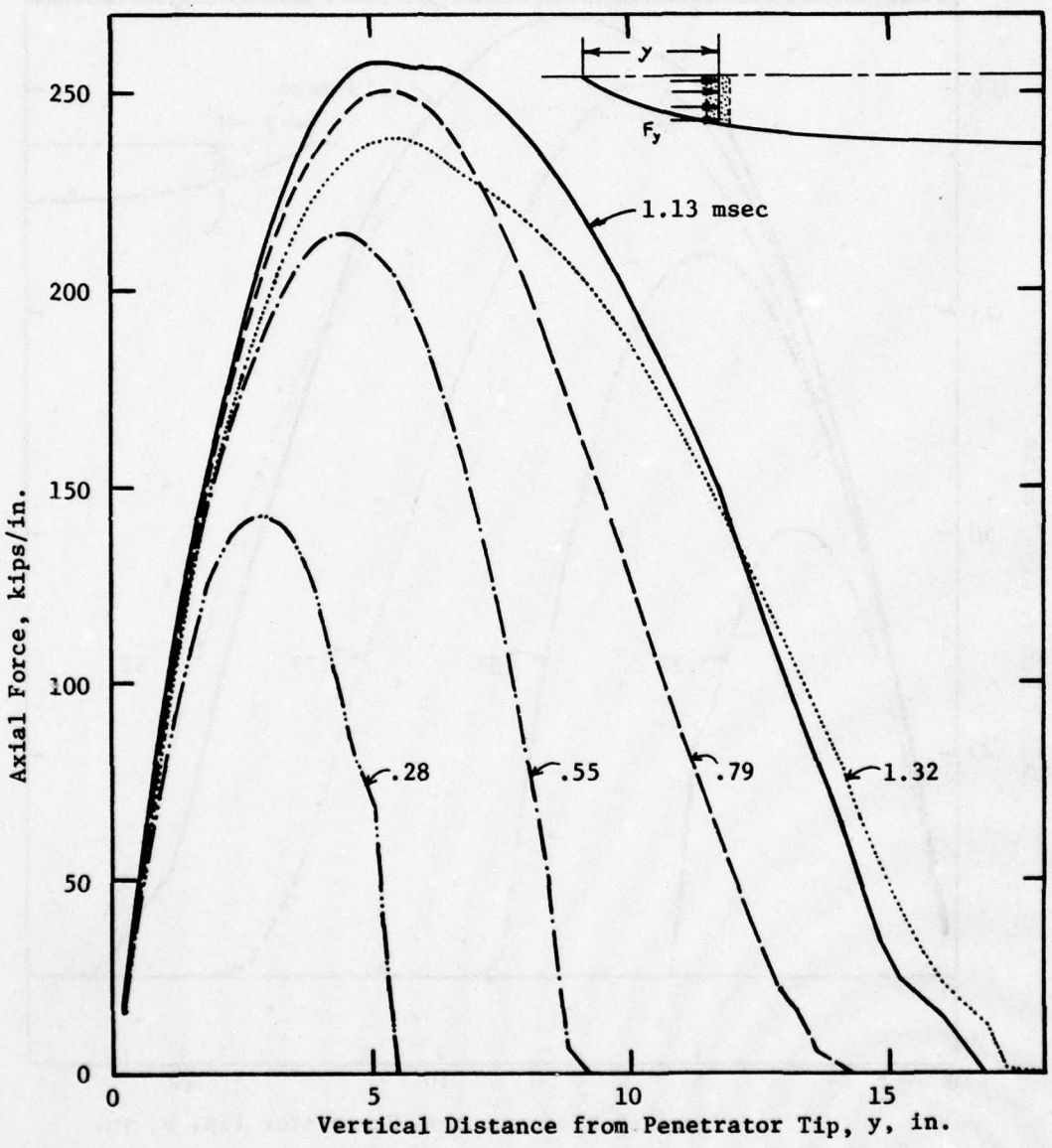


Figure 21. Distributions of Axial Force Per Unit Length of the Penetrator along Penetrator Surface

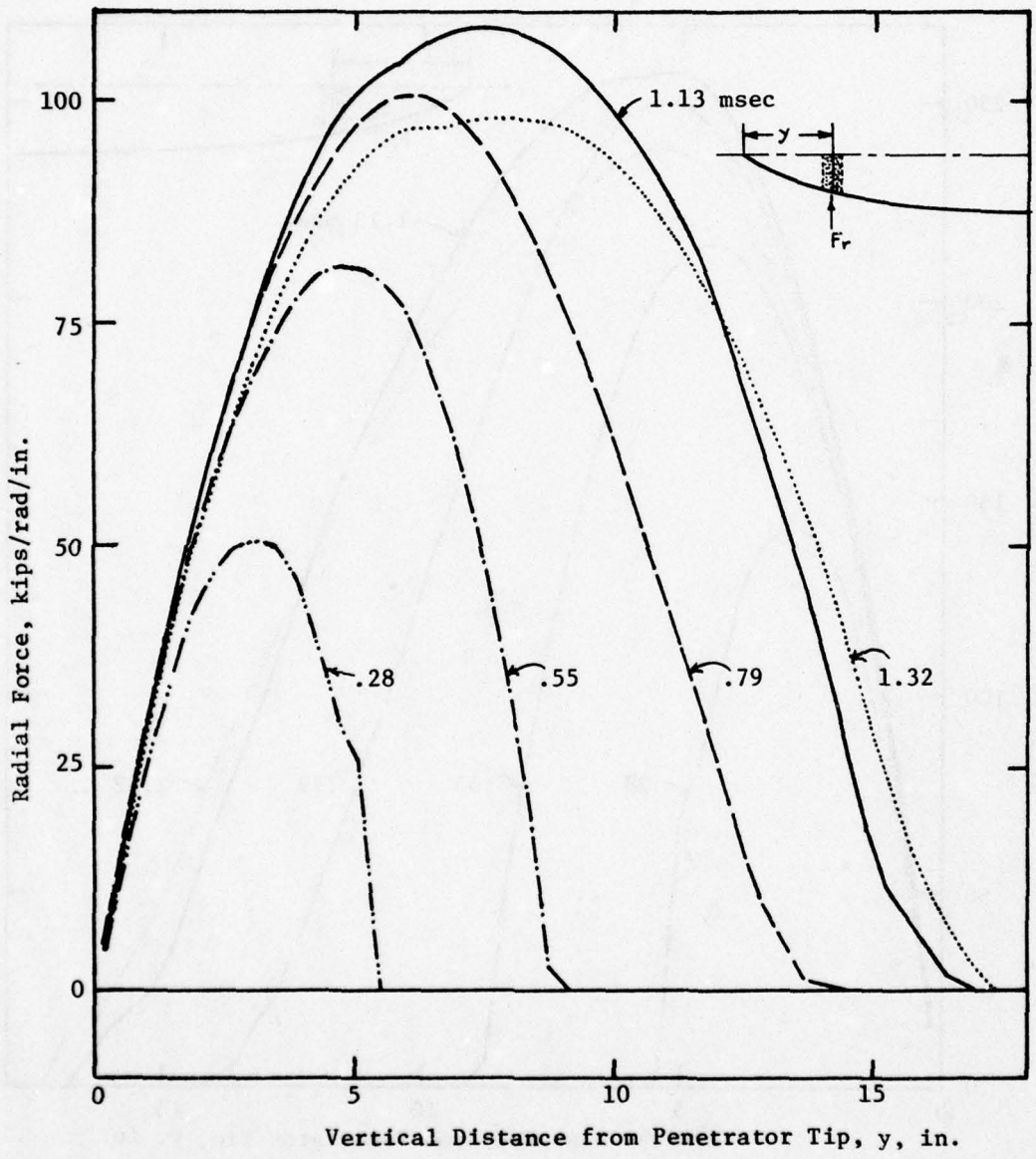


Figure 22. Distributions of Radial Force per Unit Angle per Unit Length of the Penetrator along Penetrator Surface

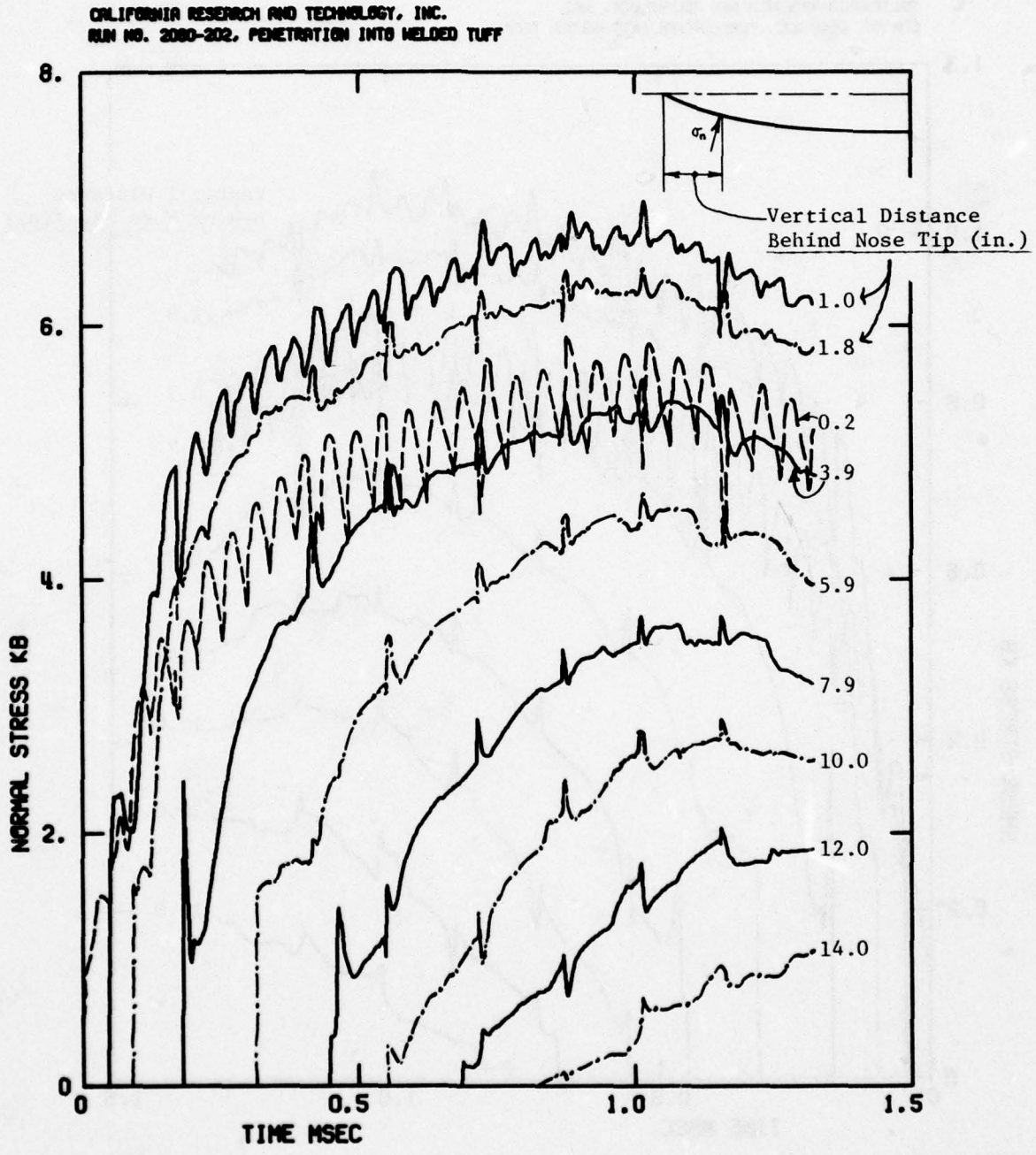


Figure 23. Normal Stress Loadings at Several Points on the Penetrator Surface

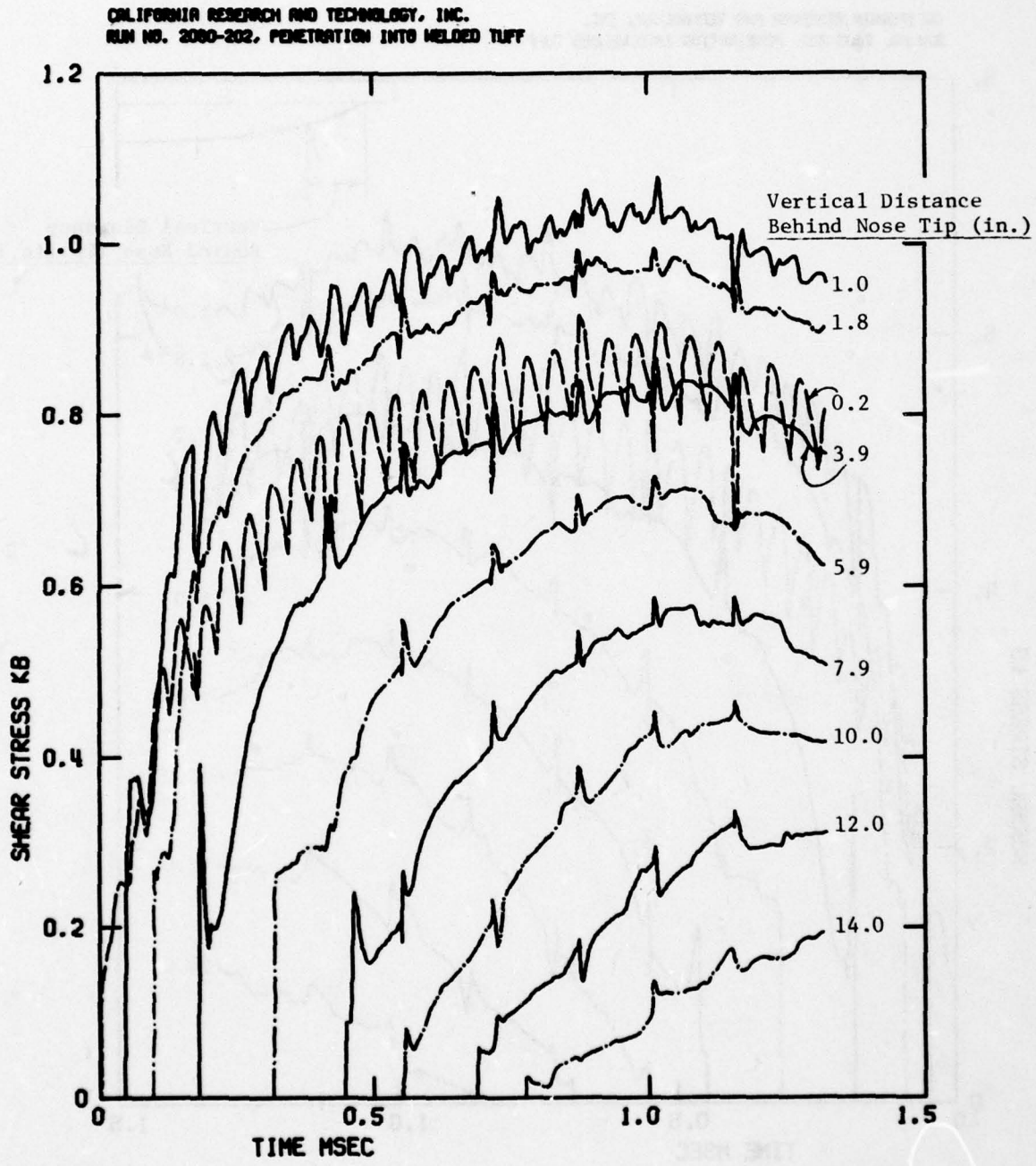


Figure 24. Shear Stress Loadings at Several Points on the Penetrator Surface

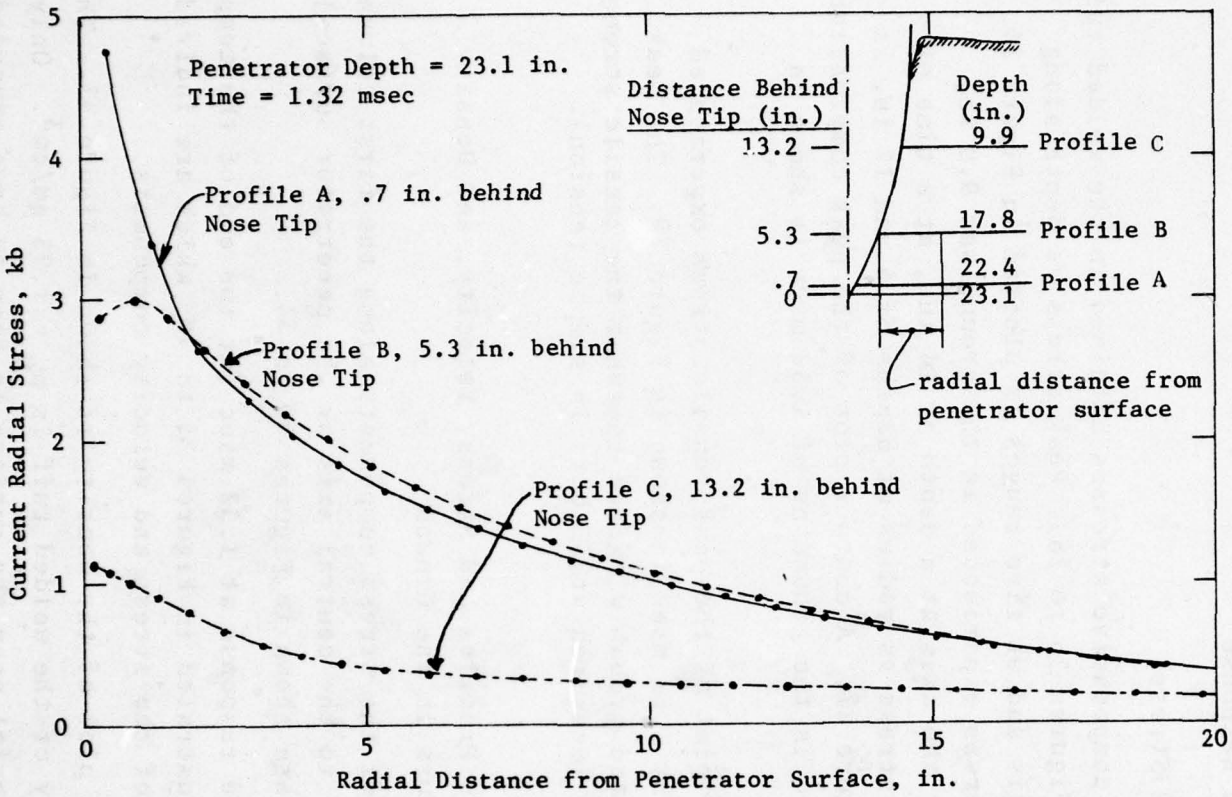


Figure 25. Radial Stress Profiles Outward from Penetrator Surface from Solution of Penetration into Welded Tuff

3.3.2 Ground Response

3.3.2.1 Peak Stress

The peak compressive stresses attained in the welded tuff are shown in Figures 26 to 28. Peak stress vs depth along the central axis and at five ranges is plotted in Figure 26. The highest stress experienced in the ground was 9.8 kb, occurring near the axis at a depth of 14 in., at a time of 1 msec. Peak stress vs radius at depths of 6 and 12 in. is plotted in Figure 27. A contour plot of the peak compressive stress attained in the ground as of 1.32 msec is shown in Figure 28.

A contour plot of the peak tensile stress experienced in the ground by 1.32 msec is shown in Figure 29. The peak tensions computed probably exceed somewhat the tensile strength of welded tuff (measured at 33 bars in simple tension).

3.3.2.2 Stress Profiles and Stress, Velocity, and Density Contours in the Ground

Profiles of the stress components along the first column of cells (next to the central axis or the penetrator surface) for several times are shown in Figures 30 to 34.

The ground response at 1.32 msec (at the end of the computation) is illustrated in Figures 35 to 40, which are individual contour plots of the stress and velocity components.

A contour plot of the density is shown in Figure 41. The initial density of the welded tuff is $\rho_o = 1.95$ gm/cm^3. Only the ground material near the surface is seen to have expanded out by this time (1.32 msec) in the event.

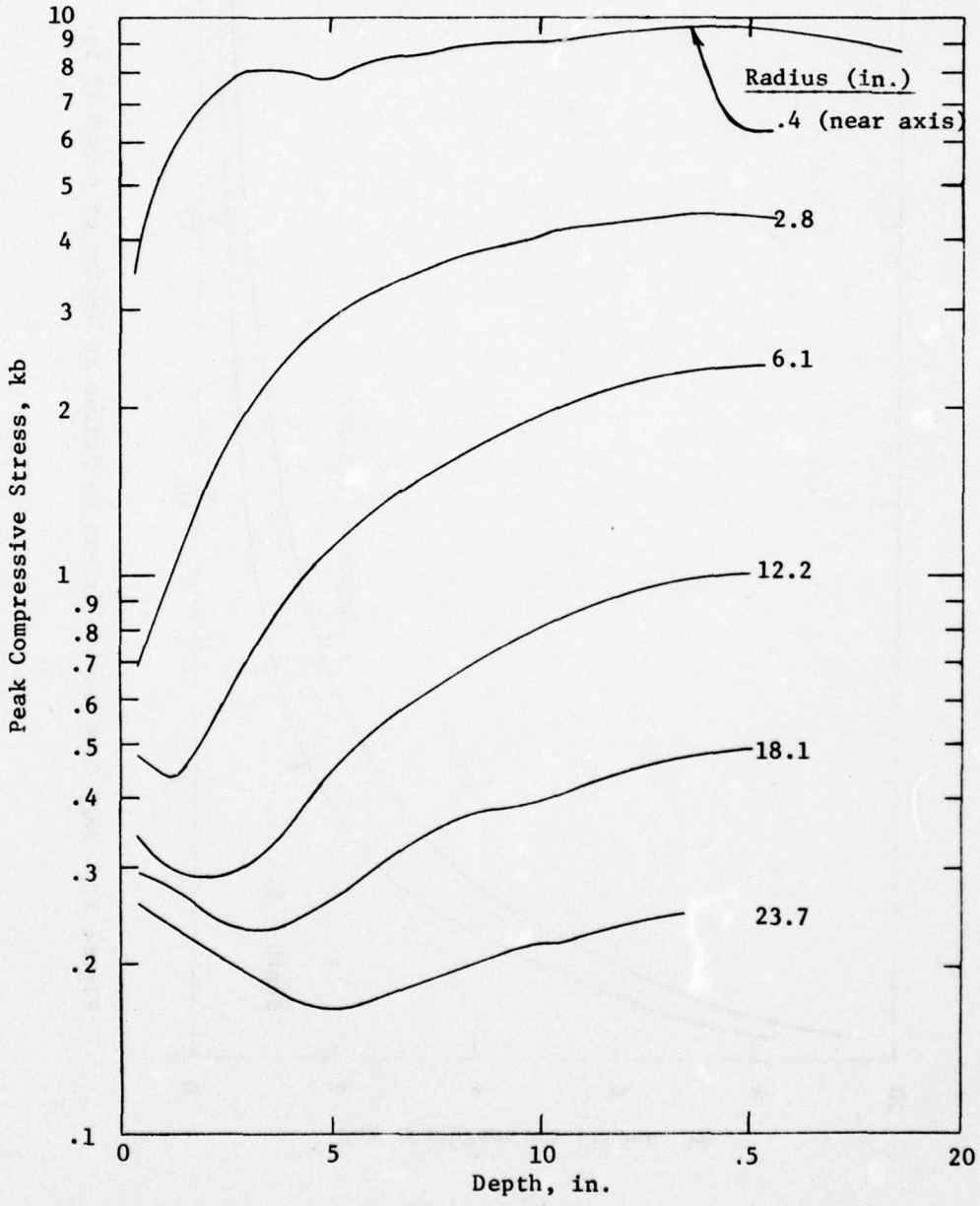


Figure 26. Peak Compressive Stress vs Depth for Several Radii

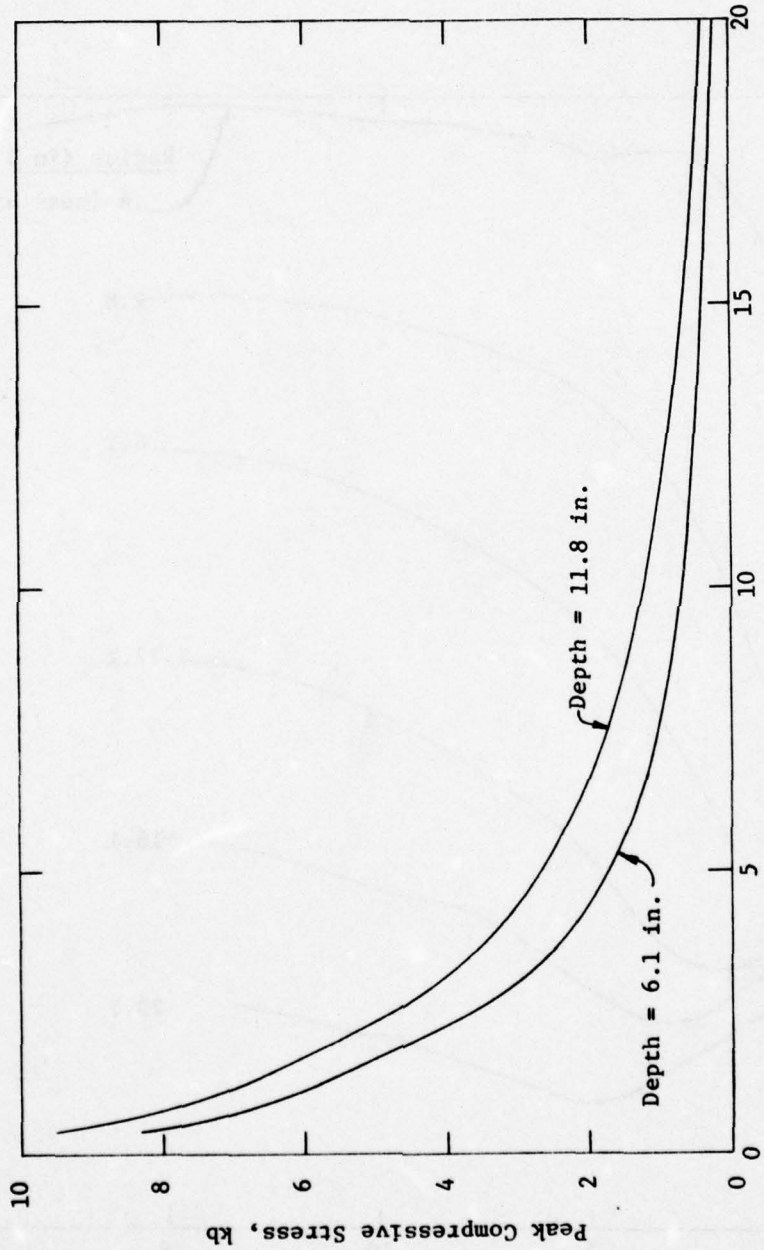


Figure 27. Peak Compressive Stress vs Radius at Depths of 6 and 12 in.

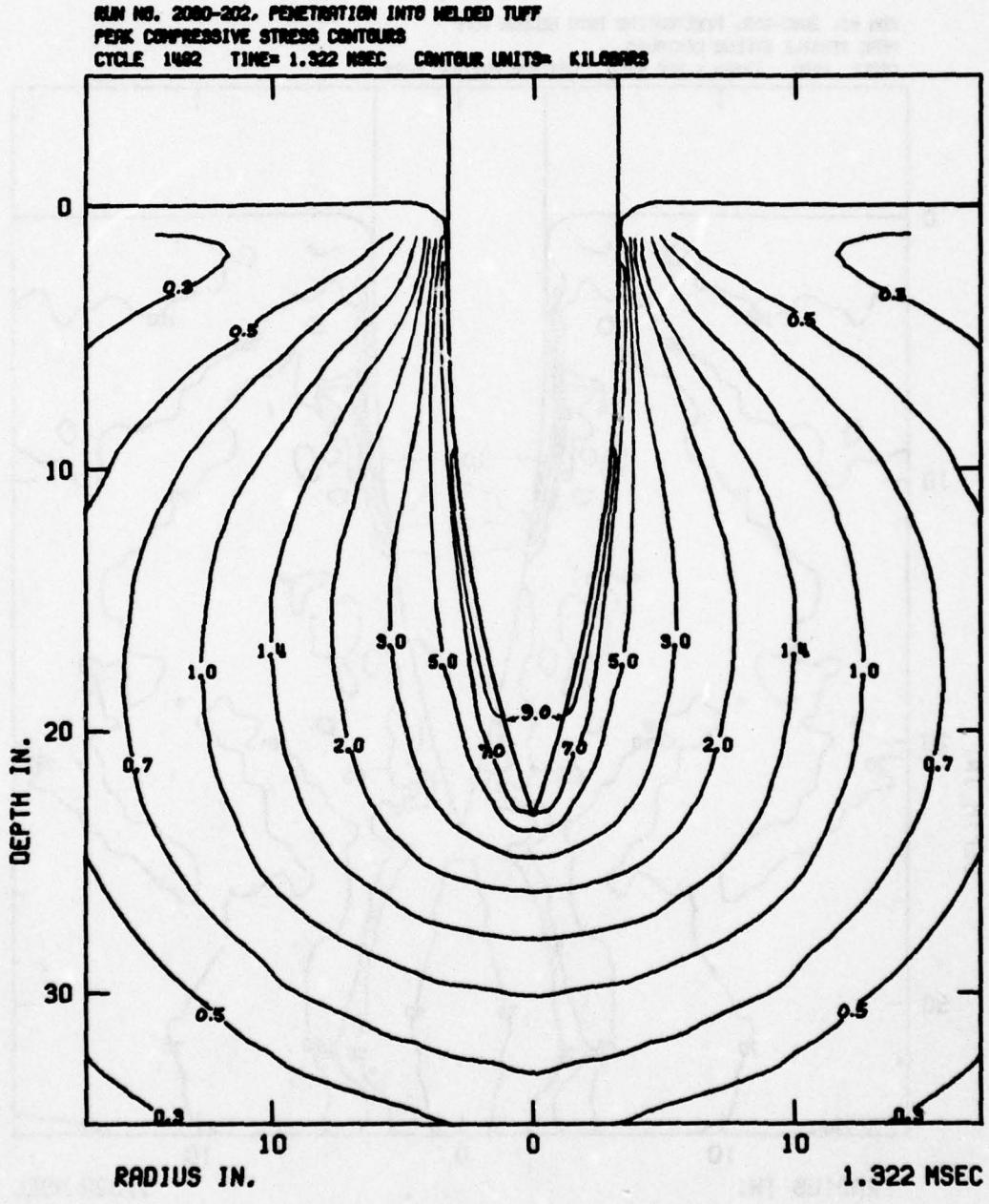


Figure 28. Contours of Peak Compressive Stress (kb) Experienced by 1.32 msec in Welded Tuff

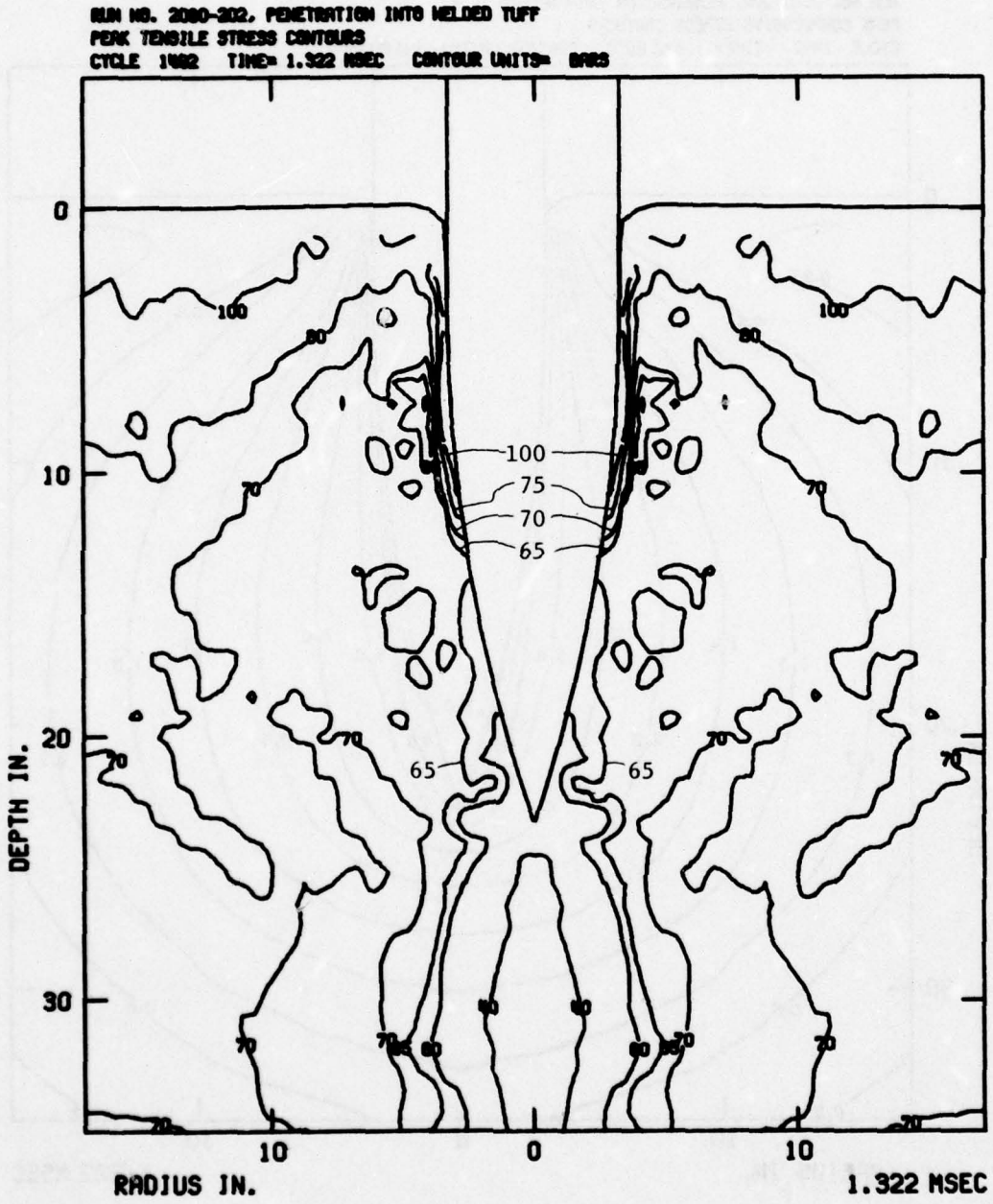


Figure 29. Contours of Peak Tensile Stress (bars) Experienced by 1.32 msec in Welded Tuff

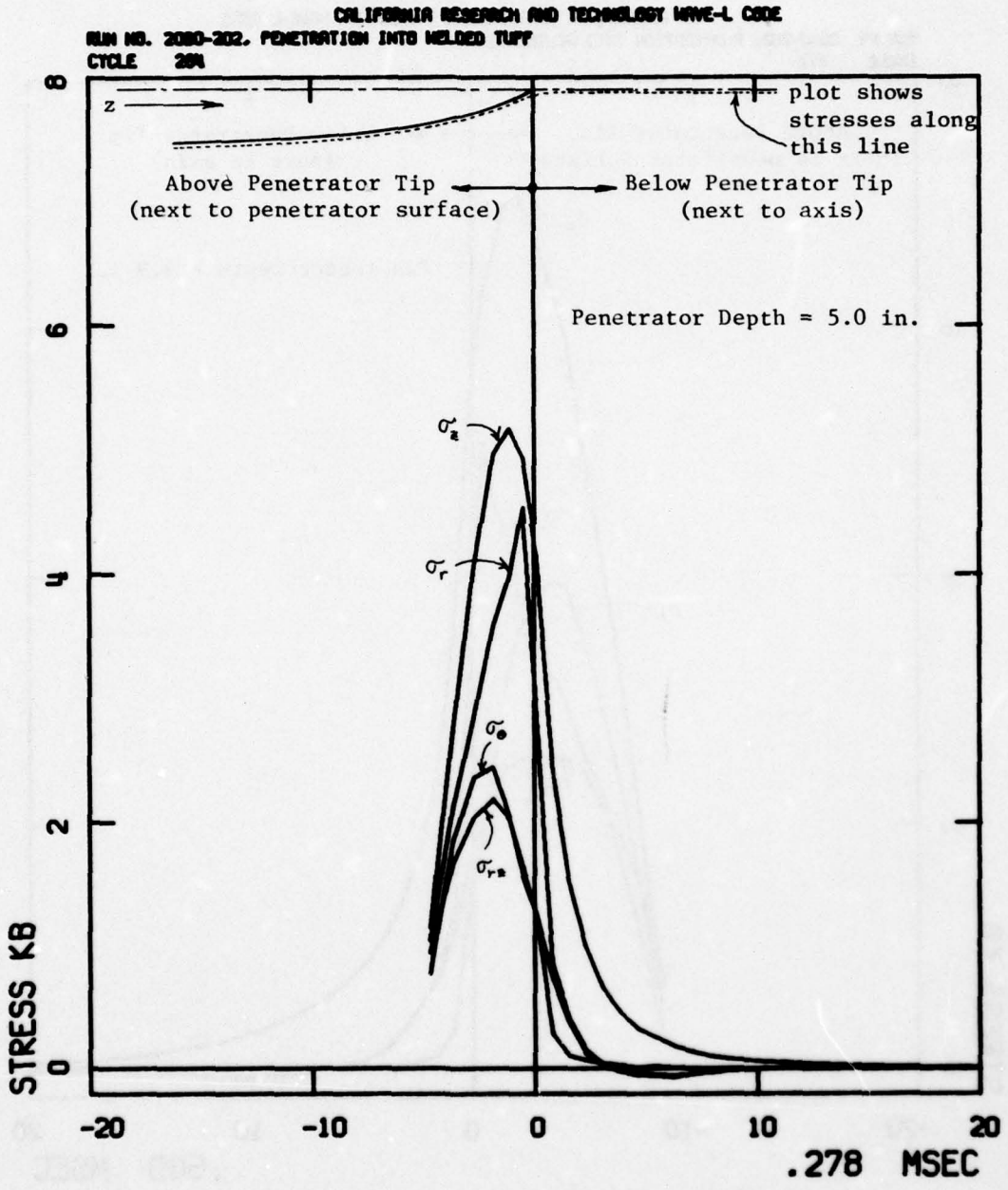


Figure 30. Stress Profiles in Welded Tuff along Central Axis or Penetrator Surface, t = .278 msec

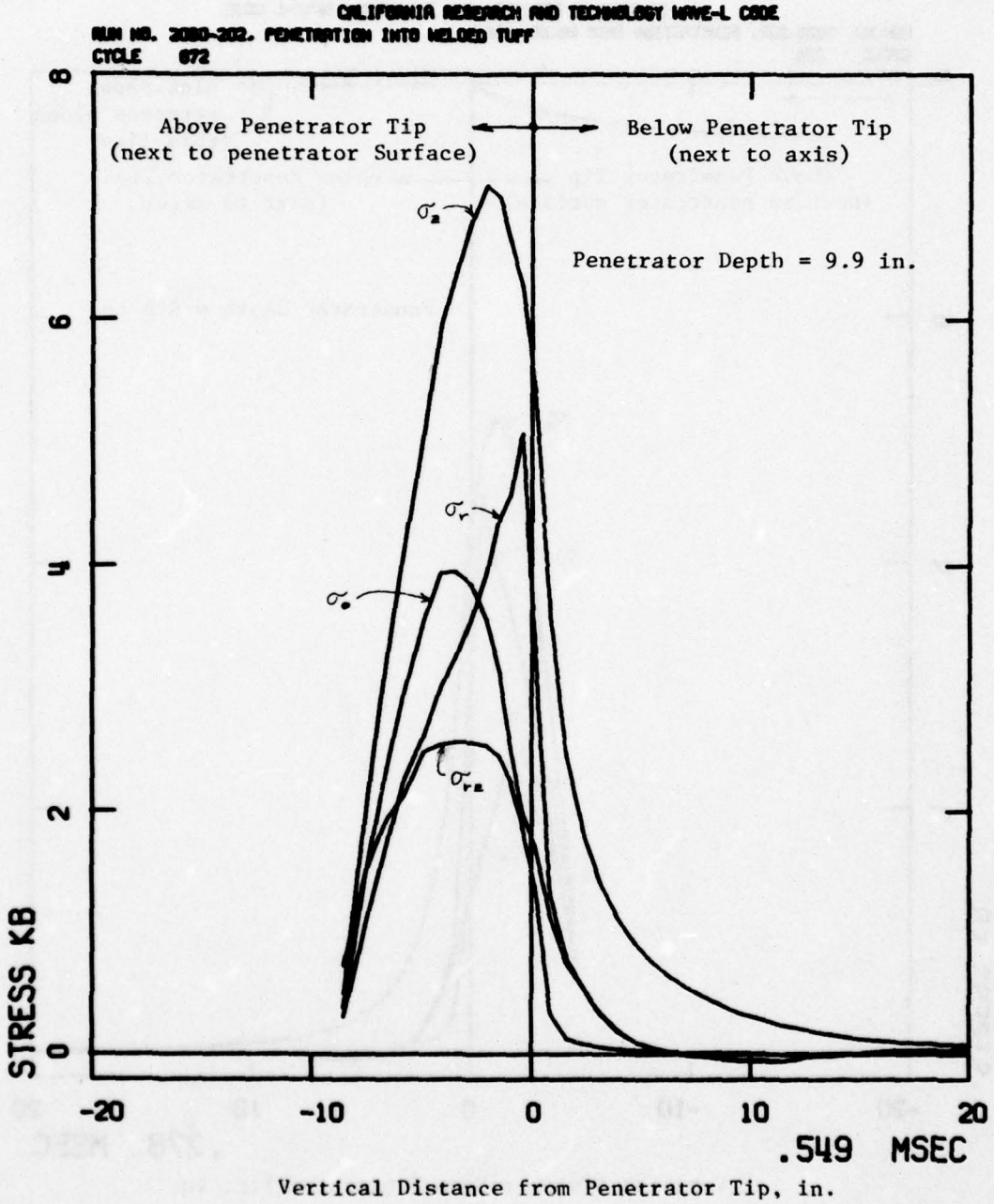


Figure 31. Stress Profiles along Central Axis or Penetrator Surface, t = .549 msec

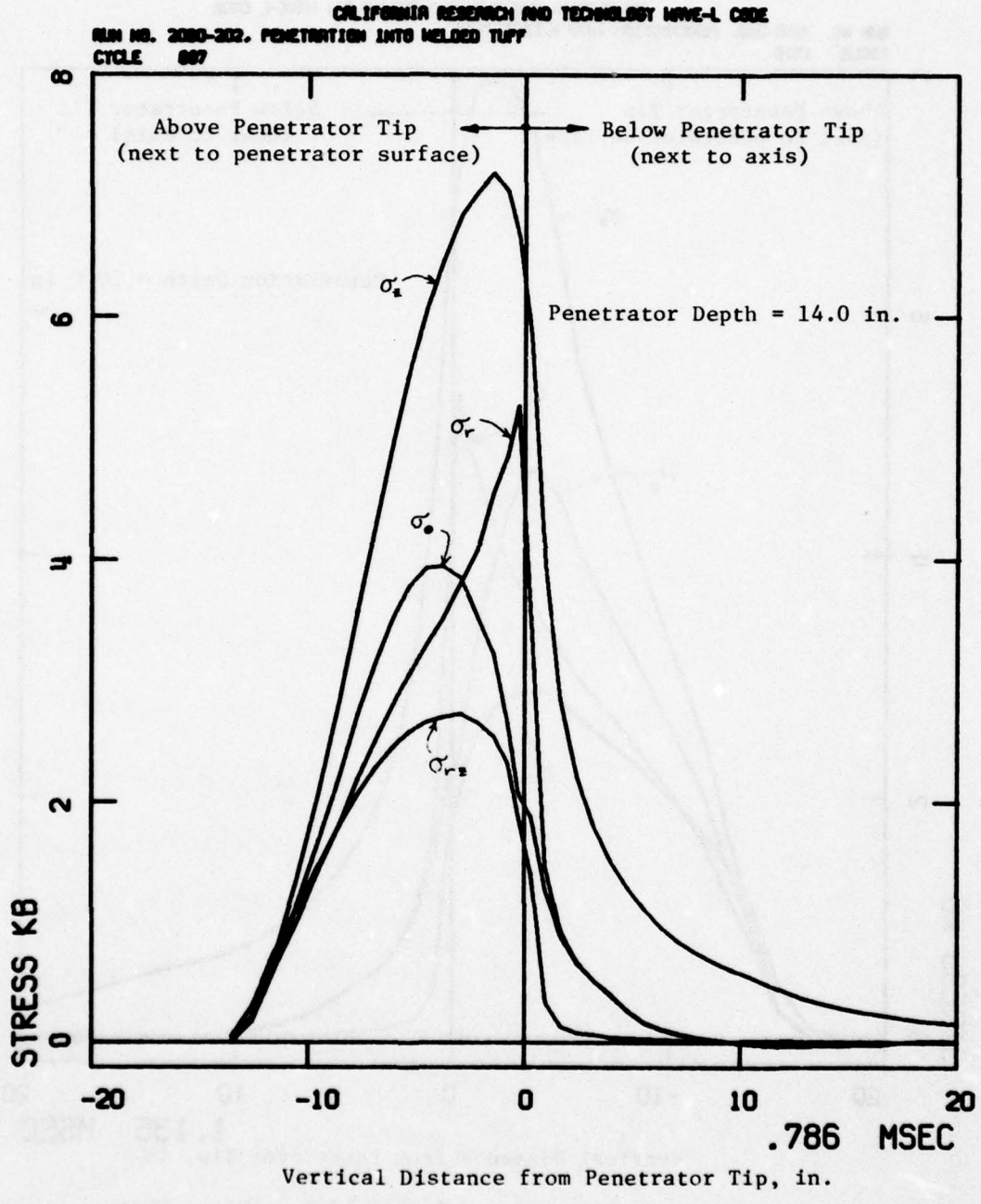


Figure 32. Stress Profiles along Central Axis or Penetrator Surface, t = .786 msec

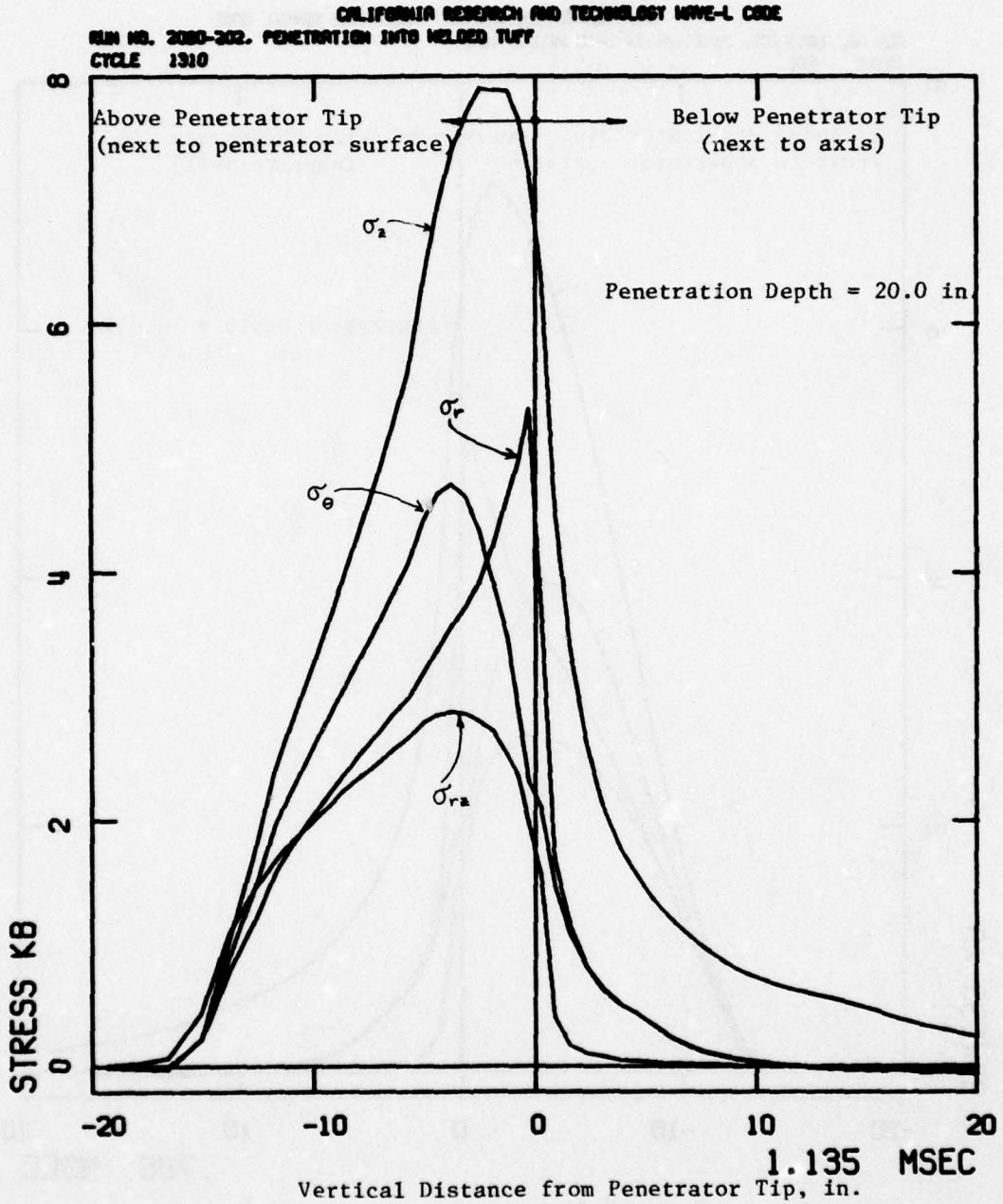


Figure 33. Stress Profiles along Central Axis or Penetrator Surface, t = 1.135 msec

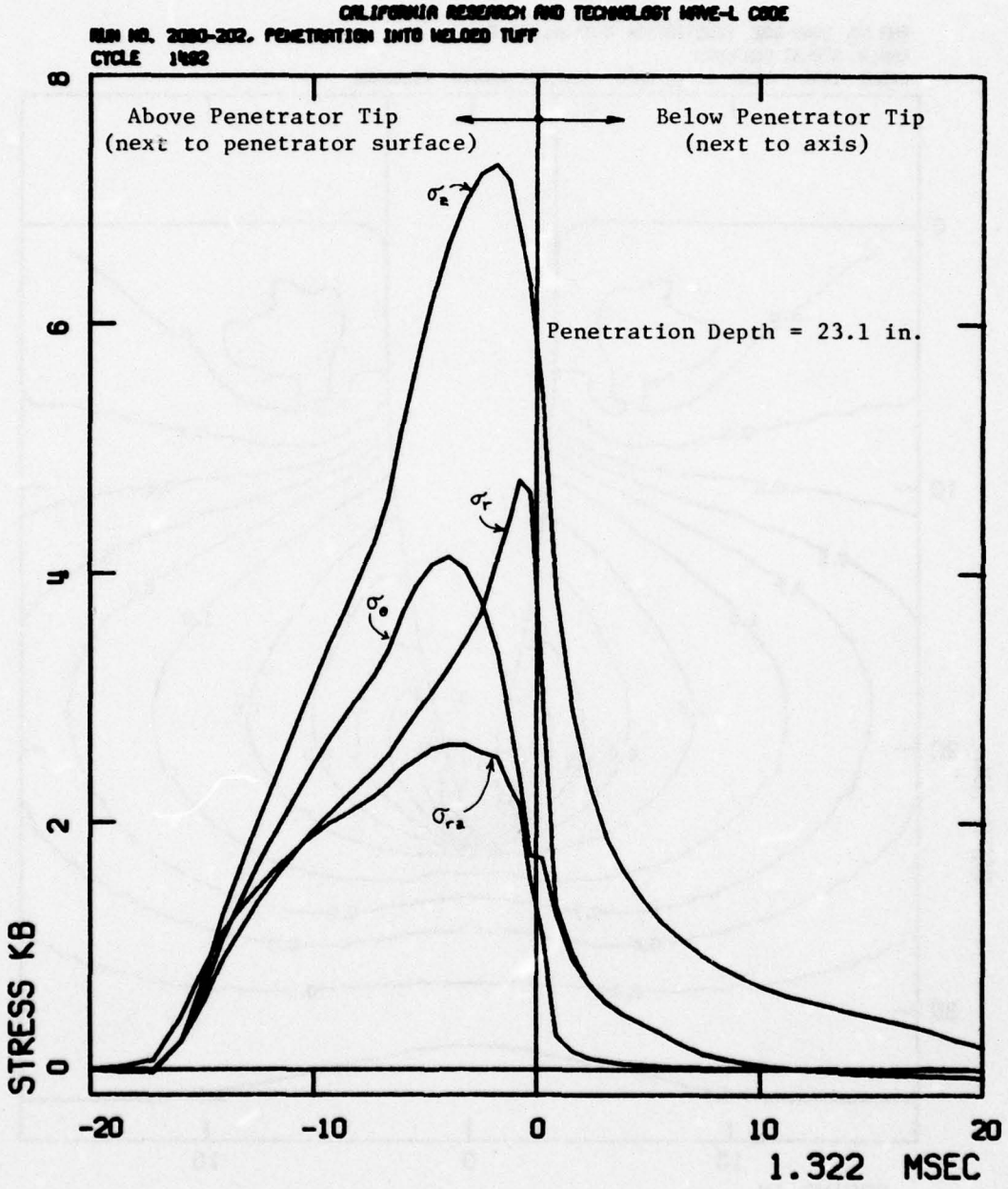


Figure 34. Stress Profiles along Central Axis or Penetrator Surface t = 1.322 msec

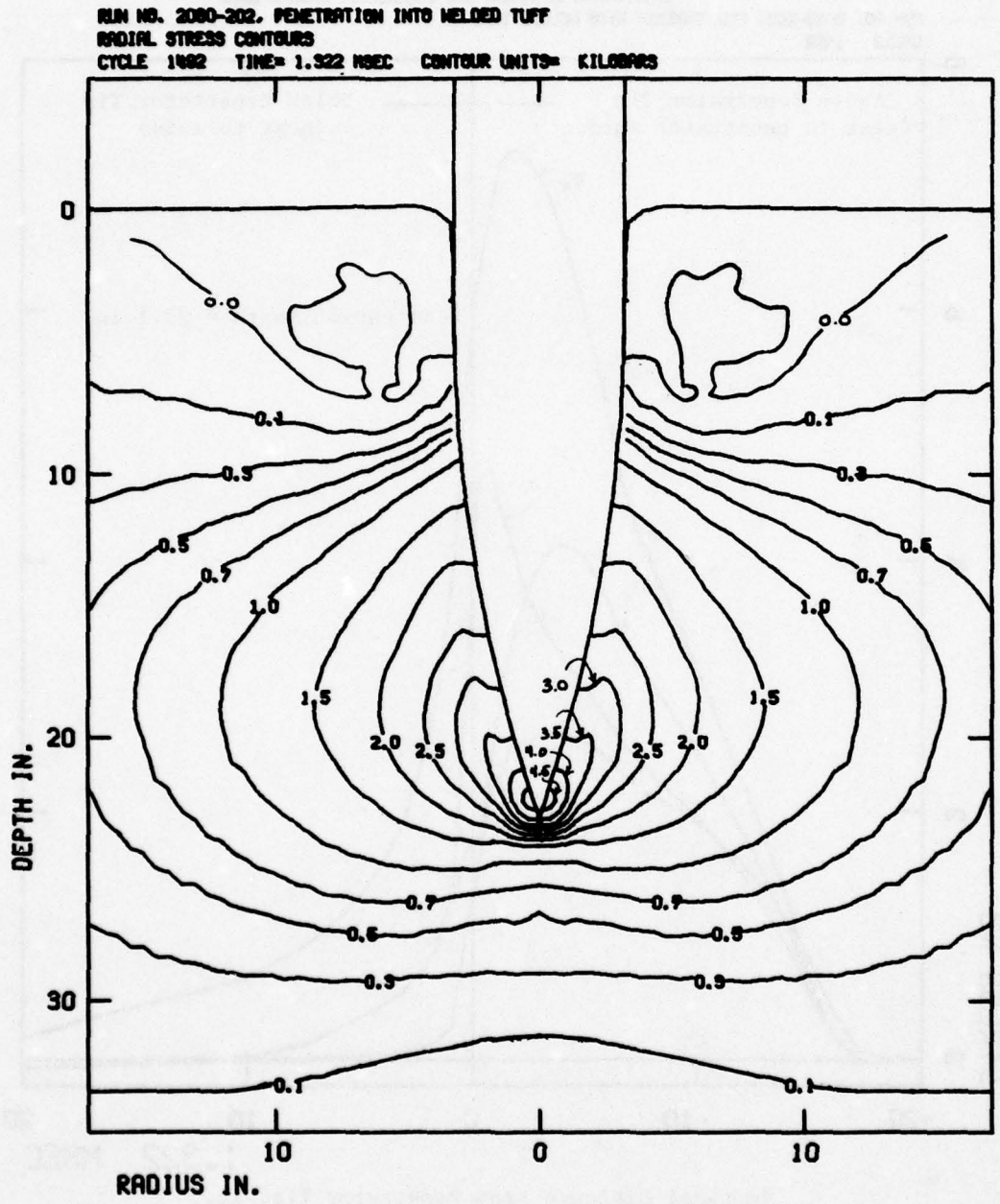


Figure 35. Contours of Radial Stress (kb) in Welded Tuff at 1.32 msec

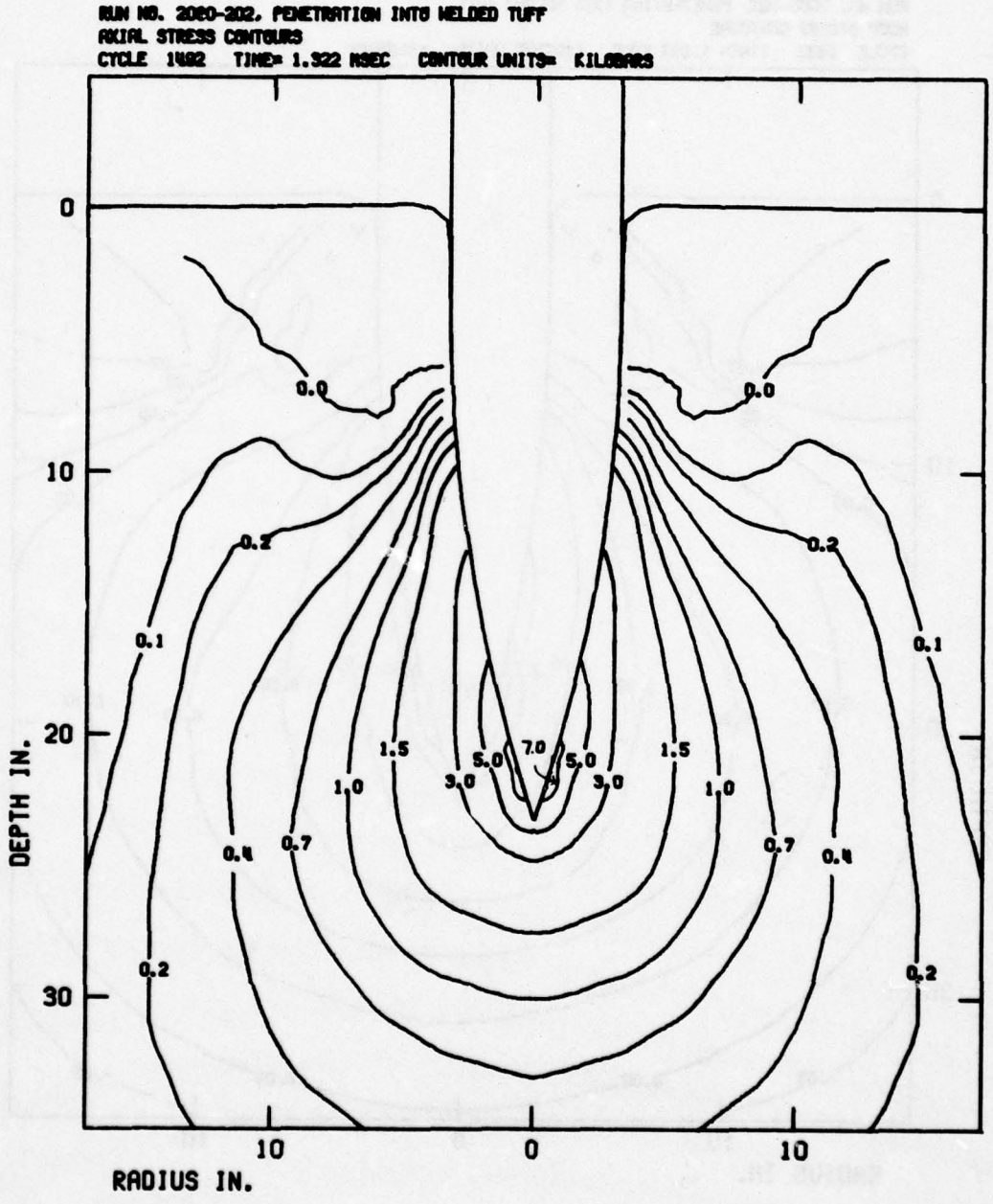


Figure 36. Contours of Axial Stress (kb) in Welded Tuff at 1.32 msec

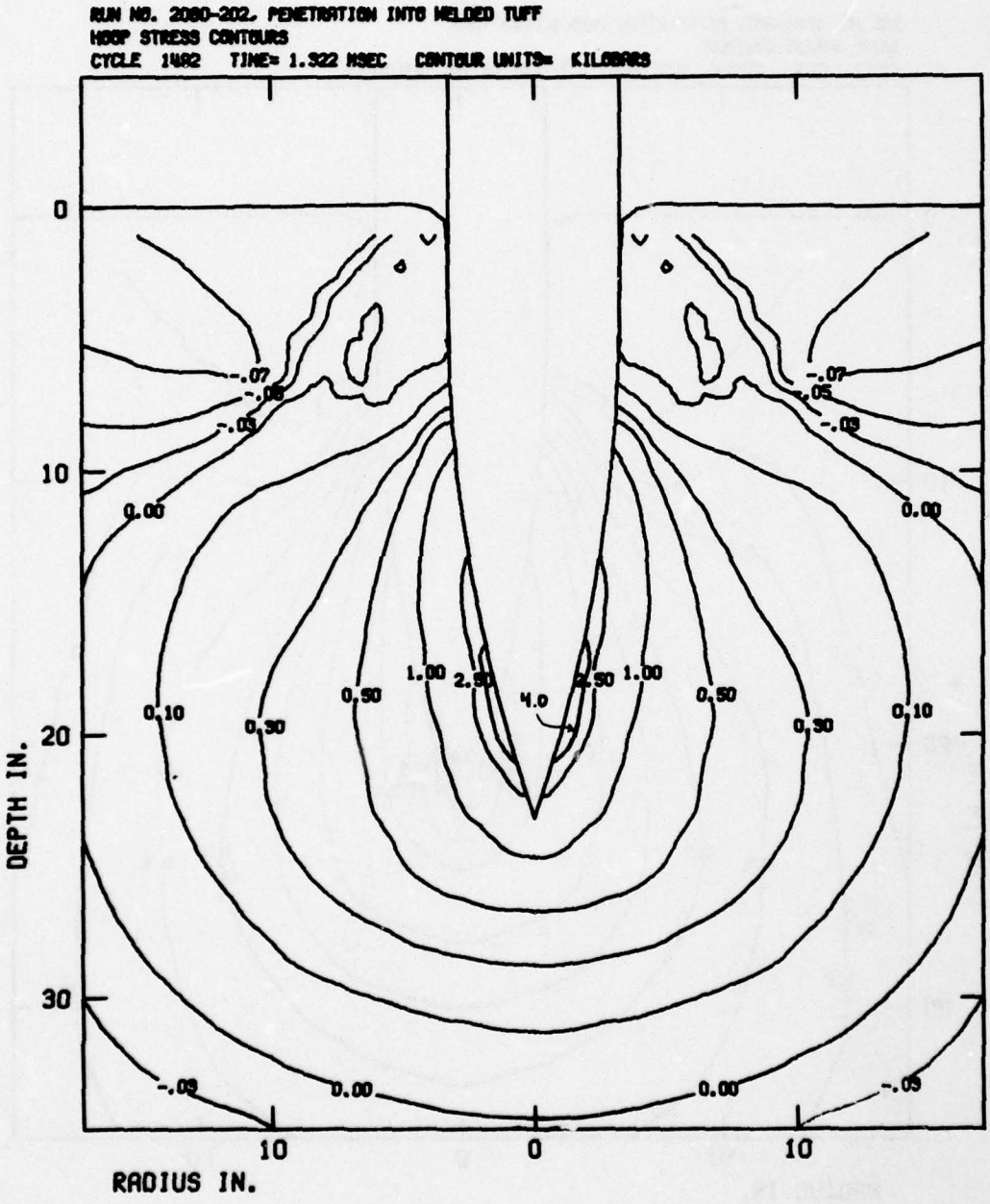


Figure 37. Contours of Hoop Stress (kb) in Welded Tuff at 1.32 msec

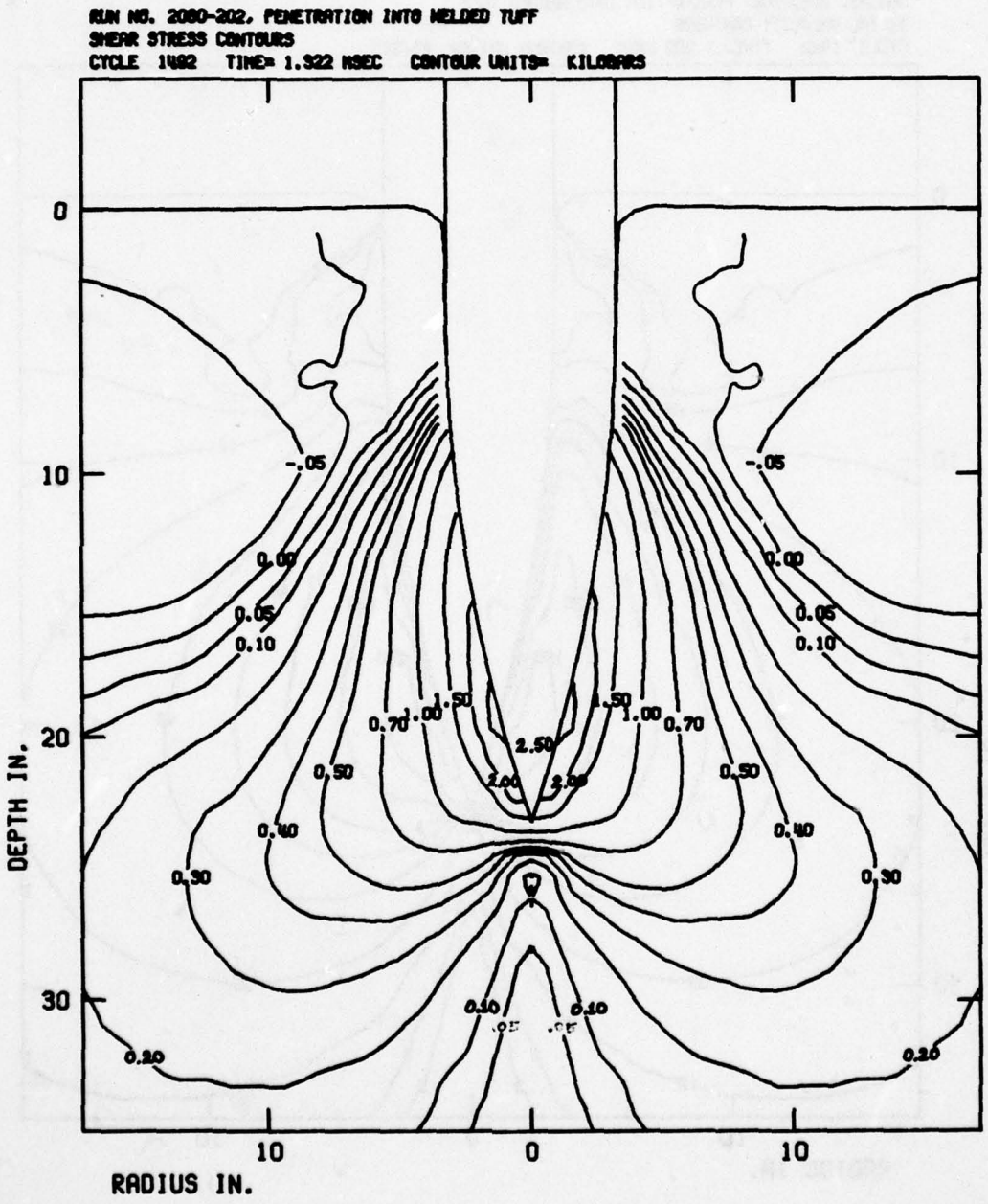


Figure 38. Contours of Shear Stress (kb) in Welded Tuff at 1.32 msec

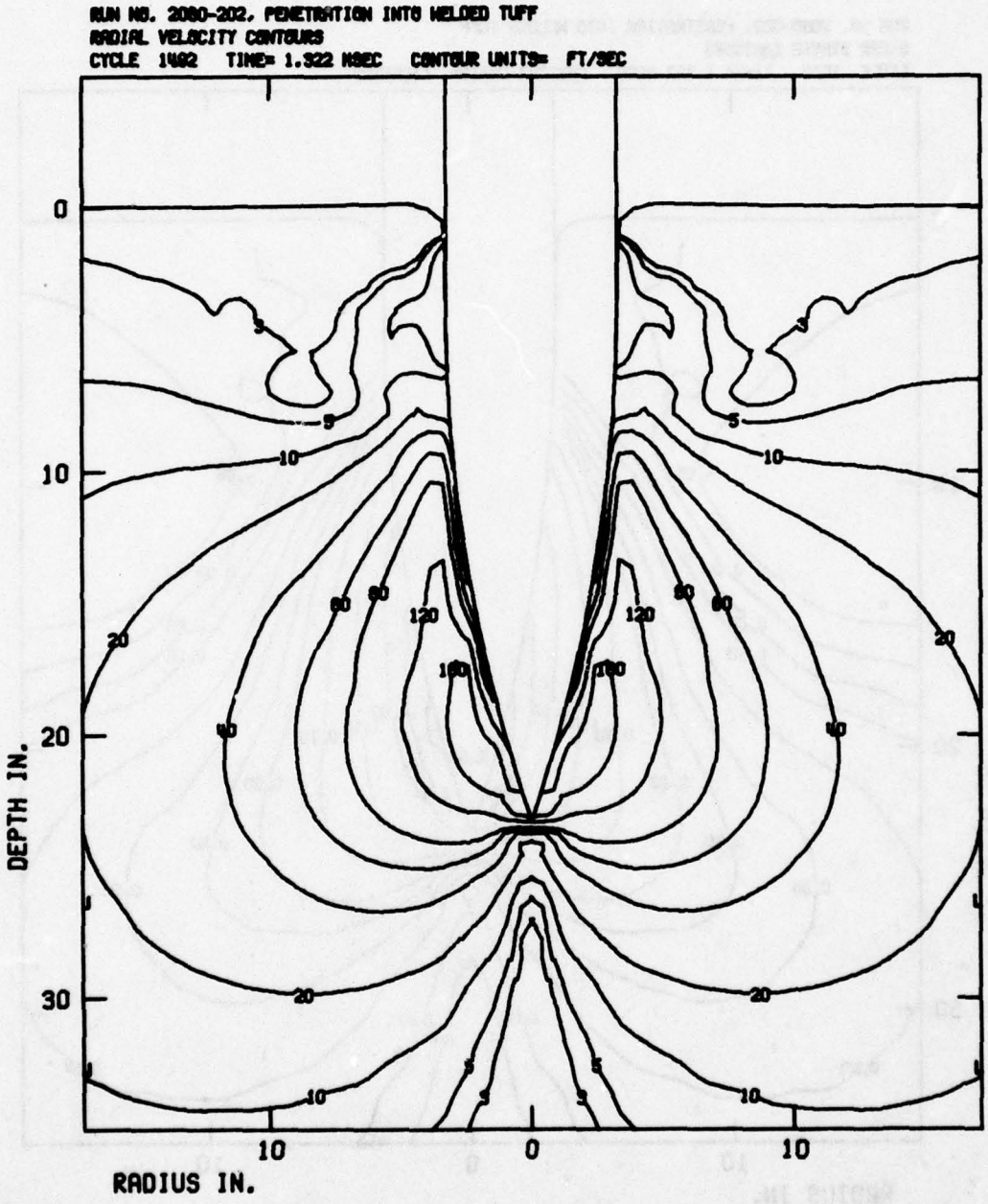


Figure 39. Contours of Radial Velocity (ft/sec) in Welded Tuff at 1.32 msec

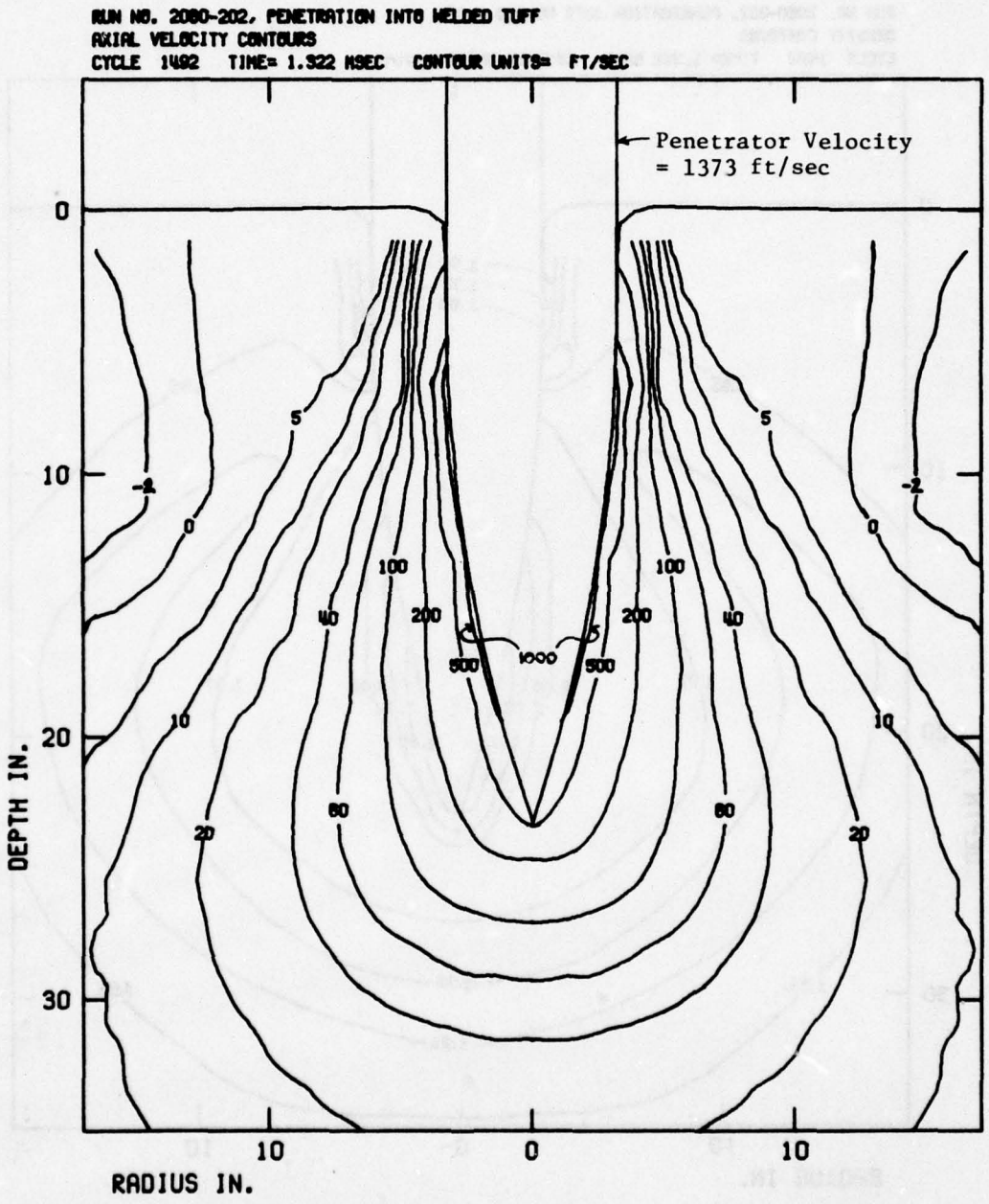


Figure 40. Contours of Axial Velocity (ft/sec) in Welded Tuff at 1.32 msec

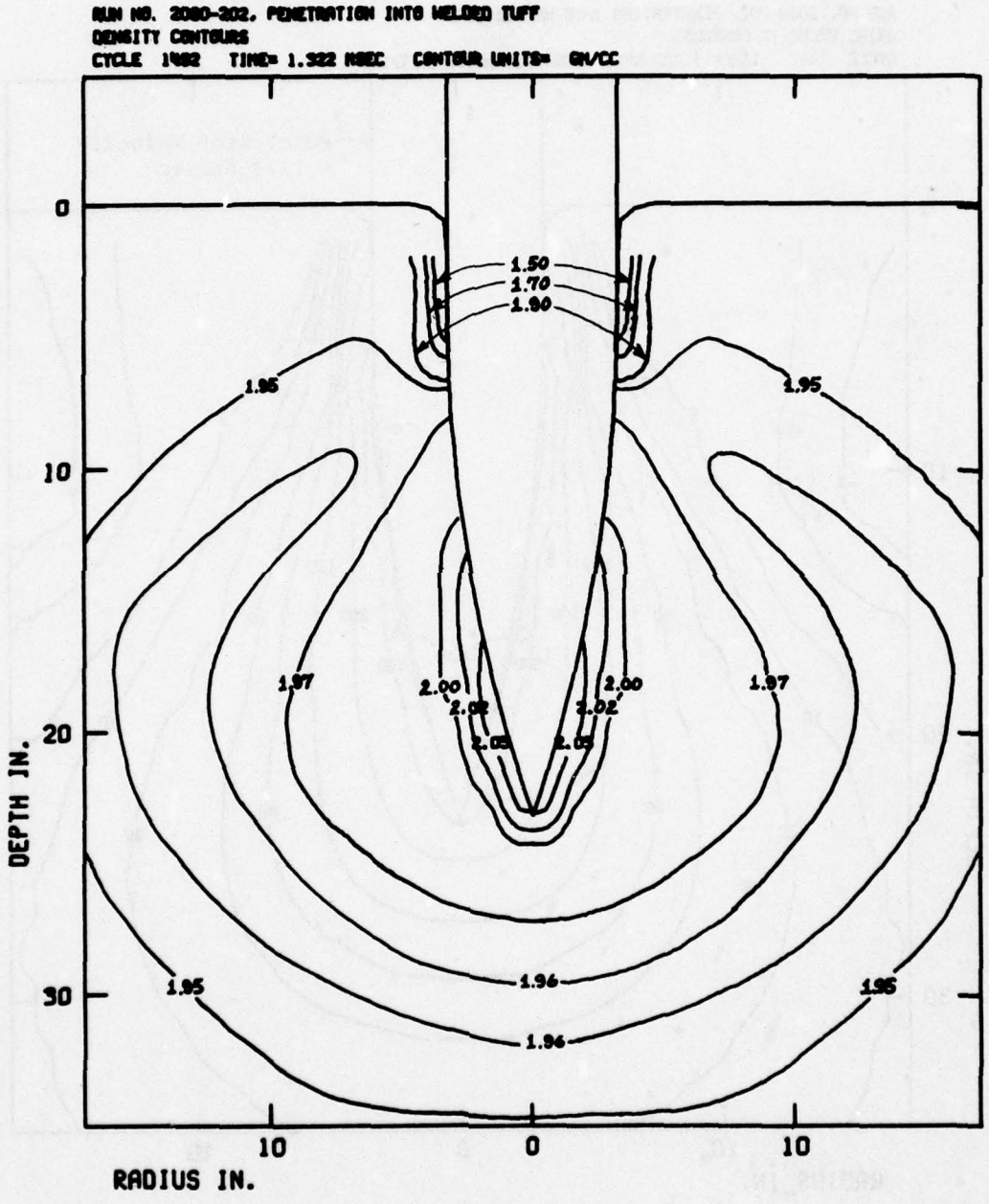


Figure 41. Contours of Density (gm/cm^3) in Welded Tuff at 1.32 msec

3.3.2.3 Compression - Extension States

The property tests on welded tuff samples showed that the failure surface was not symmetrical for triaxial compression and triaxial extension tests, with the extension failure surface having a lower amplitude. This is not unusual for geological materials; nonetheless, most material models have used symmetrical failure surfaces, usually consisting of a surface of revolution about the (1,1,1) line in (σ_1, σ_2, σ_3) principal stress space. The symmetrical failure surfaces have usually been used since in many cases only triaxial compression data were available, or the asymmetry was not considered to be significant. Considerably more effort is entailed in developing asymmetric failure models, as well, and data under torsion or biaxial loading, which are required to determine the characteristics of the failure surface between the triaxial compression and triaxial extension lines, are usually not available.

A general model has been worked out which can be employed to fit data obtained under arbitrary loading conditions. This model was used to fit Solenhofen limestone, for which a large body of data under conditions of triaxial compression, triaxial extension, torsion, and biaxial loading was available. The model is described in Reference 20.

For the welded tuff model, there was not time to investigate the possiblity of using a general model. However, it was decided to examine the stress states occurring in the solution to see to what extent they departed from the line of triaxial compression, upon which the symmetrical model was based.

By using a rotated principal stress space, where

$$x = (\sigma_1 - 2\sigma_2 + \sigma_3)/\sqrt{6}$$

$$y = (\sigma_1 - \sigma_3)/\sqrt{2}$$

$$z = (\sigma_1 + \sigma_2 + \sigma_3)/\sqrt{3}$$

and projecting the resulting states onto the x,y plane, the stress conditions can be visualized, as shown in Figure 42 (this technique is more fully described in Reference 20). If the stresses are ordered according to $\sigma_1 \geq \sigma_2 \geq \sigma_3$, all states will lie in the sector shown. The sector boundaries correspond to triaxial extension and triaxial compression as indicated.

Figures 43 to 45 show the stress states occurring at 1.32 msec. The stress states in each vertical column of cells starting from the central axis are plotted (corresponding to .4 to 12.2 in. radii). Generally, the stress states at ground depths below the depth of the penetrator tip are seen to lie close to the triaxial compression line. States lying above the penetrator tip are seen to diverge toward the y axis (line of torsion). At the higher radii, some low-stress extension states are seen. Since the actual yield surface would have downward-slanting lines across the sector from right to left (see Figure 42), the stress states lying off the triaxial compression boundary would be forced downward from their present position, limiting the buildup of deviatoric stress. The material strength is thus *overestimated* with the symmetrical model.

3.3.2.4 Energy Partition

The energy partitioning between the penetrator and the ground during the solution is given in Figure 46.

Additional computational results are contained in Appendix B; included are time histories of stress and velocity and stress paths at several locations in the ground, and additional deformation, velocity, and stress field plots at intermediate times.

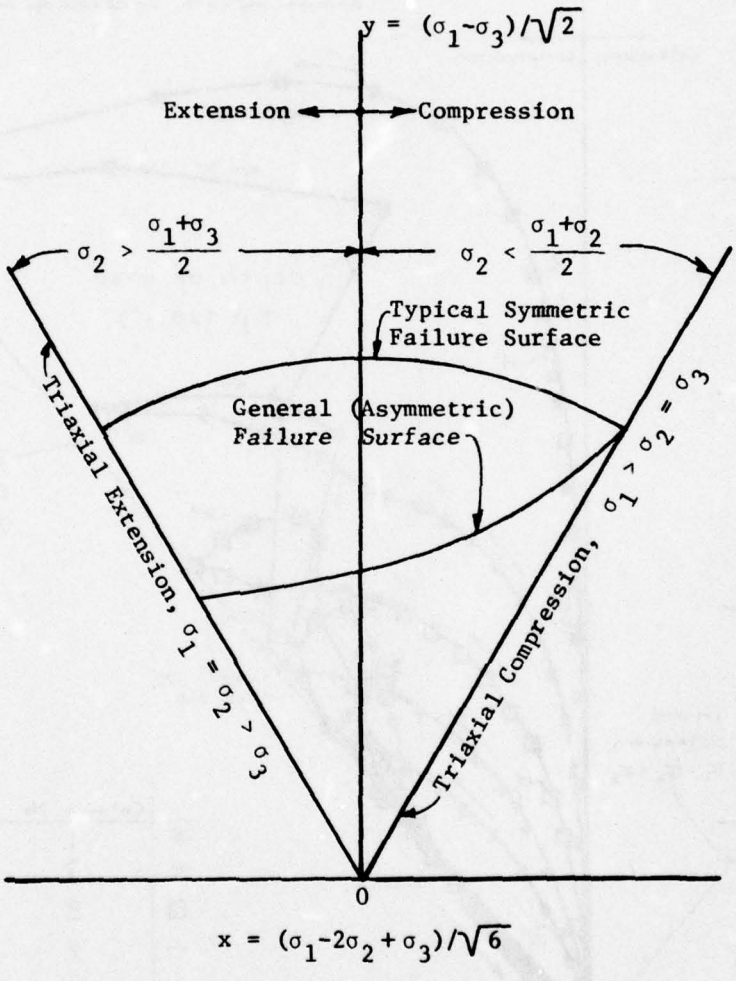


Figure 42. $\sigma_1 \geq \sigma_2 \geq \sigma_3$ Sector of Rotated Principal Stress (x,y) Plane Showing Yield Surface Forms at a Given Pressure

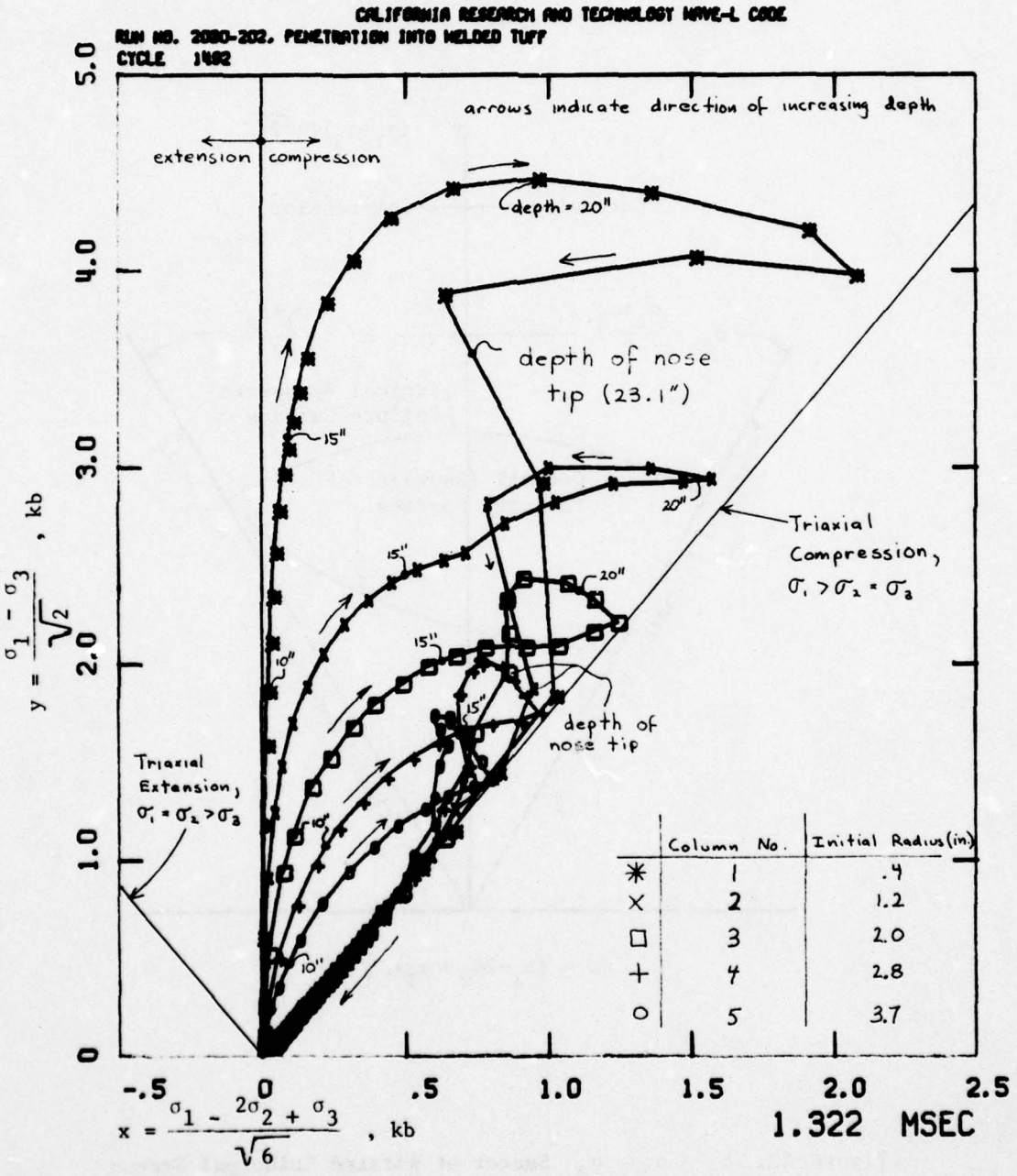


Figure 43. Stress States in Rotated Principal Stress Space, Columns 1 to 5

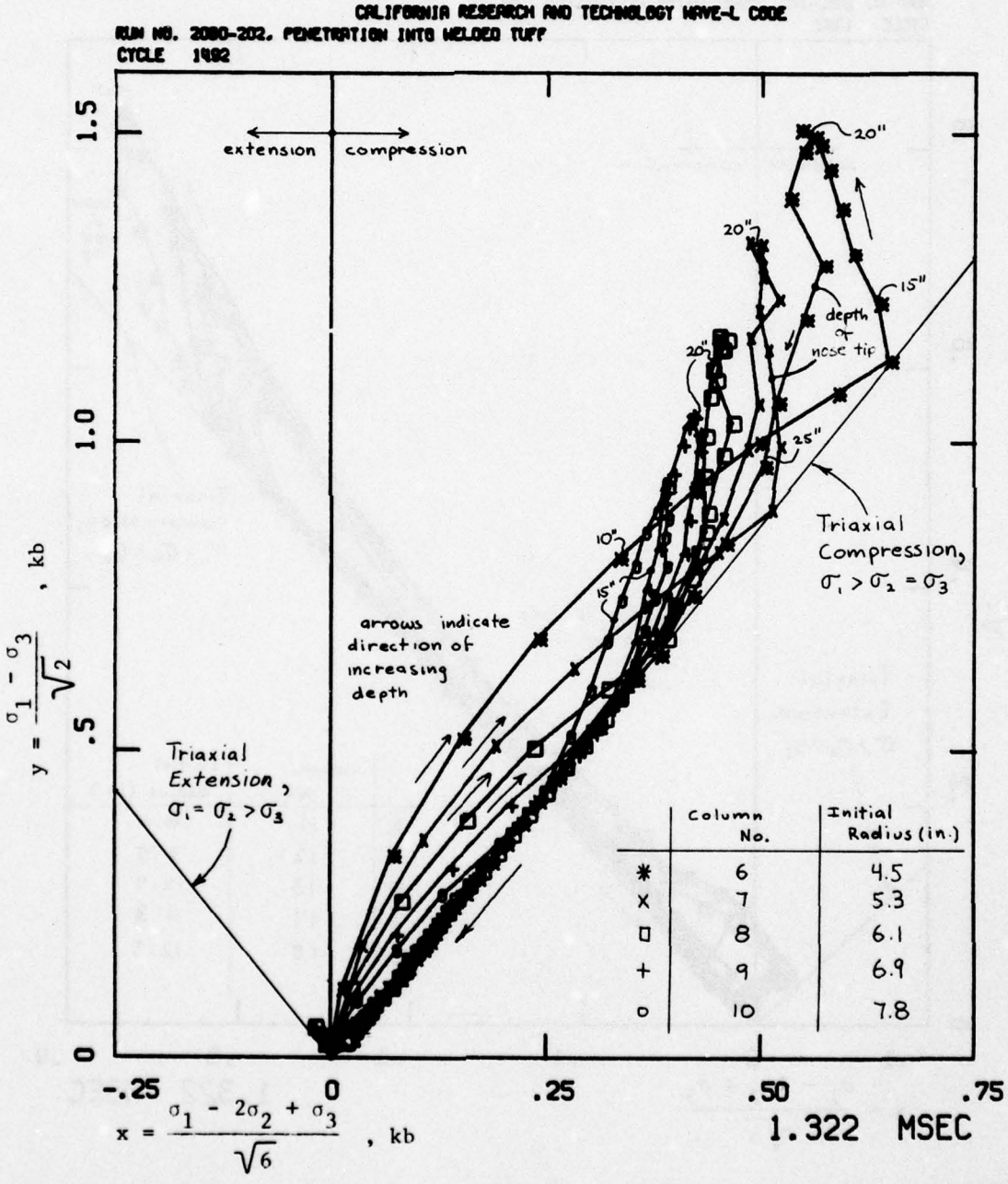


Figure 44. Stress States in Rotated Principal Stress Space, Columns 6 to 10

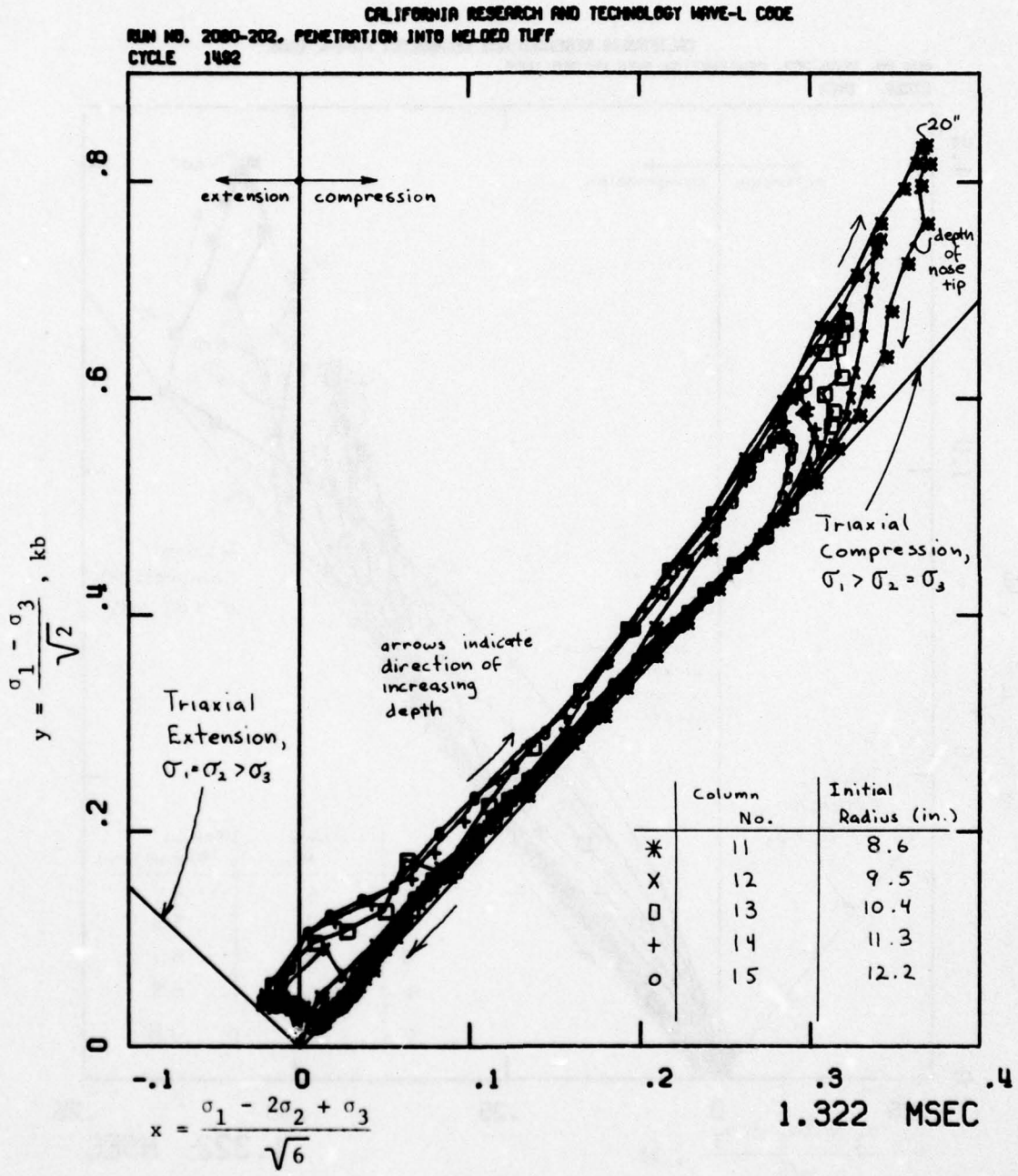


Figure 45. Stress States in Rotated Principal Stress Space, Columns 11 to 15

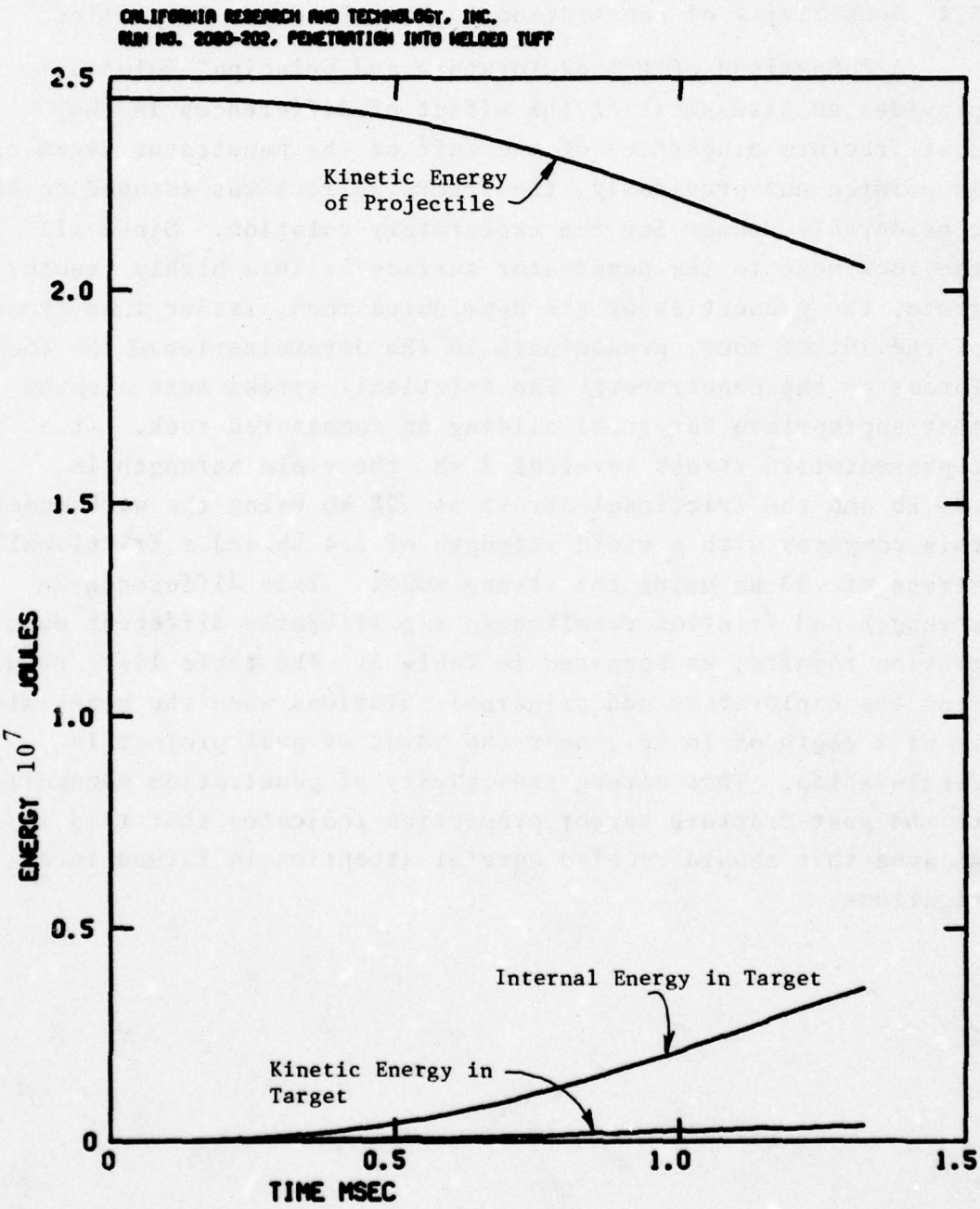


Figure 46. Energy Partition vs Time

3.4 Sensitivity of Penetration to Post-Fracture Properties

A comparison of the exploratory and principal solutions provides an assessment of the effect of differences in the post-fracture properties of the tuff on the penetrator dynamics. As pointed out previously, the fractured rock was assumed to be considerably weaker for the exploratory solution. Since all the rock next to the penetrator surface is in a highly fractured state, the properties of the comminuted rock, rather than those of the intact rock, predominate in the determination of the local forces on the penetrator. The frictional stress must also be that appropriate for steel sliding on comminuted rock. At a representative stress level of 2 kb, the yield strength is .95 kb and the frictional stress is .08 kb using the weak model; this compares with a yield strength of 2.4 kb and a frictional stress of .33 kb using the strong model. This difference in strength and friction resulted in significantly different penetration results, as compared in Table 3. The table lists results from the exploratory and principal solutions when the penetrator is at a depth of 16 in., near the point of peak projectile deceleration. This strong sensitivity of penetration mechanics to the post-fracture target properties indicates that this is an area that should receive careful attention in future investigations.

TABLE 3. COMPARATIVE RESULTS FROM PENETRATION SOLUTIONS

	Exploratory Solution (Weak Post-Fracture Properties)	Principal Solution (Strong Post-Fracture Properties)
Penetrator Deceleration, g's	1790	4510
Axial Force on Penetrator, kips/rad	147	371
Frictional Component of Axial Force, kips/rad	25	158
Radial Force on Penetrator, kips/rad	564	943
Peak Normal Stress on Penetrator, kb	3.5	6.8
Peak Tangential Stress on Penetrator, kb	.1	1.0
Peak Compressive Stress in Tuff, kb	3.6	9.5

Values listed are for penetration depth of 16 in.

SECTION IV

CONCLUSIONS

An objective of this effort was to develop and verify "first-principle" hydrocode techniques for obtaining detailed descriptions of penetration dynamics occurring for the normal impact and penetration of projectiles into rock media. The results described in this report indicate that development of the techniques has been essentially completed.

An important result of the effort was recognition of the importance of the fracture and comminution of rock occurring during projectile penetration. Since the penetrator is enveloped by comminuted material during the penetration process, it becomes essential to incorporate a model of comminution that predicts fracture and then ascribes appropriate post-fracture properties to the broken-up material. This important part of the model appears to be working properly, with predicted fracture patterns appearing to be in general agreement with that observed.

Probably the most uncertain aspect of the penetration process concerns the amount of frictional force being applied to the penetrator. The severe dragdown of material next to the penetrator and lack of debris blowoff near the surface (as shown in Figure 7) indicates that friction was probably overspecified in this solution. The results of the exploratory solution, which used a model with a smaller amount of friction, gave a velocity pattern which appears to be physically more realistic (Figure 47). Post-test surveys and analysis of the field event records should provide some guidance on this problem. It is known that considerable heating and some melting takes place at the projectile surface, since patches of metal film and comminuted rock fused together were found along the hole wall.

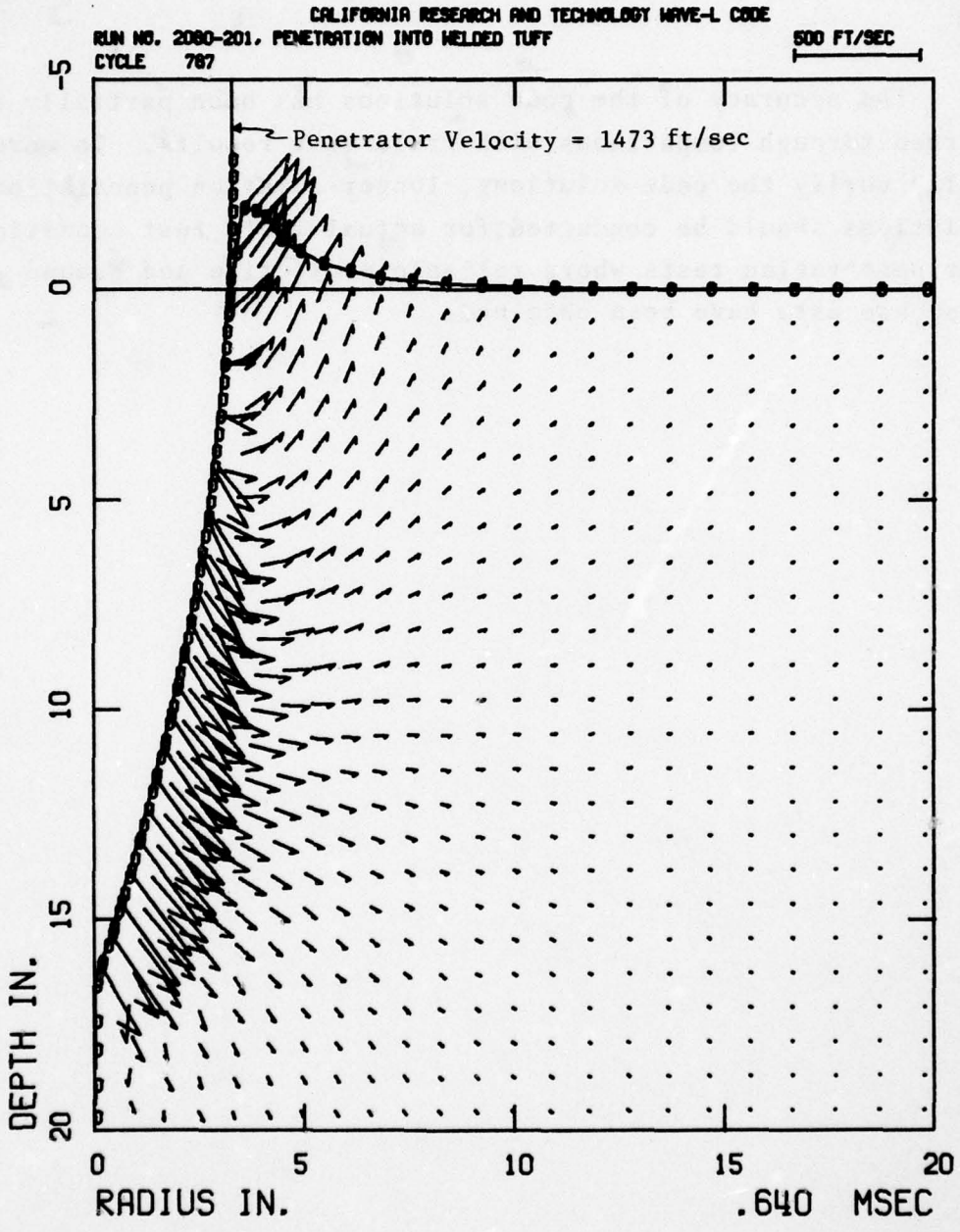


Figure 47. Particle Velocity Field in Welded Tuff, Preliminary Solution

The accuracy of the code solutions has been partially confirmed through comparisons with field test results. To more fully verify the code solutions, longer-duration penetration solutions should be conducted for actual field test conditions for penetration tests where reliable projectile and ground response data have been obtained.

REFERENCES

1. M. H. Wagner, K. N. Kreyenhagen, and W. S. Goerke, *Numerical Analysis of DNA Earth Penetrator Experiment at DRES*, Defense Nuclear Agency, Report DNA 3537F, 18 June 1975.

2. M. H. Wagner, K. N. Kreyenhagen, and W. S. Goerke, *Numerical Analysis of Projectile Impact and Deep Penetration into Earth Media*, U. S. Army Engineer Waterways Experiment Station, Report S-75-4, August 1975.

3. Y. M. Ito, K. N. Kreyenhagen, G. E. Eggum, and W. S. Goerke, *Analysis of Dynamic Stresses within a Terminal Delivery Vehicle during Penetration of a Hard Earth Target*, U. S. Army Engineer Waterways Experiment Station, Report S-75-1, February 1975.

4. W. J. Patterson, *Projectile Penetration of In Situ Rock*, Sandia Laboratories, Report SLA-73-0831, November 1973.

5. P. F. Hadala, *Tentative Plan for Constitutive Property Testing at the Mount Helen Site, Tonopah Test Range, Nevada*, U. S. Army Engineer Waterways Experiment Station, Memorandum for Record, 4 December 1974.

6. M. H. Wagner, C. C. Fulton, and K. N. Kreyenhagen, *Parametric Study of the Effects of Target Properties, Projectile Design, and Impact Conditions on Earth Penetration Processes*, California Research & Technology, Topical Report CRT 2080-3 (Draft), November 1976.

7. P. F. Hadala, *A Data Package for Use in the Calculation of a DNA Penetration Test in Thirsty Canyon Welded Tuff*, U. S. Army Engineer Waterways Experiment Station, 20 May 1975.

8. D. K. Butler, *Constitutive Property Investigations in Support of Full Scale Penetration Tests, Report 1, Thirsty Canyon Welded Tuff, Tonopah Test Range, Nevada*, U. S. Army Engineer Waterways Experiment Station, Preliminary Report, March 1975.

9. S. W. Butters, H. S. Swolfs, and J. N. Johnson, *Field Laboratory and Modeling Studies on Mount Helen Welded Tuff for Earth Penetrator Test Evaluation*, Terra Tek, Report TR-75-9, January 1975.

10. *Earth Penetrating Weapon Program Review Meeting*, Defense Nuclear Agency, 5 October 1976 (Relevant reports to be published).

11. Y. M. Ito and M. H. Wagner, *Internal Response Analyses of Earth Penetrators*, California Research & Technology, Topical Report CRT 2080-1 (Draft), August 1975.

12. S. W. Butters, Terra Tek, Letter dtd 25 June 1975.

13. D. K. Butler, U. S. Army Engineer Waterways Experiment Station, Letter dtd 18 June 1975.

14. P. F. Hadala, U. S. Army Engineer Waterways Experiment Station, Personal Communication, 12 June 1975.

15. C. W. Smith, *Lithium Niobate Stress Gage Measurements on Penetrator Experiments in Welded Tuff*, Sandia Corp., Progress Report (Draft), June 1976.

16. W. J. Patterson, Sandia Corp., Letter dtd 18 June 1976.

17. P. F. Hadala, *Visit to Tonopah Test Range, 14-15 July, 1975*, U. S. Army Engineer Waterways Experiment Station, Memorandum for Record, 13 August 1975.

18. W. Young, Sandia Corp., Personal Communicaton, July 1976.

19. M. L. Wilkins, *Calculation of Elastic-Plastic Flow*, Lawrence Livermore Laboratory, UCRL-7322, Rev. 1, January 1969.

20. M. Rosenblatt and S. Timurtas, *Material Model Studies for Rocks and Soils, Part III, Fracture Model for Rocks*, Report DASA 2678, August 1971.

APPENDIX A

WELDED TUFF MATERIAL MODEL

This appendix gives the mathematical description of the material model developed for welded tuff. General features of the model are described in Section 2.2. The model was based on experimental constitutive properties data determined by WES and Terra Tek (Refs. A-1 to A-3). Differences between this version of the model and the model used for the exploratory penetration solution are indicated.

Symbol Definitions

B_ℓ = bulk modulus in loading
B_u = bulk modulus in unloading, reloading
G_ℓ = shear modulus in loading
G_u = shear modulus in unloading, reloading
J_2' = second invariant of deviatoric stresses
P_ℓ = pressure in loading
P_{max} = maximum pressure reached by a material element
P_u = pressure in unloading, reloading
Y = yield strength, basic yield surface
Y_{dgd} = degraded value of yield strength
Y_{max} = yield strength, maximum yield surface (fracture surface)
Y_{min} = yield strength, yield surface of crushed material
Y_{sh} = strain-hardened value of yield strength
$\bar{\varepsilon}^p$ = generalized plastic strain
$\bar{\varepsilon}^p_{ex}$ = excess generalized plastic strain
ε^p_{ij} = plastic strain component
$\mu = \frac{\rho}{\rho_o} - 1$ = natural volumetric strain
μ_{max} = maximum volumetric strain reached by a material element
ν_ℓ = Poisson's ratio in loading
ν_u = Poisson's ratio in unloading, reloading
ρ = density
ρ_o = normal density

Hydrostat

The model hydrostat was based on load-unload paths measured in isotropic compression tests conducted by Terra Tek and WES. This hydrostat differed slightly from the one used in the first model due to a re-interpretation of the data by the testing laboratories. The principal changes from that used before were: (a) the Terra Tek data was not shifted to eliminate an initial toe and (b) the representation given in Ref. A-1 was used solely instead of the previously recommended set of hydrostatic load-unload stress-strain curves (Ref. A-2).

Hydrostat Equations - Loading

$$
\begin{cases}
P_\ell = a_1 \mu & \mu \leq 0 \\
P_\ell = P_i + a_i(\mu-\mu_i) + b_i(\mu-\mu_i)^2 + c_i(\mu-\mu_i)^3, & \\
\qquad \mu_i < \mu \leq \mu_i + 1, \; i = 1,2,3,4 & \\
P_\ell = P_c + K_m(\mu-\mu_c) - (K_m-K_c)\mu^* \left[1-\exp\frac{\mu_c-\mu}{\mu^*}\right], & \mu > \mu_c
\end{cases}
$$

The values of the constants are:

$a_1 = .08$ Mb	$K_m = .6$ Mb
$b_1 = .261408$ Mb	$P_1 = 0.$
$c_1 = 29.8702$ Mb	$P_2 = .001$ Mb
$a_2 = .0978634$ Mb	$P_3 = .00202$ Mb
$b_2 = 1.29193$ Mb	$P_4 = .004$ Mb
$c_2 = -82.8818$ Mb	$P_c = .006$ Mb
$a_3 = .0989563$ Mb	$\mu_1 = 0.$
$b_3 = -1.18209$ Mb	$\mu_2 = .0115$
$c_3 = 15.0208$ Mb	$\mu_3 = .02145$
$a_4 = .068$ Mb	$\mu_4 = .0466$
$b_4 = -.910870$ Mb	$\mu_5 = .1$
$c_4 = 6.34517$ Mb	$\mu_c = .1$
$K_c = .025$ Mb	$\mu^* = .8$

Hydrostat - Unloading, Reloading ($\mu<\mu_{max}$)

$$\begin{cases} P_u = K_o' (\mu-\mu_s) & \mu < \mu_s \\ P_u = K_o' (\mu-\mu_s) + A(\mu-\mu_s)^{\alpha} & \mu > \mu_s \end{cases}$$

where

$$A = \frac{P_{max} - K_o' (\mu_{max}-\mu_s)}{(\mu_{max}-\mu_s)^{\alpha}}$$

$$\alpha = \frac{(\mu_{max}-\mu_s)(K_m'-K_o')}{P_{max}-K_o'(\mu_{max}-\mu_s)}$$

$$\begin{cases} K_m' = K_{uo} & \mu_{max} \le \mu_c \\ K_m' = K_m - (K_m-K_{uo}) \exp \frac{\mu_c - \mu_{max}}{\mu^*} & \mu_{max} > \mu_c \end{cases}$$

$$\begin{cases} \mu_s = 0 & \mu_{max} < \mu_a \\ \mu_s = \frac{\mu_{max} - \mu_a}{\mu_b - \mu_a} (r\ \mu_{max}) & \mu_a < \mu_{max} < \mu_b \\ \mu_s = r\ \mu_{max} & \mu_{max} \ge \mu_b \end{cases}$$

The values of the constants are:

$K_o' = .03$ Mb	$\mu_a = .01$
$K_m = .6$ Mb	$\mu_b = .04$
$K_{uo} = .16$ Mb	$\mu_u^* = .8$
$r = .15$	

Hydrostatic tension was limited by imposing a minimum value of pressure: $P_{min} = -33$ bars.

Shear Modulus - Loading

$$G_\ell = \text{Min}\left[\frac{3B_\ell(1-2\nu_\ell)}{2(1+\nu_\ell)}\ ,\ G_u\Big|_{\mu=\mu_{max}}\right]$$

where

$$B_\ell = (\mu+1)\frac{dP_\ell}{d\mu}$$

$$\nu_\ell = .2$$

Shear Modulus-Unloading, Reloading ($\mu<\mu_{max}$)

$$G_u = \frac{3B_u(1-2\nu_u)}{2(1+\nu_u)}$$

where

$$B_u = (\mu+1)\frac{dP_u}{d_\mu}$$

$$\nu_u = .5 - .32\ \exp(-10\ \mu_{max})$$

Yield/Fracture Surfaces

The yield surface, Y(P), defines the limit of elastic states; i.e., $\sqrt{3J_2'} \leq Y$. For tentative stress states lying outside the yield surface, plastic flow is computed in accordance with the Prandtl-Reuss (non-associated) flow rule.

The yield surfaces developed for the welded tuff model are shown in Figure A-1.

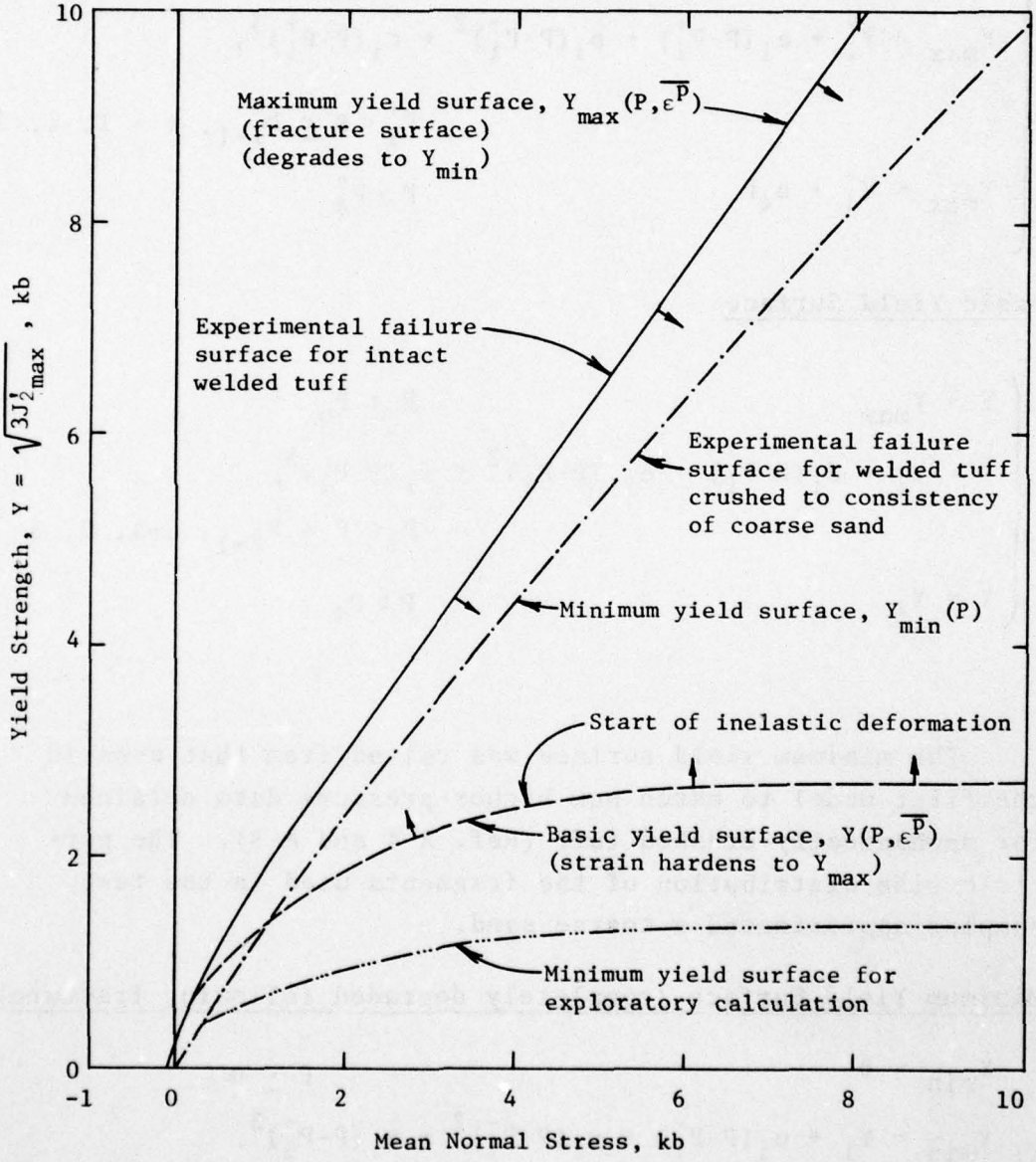


Figure A-1. Yield Surfaces for Welded Tuff Models

Maximum Yield Surface (Fracture Surface):

$$\begin{cases} Y_{max} = Y_i^+ + a_i(P-P_i^+) + b_i(P-P_i^+)^2 + c_i(P-P_i^+)^3, & P_i^+ < P \leq P_{i+1}^+,\ i = 1, 2, 3 \\ Y_{max} = Y_4^+ + a_4 P & P > P_4^+ \end{cases}$$

Basic Yield Surface

$$\begin{cases} Y = Y_{max} & P \leq P_o \\ Y = Y_i + d_i(P-P_i) + e_i\,(P-P_i)^2 + f_i(P-P_i)^3, & P_i < P \leq P_{i+1},\ i=1, 2, 3 \\ Y = Y_4 & P > P_4 \end{cases}$$

The minimum yield surface was raised from that used in the first model to match new higher-pressure data obtained for mechanically-crushed tuff (Ref. A-4 and A-5). The particle size distribution of the fragments used in the test samples approximated a coarse sand.

Minimum Yield Surface (completely degraded following fracture)

$$Y_{min} = 0 \qquad P \leq 0$$

$$Y_{min} = Y_i^- + u_i(P-P_i^-) + v_i(P-P_i^-)^2 + w_i(P-P_i^-)^3, \qquad P_i^- < P \leq P_{i+1}^-,\ i=1, 2$$

The values of the constants, for Y and P in Mb, are:

$a_1 = 13.$
$b_1 = -3.1376 \times 10^5$
$c_1 = 3.13561 \times 10^9$
$a_2 = 2.53589$
$b_2 = -3334.43$
$c_2 = 4.80632 \times 10^6$
$a_3 = 1.77131$
$b_3 = -306.452$
$c_3 = -10765.7$
$a_4 = 1.1464$

$d_1 = 1.2$
$e_1 = -466.648$
$f_1 = 128256.$
$d_2 = .702829$
$e_2 = -162.681$
$f_2 = 18133.3$
$d_3 = .269704$
$e_3 = -53.8815$
$f_3 = 3588.15$

$u_1 = 1.6$
$v_1 = -319.097$
$w_1 = 61411.9$
$u_2 = 1.04741$
$v_2 = -4.05443$
$w_2 = -974.364$

$P_1^+ = -3.3 \times 10^{-5}$
$P_2^+ = 0.$
$P_3^+ = 2.1 \times 10^{-4}$
$P_4^+ = .00118$
$Y_1^+ = 0.$
$Y_2^+ = 2 \times 10^{-4}$
$Y_3^+ = 6.3 \times 10^{-4}$
$Y_4^+ = 6.9725 \times 10^{-4}$

$P_o = 2.1 \times 10^{-4}$
$P_1 = 2.1 \times 10^{-4}$
$P_2 = .001$
$P_3 = .003$
$P_4 = .008$
$Y_o = 6.3 \times 10^{-4}$
$Y_1 = 6.3 \times 10^{-4}$
$Y_2 = .00135$
$Y_3 = .00225$
$Y_4 = .0027$

$P_1^- = 0.$
$P_2^- = .00171$
$P_3^- = .01$
$Y_o^- = 0.$
$Y_1^- = .00211$
$Y_2^- = .0067$

The basic yield surface strain hardens in accordance with:

$$Y_{sh} = Y_o + \left[Y - Y_o\right]\left[3 - 2\exp(-8\overline{\varepsilon^p}\right] \qquad \overline{\varepsilon^p} > 0,\ P > P_o$$

where

$$\overline{\varepsilon^p} = \int \left(\frac{2}{3}\, de^p_{ij} de^p_{ij}\right)^{\frac{1}{2}}$$

Strain-hardened yield strengths may not exceed the maximum yield surface (Y_{max}), however.

A state reaching the maximum yield surface signifies the onset of fracture. Material which has thus fractured is governed by the maximum yield surface, which then degrades as a function of excess generalized plastic strain, $\overline{\varepsilon^p_{ex}}$, accumulated from the onset of fracture:

$$Y_{dgd} = Y_{max}\left(1 - 11\ \overline{\varepsilon^p_{ex}}\right)$$

The degraded (post-fracture) yield surface has minimum values defined by Y_{min}, a yield surface representative of crushed welded tuff (Refs. A-3 to A-5).

The hydrostatic tension limit is similarly degraded to a final value of $P_{min}=0$ for the crushed tuff.

Model Results and Comparisons

Plots of vertical stress vs vertical strain, mean normal stress vs volumetric strain, and stress difference vs mean normal stress for uniaxial strain load-unload paths to pressure maxima of 1, 3, and 5 kb computed with the model are shown in Figures A-2 to A-4. The form of the model hydrostat up to 40 kb pressure is shown in Figure A-5.

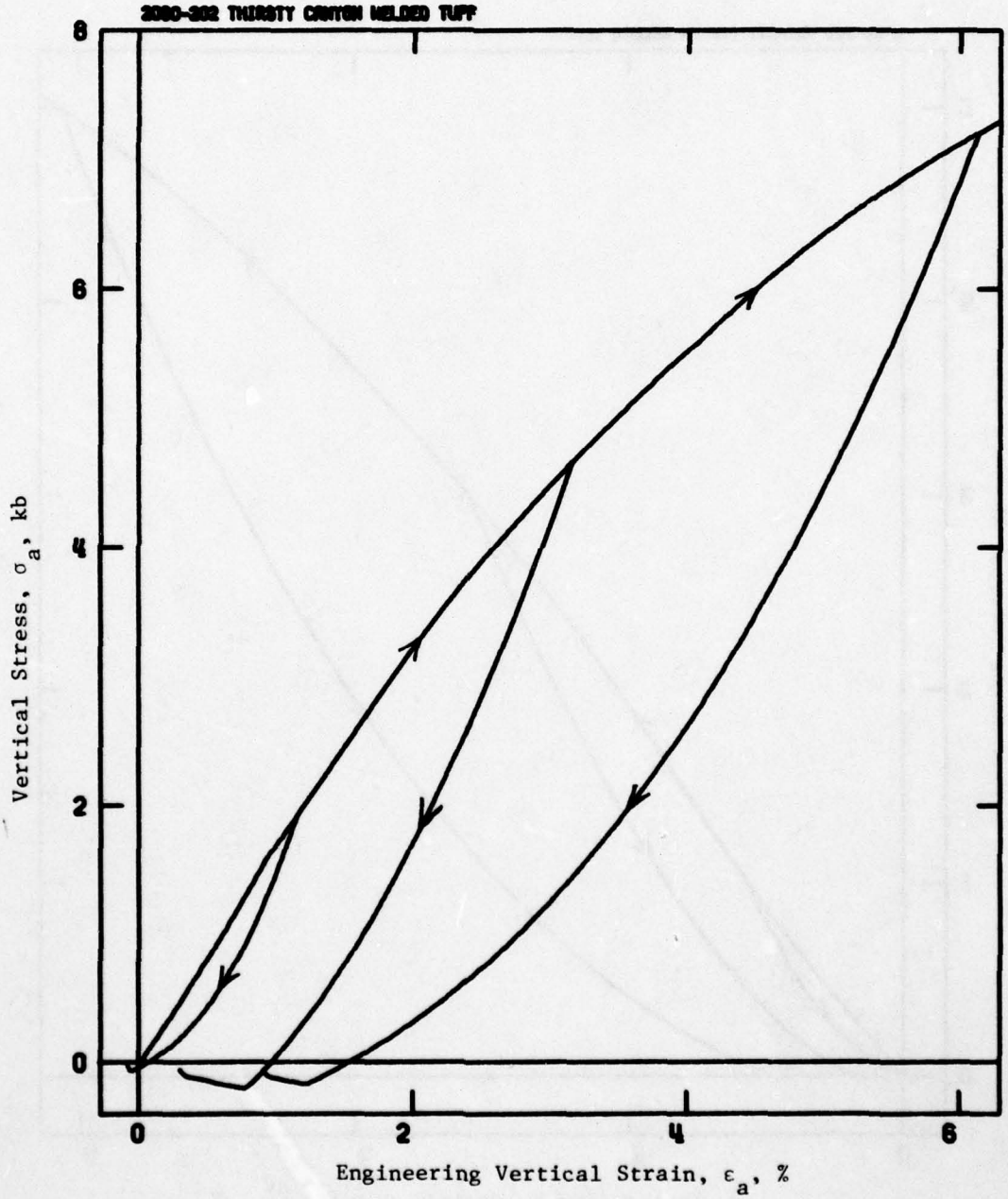


Figure A-2. Uniaxial Strain Load-Unload Stress-Strain Curves Computed with Welded Tuff Model

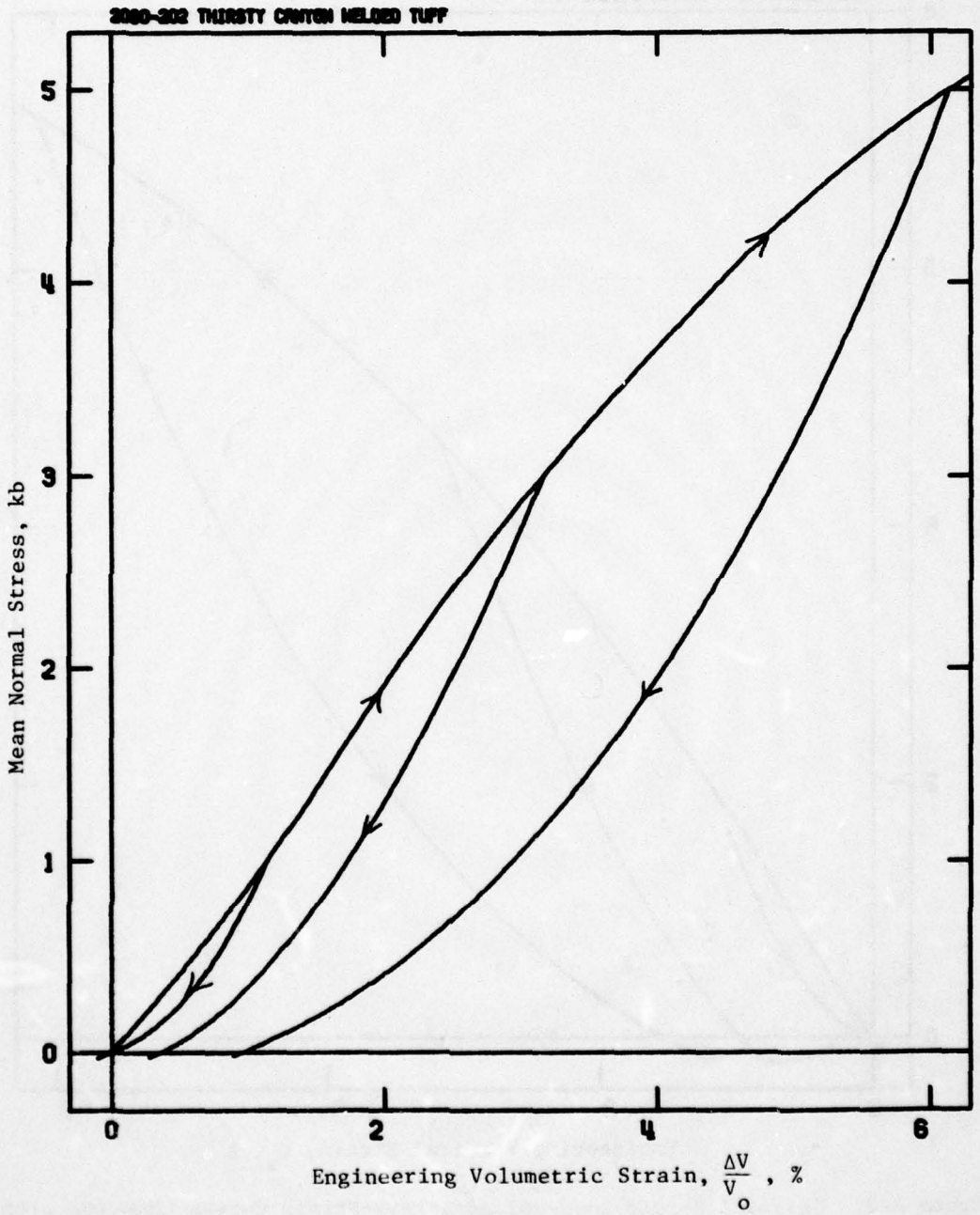


Figure A-3. Hydrostatic Load-Unload Stress-Strain Curves Computed with Welded Tuff Model

AD-A049 158 CALIFORNIA RESEARCH AND TECHNOLOGY INC WOODLAND HILLS F/G 8/7
FINITE-DIFFERENCE CODE ANALYSES OF EARTH PENETRATOR DYNAMICS IN--ETC(U)
NOV 76 M H WAGNER, C C FULTON DNA001-75-C-0147

UNCLASSIFIED CRT-2080-2 DNA-4069T NL

2 OF 2
AD
A049158



END
DATE
FILMED
3-78
DDC

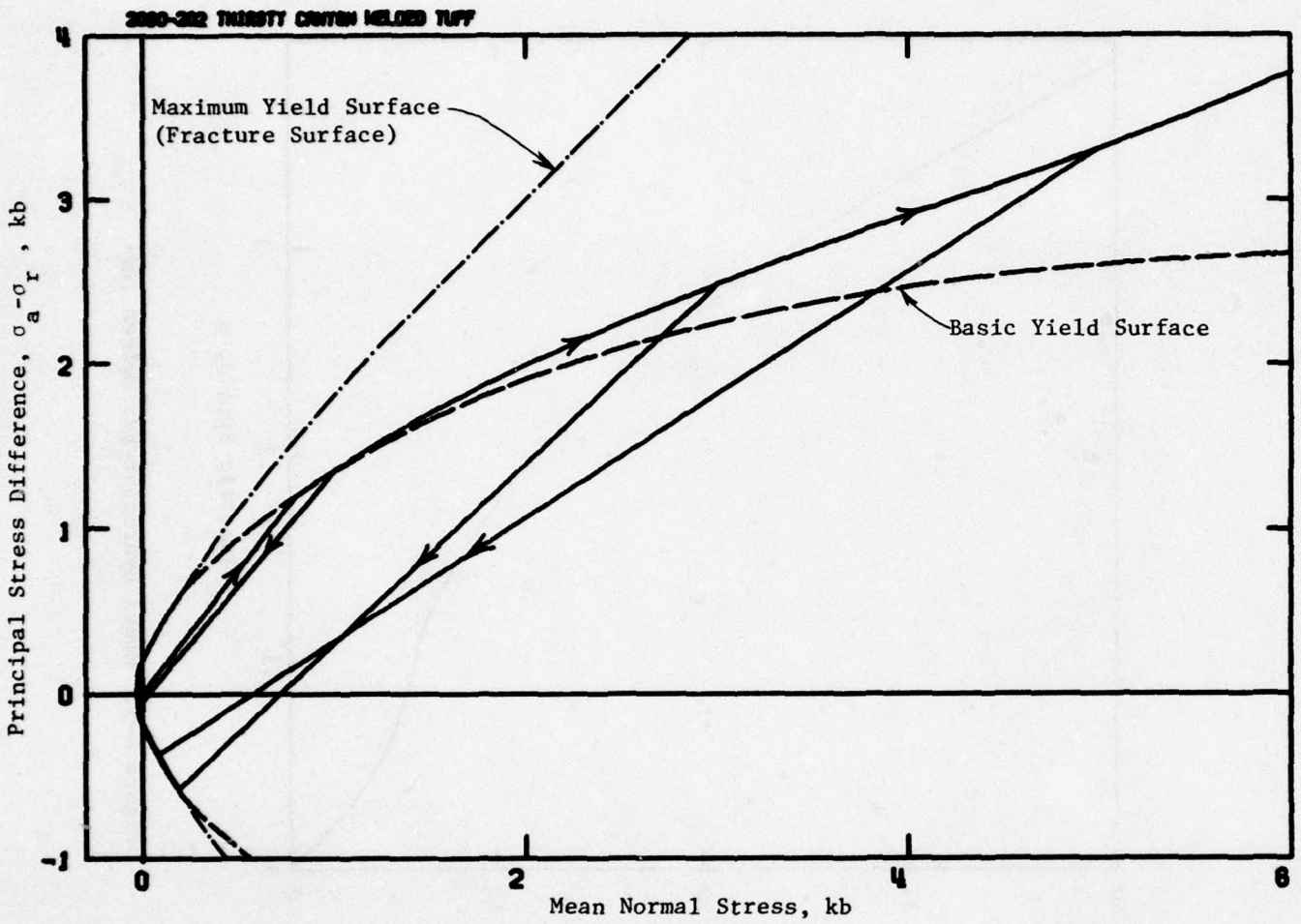


Figure A-4. Uniaxial Strain Test Stress Paths Computed with Welded Tuff Model

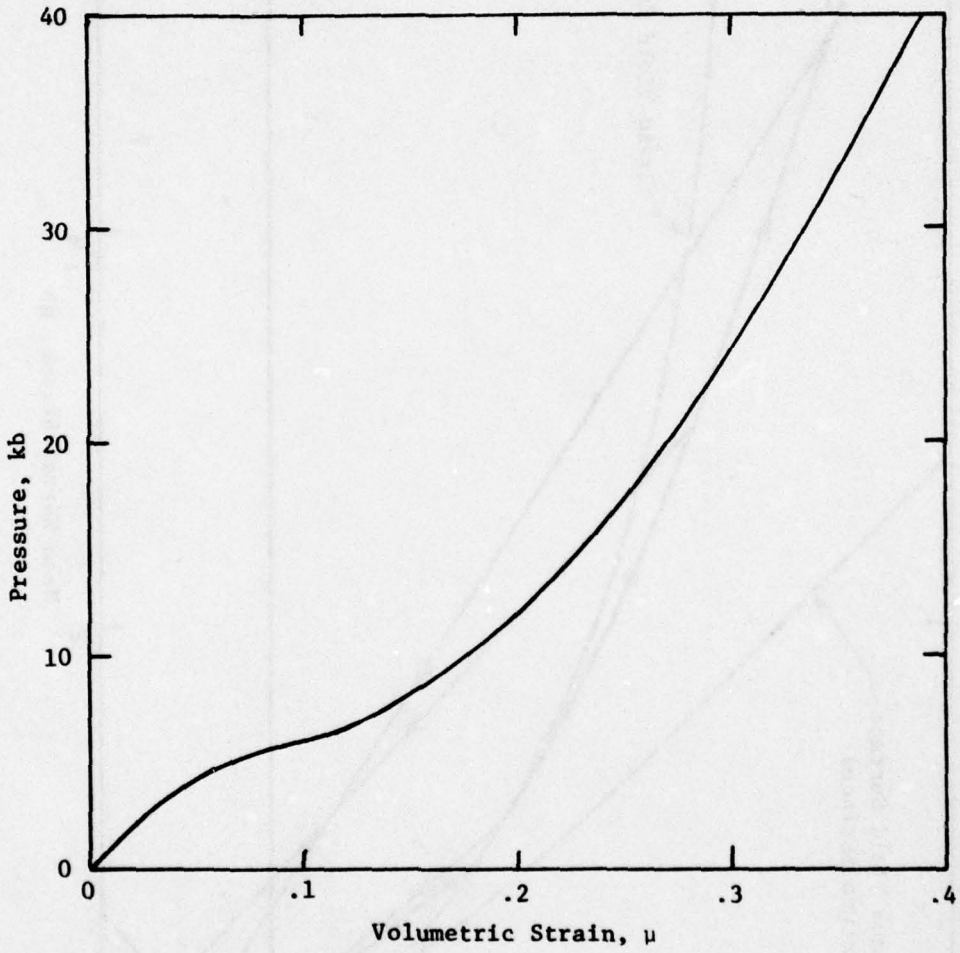


Figure A-5. Model Hydrostat for Welded Tuff

A comparison of the load-unload hydrostat with the laboratory results is shown in Figure A-6. The model is seen to provide a close fit to the isotropic compression data. Also shown on this figure is the implied load-unload path derived from curves given for a static uniaxial strain test. This curve (and Figure 8 of Ref. A-1) indicates that the material compacts in shear. Modeling of this aspect of material behavior (volume changes due to shearing) was not attempted in this effort. Comparisons of vertical stress vs vertical strain and stress difference vs mean normal stress for a uniaxial strain load-unload path are given in Figures A-7 and A-8. Since the model does not exhibit shear compaction, the model stress-strain curve lies somewhat above the test data (Figure A-7). The fit to the uniaxial strain stress path is, however, reasonably close (Figure A-8).

Comparisons of the model with experimental triaxial shear stress-strain load-unload paths are shown in Figure A-9. These comparisons were made after the model development, as a stress-controlled driver program was not available at that time. In the initial assessment of the constants for the strain-hardening portion of the model, analysis of the triaxial shear stress-strain data indicated a certain rate of strain-hardening. This rate was subsequently lowered to provide a better fit to the uniaxial strain data. By using the faster strain-hardening law (by changing the value of the constant in the strain-hardening equation on Page 89 from 8 to 80), an improved fit to the triaxial data is obtained, as shown in Figure A-10. (The model with the lower value, giving the fit shown in Figure A-9, was used in the calculation.) Note that this model can produce a reduction in stress difference before the maximum strain difference is reached. This is achieved through the degradation model following fracture.

Friction Rule

The friction rule employed for the welded tuff is described in Section 2.2.

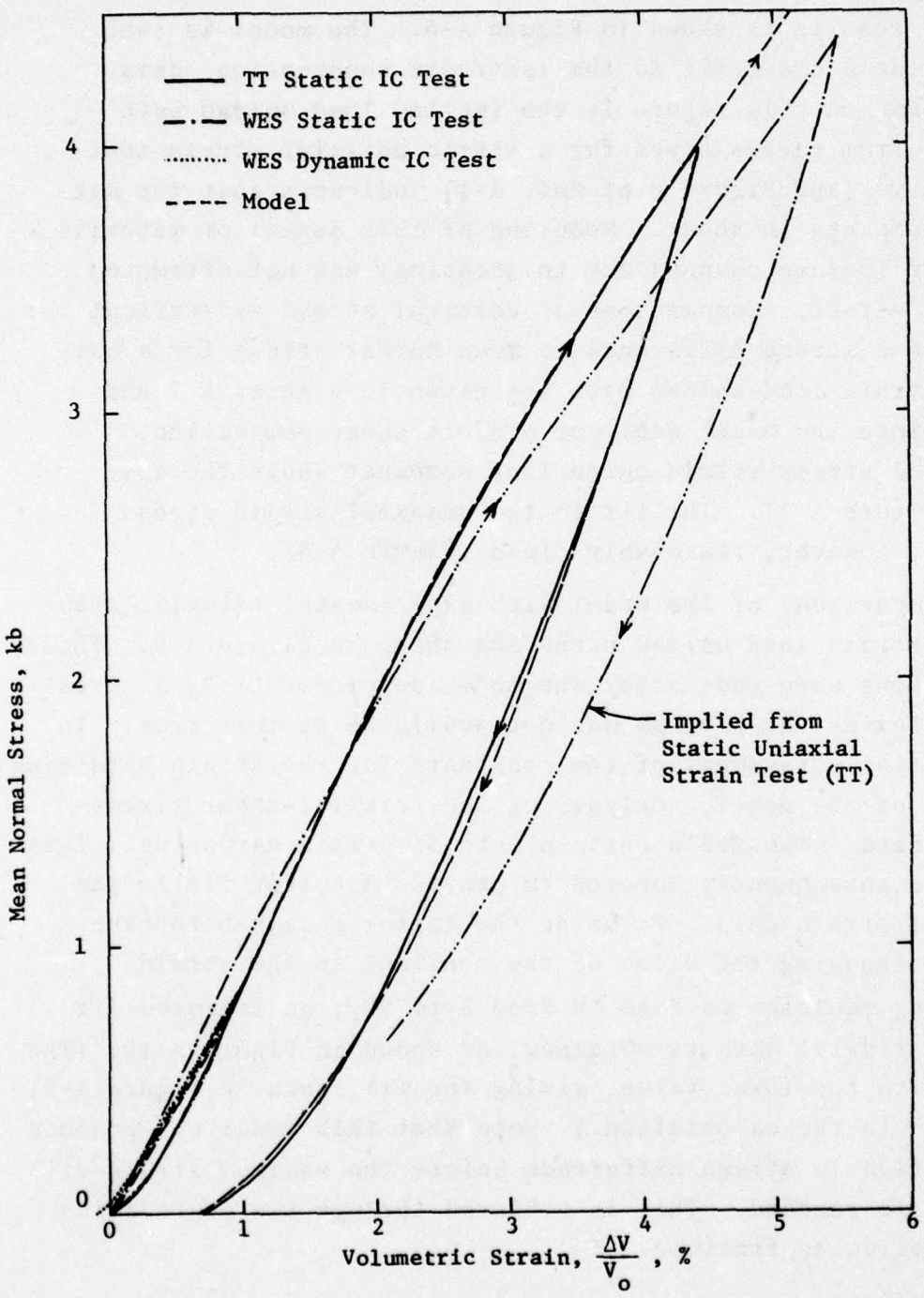


Figure A-6. Comparison of Hydrostatic Load-Unload Stress-Strain Curves

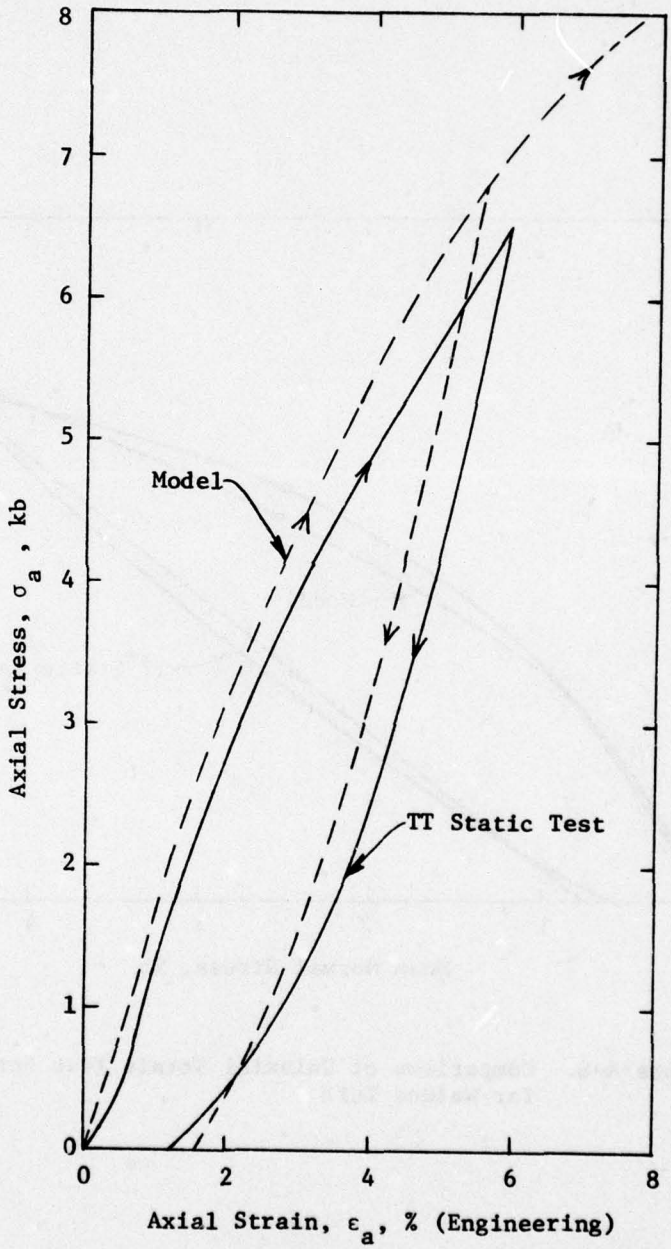


Figure A-7. Comparison of Uniaxial Strain Test Load-Unload Stress-Strain Curves

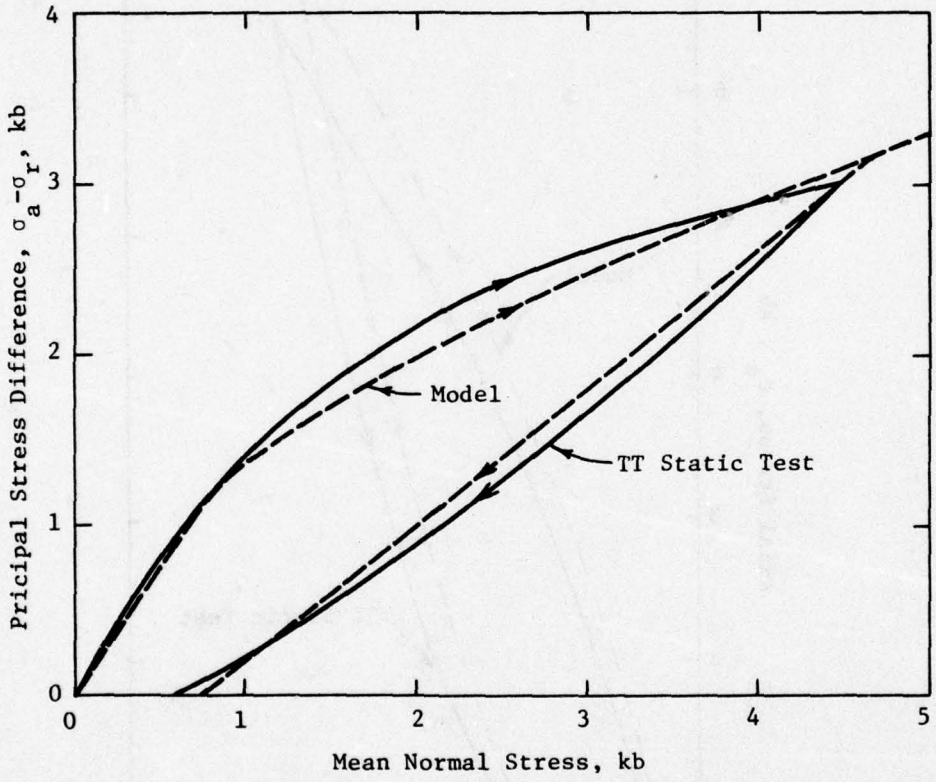


Figure A-8. Comparison of Uniaxial Strain Test Stress Paths for Welded Tuff

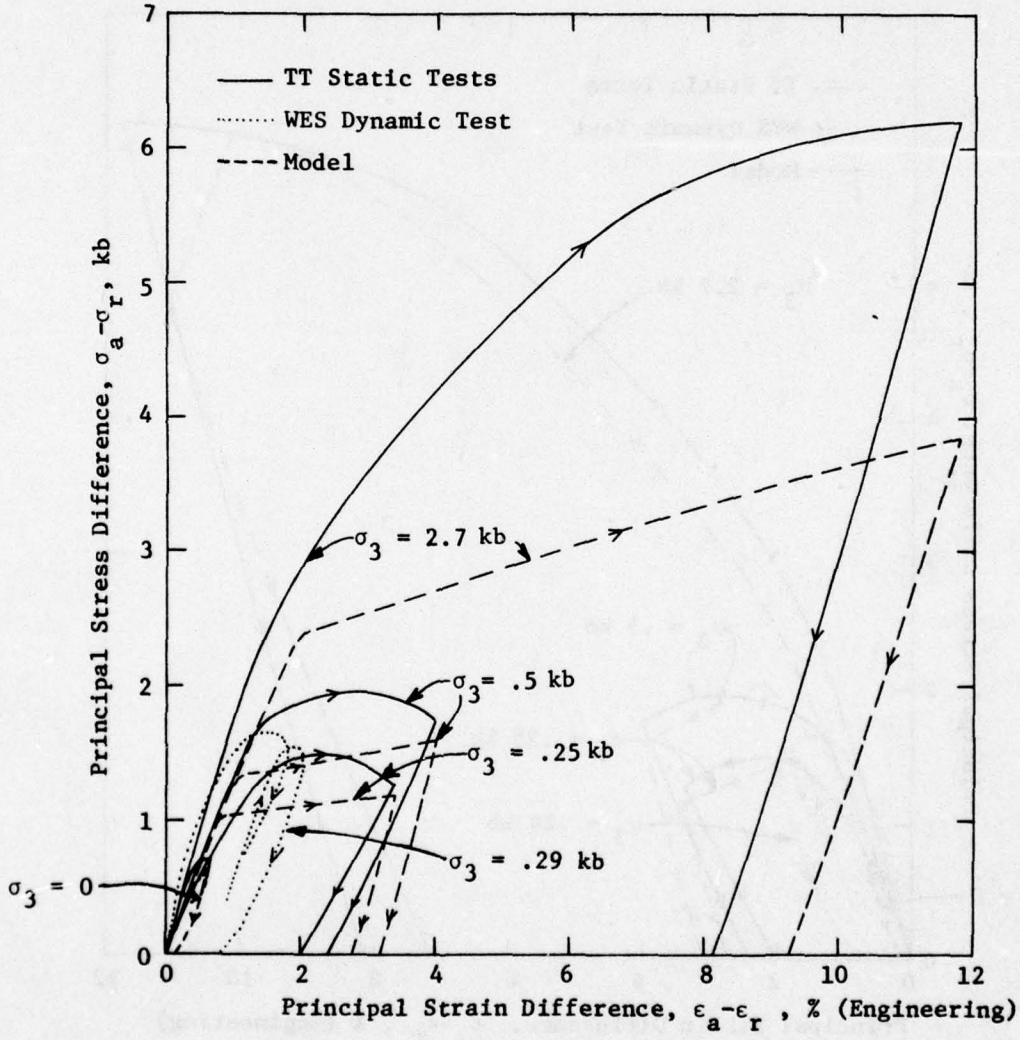


Figure A-9. Comparison of Triaxial Test Principal Stress Difference-Principal Strain Difference Paths

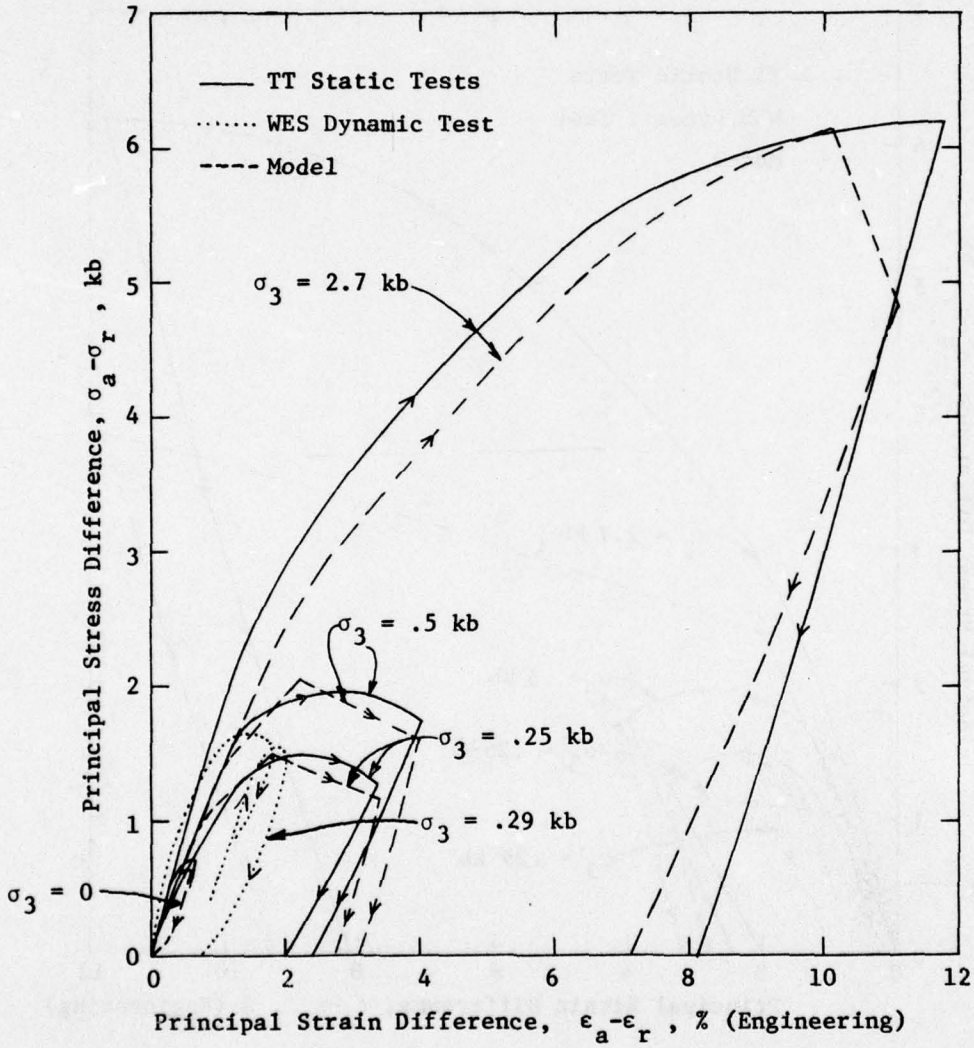


Figure A-10. Comparison of Triaxial Test Principal Stress Difference-Principal Strain Difference Paths with Increased Rate of Strain Hardening in Model

References

A-1. S. W. Butters, H. S. Swolfs, and J. N. Johnson, *Field Laboratory and Modeling Studies on Mount Helen Welded Tuff for Earth Penetrator Test Evaluation*, Terra Tek, Report TR-75-9, January 1975.

A-2. P. F. Hadala, *A Data Package for Use in the Calculation of a DNA Penetration Test in Thirsty Canyon Welded Tuff*, U. S. Army Engineer Waterways Experiment Station, 20 May 1975.

A-3. D. K. Butler, *Constitutive Property Investigations in Support of Full Scale Penetration Tests, Report 1, Thirsty Canyon Welded Tuff, Tonopah Test Range, Nevada*, U. S. Army Engineer Waterways Experiment Station, Preliminary Report, March 1975.

A-4. D. K. Butler, U. S. Army Engineer Waterways Experiment Station, Letter dated 18 June 1975.

A-5. S. W. Butters, Terra Tek, Letter dated 25 June 1975.

APPENDIX B

ADDITIONAL COMPUTATIONAL RESULTS - GROUND RESPONSE

B.1 STRESS AND VELOCITY TIME HISTORIES AND STRESS PATHS IN THE FIELD

Time histories of stress and velocity were obtained at 15 locations in the ground. The following parameters are plotted:

a.	Radial stress	σ_r
	Vertical stress	σ_z
	Hoop stress	σ_θ
	Shear stress	σ_{rz}
b.	Radial particle velocity	$\dot{r}$
	Vertical particle velocity	$\dot{z}$

Positive stresses are compressive. Positive $\dot{r}$ is radially outward. Positive $\dot{z}$ is vertically down.

In addition, the stress paths ($\sqrt{J_2'}$ vs P) at these stations were obtained. In these plots, the dots indicate loading and the pluses indicate unloading. Also shown on these plots are the initial position of the maximum yield surface (Y_{max}) and the minimum yield surface (Y_{min}). (The maximum yield surface degrades toward the minimum yield surface as a function of generalized plastic strain.) These plots can provide guidance as to the type of lab tests which should be run to simulate the loadings experienced in a penetration event. The loadings are characterized by a rapid rise in deviatoric stress at low mean stress, which are steeper than attained in a triaxial compression test at zero confining pressure. Also, the unload paths maintain a high deviatoric

PRECEDING PAGE BLANK-NOT FILMED

stress, often staying on the yield surface. (Note that the popular uniaxial strain load-unload lab tests are not at all representative of the stress paths indicated by the penetration calculations. Since this behavior had been discovered in previous soil penetration calculations, the laboratory tests for this project were set up to include the more representative triaxial tests.)

The locations of the field stations are indicated in Figure B-1. The plots obtained at each of these stations are given in Figures B-2 to B-46. Some of the "choppiness" in the plots along the axis are due to repositioning of the points at rezones.

B-2 FIELD PLOTS OF DEFORMATION, VELOCITY, AND PRINCIPAL STRESS

In addition to the field plots shown in Figures 6 to 8 depicting the final solution results, field plots were obtained at intermediate times during the solution. Field plots for penetration depths of 5, 10, and 15 in. are shown in Figures B-47 to B-55. For each depth, plots of the Lagrangian grid and fracture pattern, velocity vectors, and principal stresses are shown.

The plots of the grid indicate the development of fracture in the target; the following symbols are used to indicate the state of each cell of material:

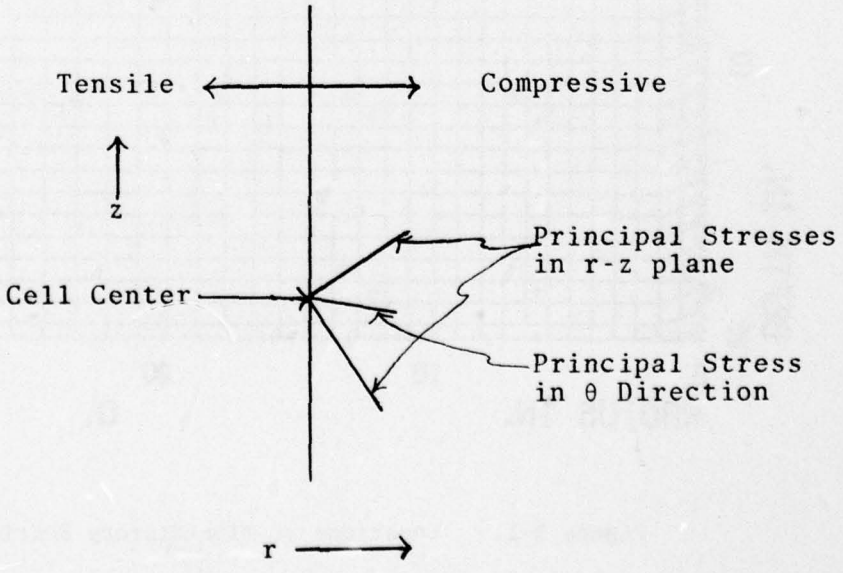
Fracture Symbol

☐	Intact, material has not fractured (has not reached Y_{max})
⊡	Lightly fractured or cracked material, $\bar{\varepsilon}^p_{ex} \leq 1\%$
⊞	Severely fractured material, $\bar{\varepsilon}^p_{ex} \geq 1\%$
☒	Comminuted material, fractured and completely degraded to Y_{min}

There is no particular significance to the dividing point of 1% in $\bar{\varepsilon}^p_{ex}$, the excess generalized plastic strain, except to quantitatively indicate the degree of fracture. There is actually a smooth gradation of $\bar{\varepsilon}^p_{ex}$, and thus severity of fracture, in the field.

The velocity vector field plots show the direction and magnitude of the particle velocity at each lattice point in the computing grid. (For clarity in viewing the ground response, the velocity vectors of the projectile are not shown.)

In the stress field plots, the principal components of the stress tensor for each cell are shown, as follows: The magnitude of the two principal stresses in the r-z plane are plotted in their corresponding principal directions. The third principal stress (in the azimuthal direction) is plotted along the line bisecting the other two principal directions. Vectors pointing to the right are compressive, to the left, tensile. An example of how a stress tensor is plotted is sketched below:



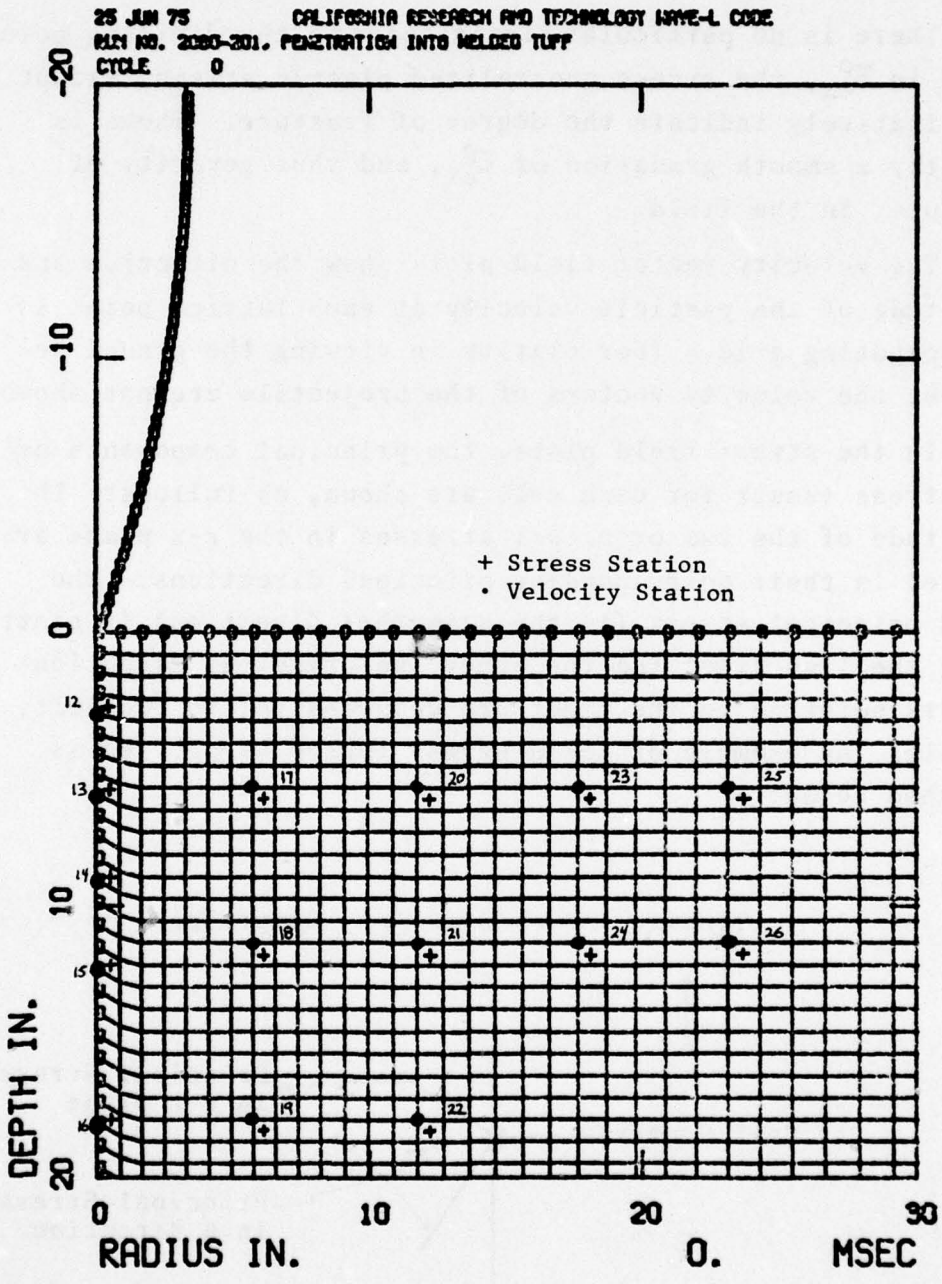


Figure B-1. Locations of Time-History Stations

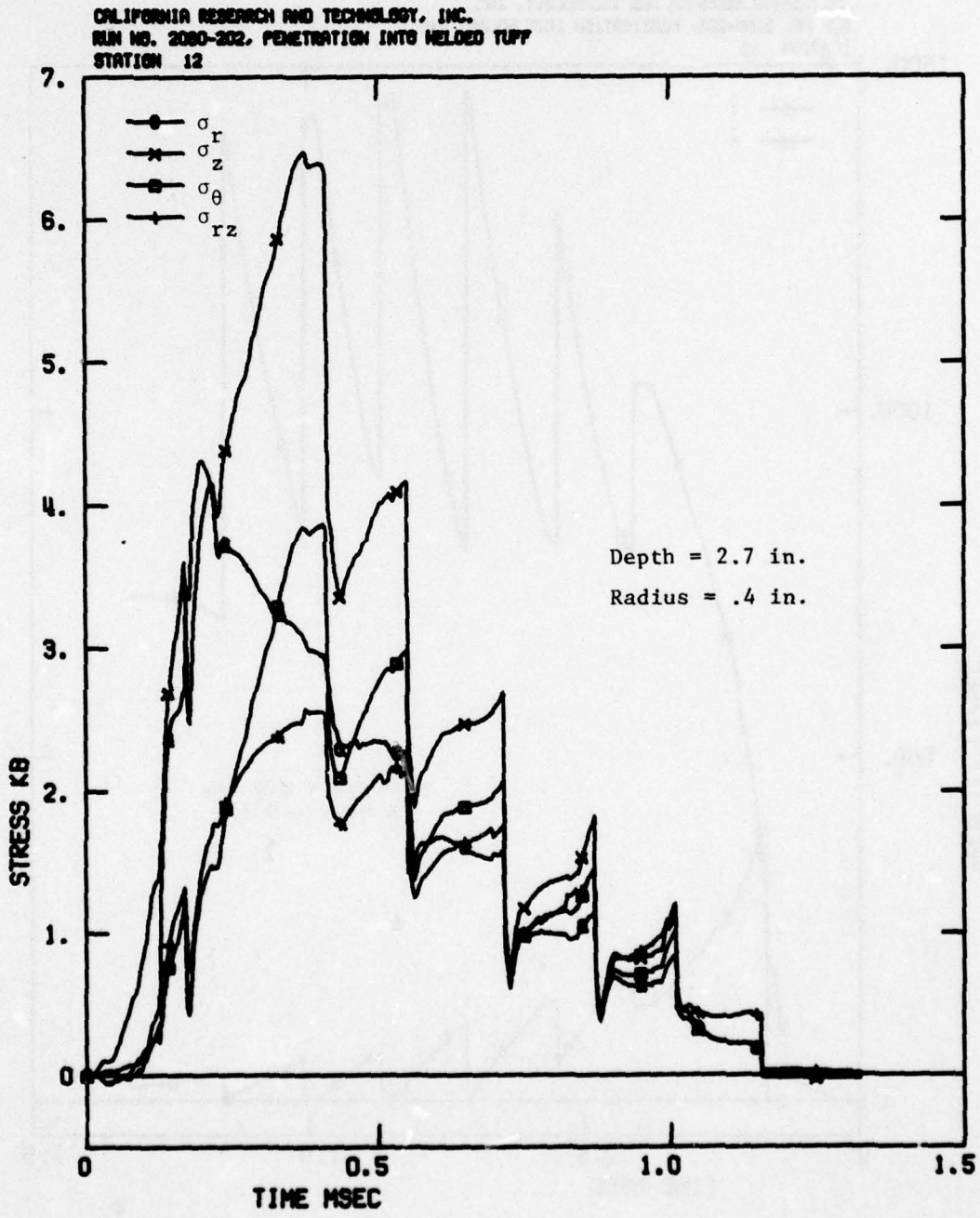


Figure B-2. Stress Components at Station 12

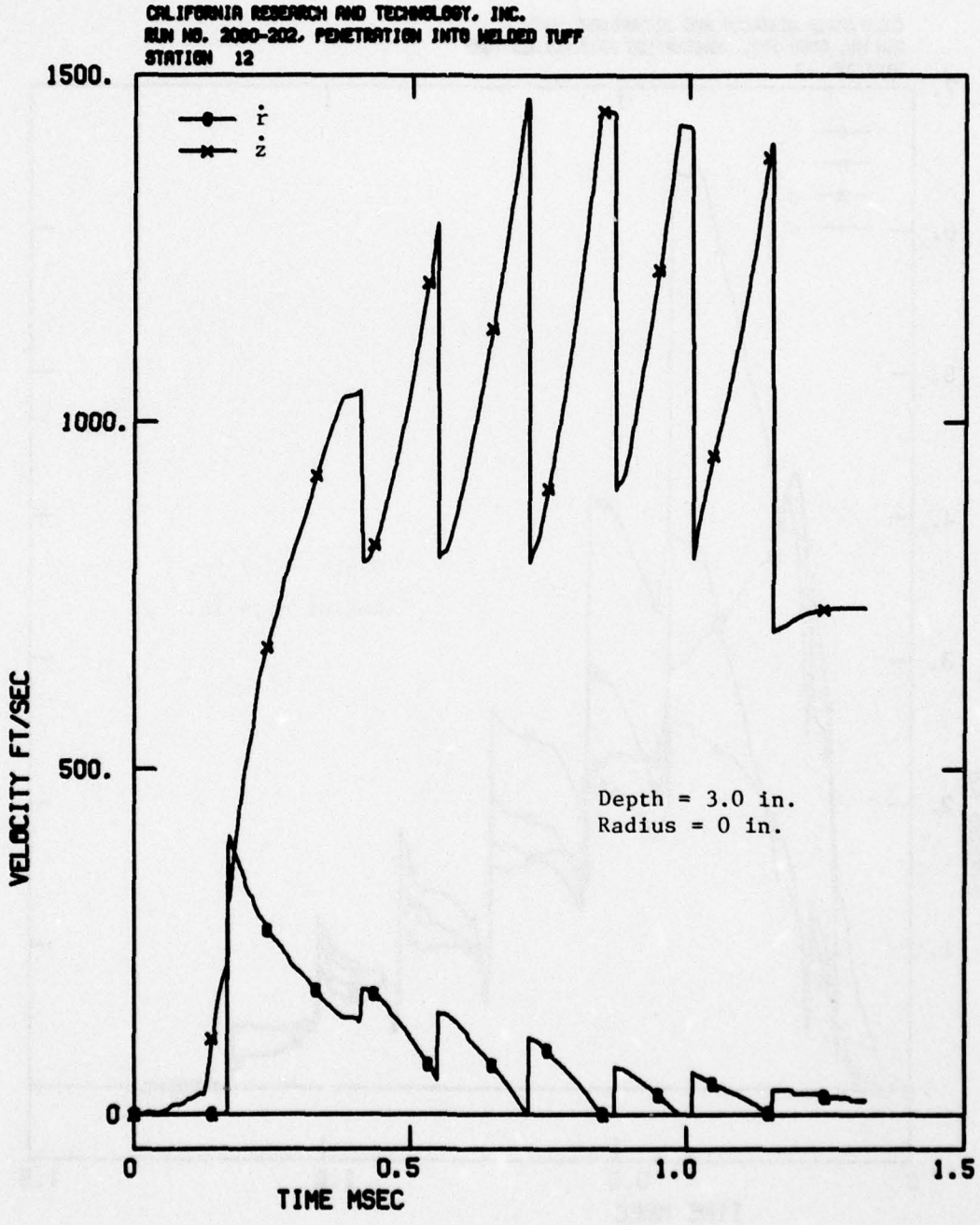


Figure B-3. Velocity Components at Station 12

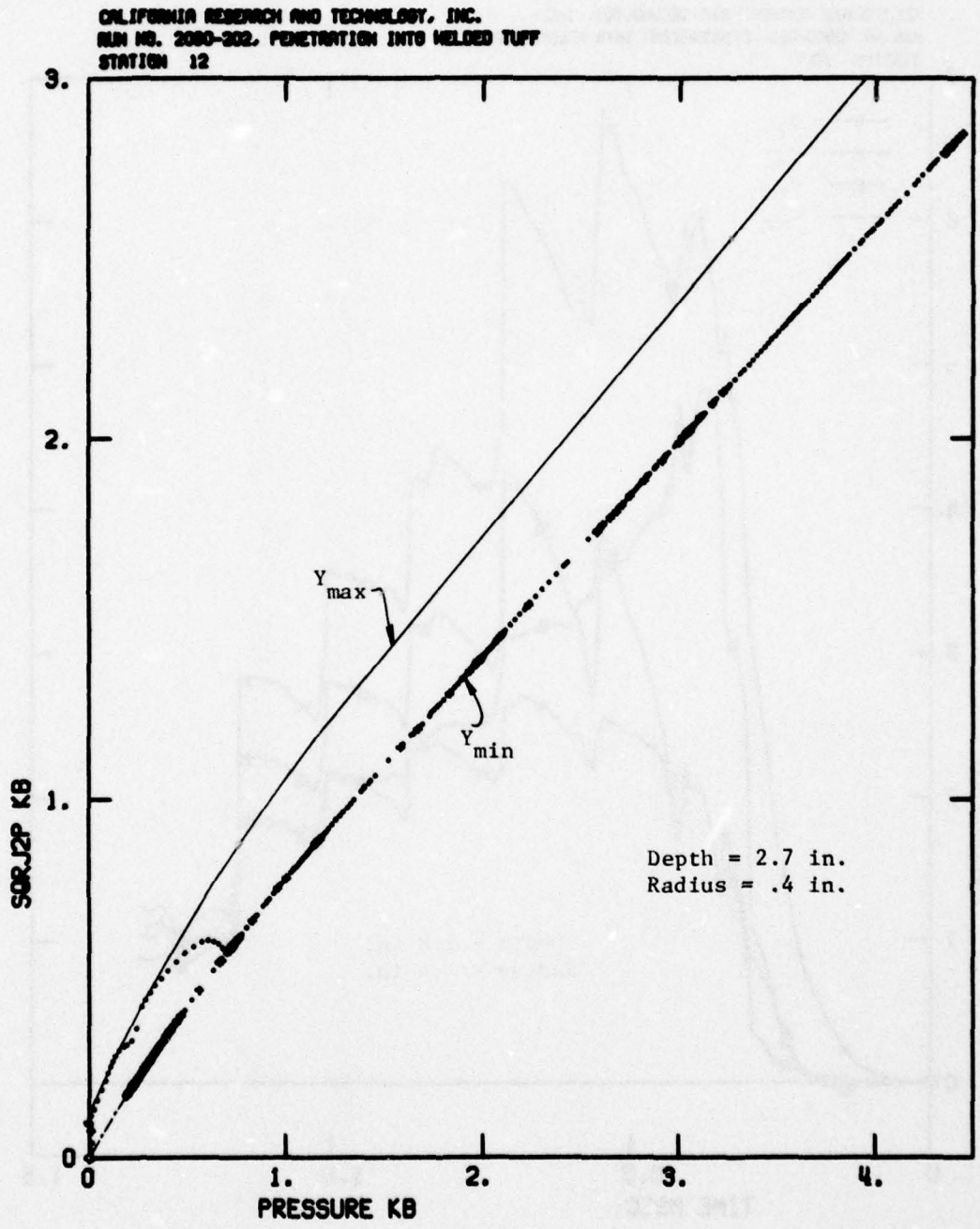


Figure B-4. Stress Path ($\sqrt{J_2'}$ vs P) at Station 12

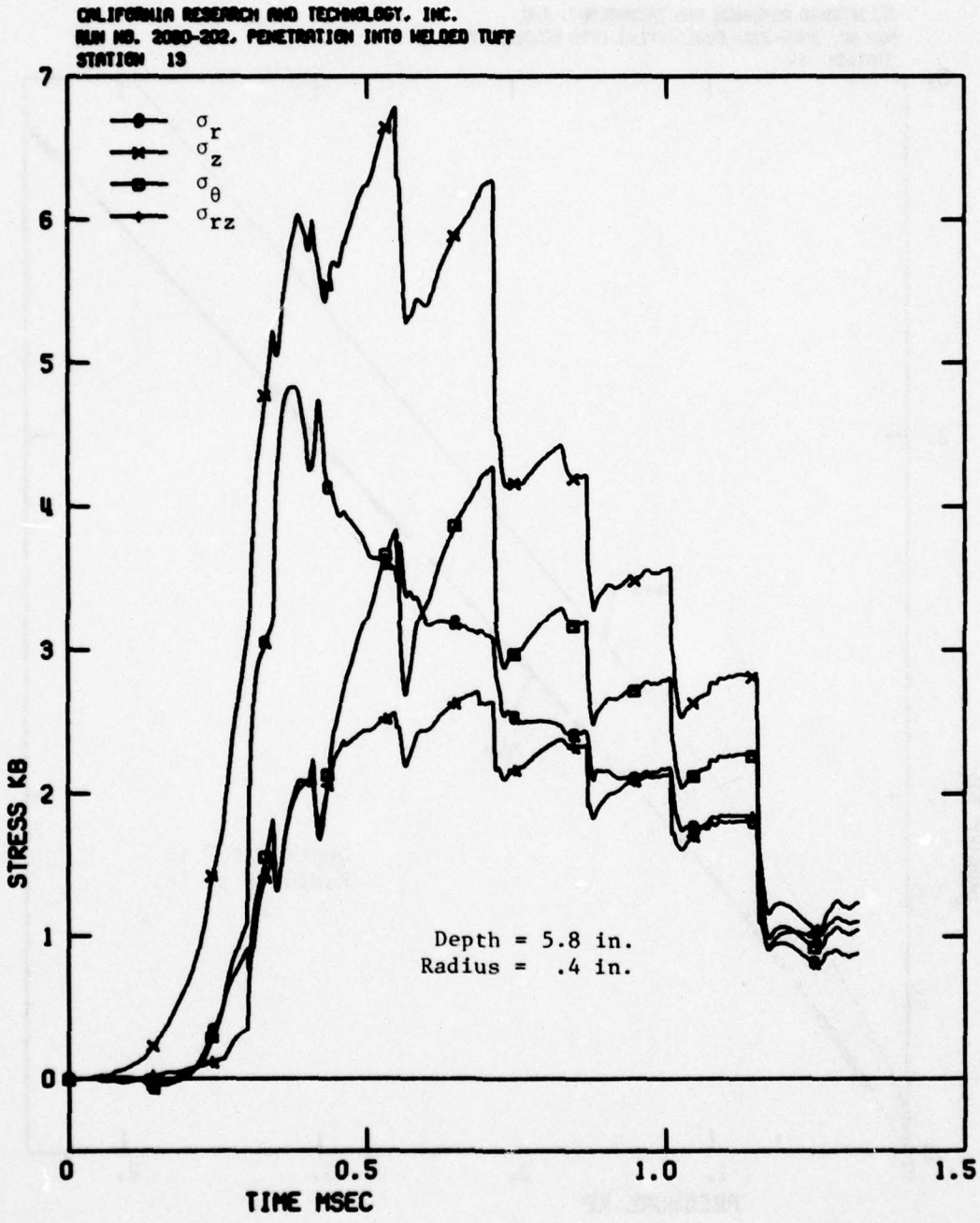


Figure B-5. Stress Components at Station 13

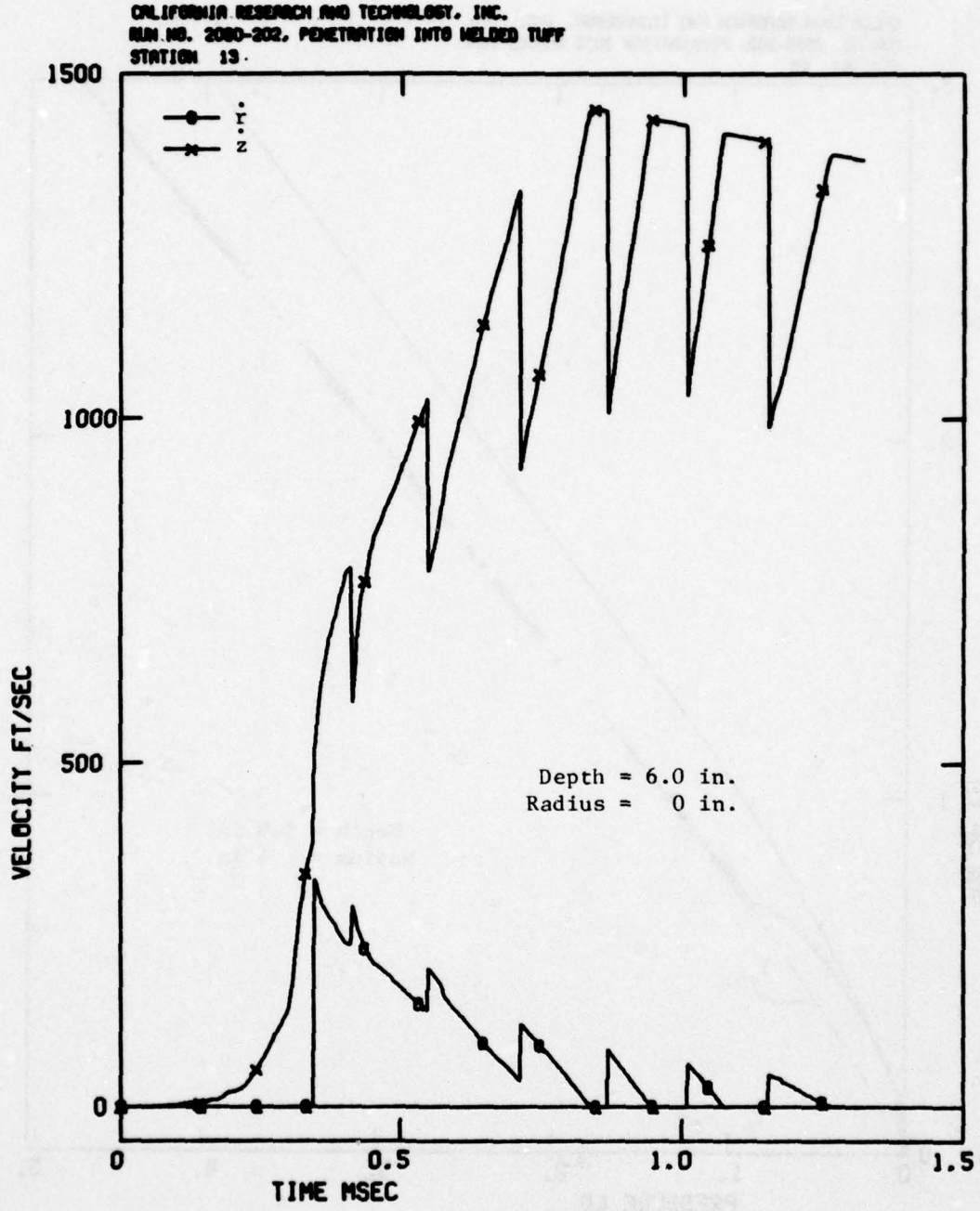


Figure B-6. Velocity Components at Station 13

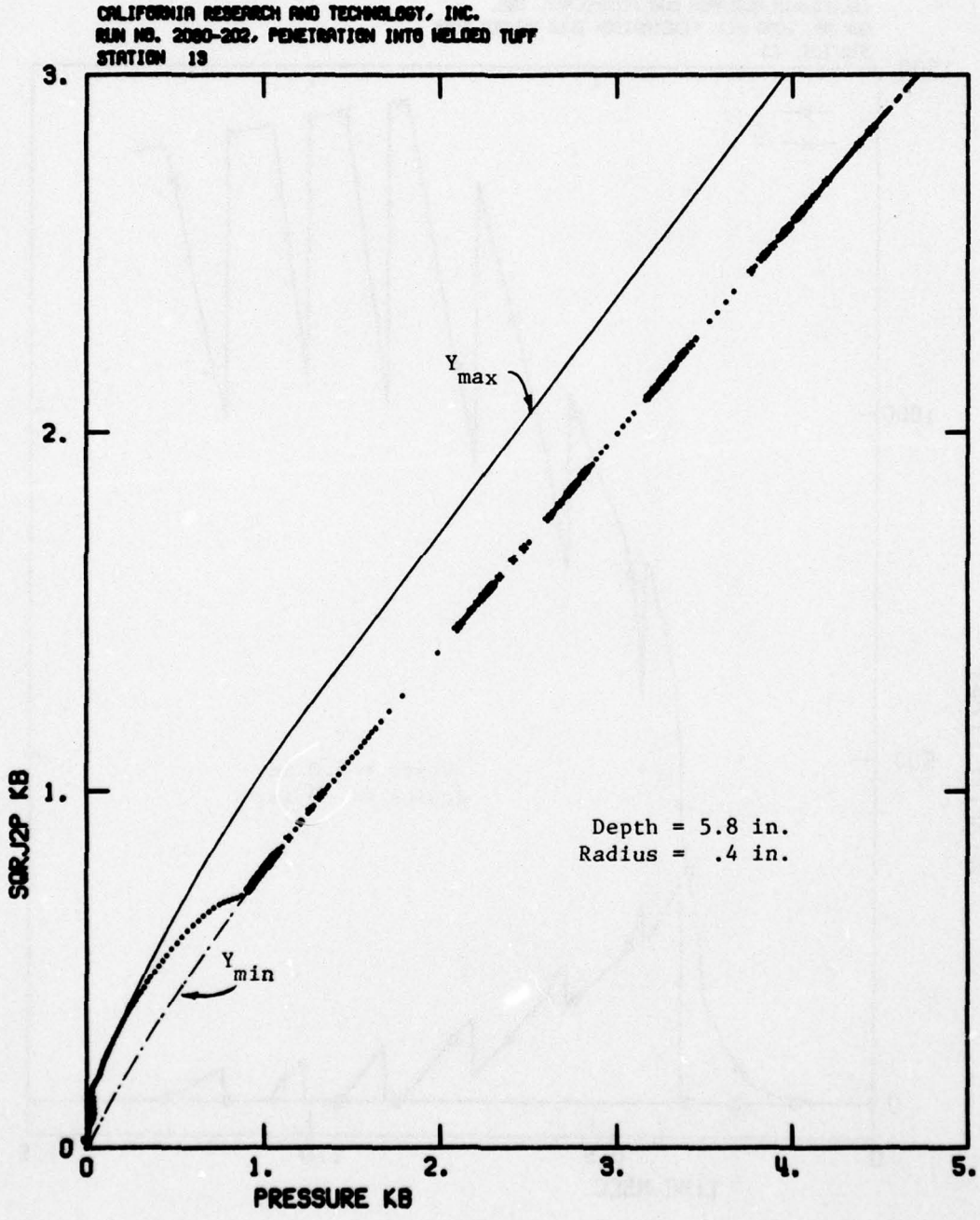


Figure B-7. Stress Path ($\sqrt{J_2'}$ vs P) at Station 13

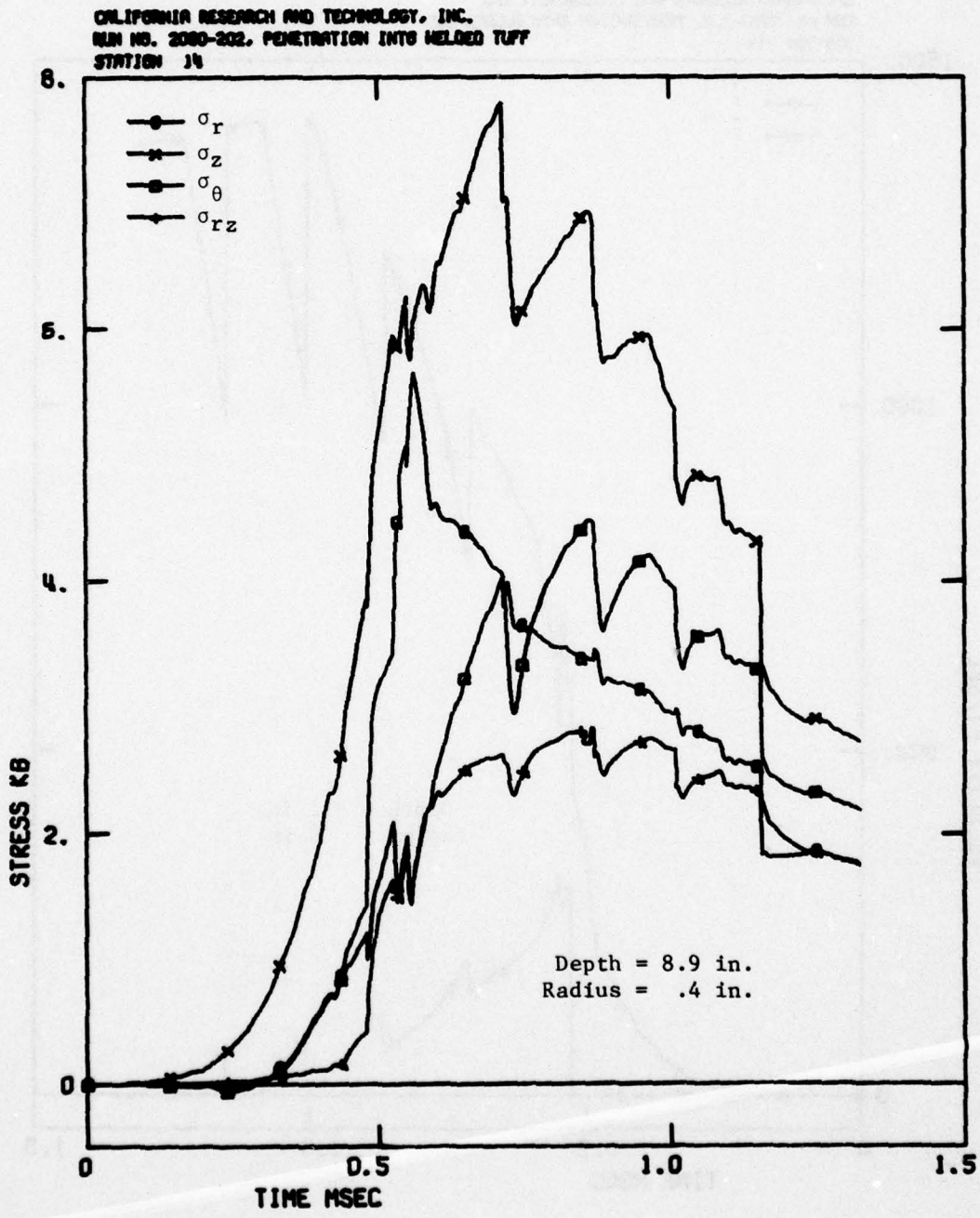


Figure B-8 Stress Components at Station 14

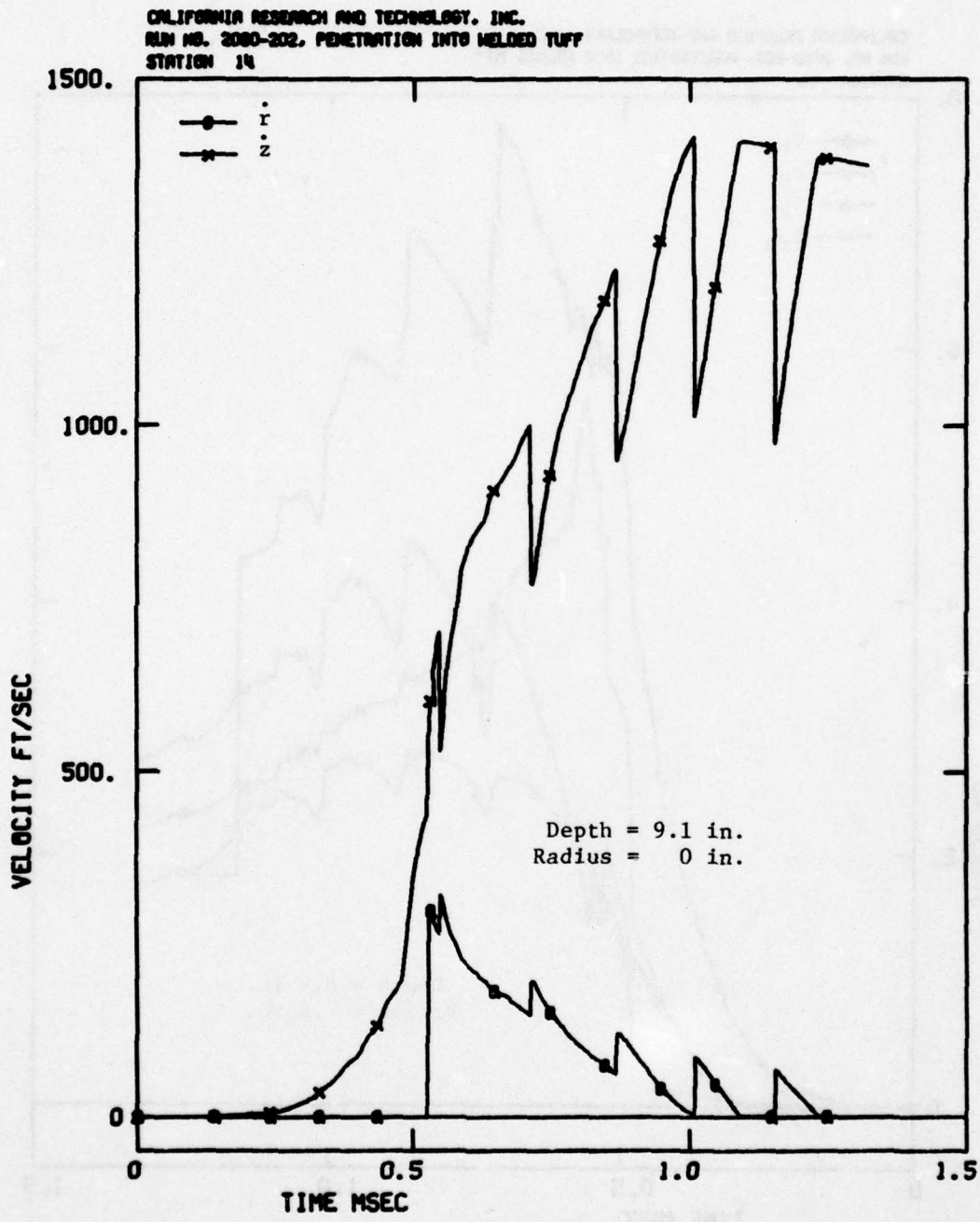


Figure B-9. Velocity Components at Station 14

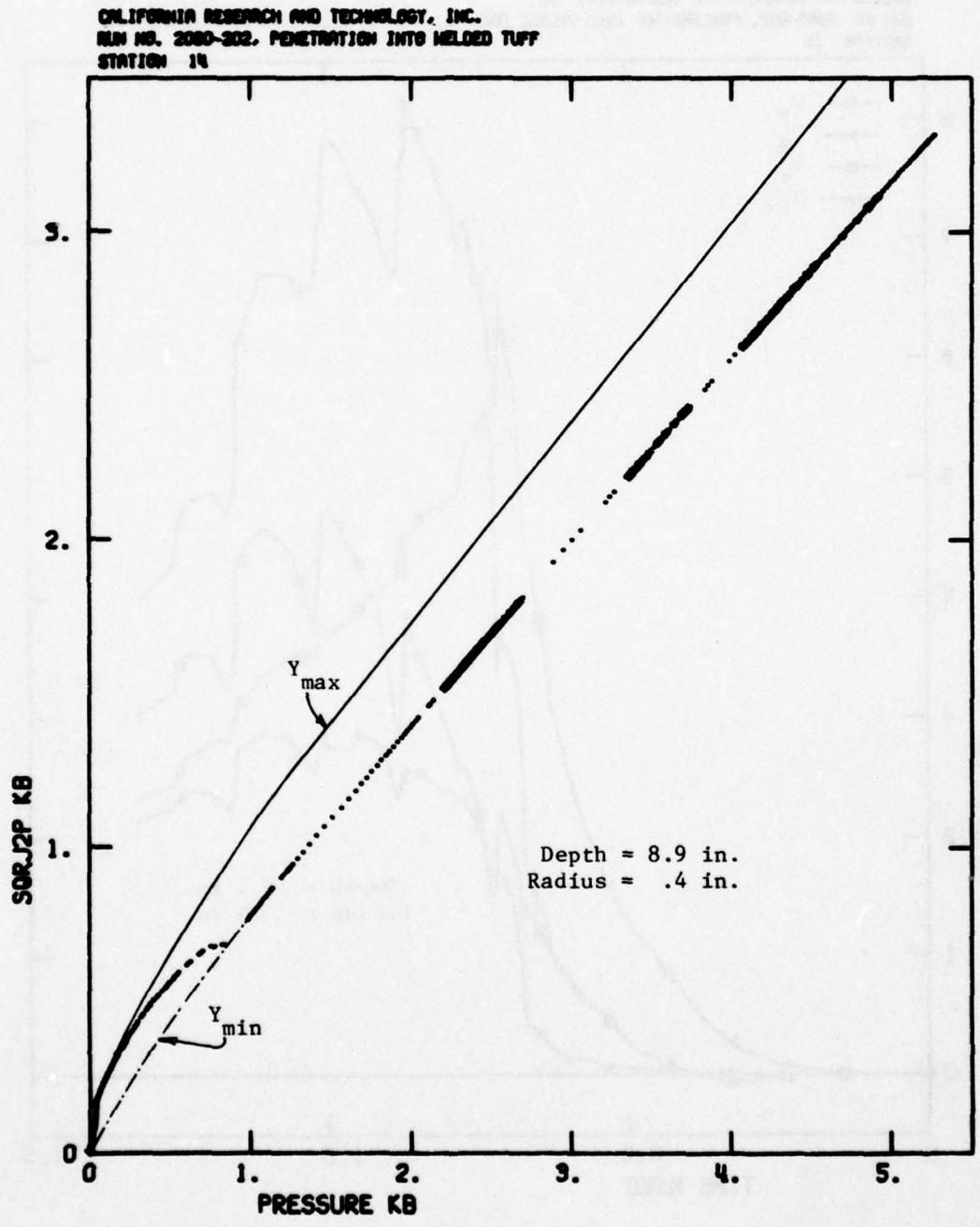


Figure B-10. Stress Path ($\sqrt{J_2'}$ vs P) at Station 14

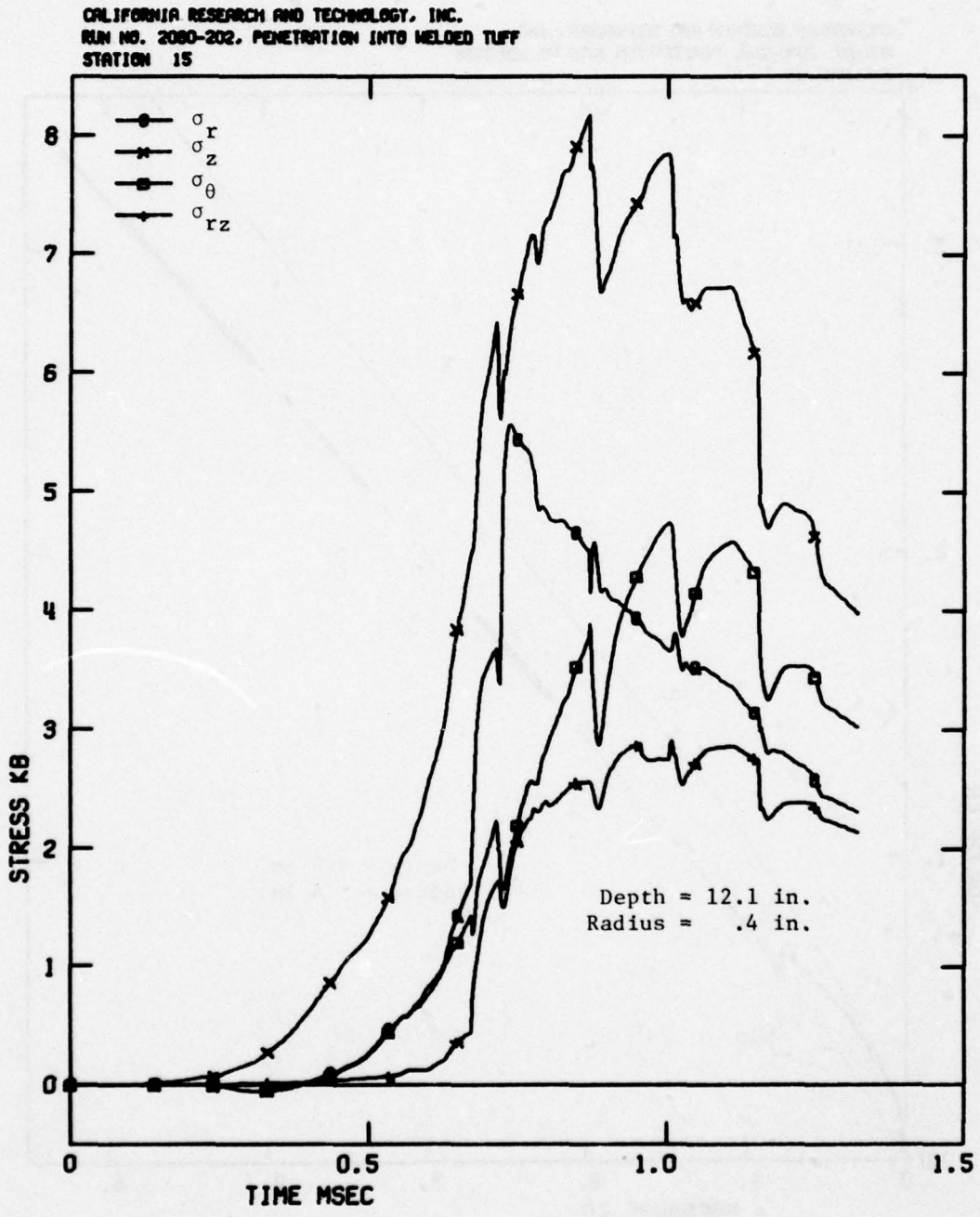


Figure B-11. Stress Components at Station 15

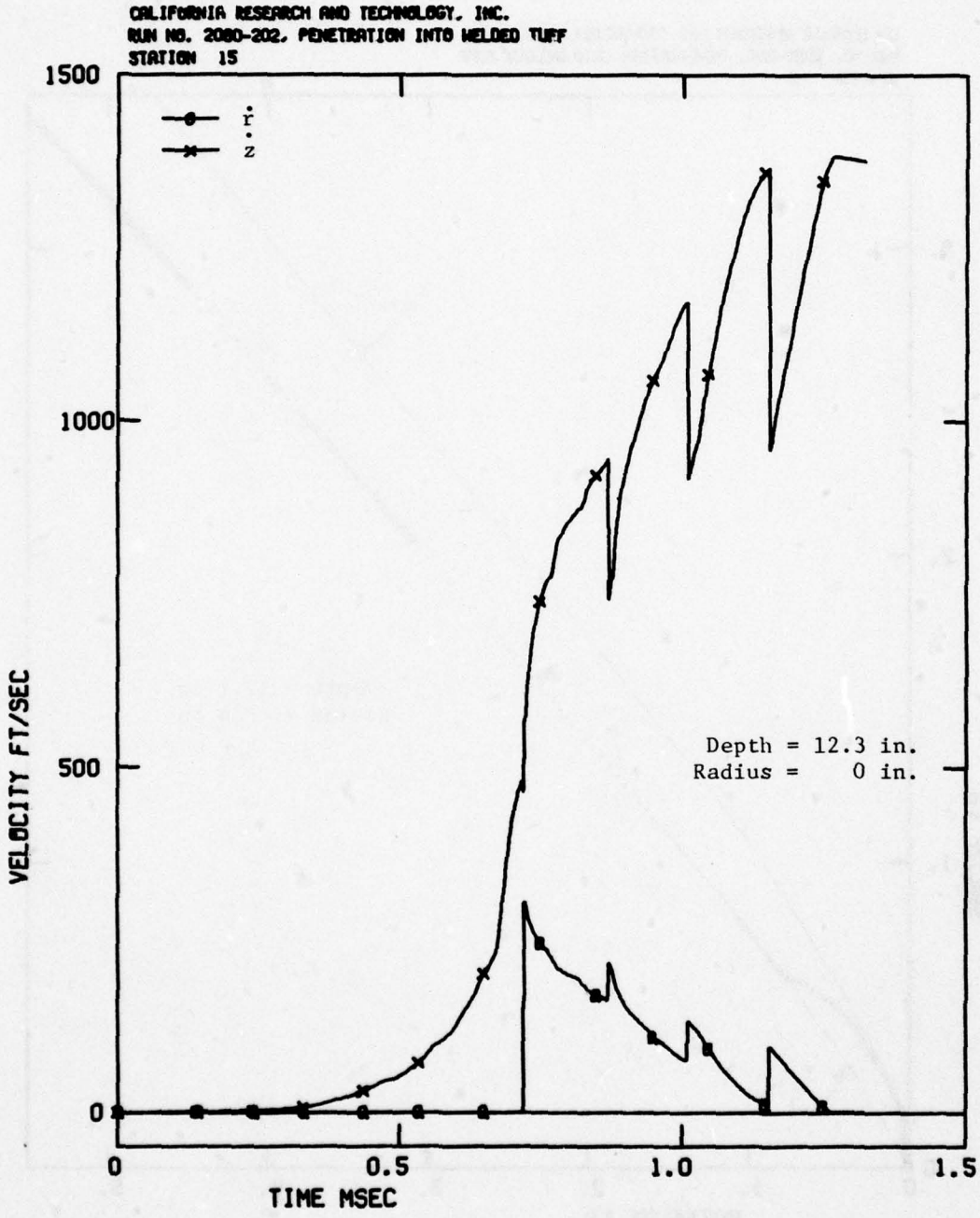


Figure B-12. Velocity Components at Station 15

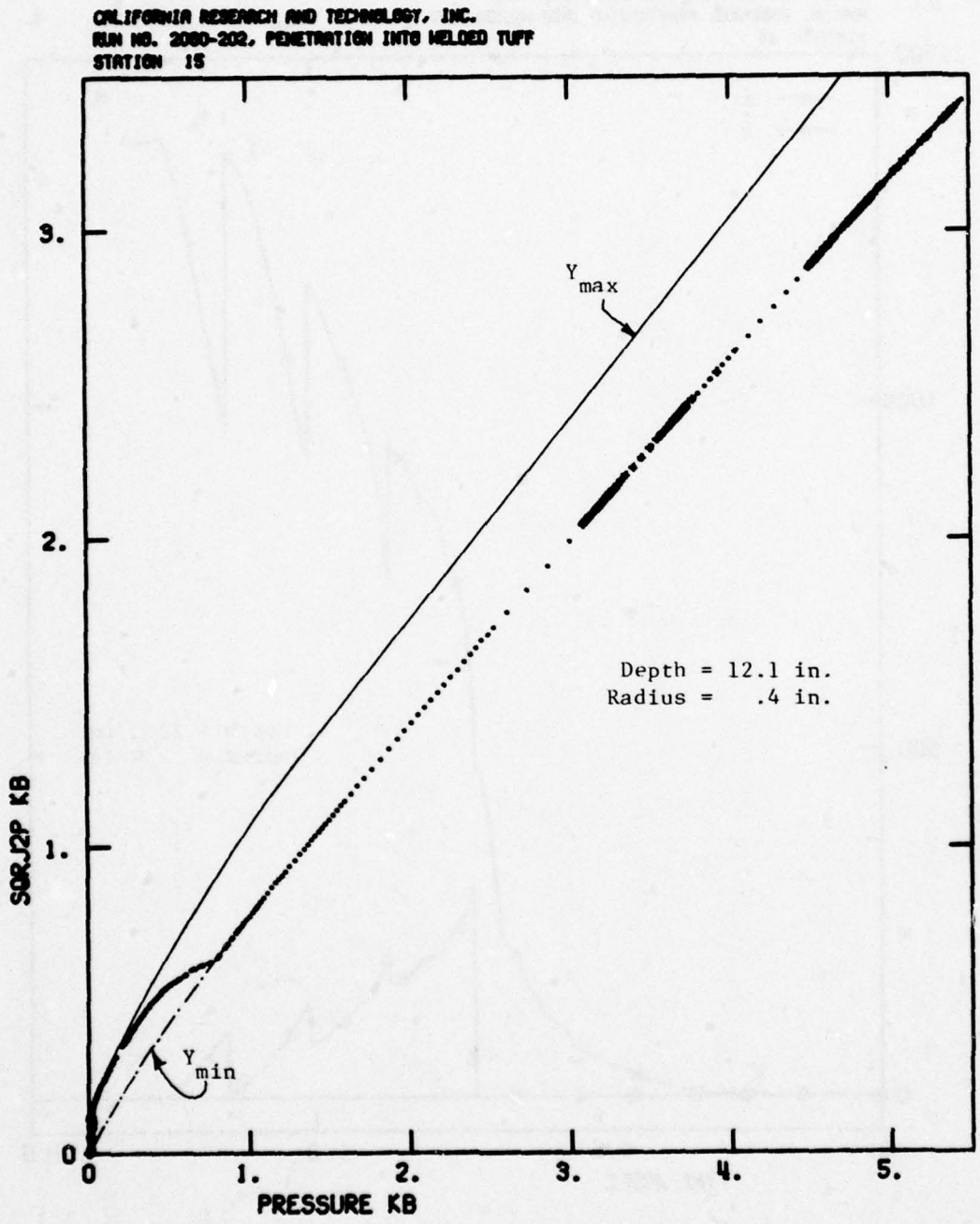


Figure B-13. Stress Path ($\sqrt{J_2'}$ vs P) at Station 15

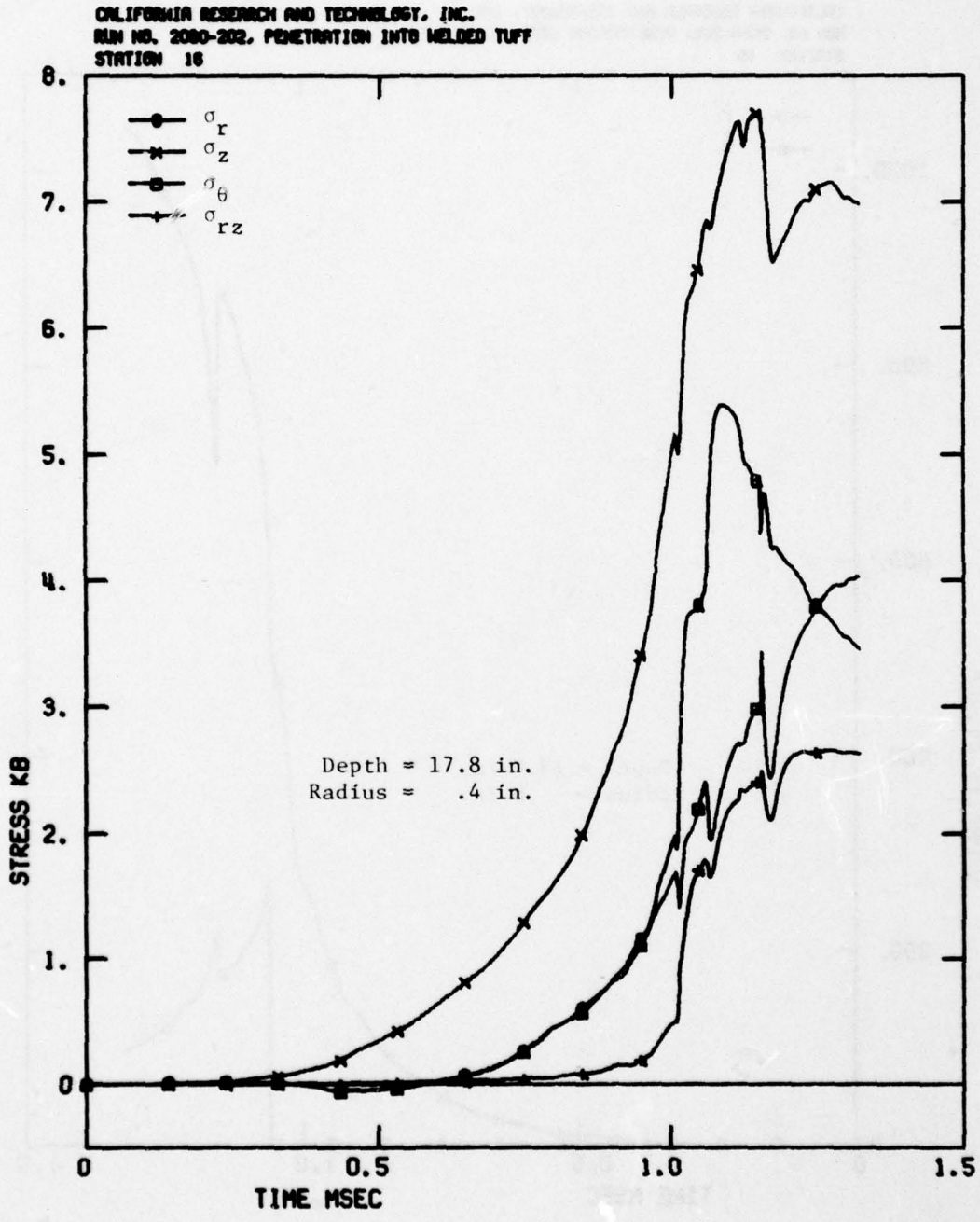


Figure B-14. Stress Components at Station 16

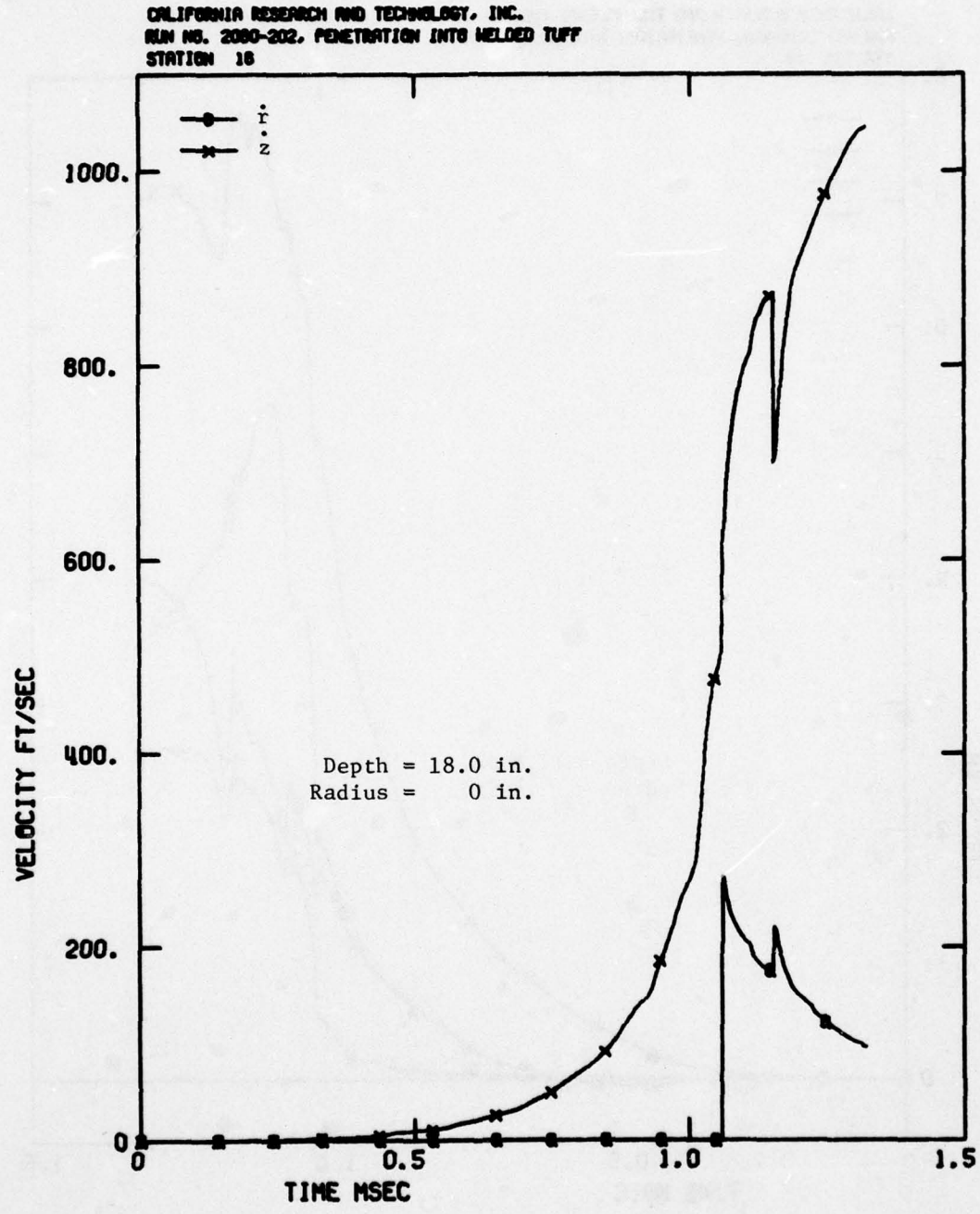


Figure B-15. Velocity Components at Station 16

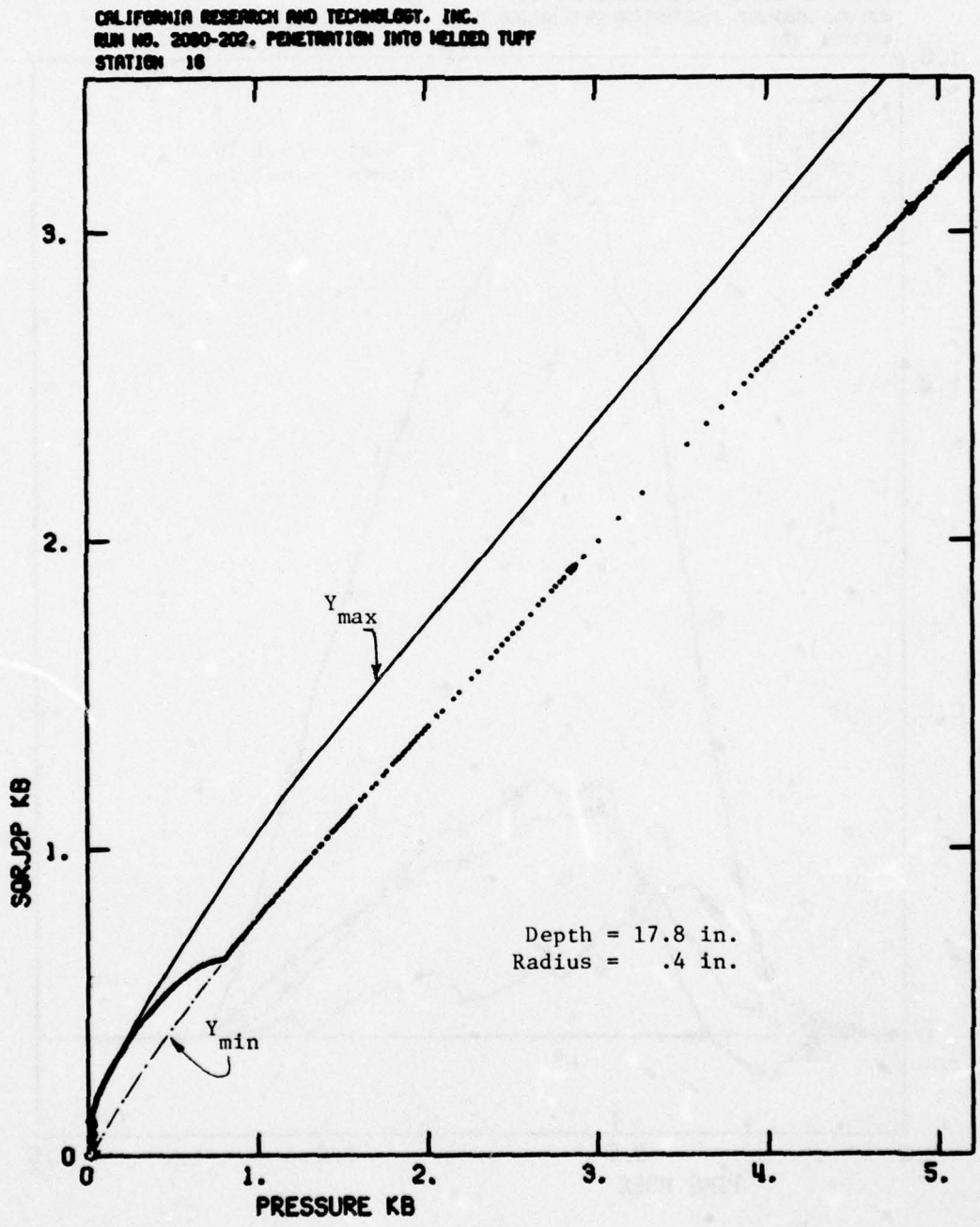


Figure B-16. Stress Path ($\sqrt{J_2'}$ vs P) at Station 16

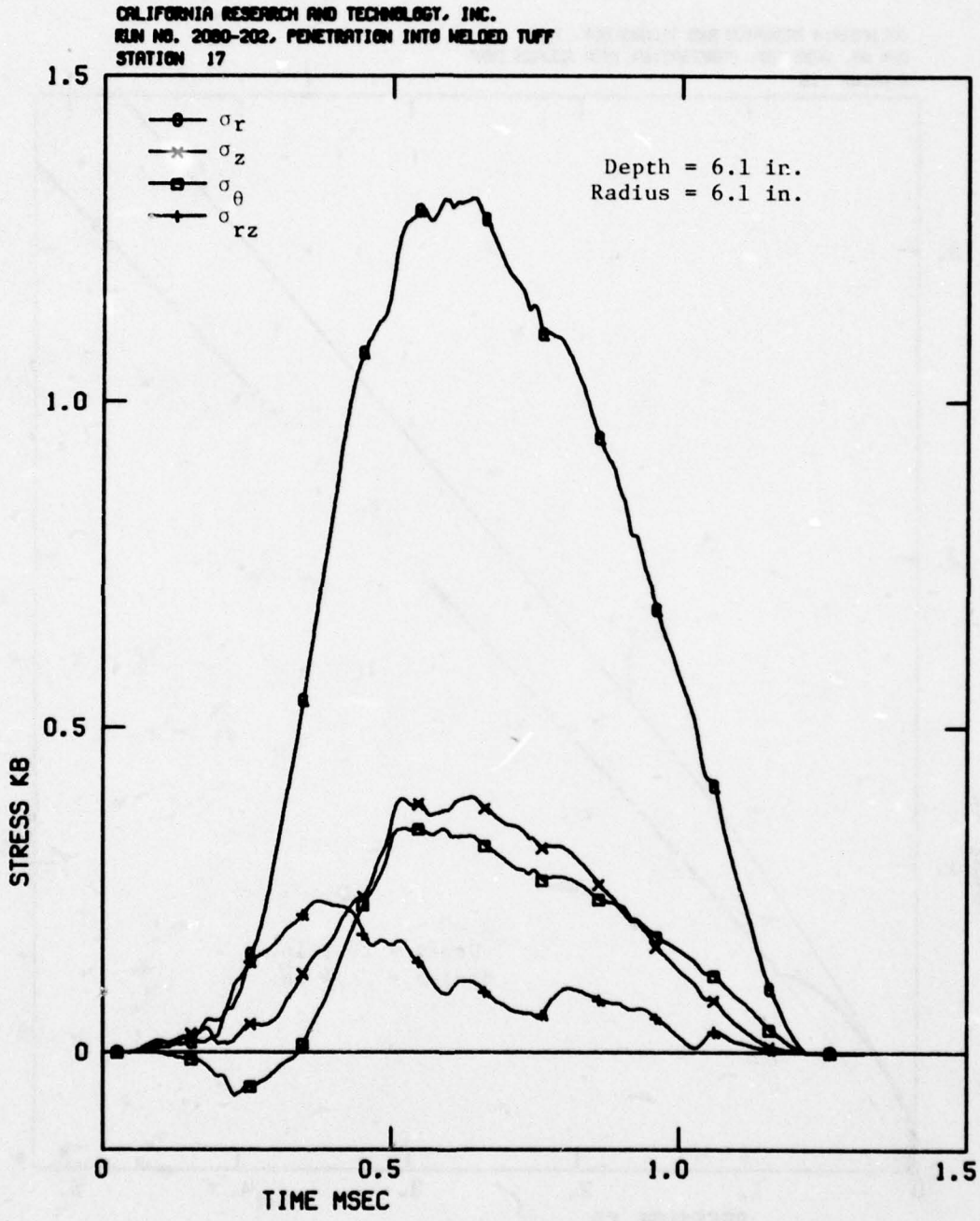


Figure B-17. Stress Components at Station 17

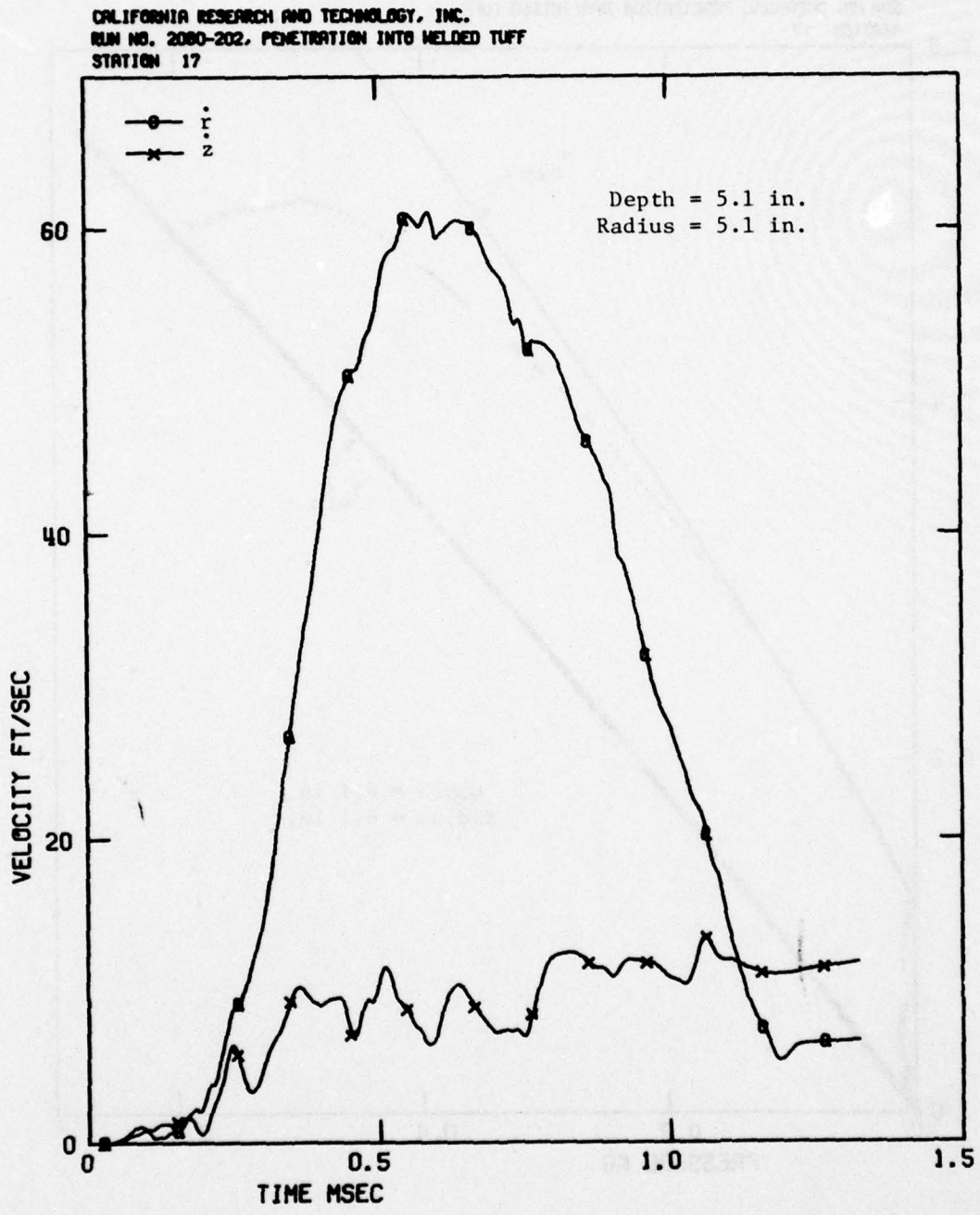


Figure B-18. Velocity Components at Station 17

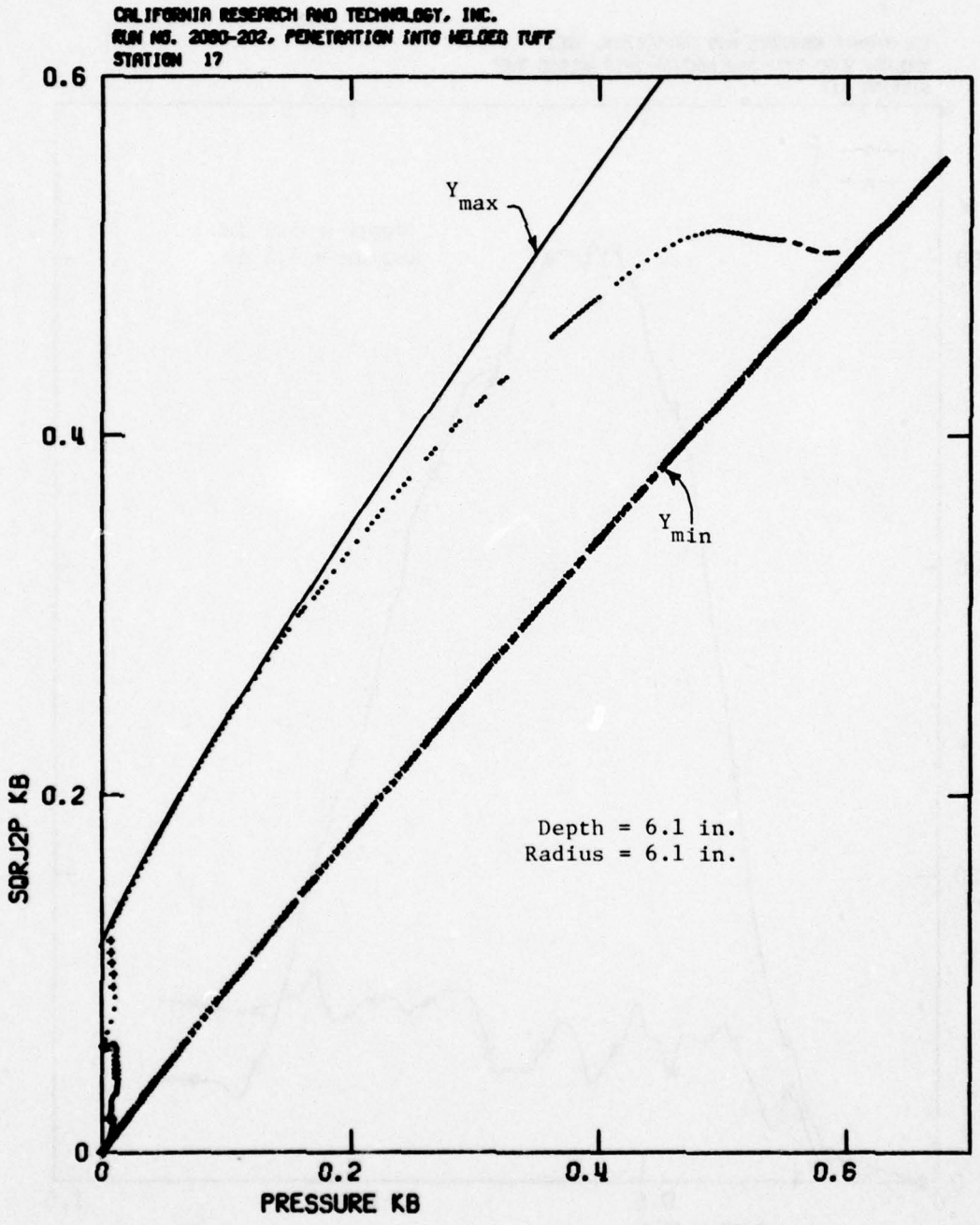


Figure B-19. Stress Path ($\sqrt{J_2'}$ vs P) at Station 17

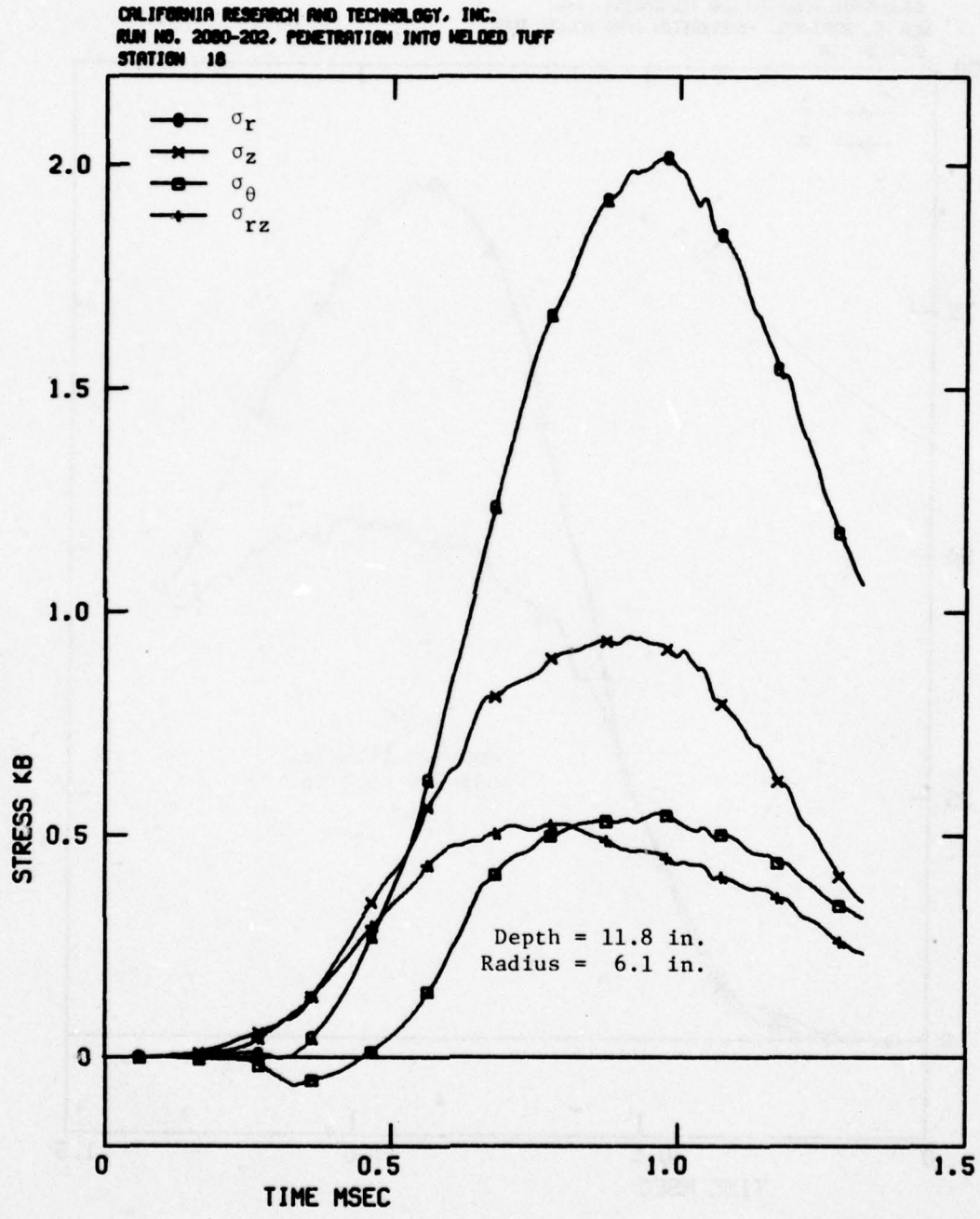


Figure B-20. Stress Components at Station 18

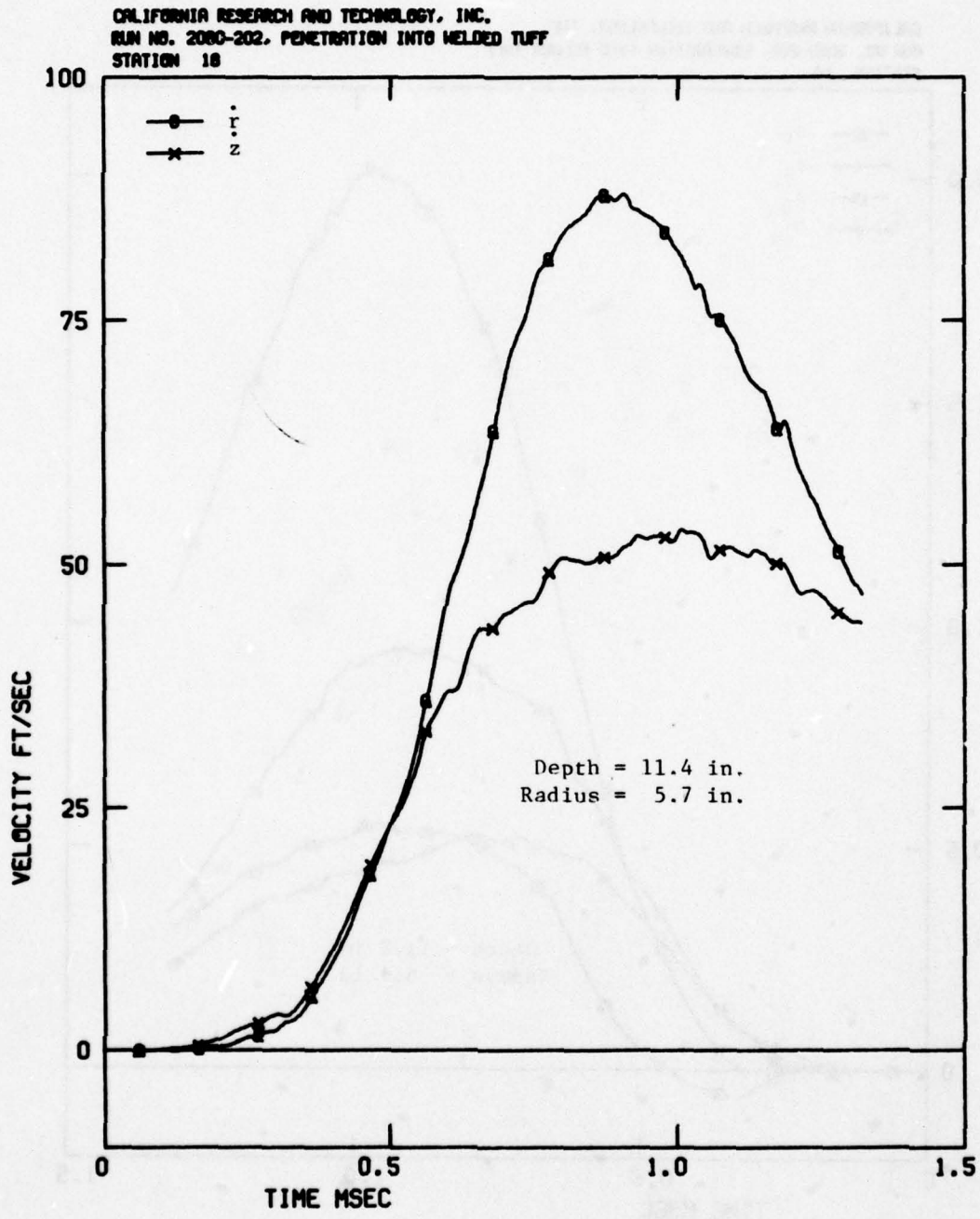


Figure B-21. Velocity Components at Station 18

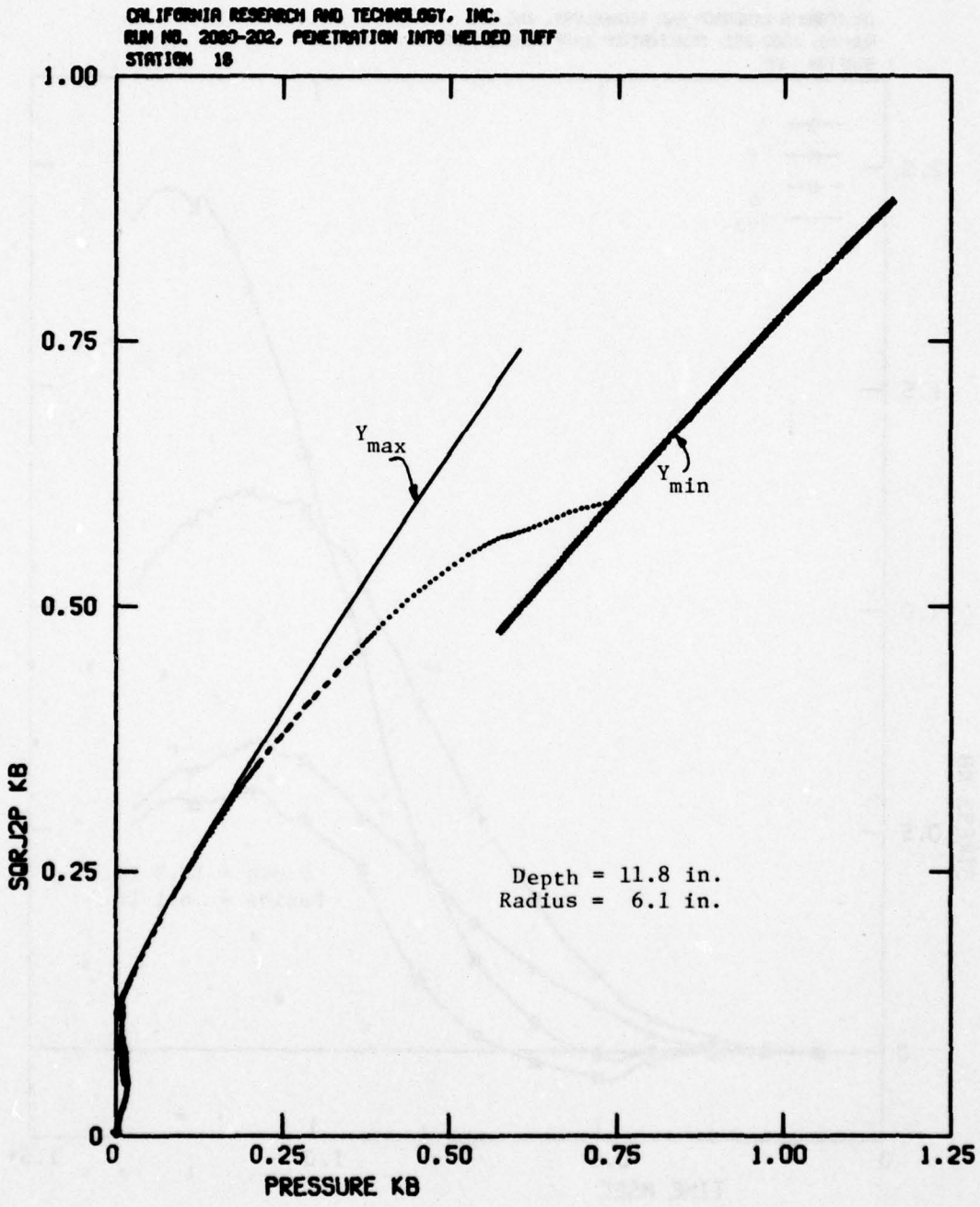


Figure B-22. Stress Path ($\sqrt{J_2'}$ vs P) at Station 18

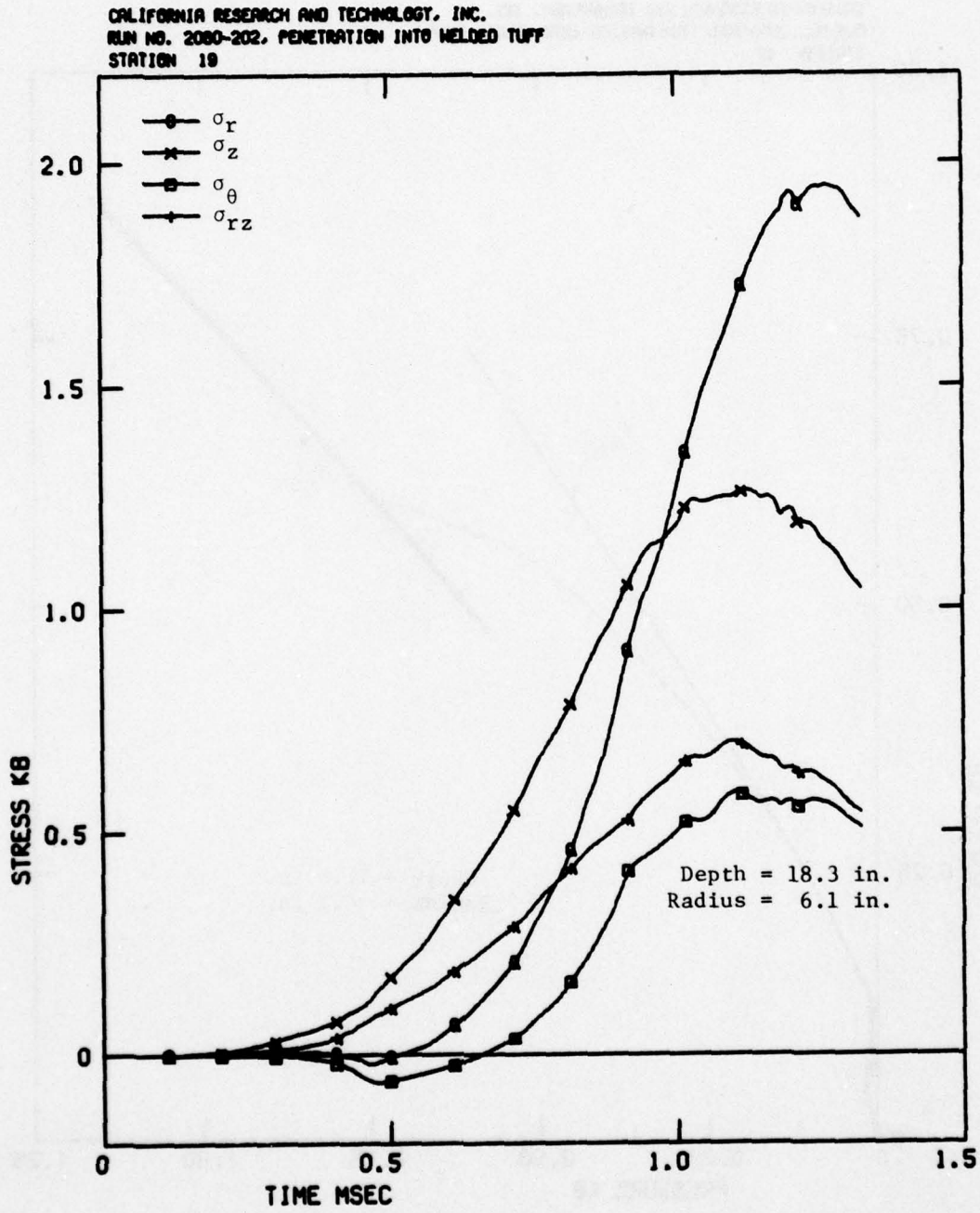


Figure B-23. Stress Components at Station 19

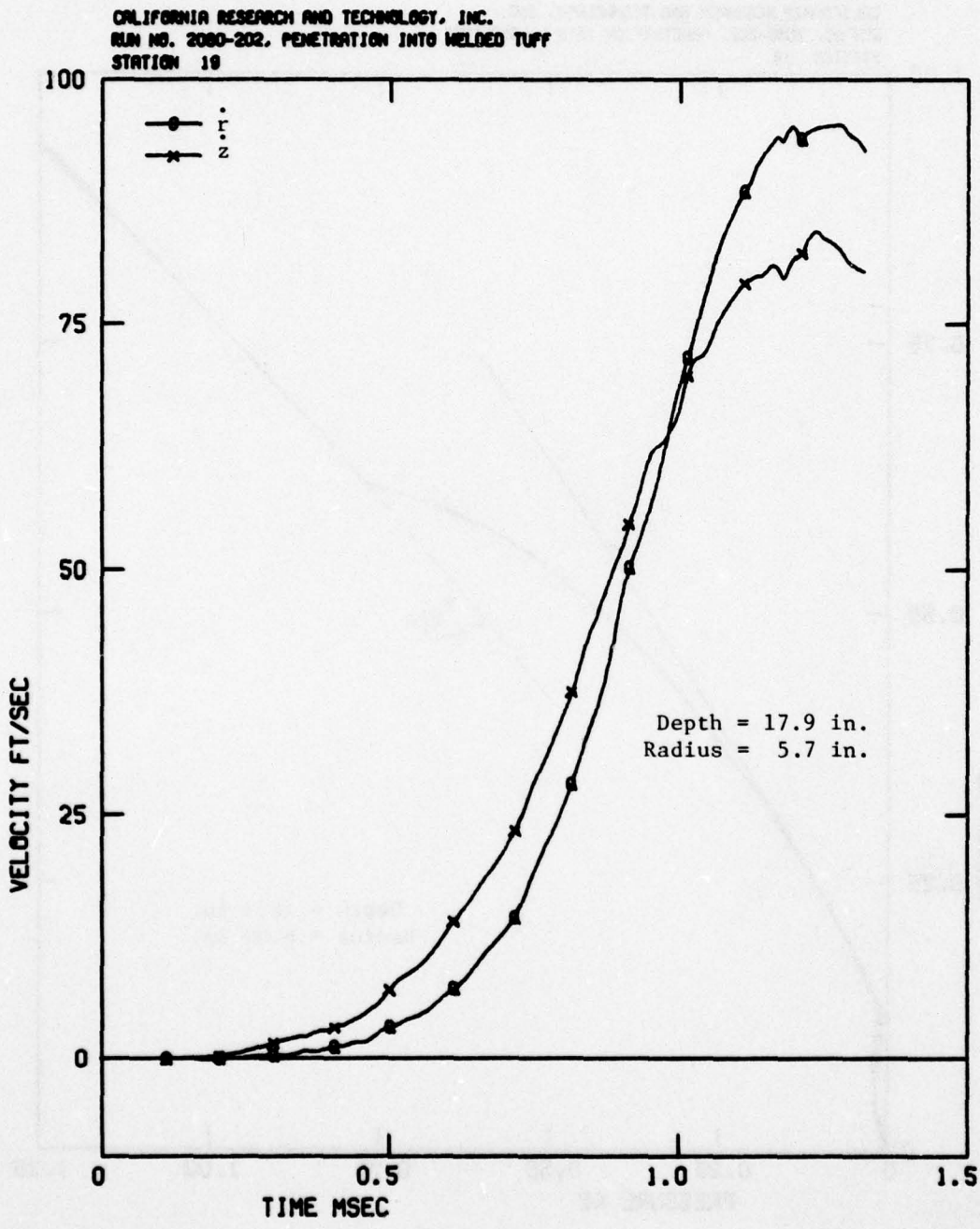


Figure B-24. Velocity Components at Station 19

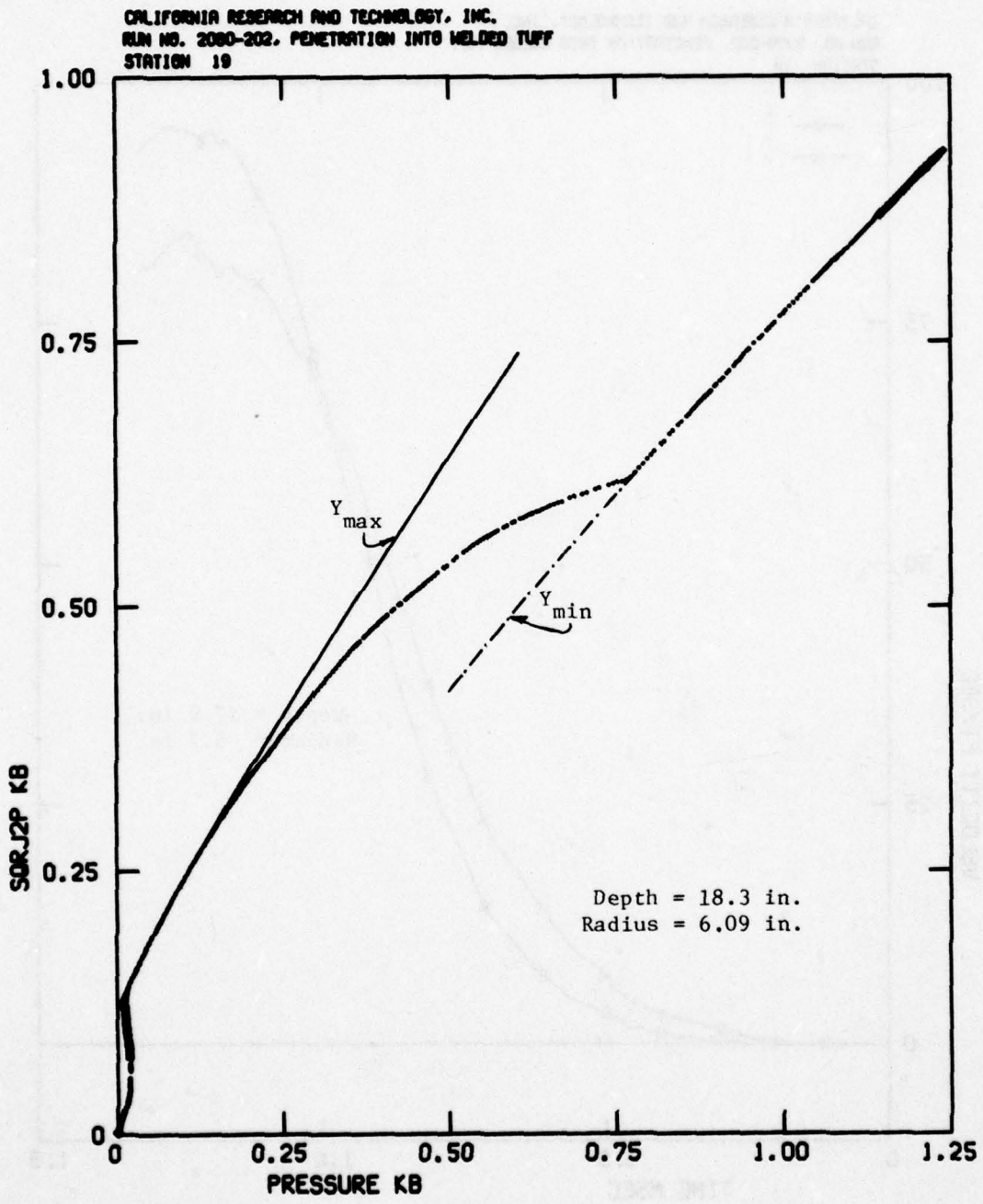


Figure B-25. Stress Path ($\sqrt{J_2'}$ vs P) at Station 19

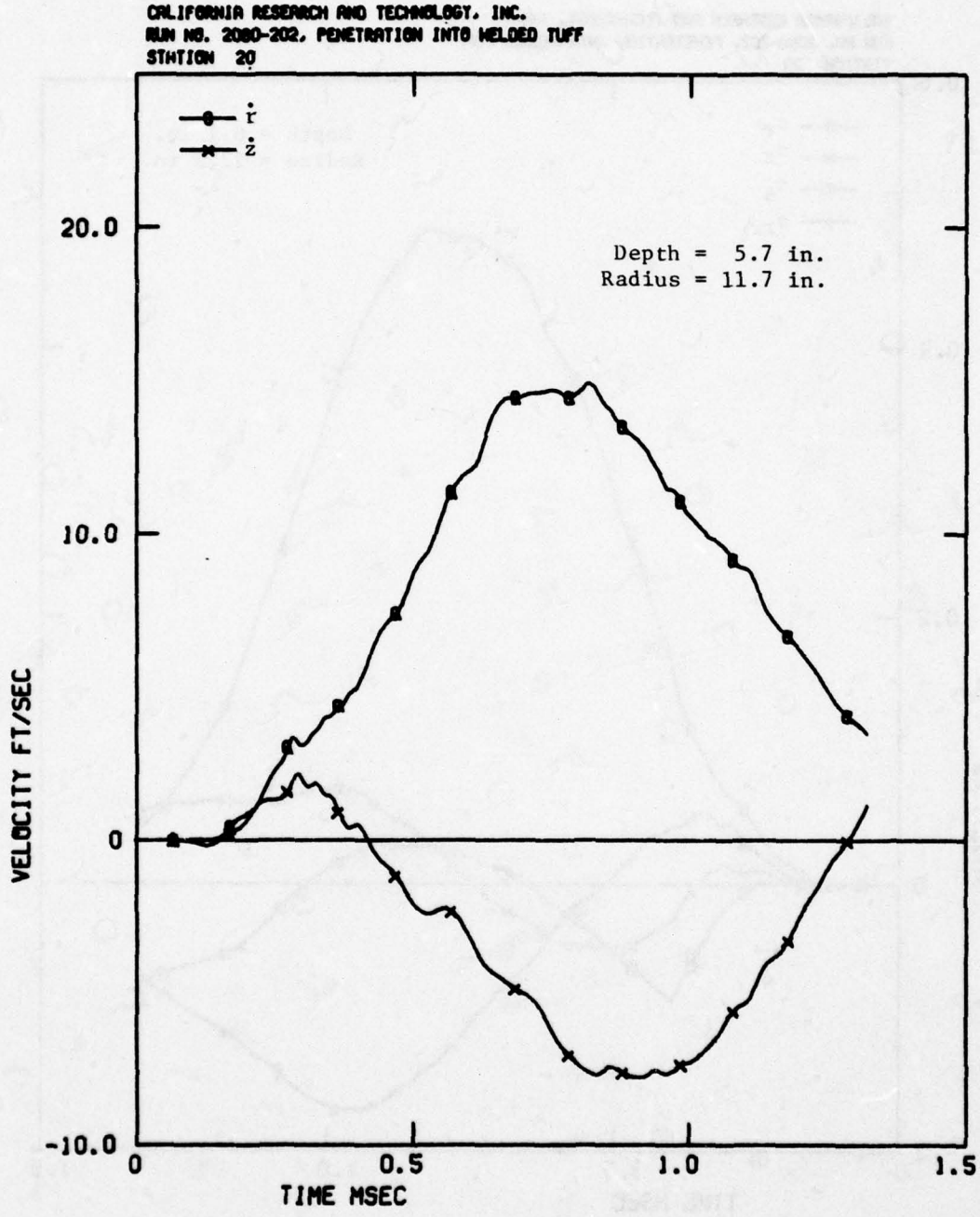


Figure B-27. Velocity Components at Station 20

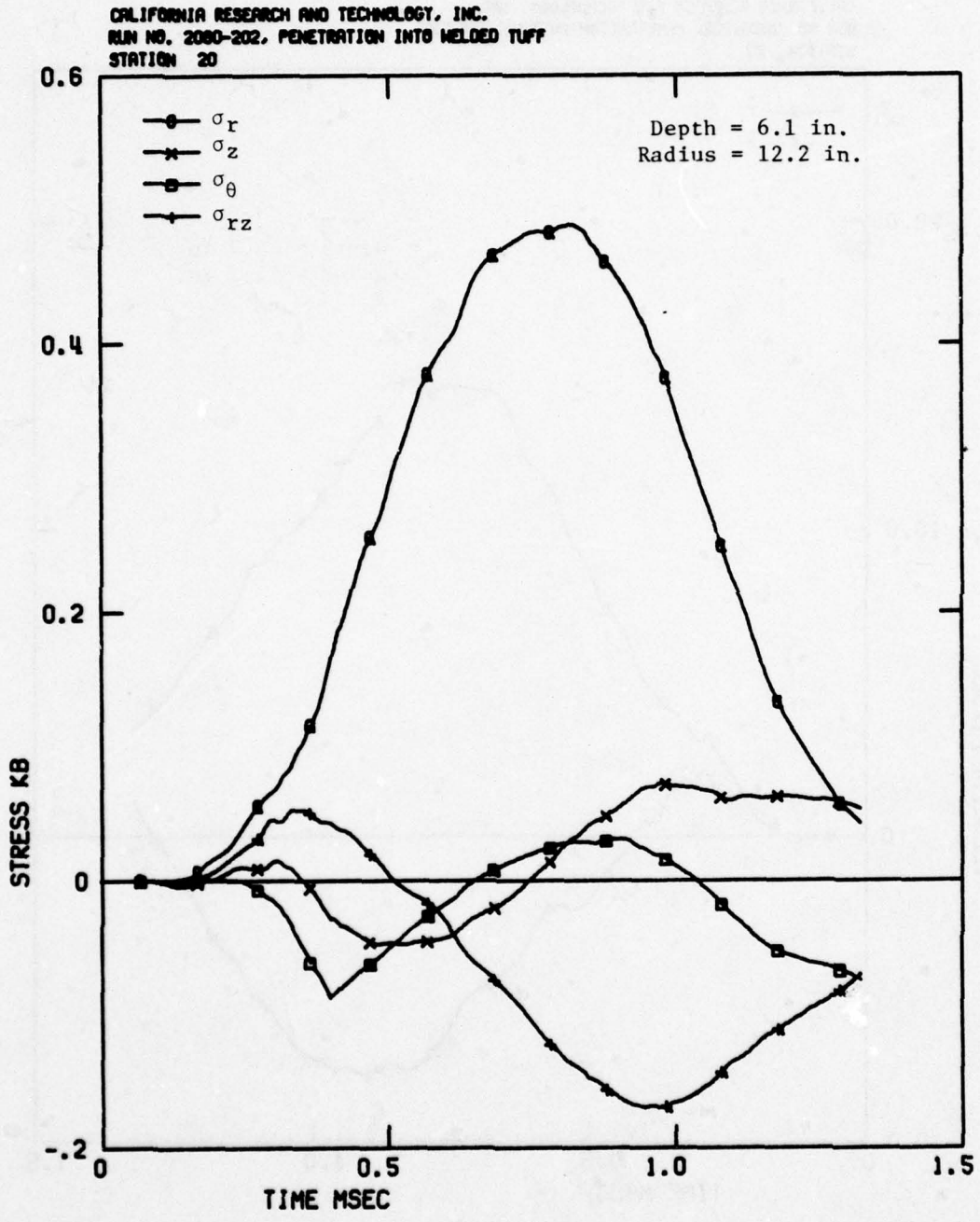


Figure B-26. Stress Components at Station 20

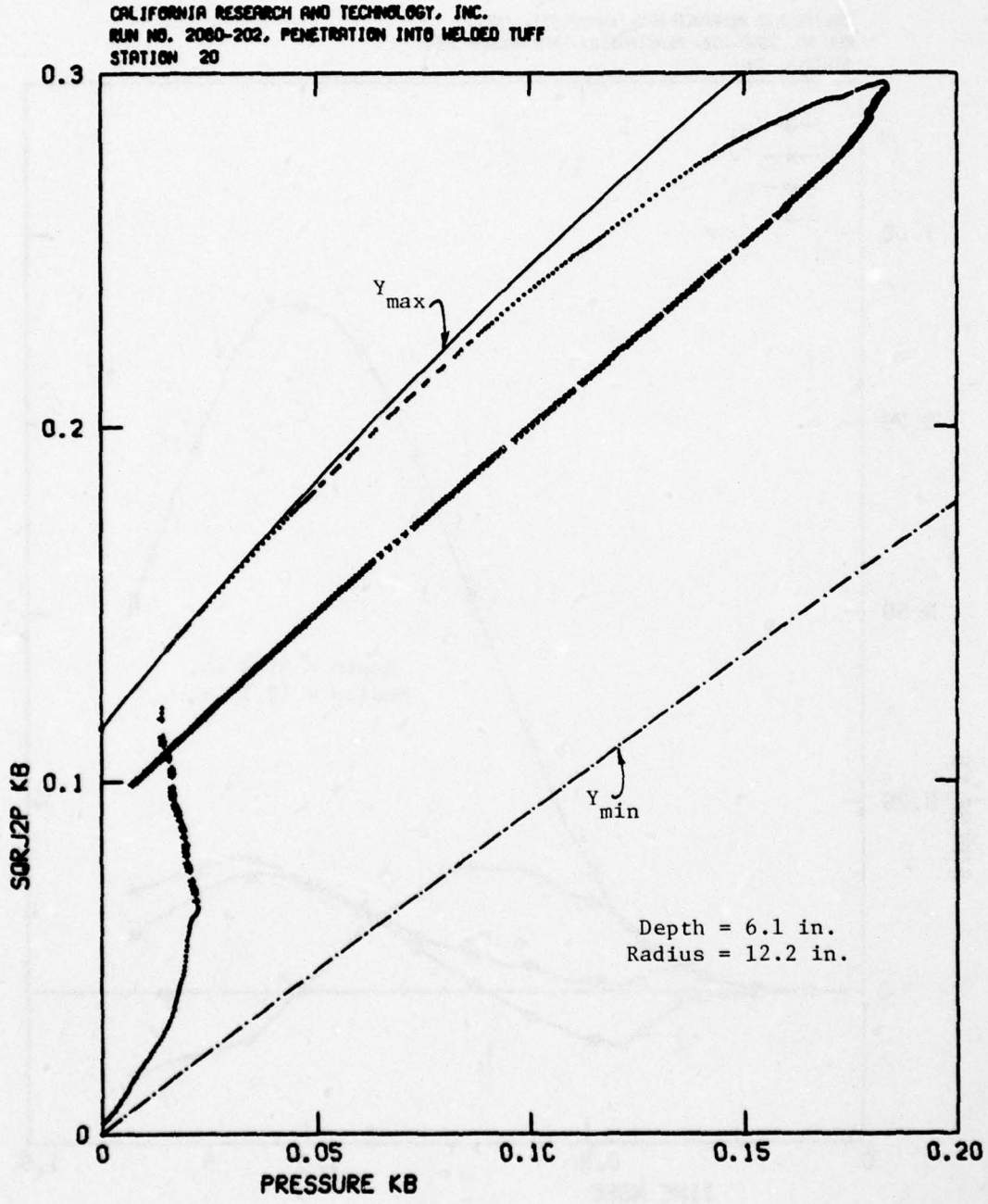


Figure B-28. Stress Path ($\sqrt{J_2'}$ vs P) at Station 20

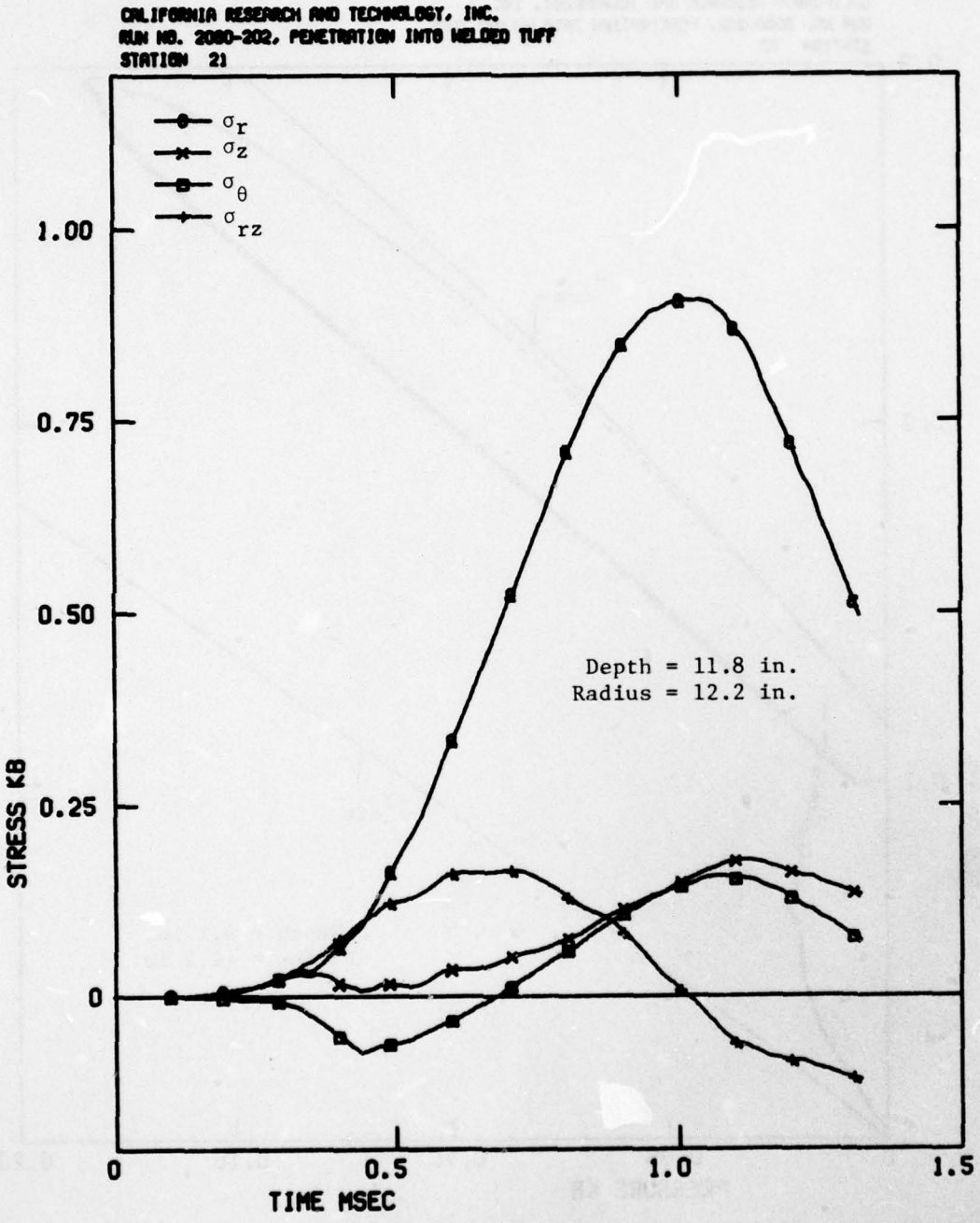


Figure B-29. Stress Components at Station 21

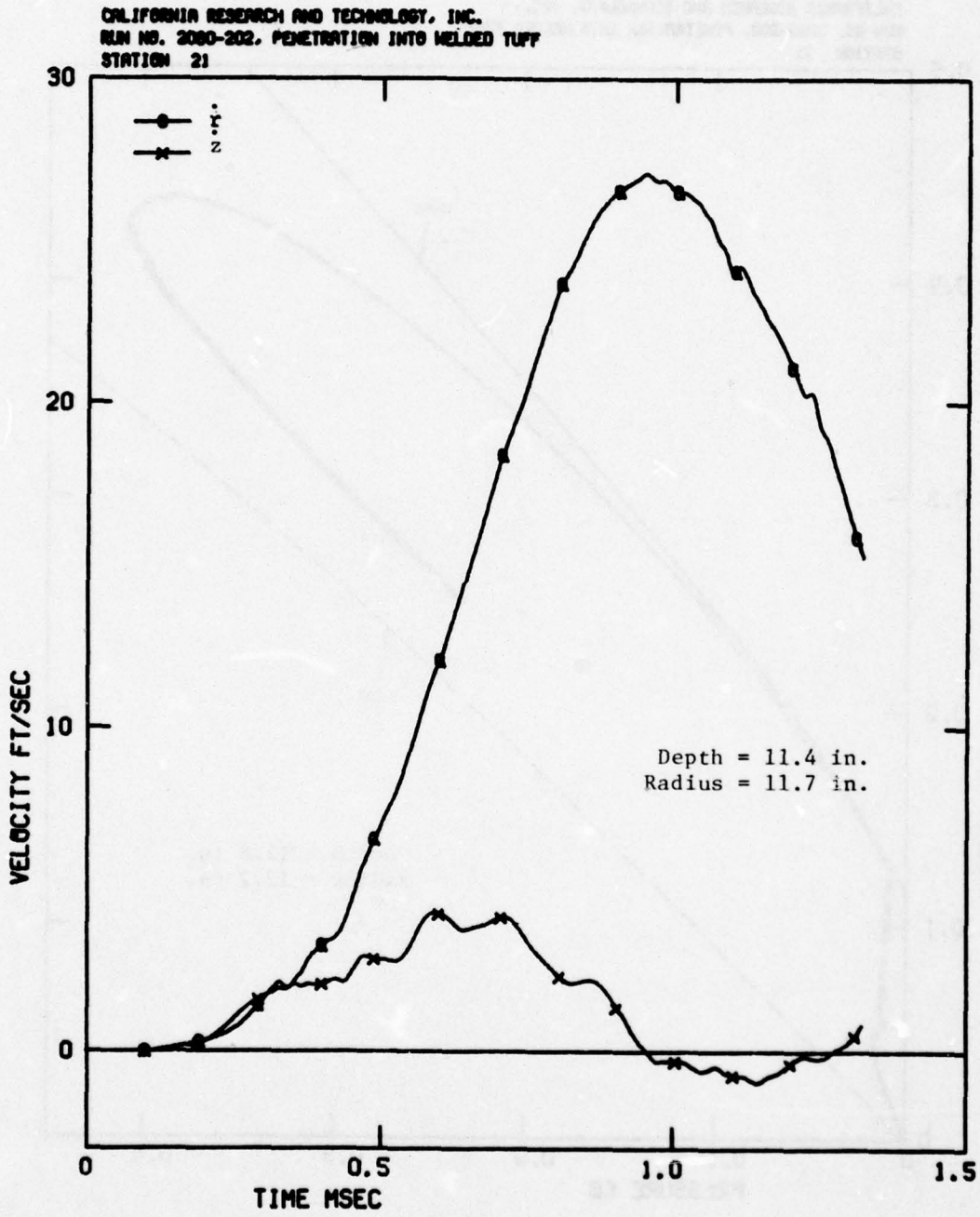


Figure B-30. Velocity Components at Station 21

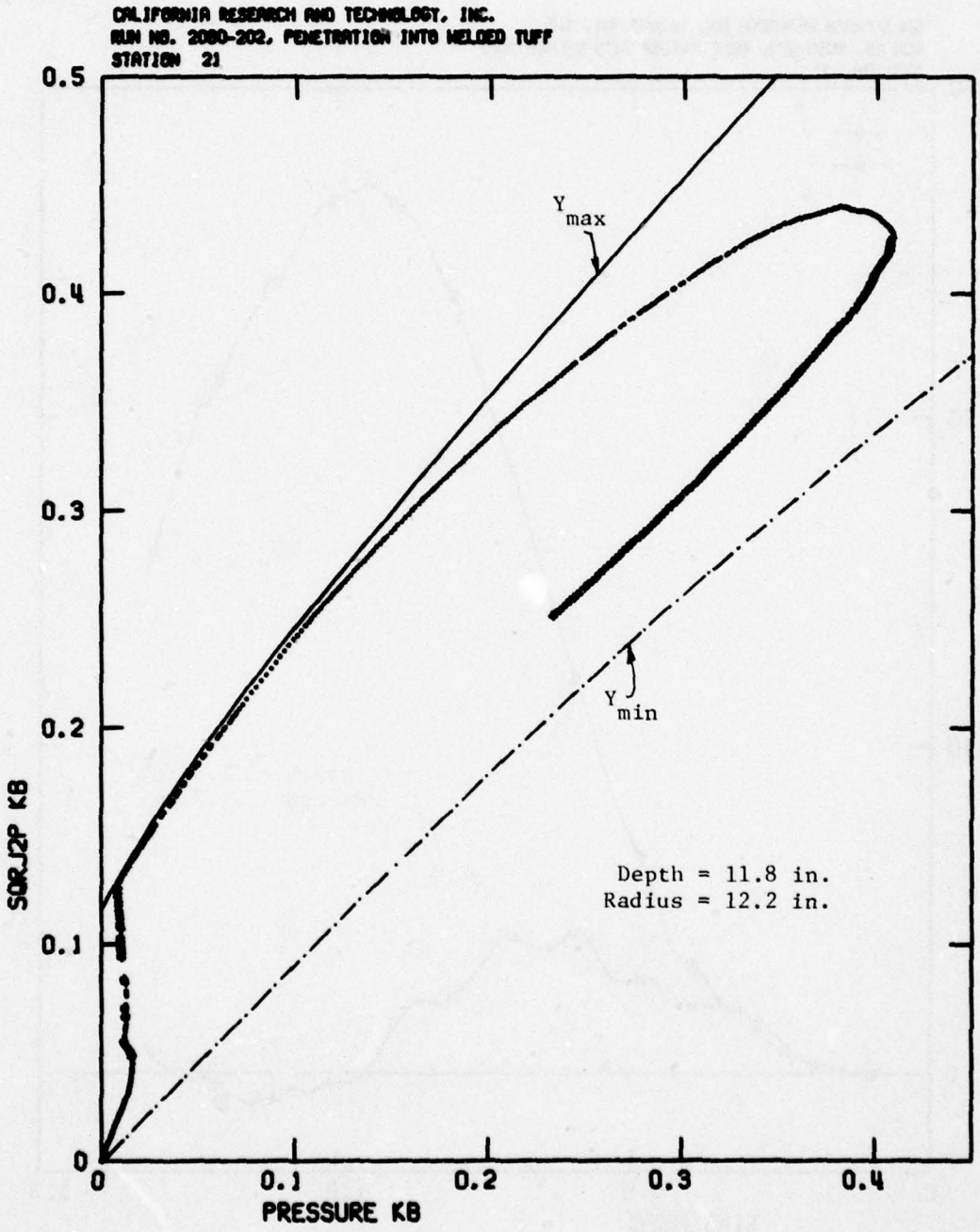


Figure B-31. Stress Path ($\sqrt{J_2'}$ vs P) at Stations 21

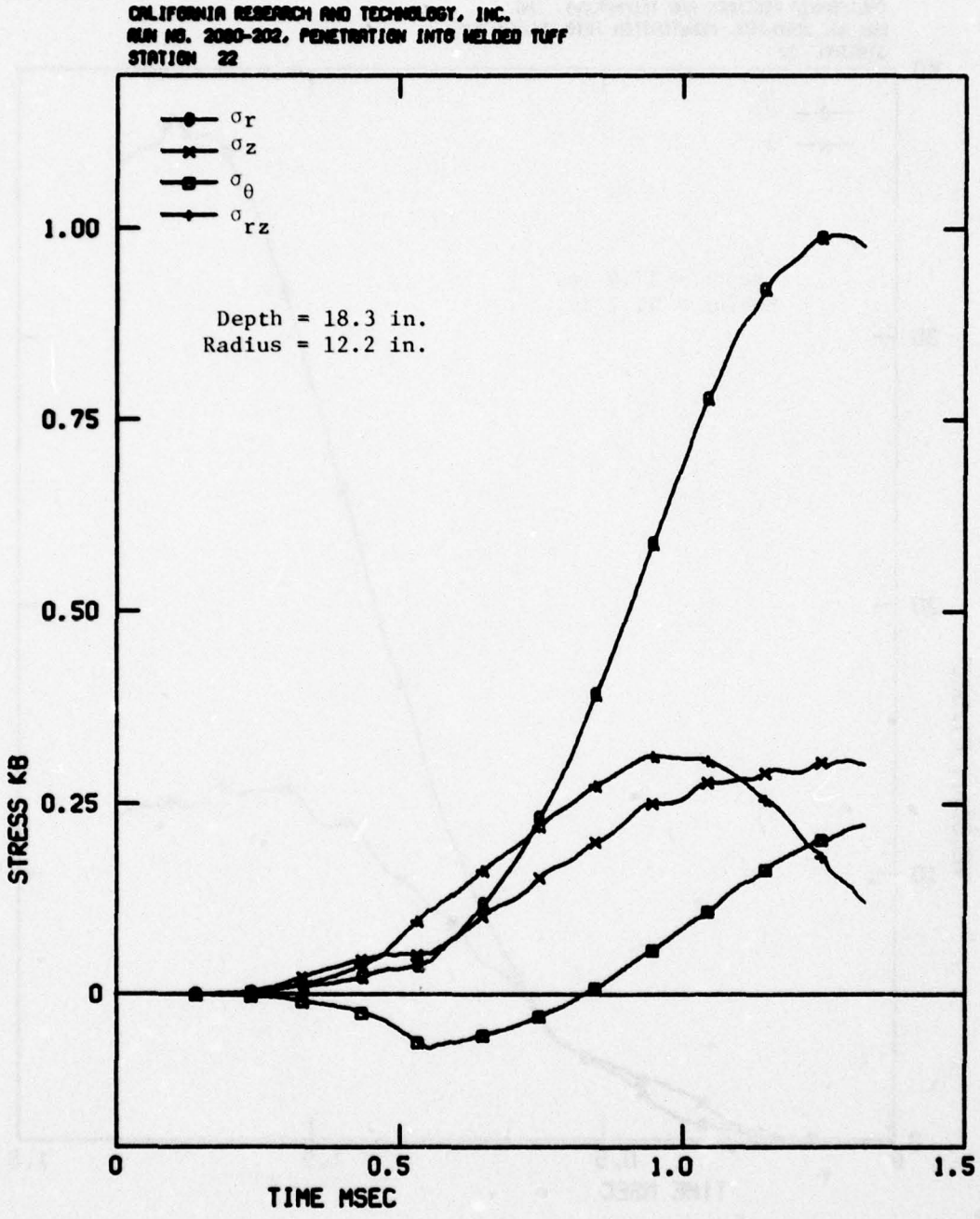


Figure B-32. Stress Components at Station 22

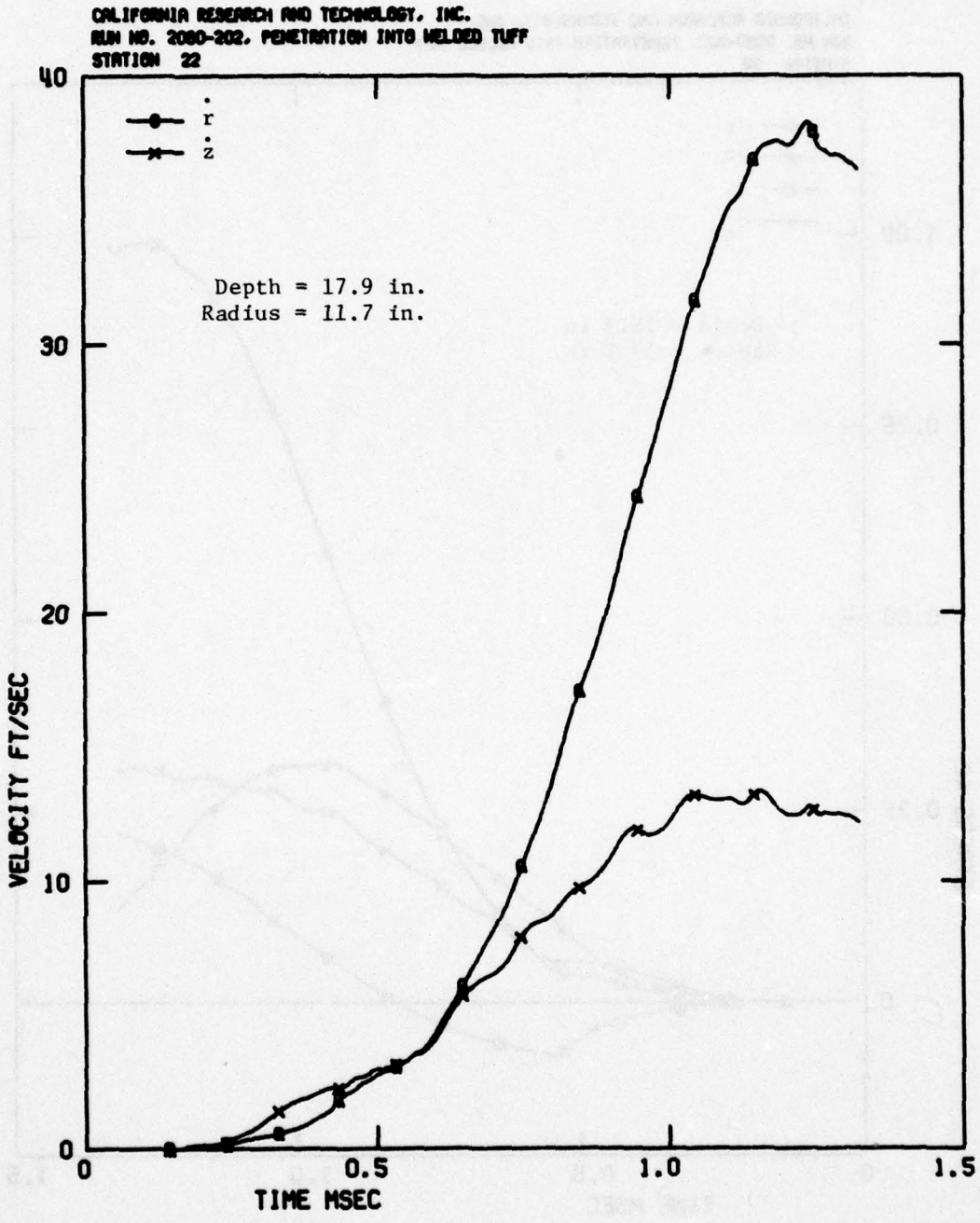


Figure B-33. Velocity Components at Station 22

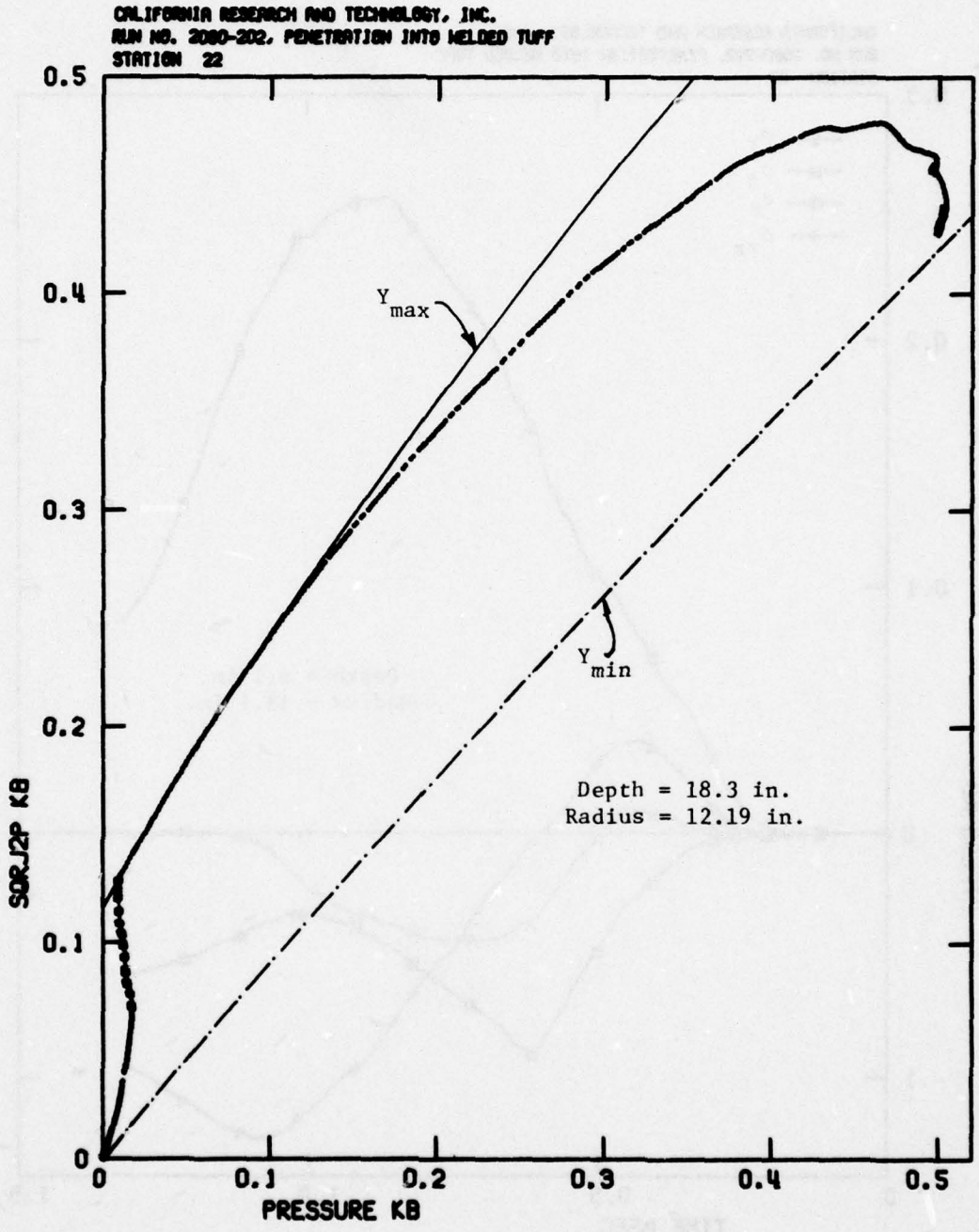


Figure B-34. Stress Path ($\sqrt{J_2'}$ vs P) at Station 22

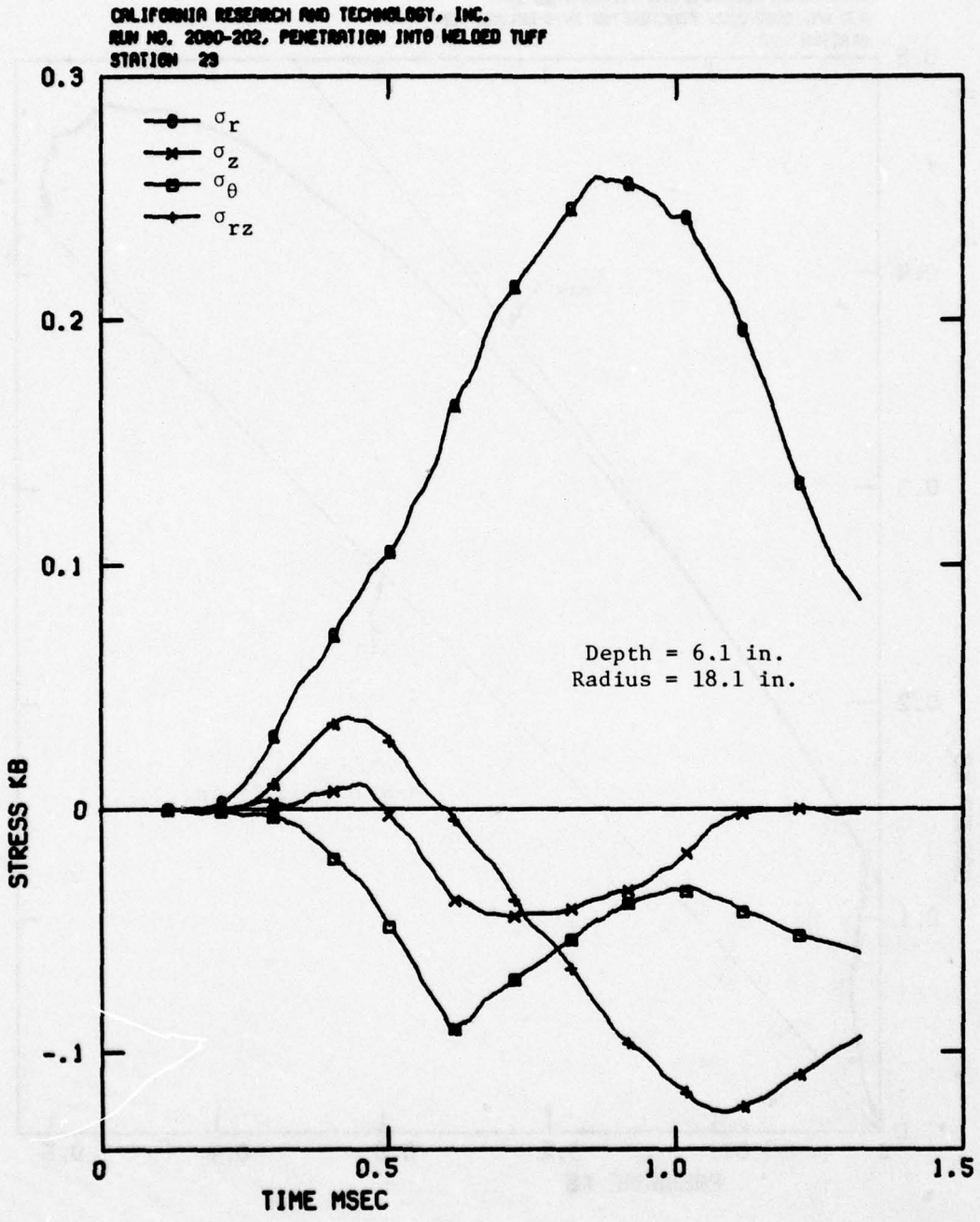


Figure B-35. Stress Components at Station 23

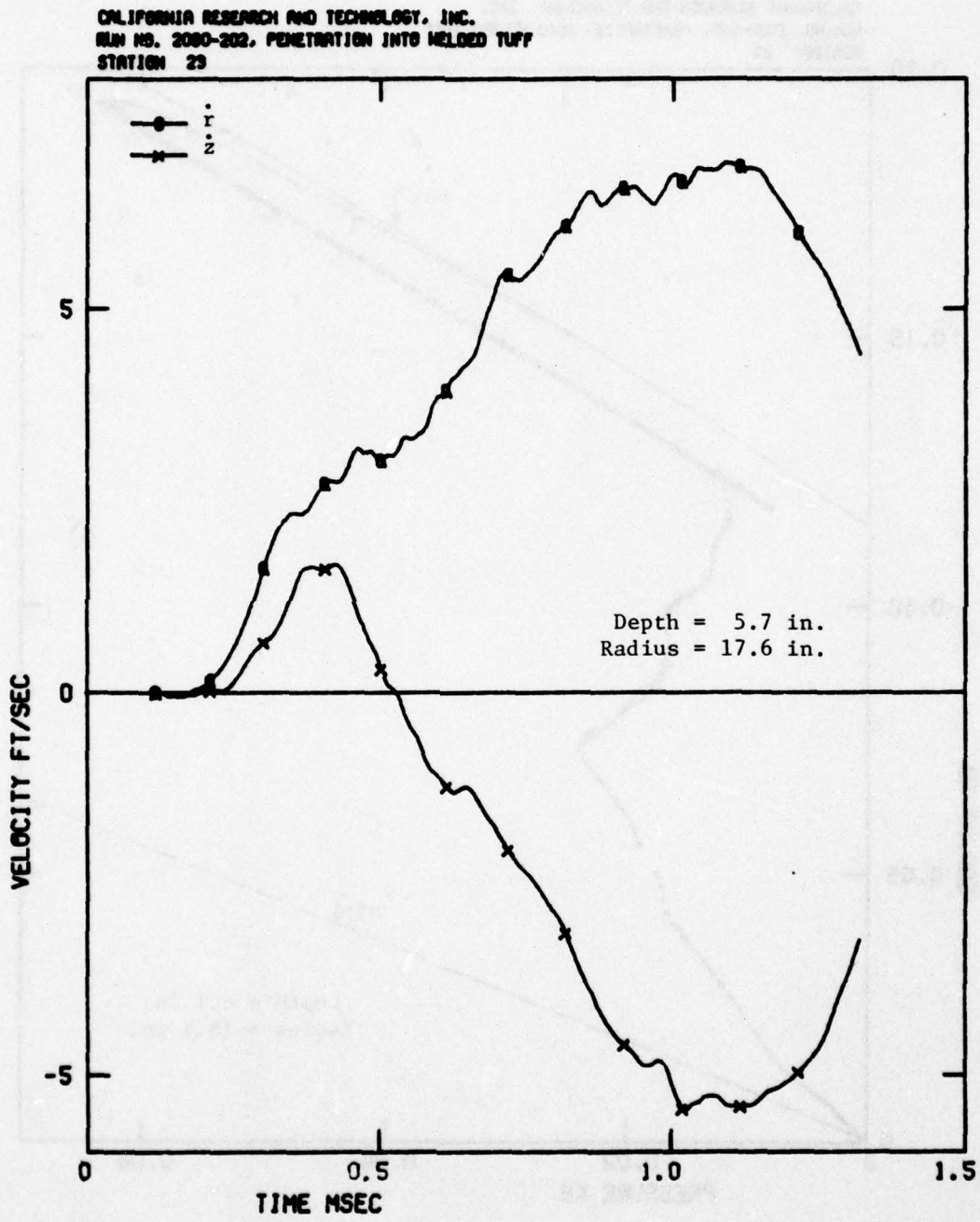


Figure B-36. Velocity Components at Station 23

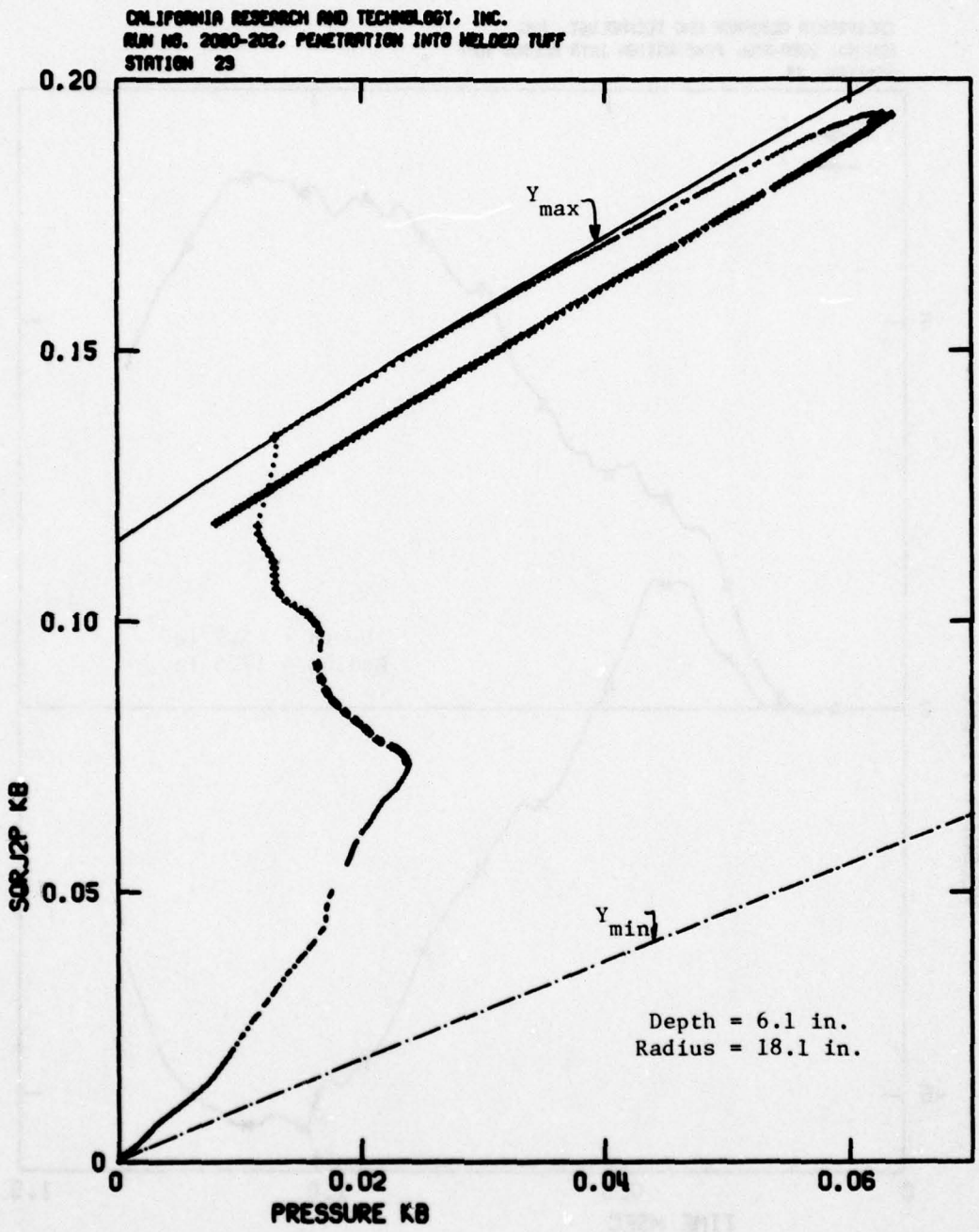


Figure B-37. Stress Path ($\sqrt{J_2'}$ vs P) at Station 23

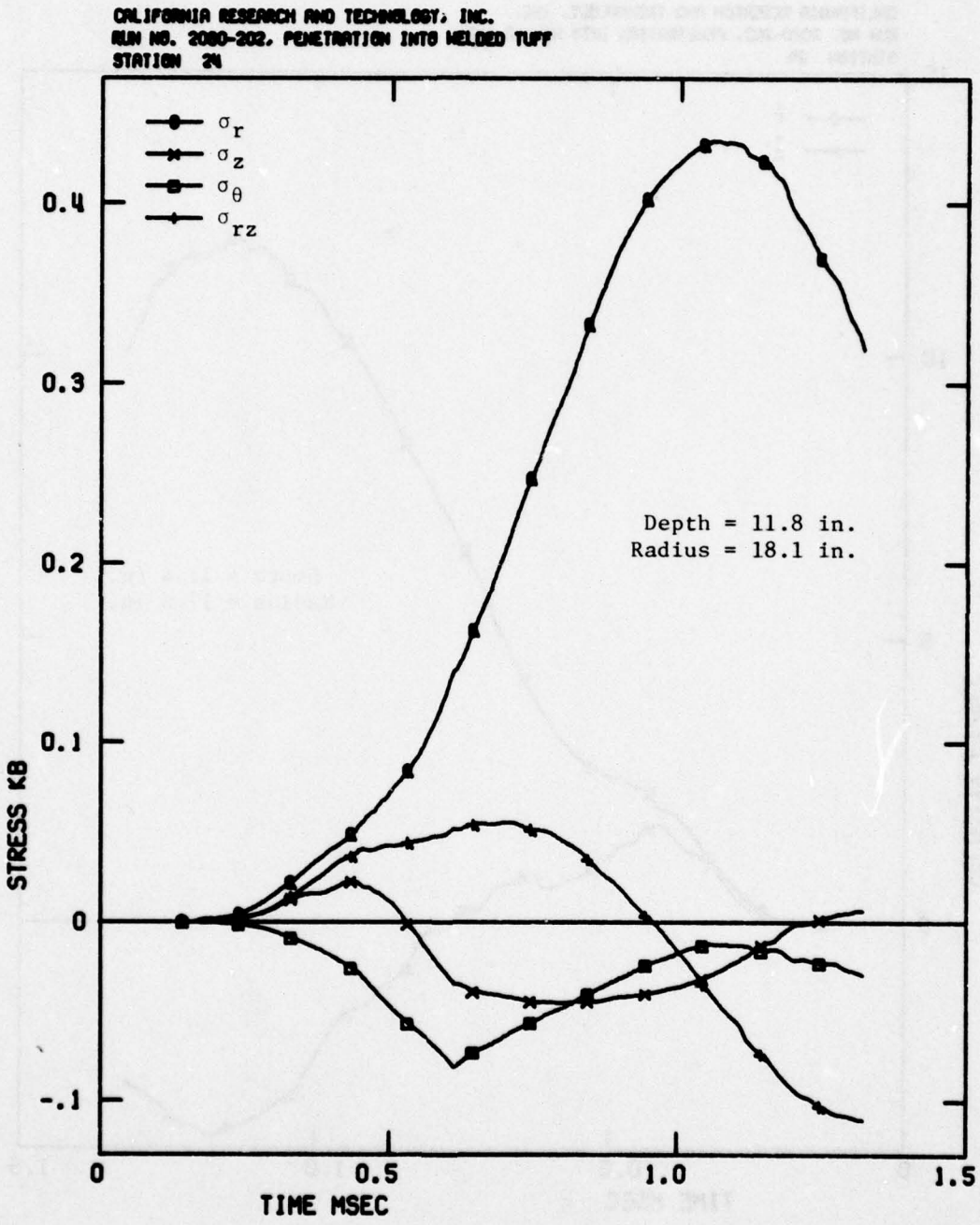


Figure B-38. Stress Components at Station 24

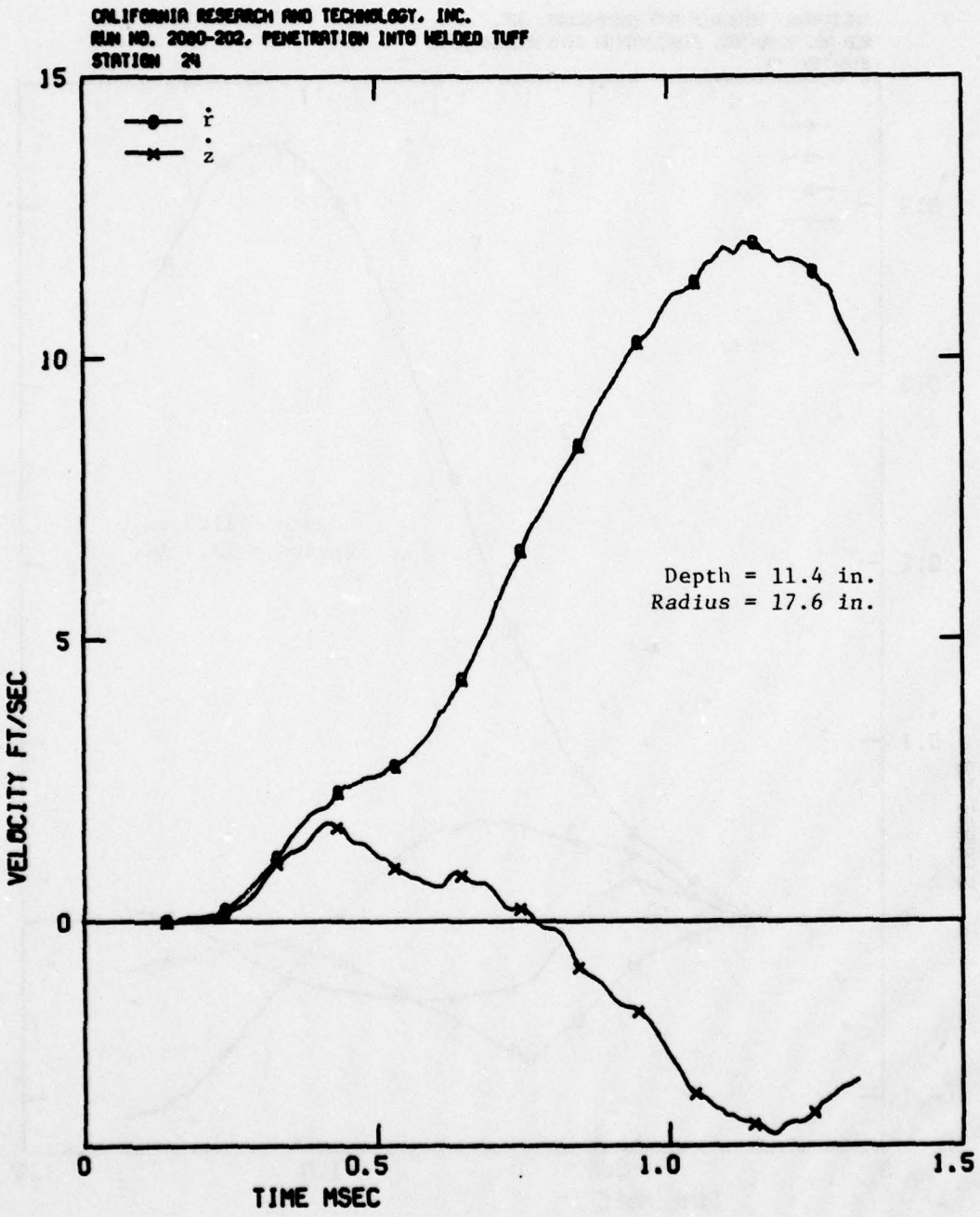


Figure B-39. Velocity Components at Station 24

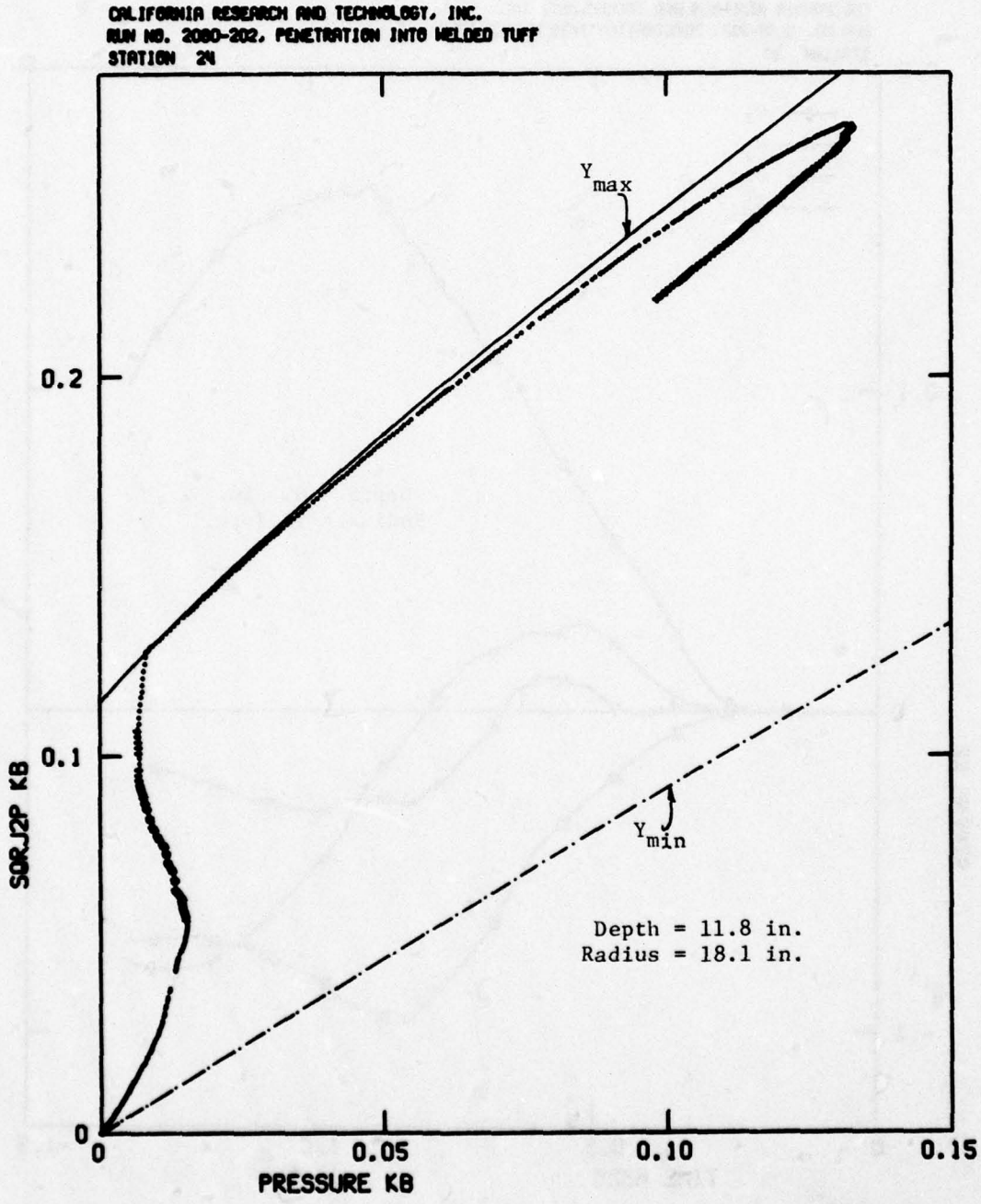


Figure B-40. Stress Path ($\sqrt{J_2'}$ vs P) at Station 24

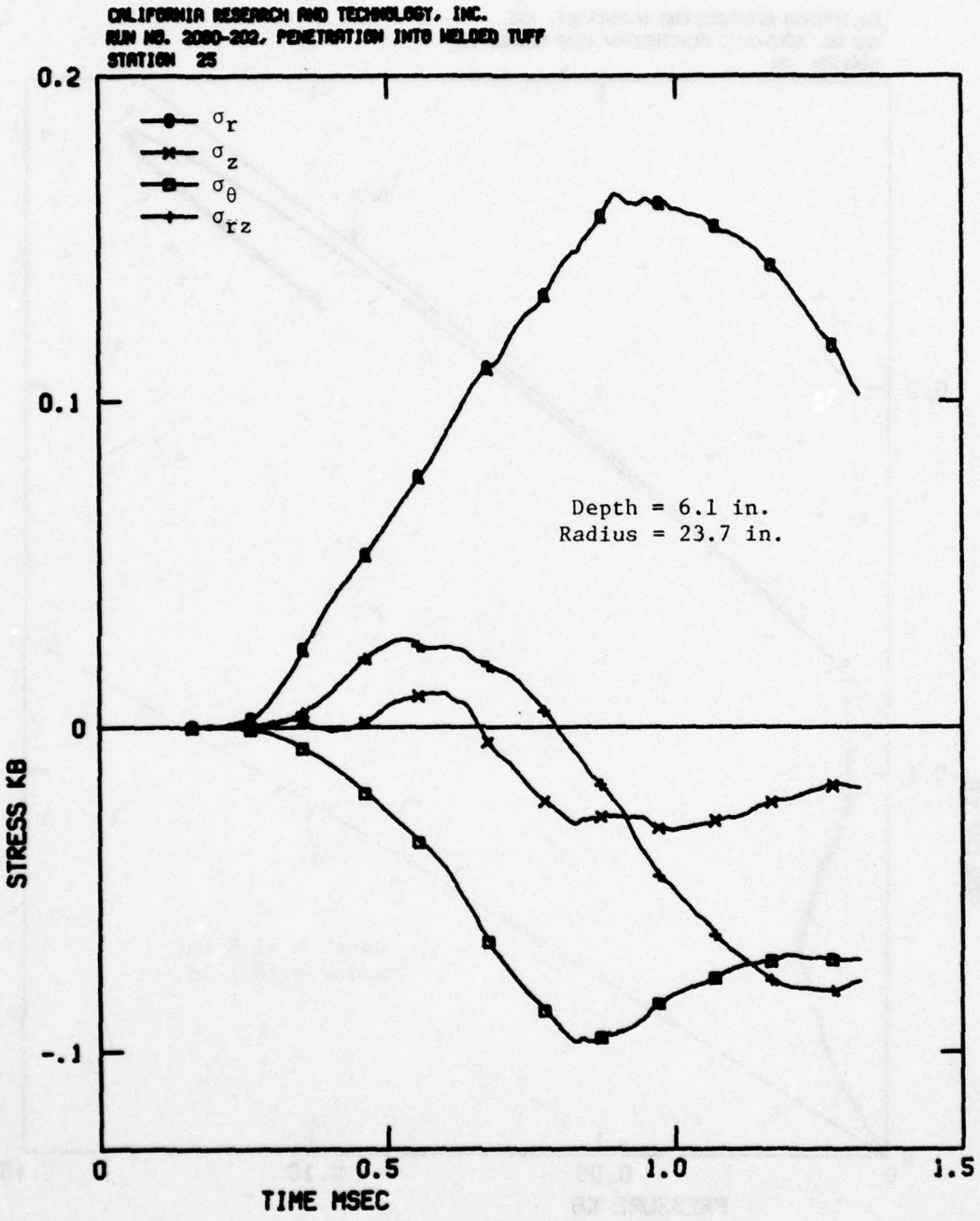


Figure B-41. Stress Components at Station 25

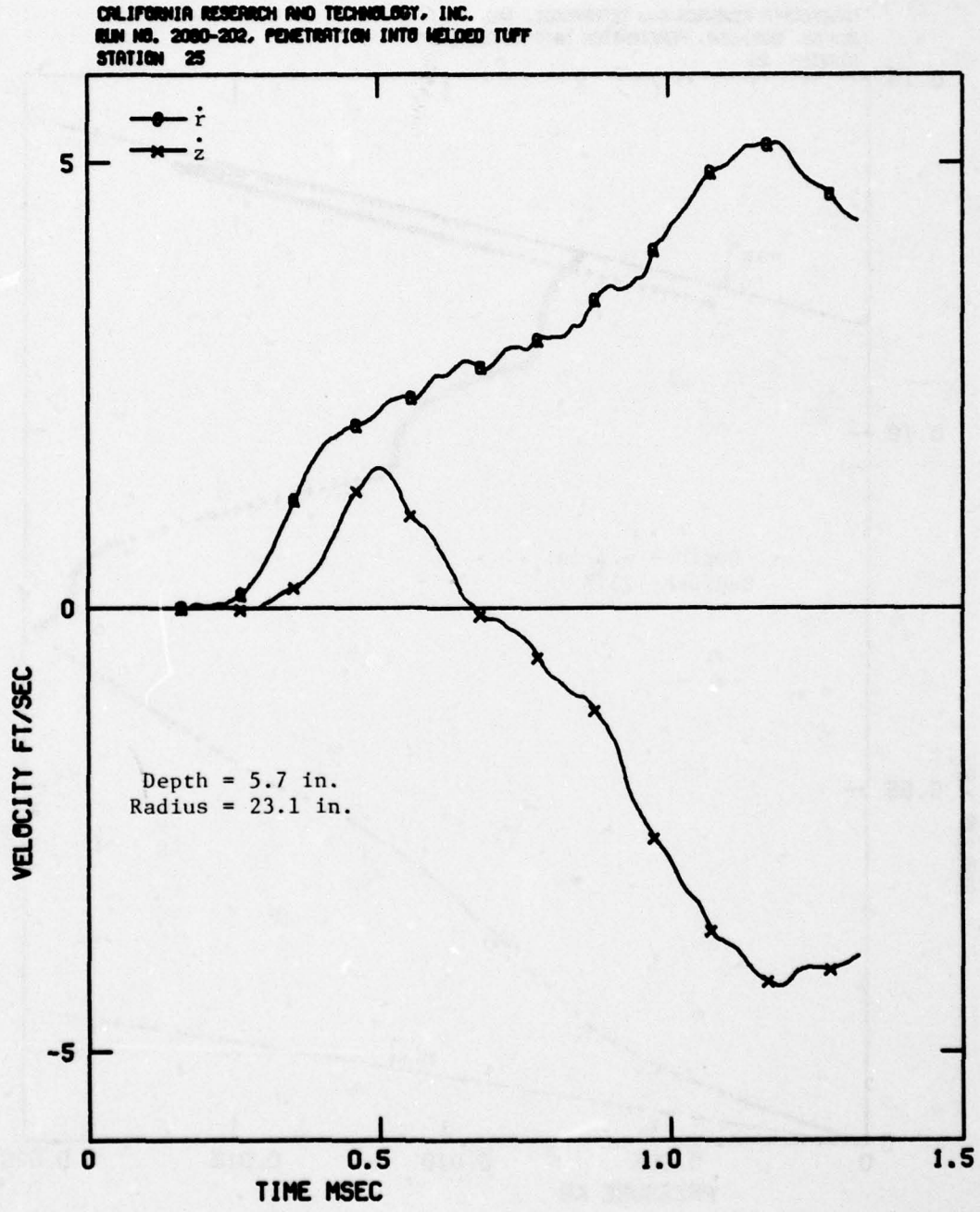


Figure B-42. Velocity Components at Station 25

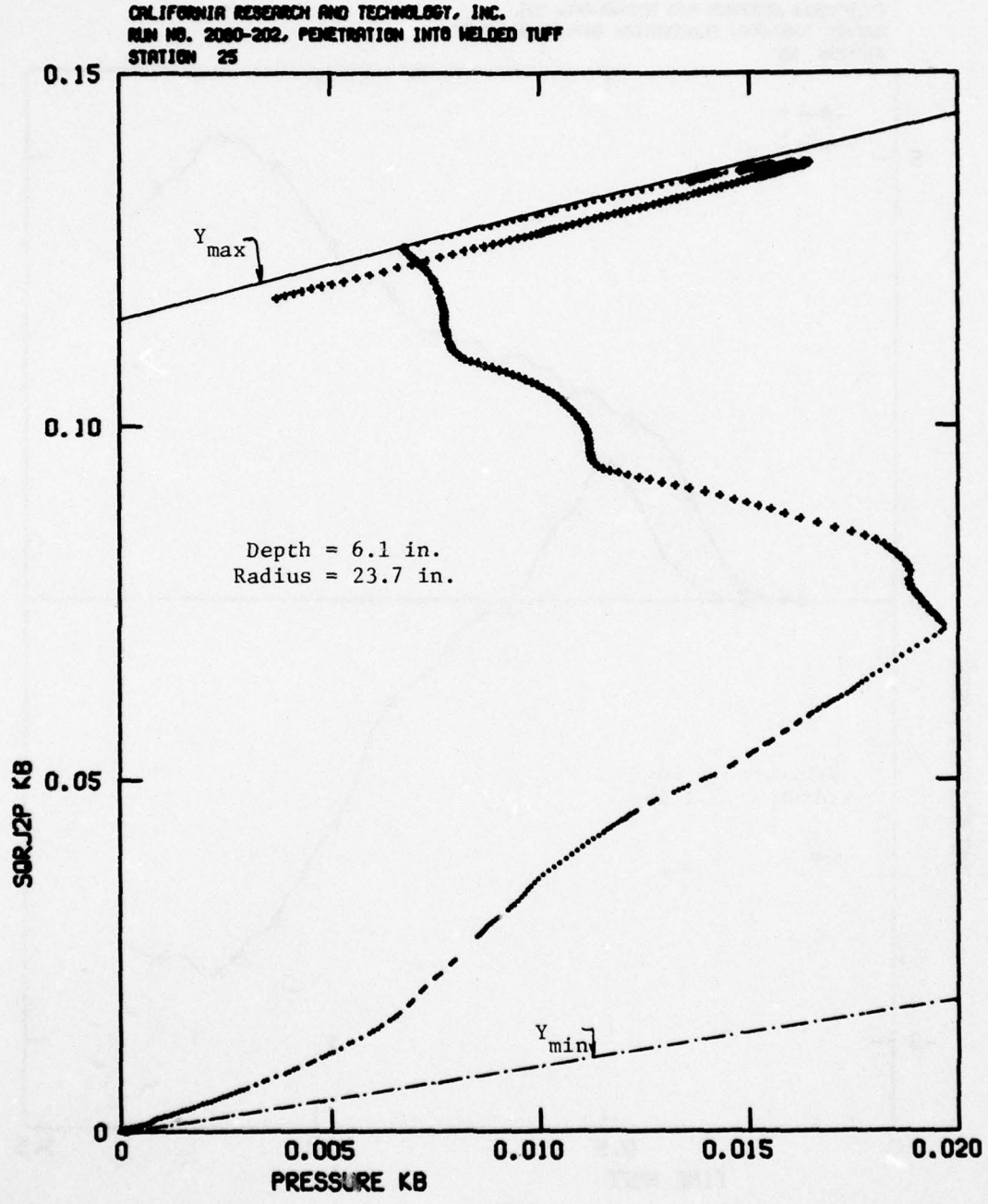


Figure B-43. Stress Path ($\sqrt{J_2'}$ vs P) at Station 25

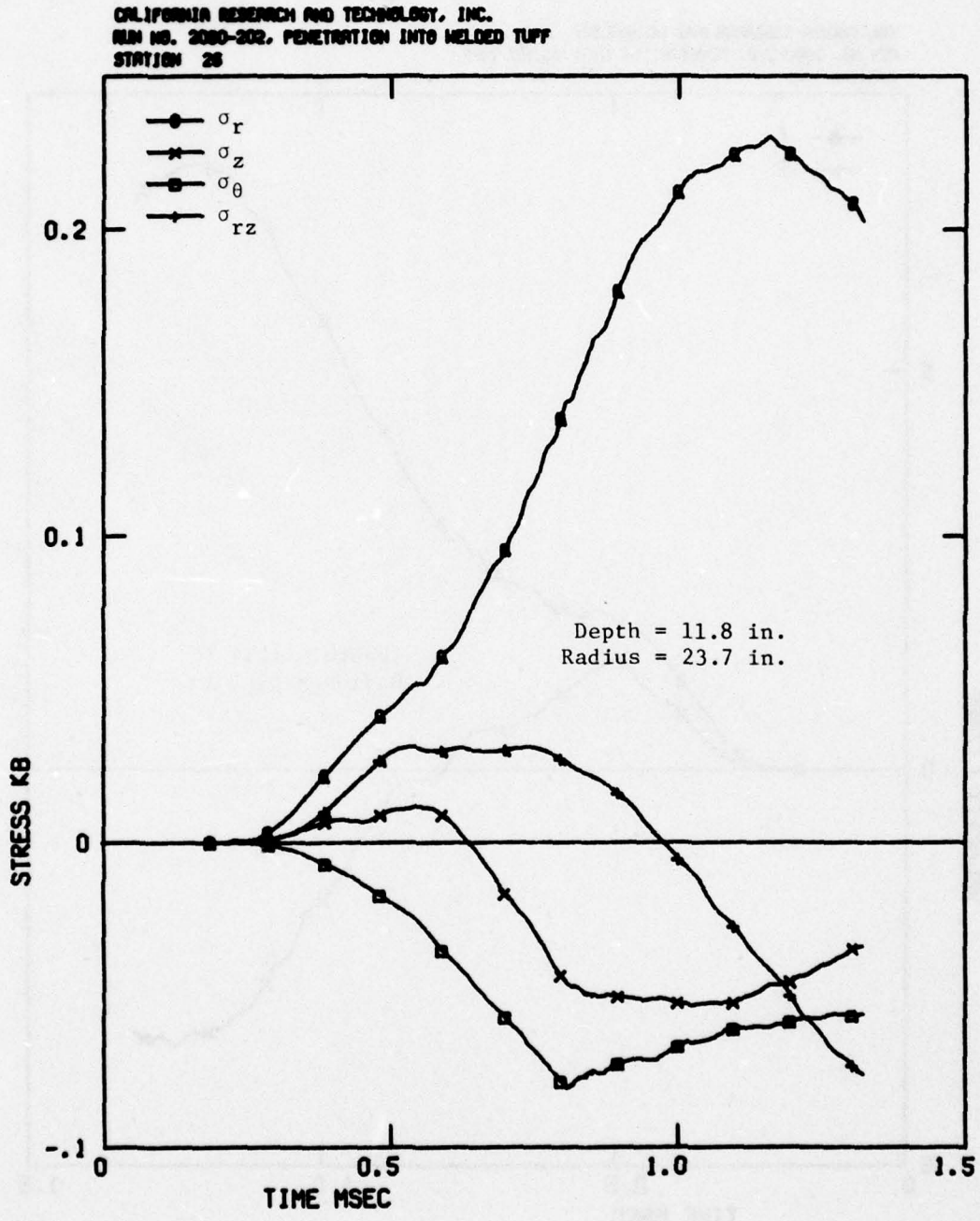


Figure B-44. Stress Components at Station 26

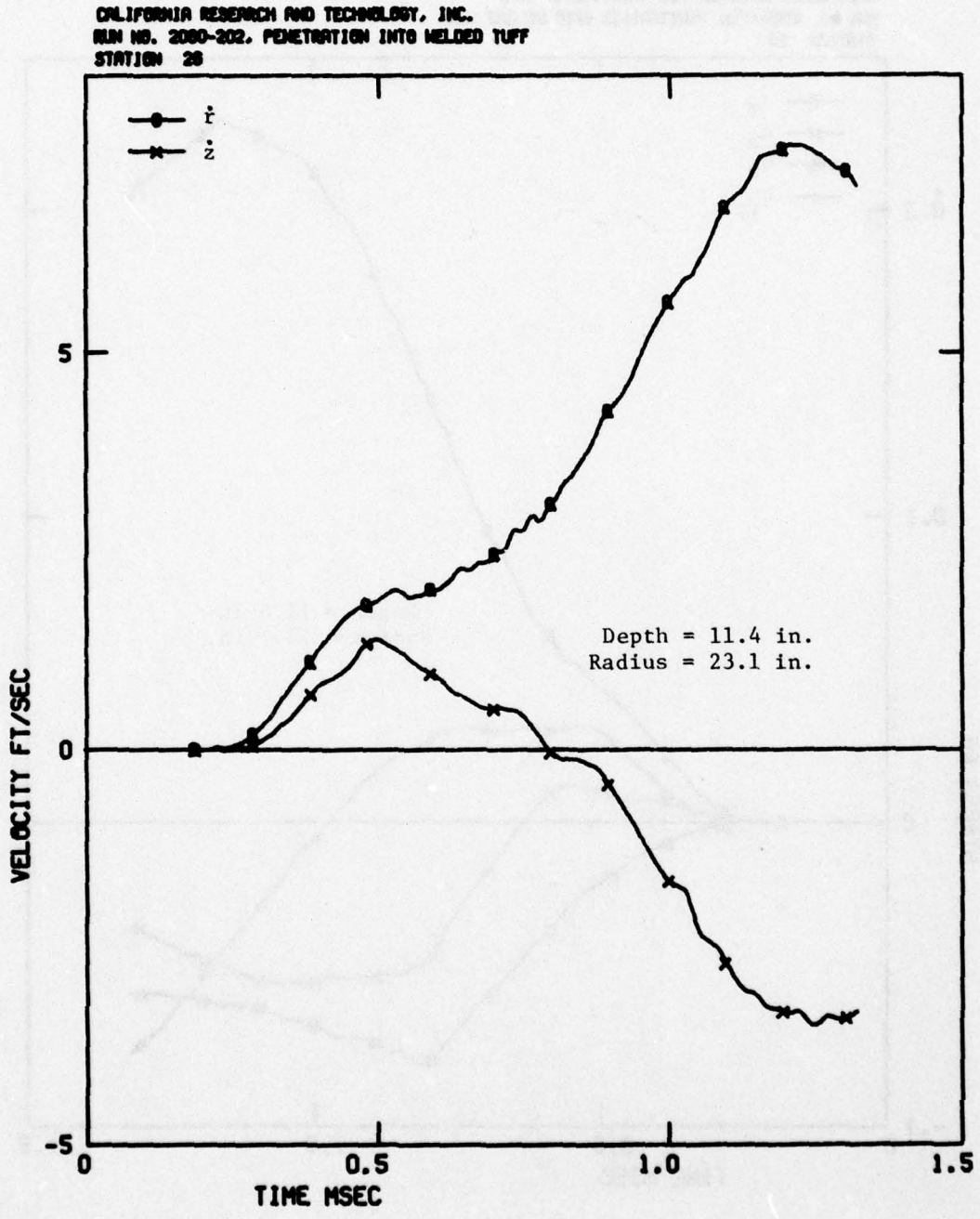


Figure B-45. Velocity Components at Station 26

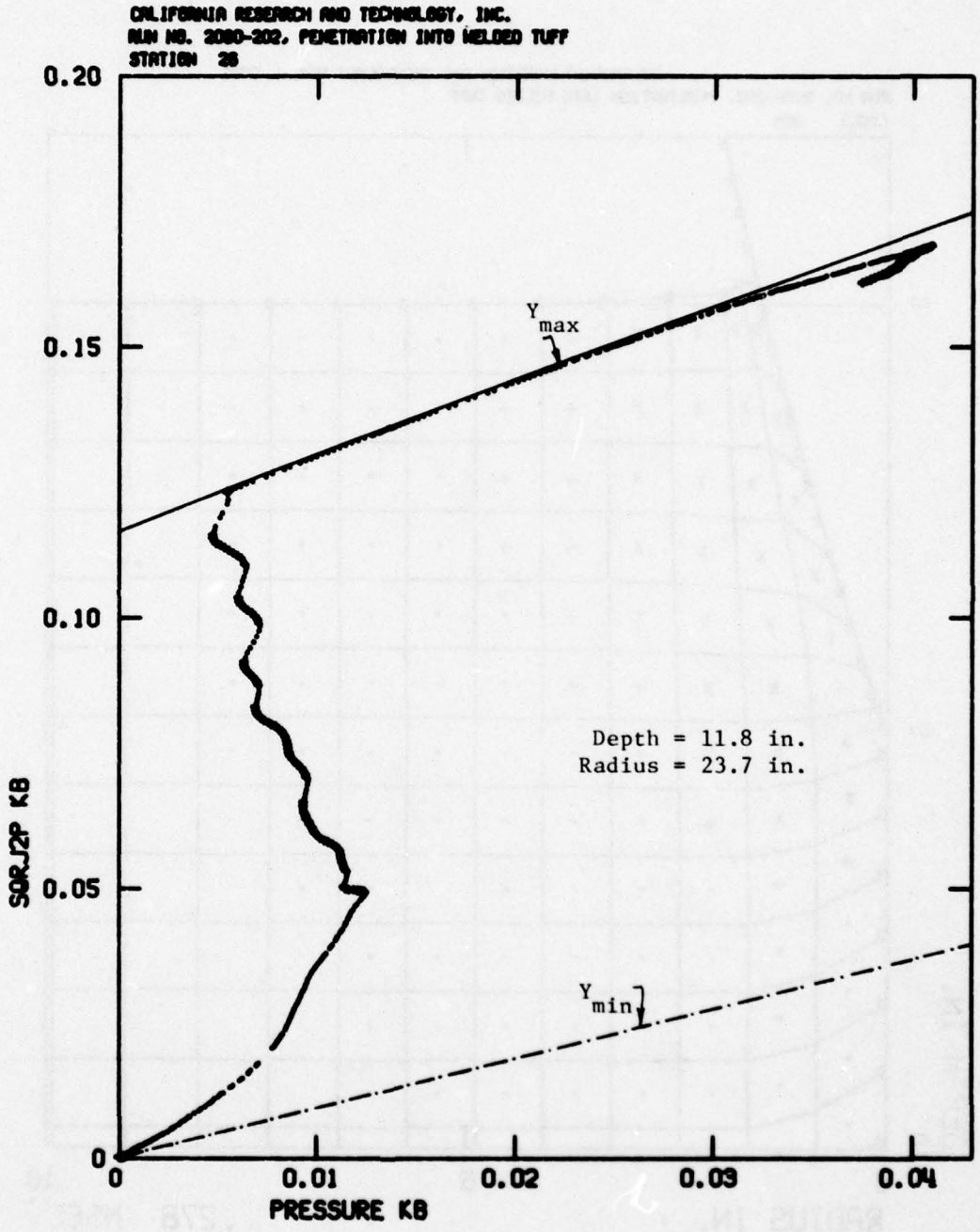


Figure B-46. Stess Path ($\sqrt{J_2'}$ vs P) at Station 26

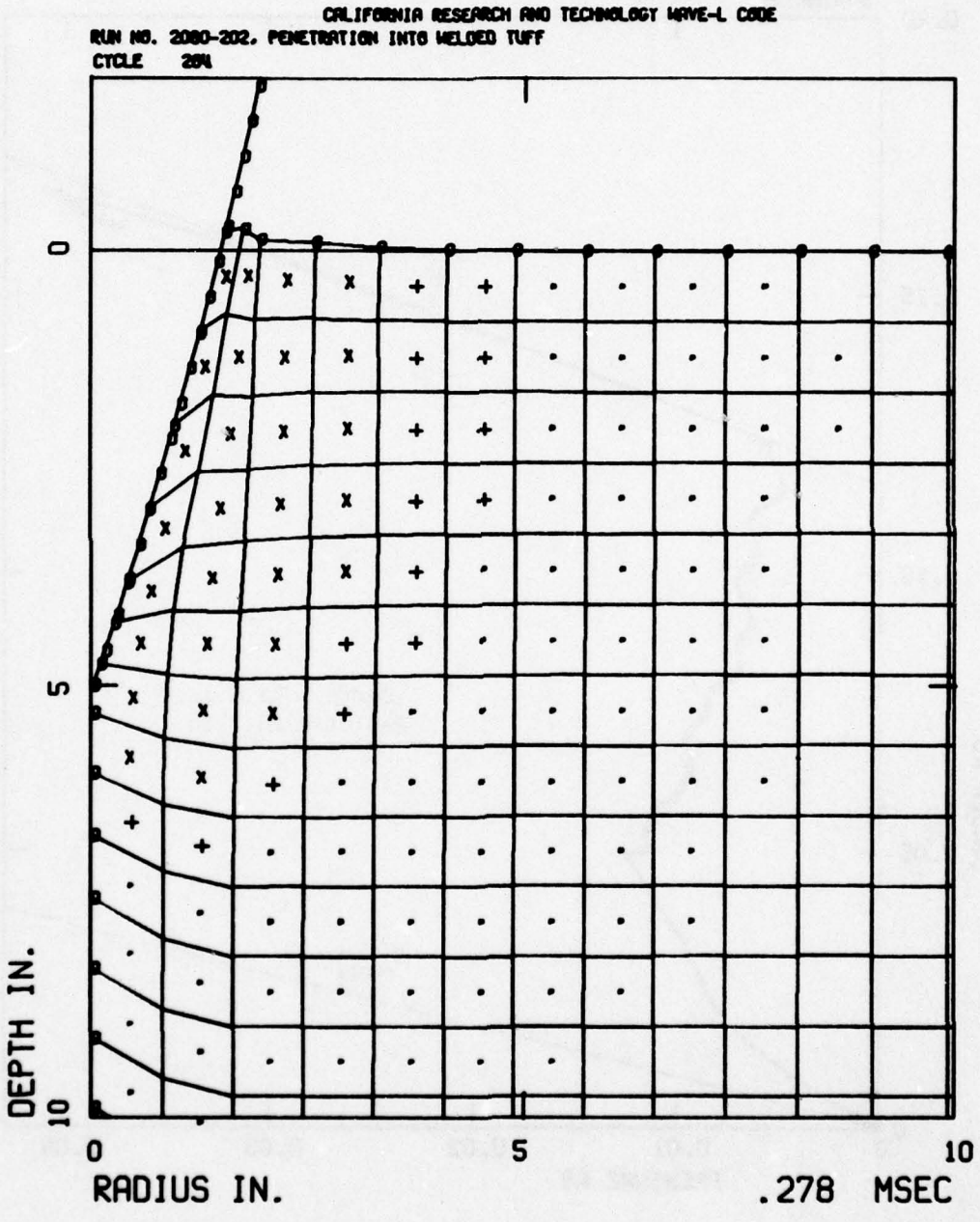


Figure B-47. Lagrangian Grid and Fracture Pattern in Welded Tuff at 5 in. Depth of Penetration

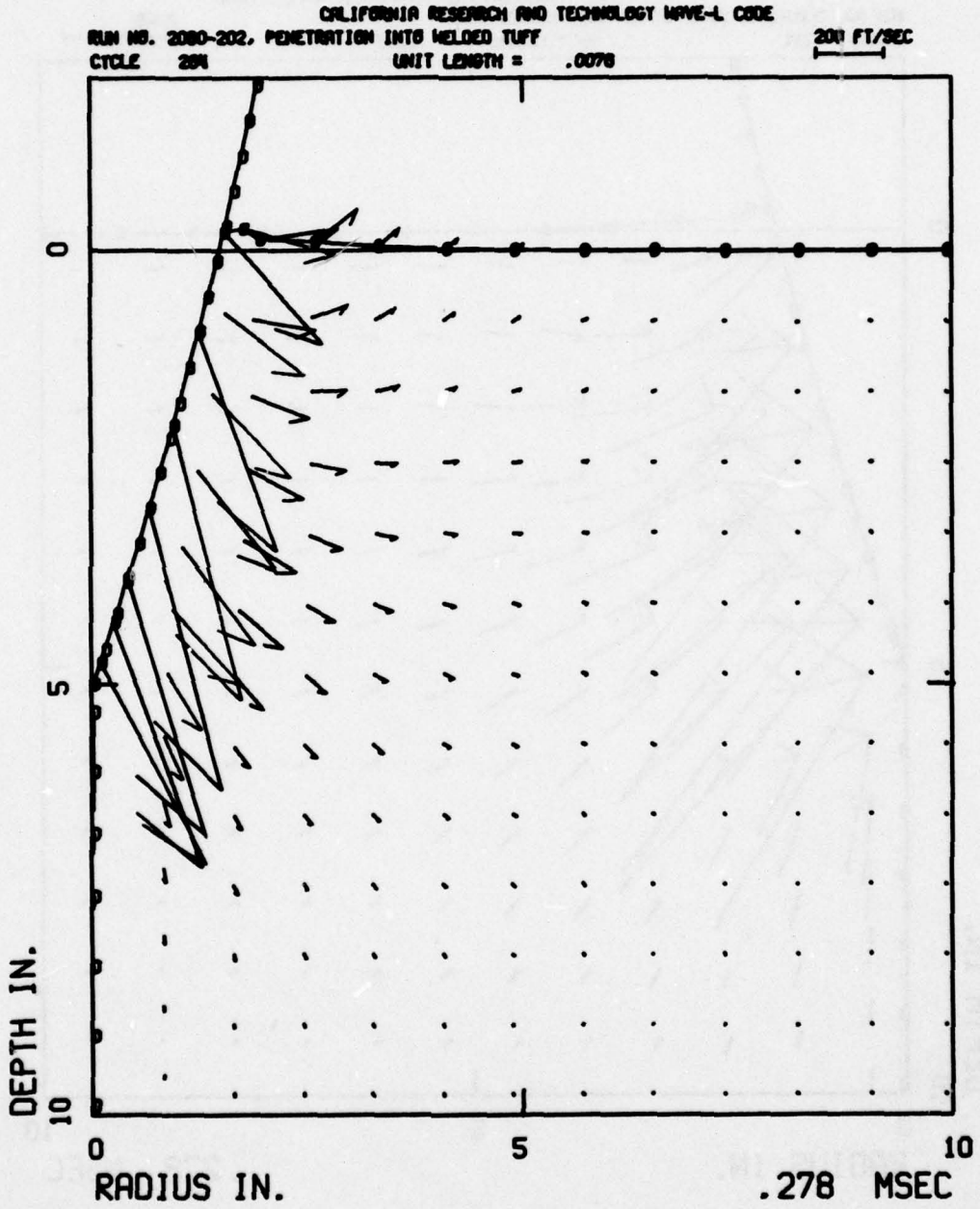


Figure B-48. Particle Velocity Field in Welded Tuff at 5 in. Depth of Penetration

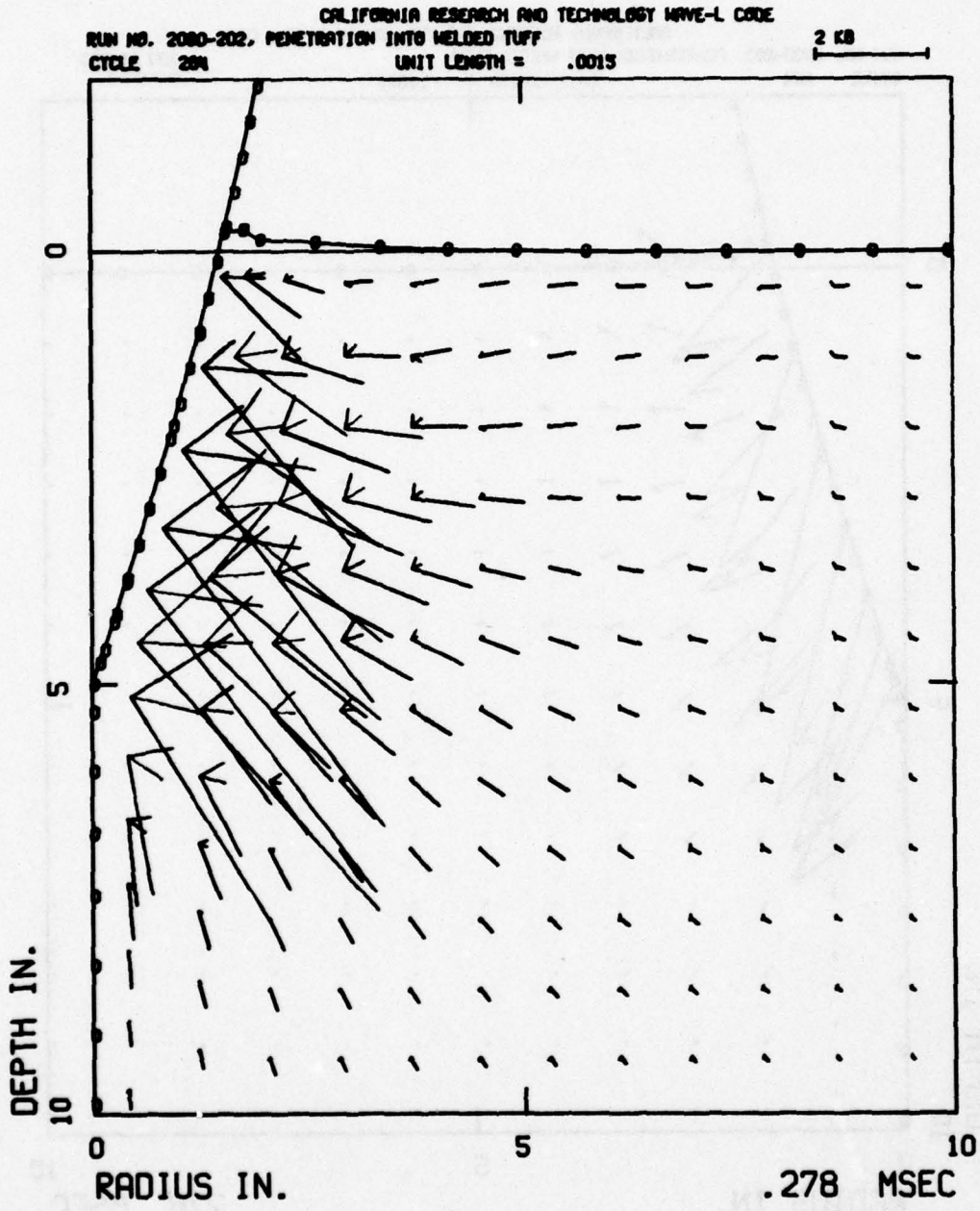


Figure B-49. Principal Stress Field in Welded Tuff at 5 in. Depth of Penetration

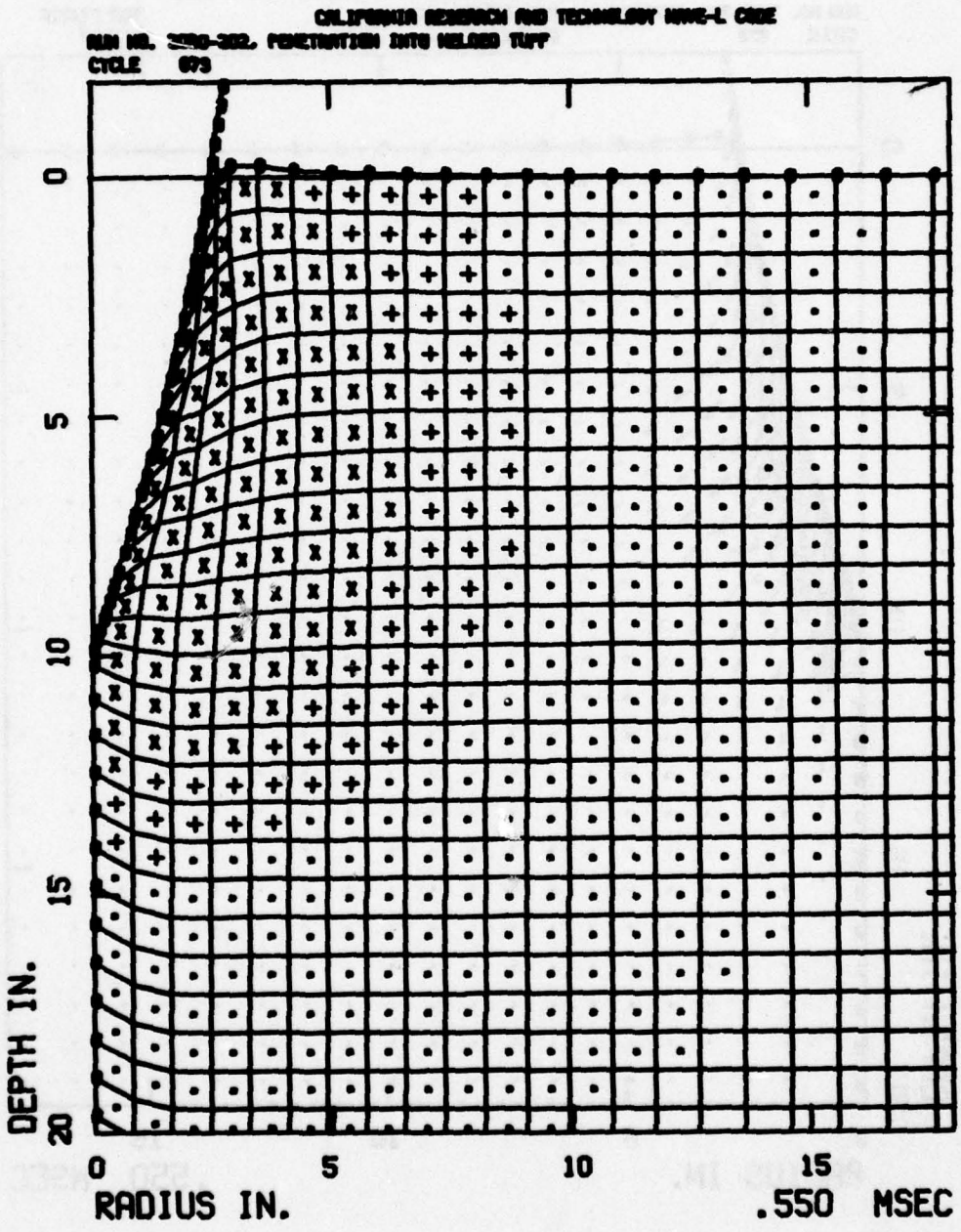


Figure B-50. Lagrangrian Grid and Fracture Pattern in Welded Tuff at 10 in. Depth of Penetration

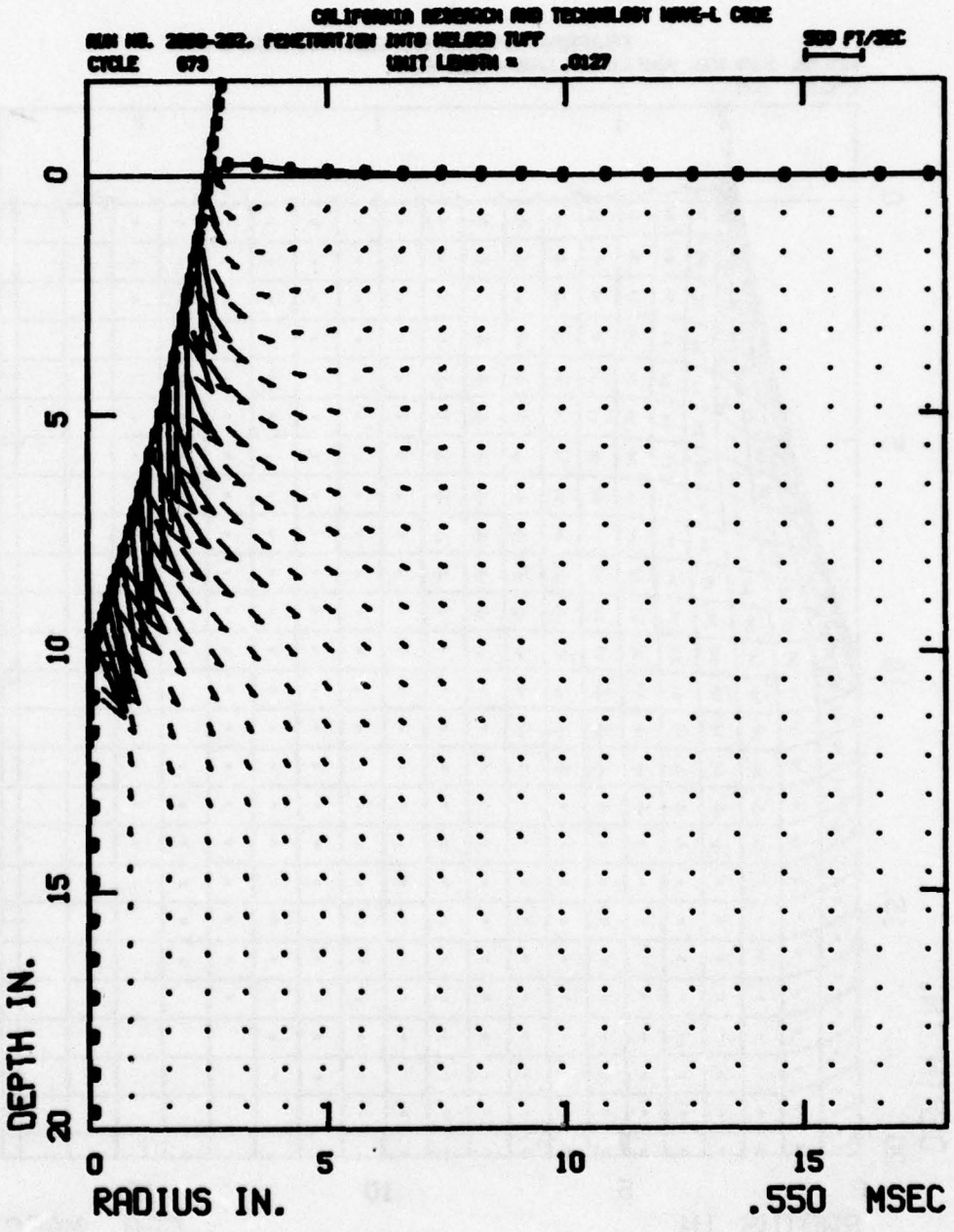


Figure B-51. Particle Velocity Field in Welded Tuff at 10 in. Depth of Penetration

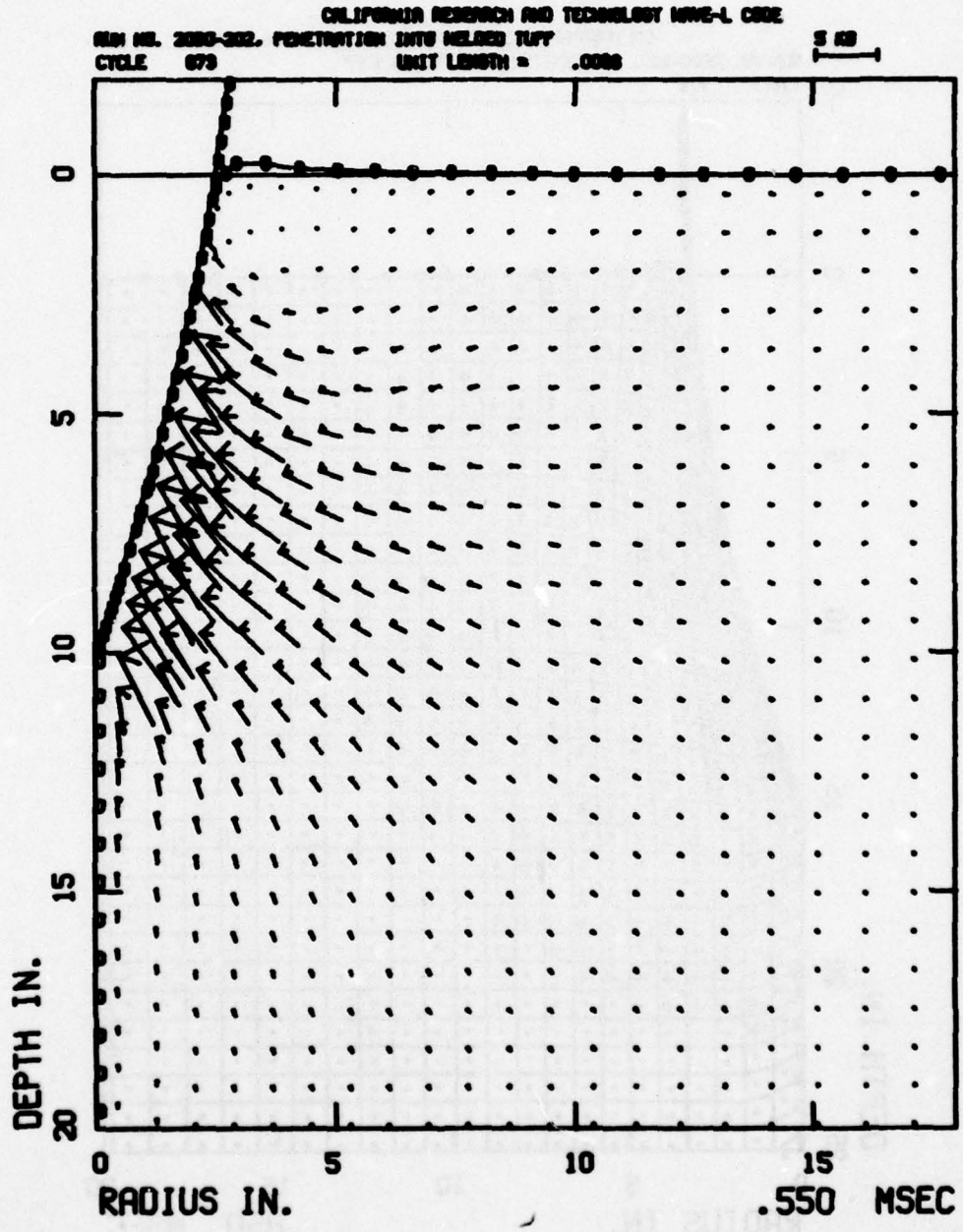


Figure B-52. Principal Stress Field in Welded Tuff at 10 in. Depth of Penetration

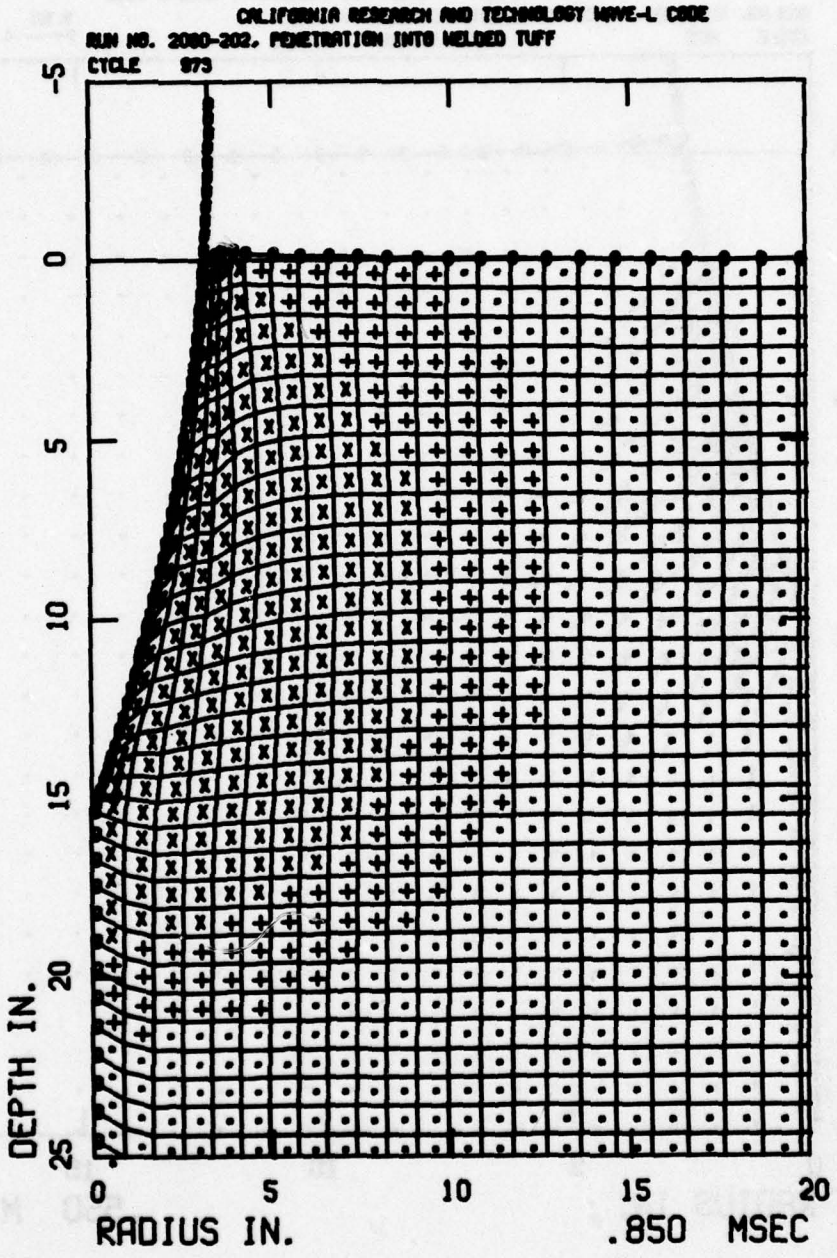


Figure B-53. Lagrangian Grid and Fracture Pattern in Welded Tuff at 15 in. Depth of Penetration

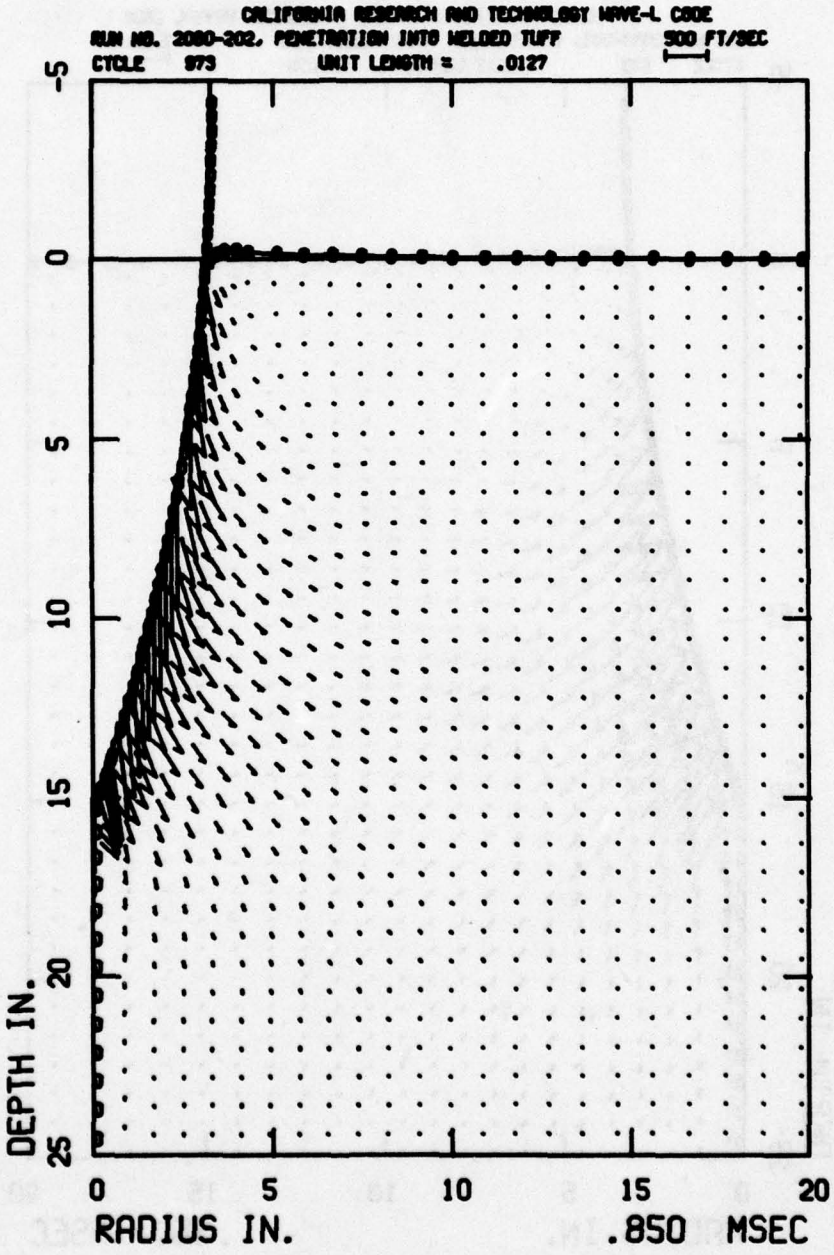


Figure B-54. Particle Velocity Field in Welded Tuff at 15 in. Depth of Penetration

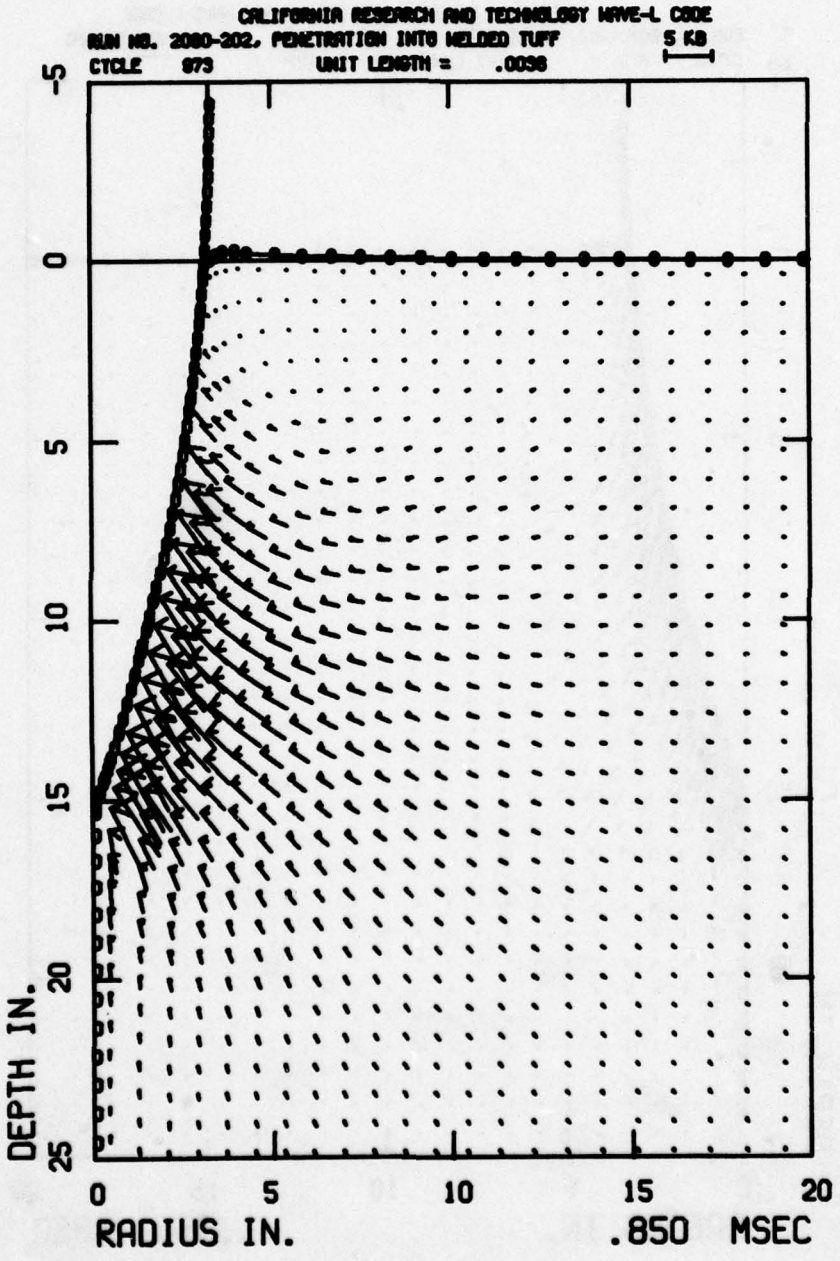


Figure B-55. Principal Stress Field in Welded Tuff at 15 in. Depth of Penetration

APPENDIX C

EXPLORATORY PENETRATION SOLUTION

A short exploratory calculation of the penetrator firing at the Tonopah site was conducted to assess the material model, in particular, the behavior of the comminution and post-fracture models, and to provide tentative pre-test information on expected penetrator stress loadings and stress levels in the ground. Also, at this point in the program, it was thought that the penetrator firing date was imminent, and it became desirable to provide some pre-test calculational results. As it turned out, the penetrator firing was subsequently postponed, giving time to determine new experimental properties data, revise the material model, and perform the principal penetration solution described in the main text.

This solution used the first material model developed, which included the newly formulated comminution and post-fracture models. The significant differences between this model and the subsequent revised model were that the comminuted rock was considerably weaker and that a lower frictional stress was applied. These differences are illustrated in comparative plots of the yield surfaces and the friction rules, Figures 13 and 16, Section 2.2.

To provide a shorter run-up time to peak loadings on the penetrator, this solution was started with the penetrator initially buried 5 in. into the ground. The initial Lagrangian grid is shown in Figure C-1. The tuff cells around the penetrator nose are initially unstressed and intact. The basic zoning in the target was ~.8 x .8 in. cells, or a zone width of 1/4 the projectile radius. The projectile was the same as previously described (Section 2.1), weighing 517 lb and having an initial velocity of 1500 ft/sec.

The calculation of the penetration was carried out to a time of .64 msec and a penetration depth of 16.4 in. The resulting time histories of penetrator deceleration and axial forces on the penetrator are shown in Figure C-2. These histories have an interesting character, in that there is a rapid build-up of force at early times as the tuff loads up to the fracture surface, followed by a reduction in force as the fractured material degrades in strength. After this initial excursion, the forces climb smoothly as the penetrator buries deeper. This excursion does not occur if the impact starts on the ground surface. The deceleration is seen to be leveling off at the end of the solution, having reached about 1800 g's. The contributions of force due to normal and frictional applied stresses are separately shown on the plot. At the end of the solution, 17% of the total axial force being applied was due to friction.

The ground response at the end of the solution, at t=.64 msec, is depicted in Figures C-3 to C-5, which show the Lagrangian grid and fracture regions, particle velocity field, and principal stress field. As discussed in Section 1.3, these results indicated that the material model appeared to be providing a qualitatively correct media response to penetration.

The normal and tangential stress distributions applied along the penetrator at t=.64 msec are shown in Figure C-6. The peak normal stress is 3.5 kb, occurring 1.4 in. back from the nose tip. The peak compressive stress occurring in the rock next to the penetrator as a function of depth is shown in Figure C-7. Except for the material initially next to the buried portion of the nose, the peak ground stress has an approximately constant level of 3.6 kb. Finally, profiles of radial stress vs radius along three horizontal planes next to the penetrator are shown in Figure C-8. These moderate-to-shallow stress gradients appear to be reasonably well-resolved with the zoning employed, as indicated by the dots on the curves.

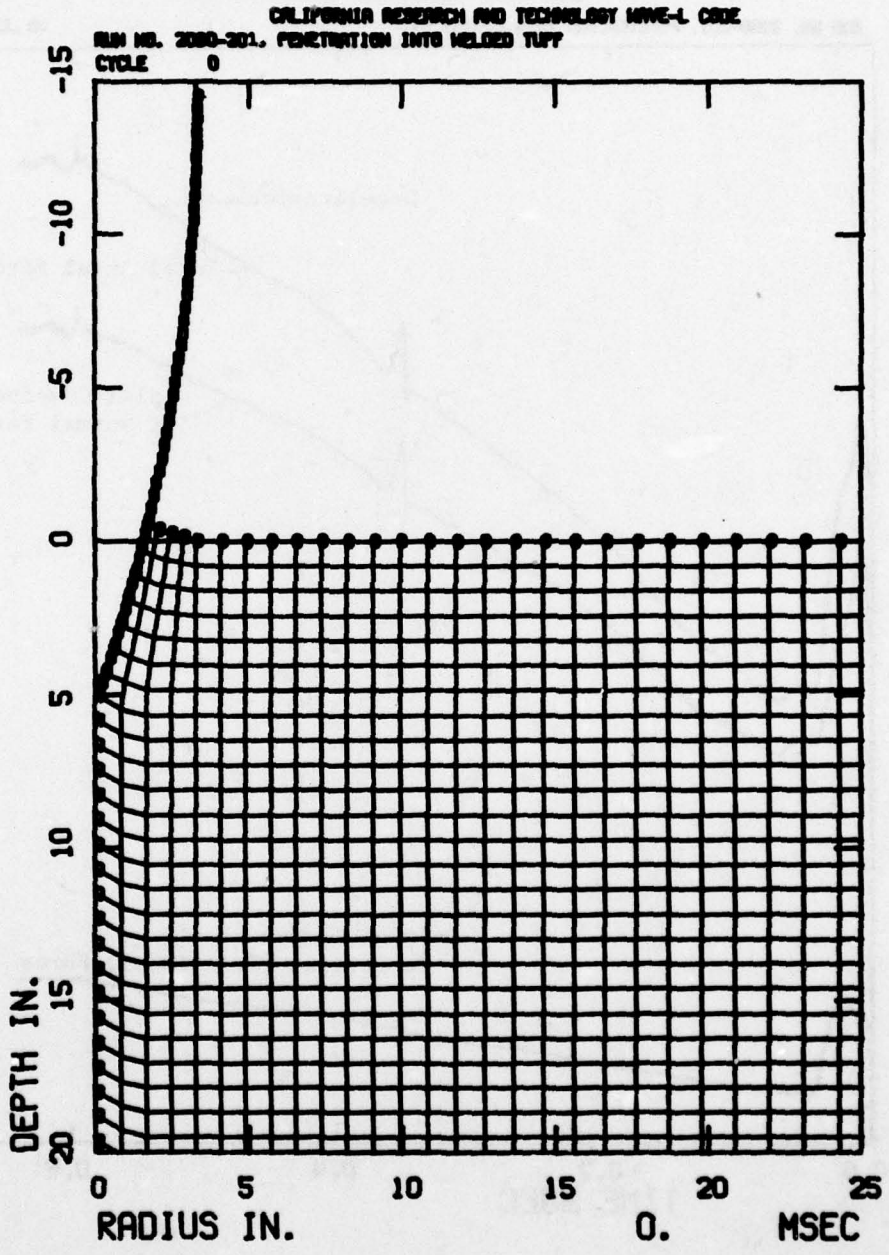


Figure C-1. Initial Computational Grid for Exploratory Solution of Penetration into Welded Tuff

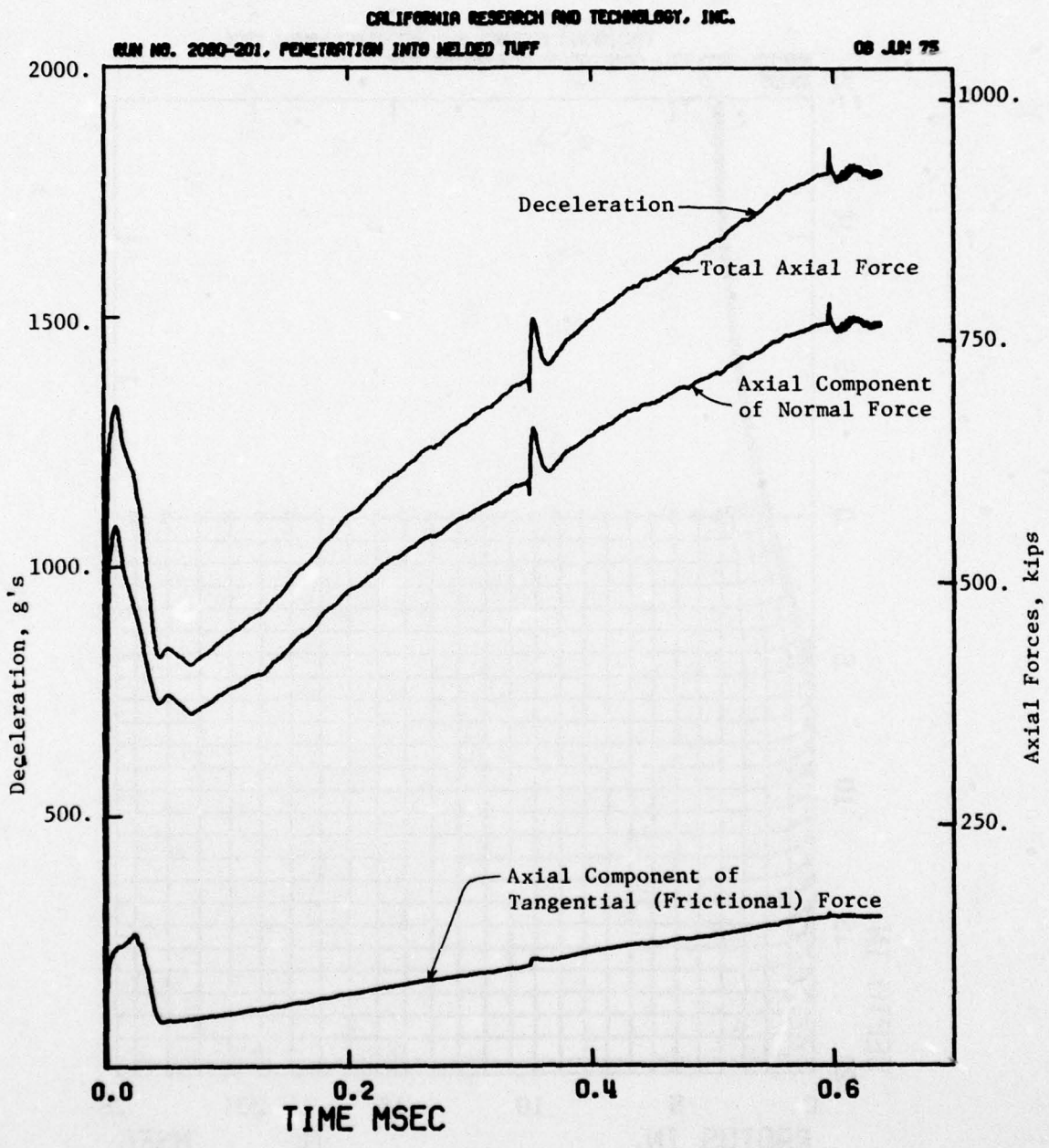


Figure C-2. Penetrator Deceleration and Axial Forces on Penetrator vs Time, Exploratory Solution

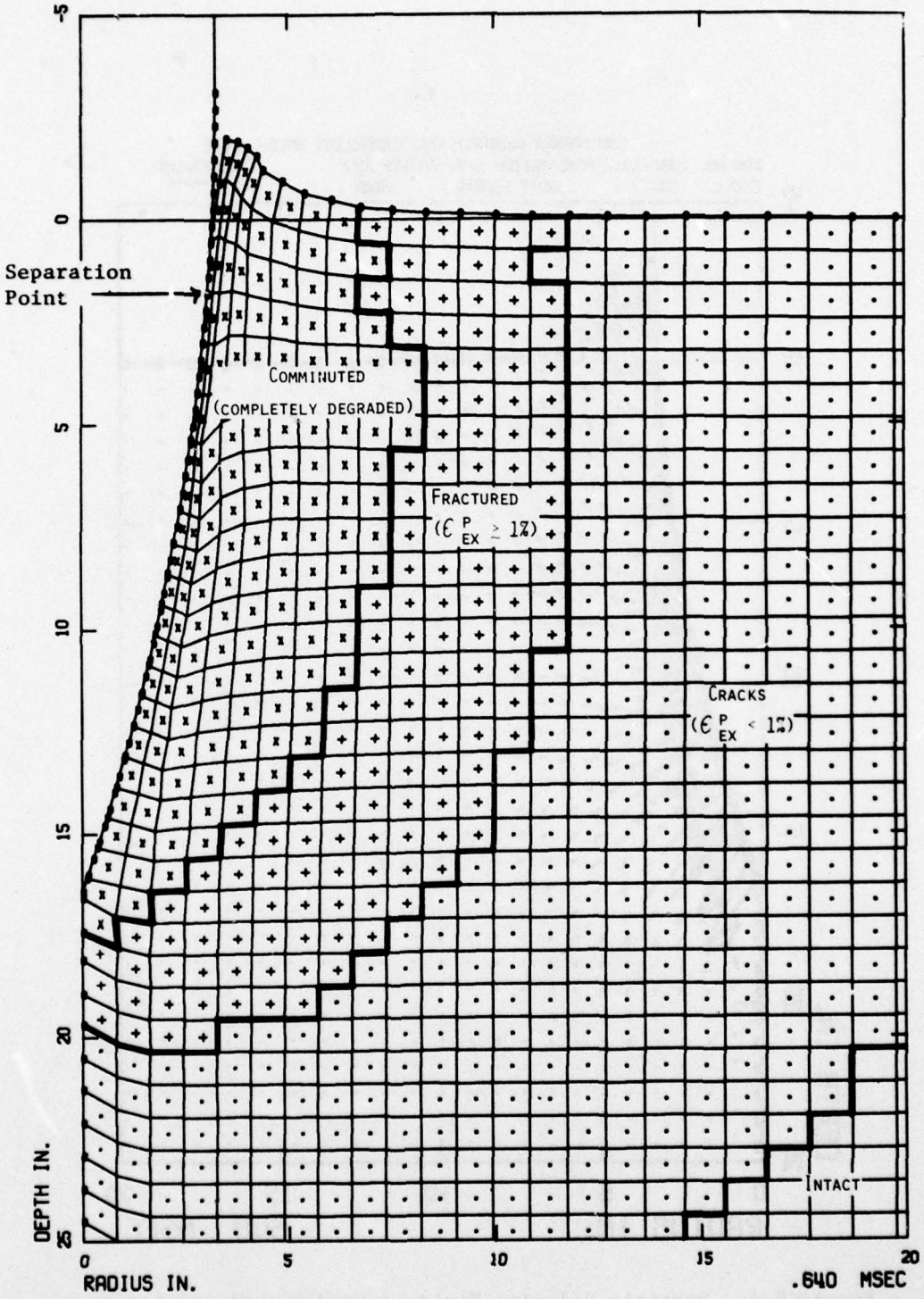


Figure C-3. Lagrangian Grid and Fracture Pattern in Welded Tuff, Exploratory Solution

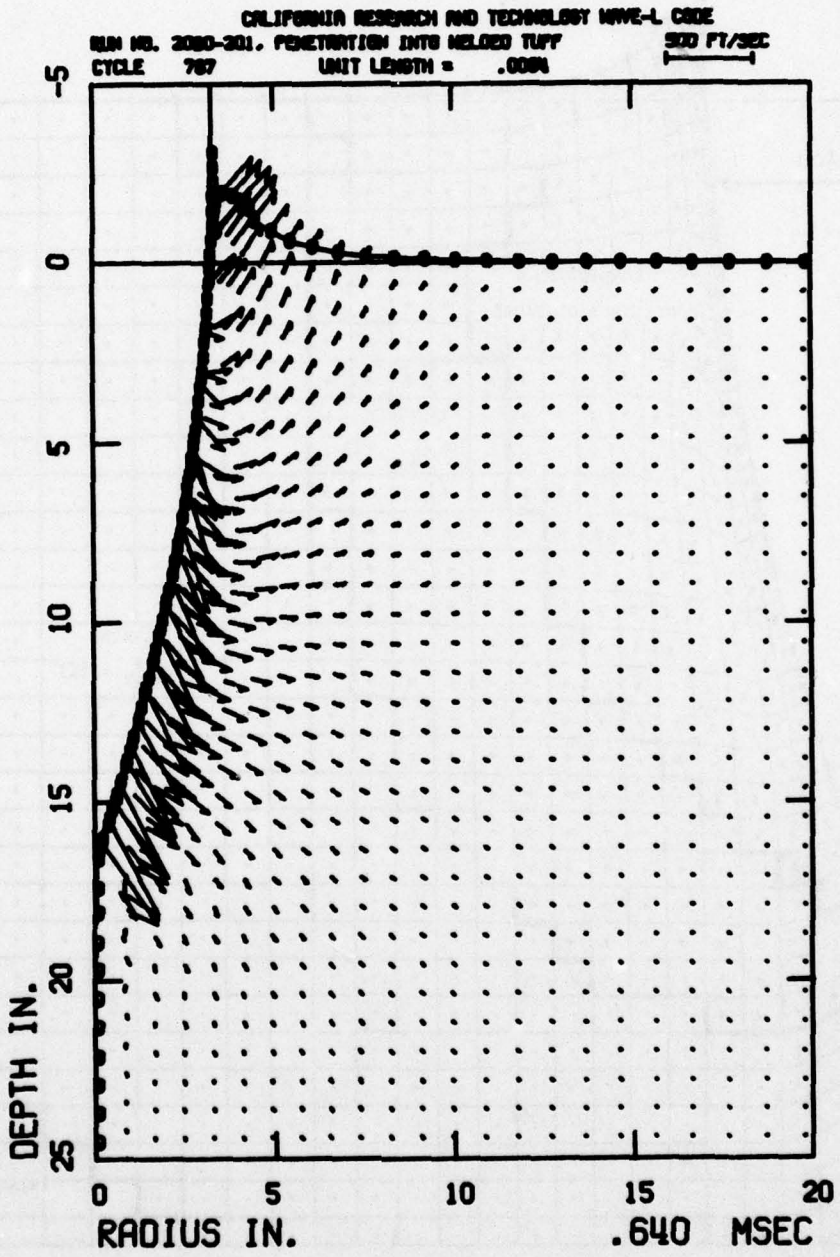


Figure C-4. Particle Velocity Field in Welded Tuff, Exploratory Solution

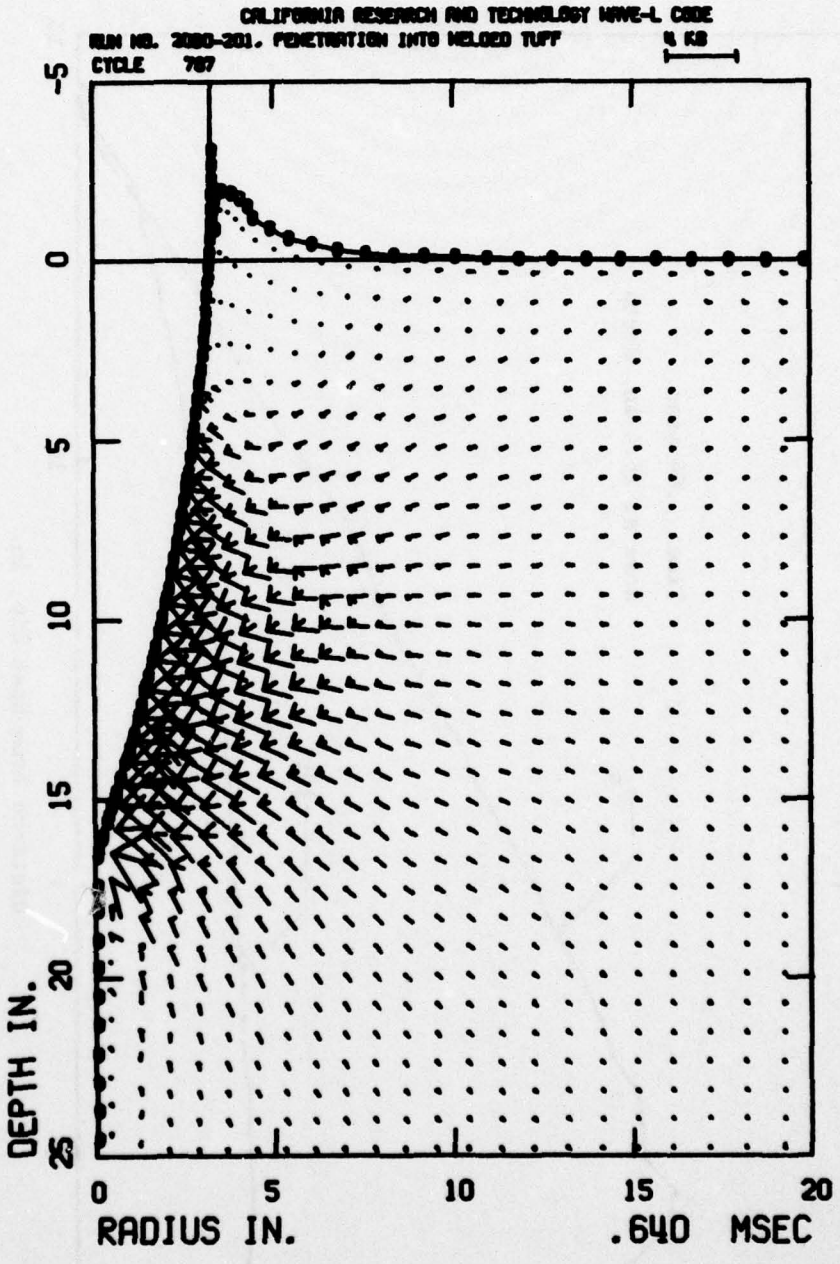


Figure C-5. Principle Stress Field in Welded Tuff, Exploratory Solution

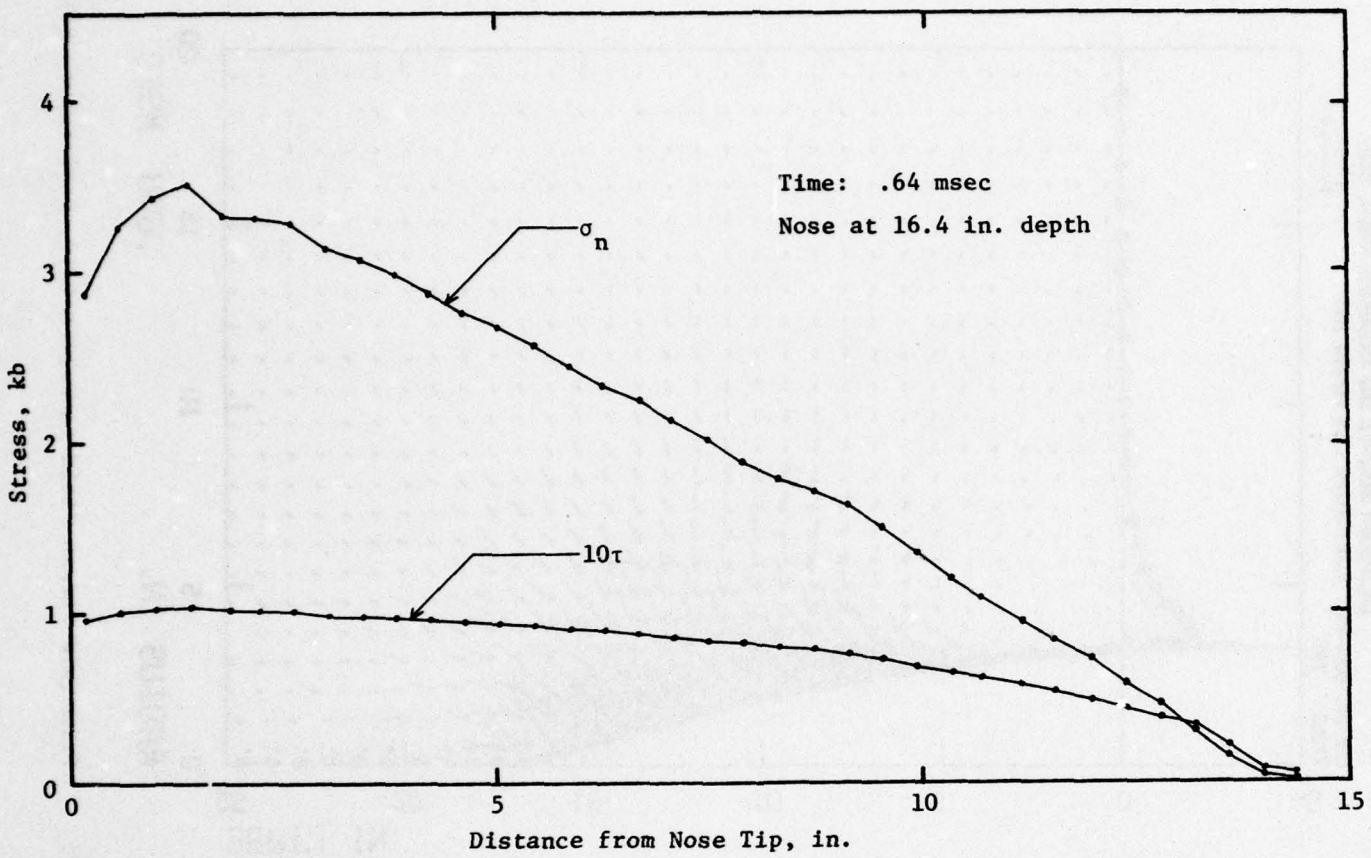


Figure C-6. Normal and Tangential Stress Distributions along Penetrator Nose

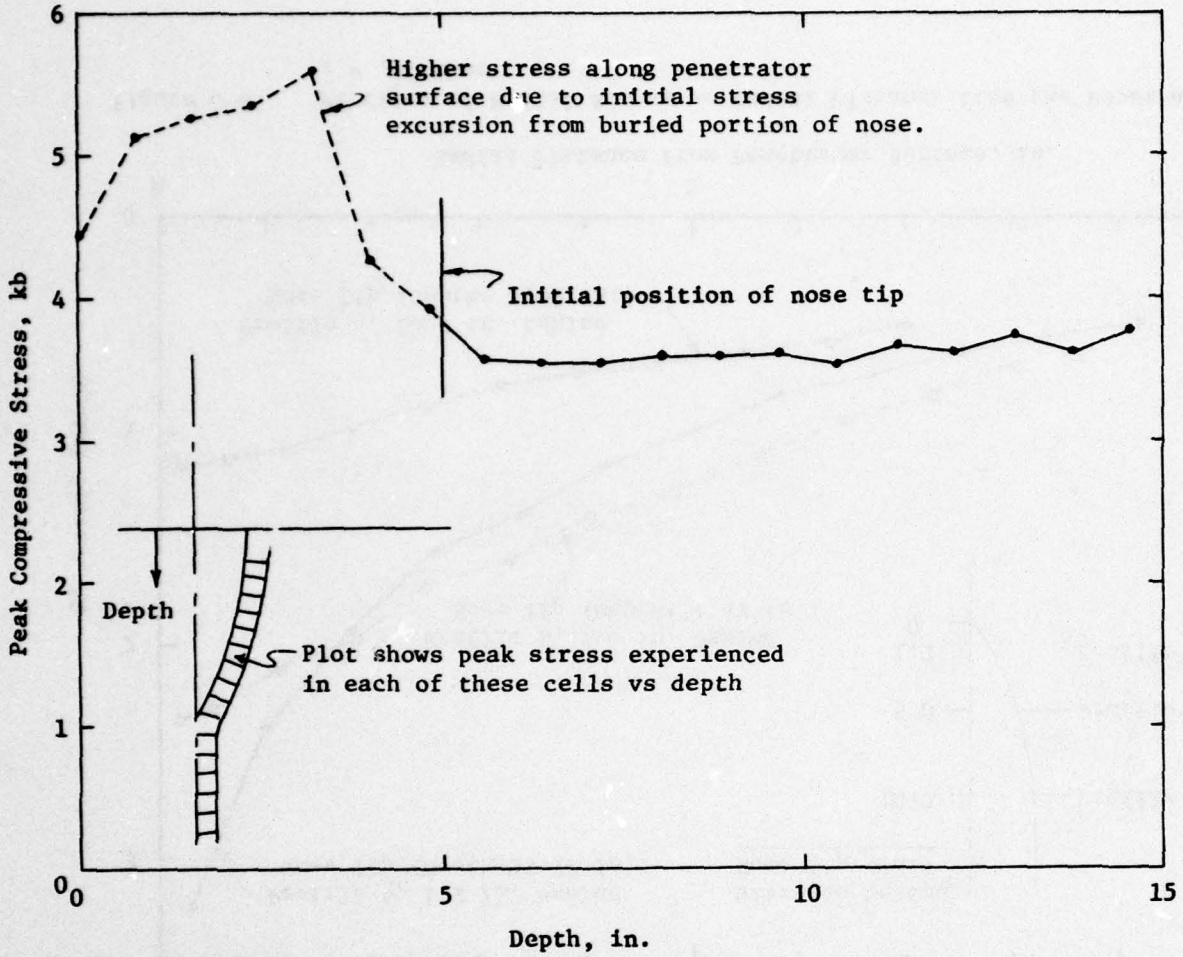


Figure C-7. Peak Compressive Stress in Welded Tuff Along Axis or Along Penetrator Surface

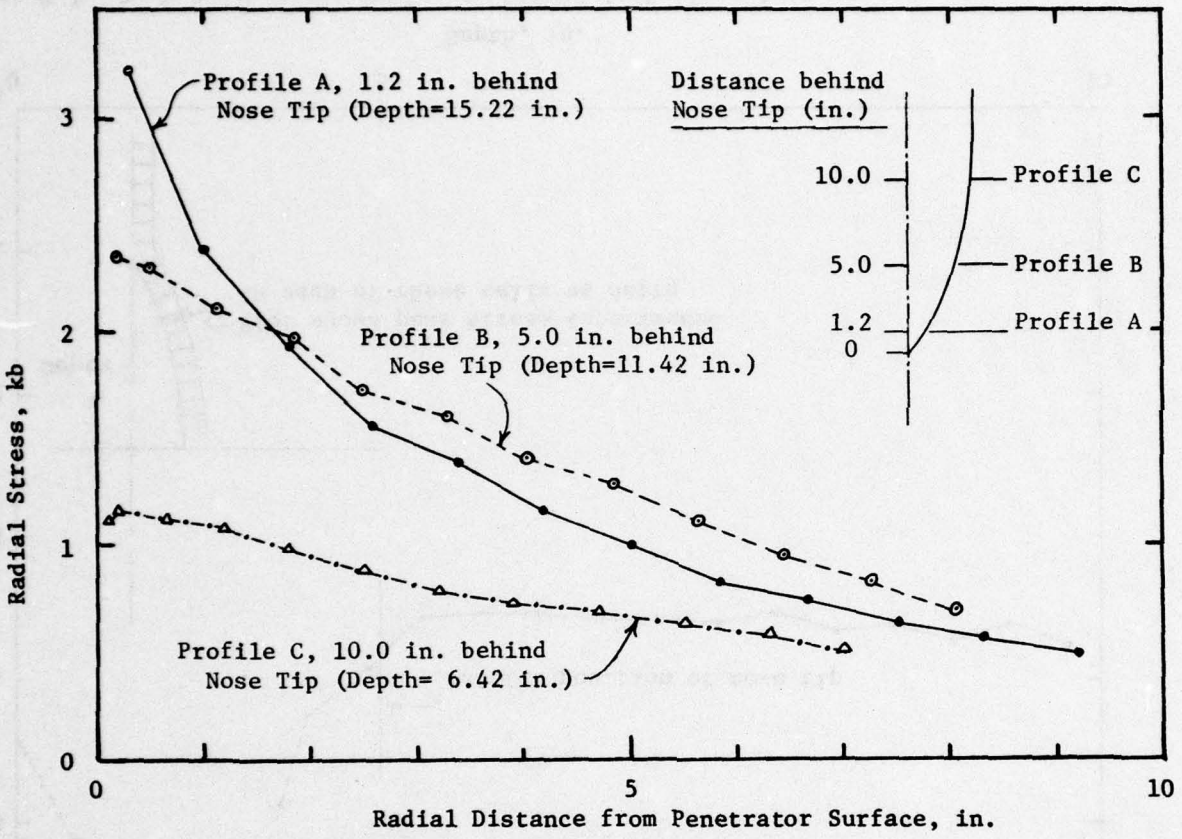


Figure C-8. Profiles of Radial Stress vs Radial Distance from the Penetrator, t = .64 msec

DISTRIBUTION LIST

DEPARTMENT OF DEFENSE

Director
Defense Advanced Rsch. Proj. Agency
ATTN: Technical Library
ATTN: NMRO

Director
Defense Civil Preparedness Agency
Assistant Director for Research
ATTN: Admin. Officer

Defense Documentation Center
Cameron Station
12 cy ATTN: TC

Director
Defense Intelligence Agency
ATTN: Technical Library

Director
Defense Nuclear Agency
2 cy ATTN: SPSS
ATTN: DDST
ATTN: SPAS
ATTN: TISI, Archives
3 cy ATTN: TITL, Tech. Library

Asst. to the Secretary of Defense
Atomic Energy
Department of Defense
ATTN: Honorable Donald R. Cotter
ATTN: Colonel R. N. Brodie

Dir. of Defense Rsch. & Engineering
Department of Defense
ATTN: S&SS (OS)
ATTN: AD/SW

Commander
Field Command
Defense Nuclear Agency
ATTN: FCPR

Director
Interservice Nuclear Weapons School
ATTN: Document Control

Director
Joint Strat. Target Planning Staff, JCS
ATTN: STINFO Library

Chief
Livermore Division, Field Command, DNA
Lawrence Livermore Laboratory
ATTN: FCPRL

Director
Defense Mapping Agency
ATTN: H. Lindsey

DEPARTMENT OF THE ARMY

Dep. Chief of Staff for Rsch. Dev. & Acq.
Department of the Army
ATTN: DAMA-CSM-N, LTC G. Ogden
ATTN: Technical Library
ATTN: DAMA(CS), Major A. Gleim

Chief of Engineers
Department of the Army
2 cy ATTN: DAEN-MCE-D
2 cy ATTN: DAEN-RDM

Deputy Chief of Staff for Ops. & Plans
Department of the Army
ATTN: Dir. of Chem. & Nuc. Ops.
ATTN: Technical Library

Chief
Engineer Strategic Studies Group
ATTN: DAEN-FES

Commander
Frankford Arsenal
ATTN: L. Baldini

Project Manager
Gator Mine Program
ATTN: E. J. Linddsey

Commander
Harry Diamond Laboratories
ATTN: DRXDO-NP
ATTN: DRXDO-RBH, James H. Gwaltney

Commander
Picatinny Arsenal
ATTN: B. Shulman, DR-DAR-L-C-FA
ATTN: SMUPA-AD-D-A-7
ATTN: Paul Harris
ATTN: P. Angelloti
ATTN: SMUPA-AD-D-M
ATTN: SMUPA-AD-D-A
ATTN: Jerry Pental
ATTN: Technical Library
ATTN: Marty Margolin
ATTN: Ernie Zimpo
ATTN: Ray Moesner

Commander
Redstone Scientific Information Center
US Army Missile Command
ATTN: Chief, Documents

Commander
US Army Armament Command
ATTN: Tech. Lib.

Commander & Director
US Army Cold Region Res. Engr. Lab.
ATTN: G. Swinzow

DEPARTMENT OF THE ARMY (Continued)

Director
US Army Ballistic Research Labs.
ATTN: J. W. Apgar
2 cy ATTN: Tech. Lib., Edward Baicy
ATTN: A. Ricchiazzi
ATTN: G. Roecker
ATTN: G. Grabarek
ATTN: DRXBR-TB
ATTN: J. H. Keefer, DRDAR-BLE
ATTN: DRXBR-X

Commander
US Army Comb. Arms Combat Dev. Acty.
ATTN: LTC Pullen
ATTN: LTC G. Steger

Commander
US Army Engineer Center
ATTN: ATSE-DT-LRC

Division Engineer
US Army Engineer Div. Huntsville
ATTN: HNDED-SR

Division Engineer
US Army Engineer Div. Missouri River
ATTN: Tech. Library

Commandant
US Army Engineer School
ATTN: ATSE-DTA-ADM
ATTN: ATSE-CD-CS

Director
US Army Engr. Waterways Exper. Sta.
ATTN: John N. Strange
ATTN: P. Hadala
ATTN: Technical Library
ATTN: Leo Ingram
ATTN: Guy Jackson
ATTN: Behzad Rohani
ATTN: William Flathau
ATTN: D. K. Butler

Commander
US Army Mat. & Mechanics Rsch. Center
ATTN: Technical Library

Commander
US Army Materiel Dev. & Readiness Command
ATTN: Technical Library

Director
US Army Materiel Sys. Analysis Acty.
ATTN: Joseph Sperazza

Commander
US Army Missile Command
ATTN: W. Jann
ATTN: F. Fleming
ATTN: J. Hogan

Commander
US Army Mobility Equip. R & D Center
ATTN: Technical Library
ATTN: STSFB-MW
ATIN: STSFB-XS

DEPARTMENT OF THE ARMY (Continued)

Commander
US Army Nuclear Agency
ATTN: Doc. Con.
ATTN: Tech. Lib.

Commander
US Army Training & Doctrine Command
ATTN: LTC J. Foss
ATTN: LTC Auveduti, COL Enger

Commandant
US Army War College
ATTN: Library

US Army Mat. Command Proj. Mngr. for Nuc. Munitions
ATTN: DRCPM-NUC

DEPARTMENT OF THE NAVY

Chief of Naval Operations
Navy Department
ATTN: OP 982, LTC Dubac
ATTN: Code 604C3, Robert Piacesi
ATTN: OP 982, LCDR Smith
ATTN: OP 982, CAPT Toole

Chief of Naval Research
Navy Department
ATTN: Technical Library

Officer-in-Charge
Civil Engineering Laboratory
Naval Construction Battalion Center
ATTN: Technical Library
ATTN: R. J. Odello

Commandant of the Marine Corps
Navy Department
ATTN: POM

Commanding General
Development Center
Fire Support Branch
MCDEC
ATTN: CAPT Hartneady
ATTN: LTC Gapenski

Commander
Naval Air Systems Command
Headquarters
ATTN: F. Marquardt

Commanding Officer
Naval Explosive Ord. Disposal Fac.
ATTN: Code 504, Jim Petrousky

Commander
Naval Facilities Engineering Command
Headquarters
ATTN: Technical Library

Superintendent (Code 1424)
Naval Postgraduate School
ATTN: Code 2124, Tech. Rpts. Librarian

Director
Naval Research Laboratory
ATTN: Code 2600, Tech. Lib.

DEPARTMENT OF THE NAVY (Continued)

Commander
Naval Sea Systems Command
Navy Department
ATTN: SEA-9931G
ATTN: ORD-033

Officer-in-Charge
Naval Surface Weapons Center
ATTN: Code WX21, Tech. Lib.
ATTN: M. Kleinerman
ATTN: Code WA501, Navy Nuc. Prgms. Off.

Commander
Naval Surface Weapons Center
Dahlgren Laboratory
ATTN: Technical Library

Commander
Naval Weapons Center
ATTN: Code 533, Tech. Lib.
ATTN: Carl Austin

Commanding Officer
Naval Weapons Evaluation Facility
ATTN: Technical Library

Director
Strategic Systems Project Office
Navy Department
ATTN: NSP-43, Tech. Lib.

DEPARMENT OF THE AIR FORCE

AF Armament Laboratory, AFSC
ATTN: Masey Valentine
3 cy ATTN: John Collins, AFATL/DLYV

AF Institute of Technology, AU
ATTN: Library AFIT Bldg. 640, Area B

AF Weapons Laboratory, AFSC
ATTN: SUL

Headquarters
Air Force Systems Command
ATTN: Technical Library

Assistant Secretary of the Air Force
Research & Development
Headquarters, US Air Force
ATTN: Col R. E. Steere

Commander
Armament Development & Test Center
ATTN: Tech. Lib.

Deputy Chief of Staff
Research & Development
Headquarters, US Air Force
ATTN: Col J. L. Gilbert

Commander
Foreign Technology Division, AFSC
ATTN: NICD, Library

Hq. USAF/IN
ATTN: INATA

DEPARTMENT OF THE AIR FORCE (Continued)

Hq. USAF/RD
ATTN: RDPM

Oklahoma State University
Fld. Off. for Wpns. Effectiveness
ATTN: Edward Jackett

Commander
Rome Air Development Center, AFSC
ATTN: EMTLD, Doc. Library

SAMSO/RS
ATTN: RSS

ENERGY RESEARCH & DEVELOPMENT ADMINISTRATION

Division of Military Application
US Energy Research & Dev. Admin.
ATTN: Doc. Con. for Test Office

University of California
Lawrence Livermore Laboratory
ATTN: Mark Wilkins, L-504
ATTN: Jerry Goudreau
ATTN: Tech. Info. Dept. L-3
ATTN: M. Fernandez

Los Alamos Scientific Laboratory
ATTN: Doc. Con. for Reports Lib.
ATTN: Doc. Con. for Tom Dowler

Sandia Laboratories
Livermore Laboratory
ATTN: Doc. Con. for Tech. Library

Sandia Laboratories
ATTN: Doc. Con. for John Keizur
ATTN: Doc. Con. for W. Altsmeirer
ATTN: Doc. Con. for John Colp
ATTN: Doc. Con. for 3141, Sandia Rpt. Coll.
ATTN: Doc. Con. for William Caudle
ATTN: Doc. Con. for Walter Herrmann
ATTN: Doc. Con. for William Patterson

US Energy Rsch. & Dev. Admin.
Albuquerque Operations Office
ATTN: Doc. Con. for Tech. Library

US Energy Rsch. & Dev. Admin.
Division of Headquarters Services
Library Branch G-043
ATTN: Doc. Con. for Class Tech. Lib.

US Energy Rsch. & Dev. Admin.
Nevada Operations Office
ATTN: Doc. Con. for Tech. Lib.

OTHER GOVERNMENT AGENCIES

NASA
Ames Research Center
ATTN: Robert W. Jackson

Office of Nuclear Reactor Regulation
Nuclear Regulatory Commission
ATTN: Lawrence Shao
ATTN: Robert Heineman

DEPARTMENT OF DEFENSE CONTRACTORS

Aerospace Corporation
ATTN: Tech. Info. Services

Agbabian Associates
ATTN: M. Agbabian

Applied Theory, Inc.
2 cy ATTN: John G. Trulio

Avco Research & Systems Group
ATTN: Research Lib., A830, Rm. 7201
ATTN: S. Skemp, J200
ATTN: Pat Grady
ATTN: David Henderson

Battelle Memorial Institute
ATTN: Technical Library

The BDM Corporation
ATTN: Technical Library

The Boeing Company
ATTN: Aerospace Library
ATTN: Reynold Atlas

California Research & Technology, Inc.
ATTN: Technical Library
ATTN: Ken Kreyenhagen
ATTN: M. H. Wagner
ATTN: C. C. Fulton

Civil/Nuclear Systems Corp.
ATTN: Robert Crawford

EG&G, Inc.
Albuquerque Division
ATTN: Technical Library

Communications Satellite Corp.
ATTN: Jim Petrousky

Engineering Societies Library
ATTN: Ann Mott

General Dynamics Corp.
Pomona Division
ATTN: Keith Anderson

General Electric Company
TEMPO-Center for Advanced Studies
ATTN: DASIAC

Georgia Institute of Technology
Georgia Tech. Research Institute
ATTN: S. V. Hanagud
ATTN: L. W. Rehfield

Honeywell Incorporated
Defense Systems Division
ATTN: T. N. Helvig

Institute for Defense Analyses
ATTN: IDA Librarian, Ruth S. Smith

Kaman Sciences Corporation
ATTN: Library

DEPARTMENT OF DEFENSE CONTRACTORS (Continued)

Kaman AviDyne
Division of Kaman Sciences Corp.
ATTN: Norman P. Hobbs
ATTN: Technical Library
ATTN: E. S. Criscione

Lockheed Missiles & Space Company, Inc.
ATTN: M. Culp
ATTN: Technical Library

Lockheed Missiles & Space Company, Inc.
ATTN: Tech. Info. Center D/COLL

General Electric Company
Re-Entry & Envir. Sys. Div.
ATTN: L. D. Audrea

Martin Marietta Aerospace
Orlando Division
ATTN: Al Cowen
ATTN: H. McQuaig
ATTN: M. Anthony

Merritt CASES, Incorporated
ATTN: J. L. Merritt
ATTN: Technical Library

University of New Mexico
Dept. of Campus Security & Police
ATTN: G. E. Triandafalidis

Nathan M. Newmark
Consulting Engineering Services
B106A Civil Engineering Building
University of Illinois
ATTN: W. Hall
ATTN: Nathan M. Newmark

Electric Power Research Inst.
ATTN: George Sliter

Pacifica Technology
ATTN: G. Kent
ATTN: R. Bjork

Physics International Company
ATTN: Doc. Con. for Tech. Lib.
ATTN: Doc. Con. for Larry A. Behrmann
ATTN: Doc. Con. for Charles Godfrey
ATTN: Doc. Con. for Dennis Orphal

R & D Associates
ATTN: Paul Rausch
ATTN: Arlen Fields
ATTN: Harold L. Brode
ATTN: William B. Wright, Jr.
ATTN: Technical Library
ATTN: J. G. Lewis
ATTN: Henry Cooper
ATTN: Cyrus P. Knowles

The Rand Corporation
ATTN: Technical Library

Science Applications, Inc.
ATTN: Technical Library

DEPARTMENT OF DEFENSE CONTRACTORS (Continued)

Stanford Research Institute
ATTN: George R. Abrahamson

Systems, Science & Software, Inc.
ATTN: Robert Sedgewick
ATTN: Edward Gaffney
ATTN: Technical Library

Terra Tek, Inc.
ATTN: Technical Library
ATTN: A. H. Jones
ATTN: Sidney Green

TRW Defense & Space Sys. Group
ATTN: Peter K. Dai, R1/2170
ATTN: Tech. Info. Center/S-1930

DEPARTMENT OF DEFENSE CONTRACTORS (Continued)

TRW Defense & Space Sys. Group
San Bernardino Operations
ATTN: E. Y. Wong, 527/712

Weidlinger Assoc. Consulting Engineers
ATTN: J. M. McCormick
ATTN: Melvin L. Baron

Weidlinger Assoc. Consulting Engineers
ATTN: J. Isenberg